processes

Special Issue Reprint

Synthesis and Applications of Nanomaterials

Edited by
Keith J. Stine

mdpi.com/journal/processes

MDPI

Synthesis and Applications of Nanomaterials

Synthesis and Applications of Nanomaterials

Guest Editor

Keith J. Stine

MDPI

Basel • Beijing • Wuhan • Barcelona • Belgrade • Novi Sad • Cluj • Manchester

Guest Editor
Keith J. Stine
Chemistry and Biochemistry
University of Missouri – Saint
Louis
Saint Louis
USA

Editorial Office
MDPI AG
Grosspeteranlage 5
4052 Basel, Switzerland

This is a reprint of the Special Issue, published open access by the journal *Processes* (ISSN 2227-9717), freely accessible at: https://www.mdpi.com/journal/processes/special_issues/Z64S4QU9LH.

For citation purposes, cite each article independently as indicated on the article page online and as indicated below:

Lastname, A.A.; Lastname, B.B. Article Title. *Journal Name* **Year**, *Volume Number*, Page Range.

ISBN 978-3-7258-8813-9 (Hbk)
ISBN 978-3-7258-8814-6 (PDF)
https://doi.org/10.3390/books978-3-7258-8814-6

© 2026 by the authors. Articles in this reprint are Open Access and distributed under the Creative Commons Attribution (CC BY) license. The reprint as a whole is distributed by MDPI under the terms and conditions of the Creative Commons Attribution-NonCommercial-NoDerivs (CC BY-NC-ND) license (https://creativecommons.org/licenses/by-nc-nd/4.0/).

Contents

About the Editor . . . . . **vii**

Keith J. Stine
Special Issue: Synthesis and Applications of Nanomaterials
Reprinted from: *Processes* **2026**, *14*, 1896, https://doi.org/10.3390/pr14121896 . . . . . **1**

Moudo Thiam, Vanessa O. Arnoldi Pellegrini, Ruth Celestina Condori Mamani, Fernanda Cassieri, Haryne Lizandrey Azevedo Furtado, Michael Santos Ribeiro, et al.
Antibacterial Activity and Photocatalytic Properties of Zinc Oxide Nanoparticles Biosynthesized Using *Licania tomentosa* Leaf Extract: Optimization and Kinetic Studies
Reprinted from: *Processes* **2026**, *14*, 1334, https://doi.org/10.3390/pr14091334 . . . . . **5**

Todor Batakliev, Evgeni Ivanov, Vladimir Georgiev, Verislav Angelov and Rumiana Kotsilkova
Design of Carbon Nanocomposites Based on PLA and PCL—From Microscratch Testing to Self-Healing Behavior
Reprinted from: *Processes* **2026**, *14*, 956, https://doi.org/10.3390/pr14060956 . . . . . **36**

Young Seo Kim and Gye Seok An
Tailored Shell Engineering of γ-Fe_2O_3@SiO_2 Nanoparticles for High-Performance and Recyclable Chemical Mechanical Planarization
Reprinted from: *Processes* **2026**, *14*, 902, https://doi.org/10.3390/pr14060902 . . . . . **48**

Ana Paula Souza de Sousa, Haianny Beatriz Saraiva Lima, Deibson Silva da Costa, Emerson Cardoso Rodrigues, Caroline Borges Agustini, Liliana Amaral Féris and Diego Cardoso Estumano
A Proposal for the Incorporation of Temperature into the Langmuir Model in Adsorption Isotherms
Reprinted from: *Processes* **2025**, *13*, 4036, https://doi.org/10.3390/pr13124036 . . . . . **61**

Miguel Castro, Laura Tous, Adriana Herrera, Dylan Martinez-Bernett and Manuel Saba
Effect of Aluminum Salt Precursor on the Crystalline Structure of Alumina Nanoparticles (Al_2O_3) Synthesized by Green Chemistry Using *Cymbopogon citratus* Extract
Reprinted from: *Processes* **2025**, *13*, 3876, https://doi.org/10.3390/pr13123876 . . . . . **79**

Rongrong Jia, Mingchuan Tang, Mengshan Hou, Haiheng Xing, Yuxing Cai, Jianhao Wu, et al.
Bi($C_6N_7O_3$) Nanospheres: A Novel Homogenous Photocatalyst for Efficient Treatment of Antibiotic in Water
Reprinted from: *Processes* **2025**, *13*, 3535, https://doi.org/10.3390/pr13113535 . . . . . **90**

Kaleb D. Fisher and Lingling Liu
Effect of Storage Conditions on the Composition and Bioactivity of Freeze-Dried Lemongrass Oil Nanoemulsions Stabilized by Salt-Sensitive Cellulose Nanocrystals and Tween 80
Reprinted from: *Processes* **2025**, *13*, 2752, https://doi.org/10.3390/pr13092752 . . . . . **102**

Minerva Guadalupe Ventura Muñoz, Jesús Alfredo Lara Cerón, Manuel de Jesús Gallegos Saucedo and Gregorio Guadalupe Carbajal Arizaga
Mechanochemical Loading of Doxorubicin on the Surface of Magnesium and Zinc-Based Layered Double Hydroxides
Reprinted from: *Processes* **2025**, *13*, 931, https://doi.org/10.3390/pr13040931 . . . . . **125**

Arulkumar Muniyappan, Prem Ananth Muthuvel, Anandhavelu Sanmugam, Mohammad Ahmad Wadaan, Almohannad Baabbad, Nallal Muthuchamy and Kang Hyun Park
Enhanced Tribological Performance of Laser-Textured TiN-Coated Ti_6Al_4V Alloy Surfaces: A Comparative Study with Untextured Surfaces
Reprinted from: *Processes* **2025**, *13*, 204, https://doi.org/10.3390/pr13010204 . . . . . **136**

Taiwo Musa Adeniji, Naila Haroon and Keith J. Stine
Applications of Nanomaterial Coatings in Solid-Phase Microextraction (SPME)
Reprinted from: *Processes* **2025**, *13*, 244, https://doi.org/10.3390/pr13010244 . . . . . **159**

About the Editor

Keith J. Stine

Keith J. Stine is Professor and Chair in the Department of Chemistry and Biochemistry at the University of Missouri – Saint Louis. Dr. Stine's research efforts involve studies of modified surfaces and nanostructures. The surface modification of nanostructures is pursued with a focus on their prospective applications in bioanalytical chemistry. Immobilization of proteins onto gold nanostructures and other materials is pursued. The bioanalytical application of these materials is pursued using primarily electrochemical methods. Nanoporous gold and other related materials are of particular interest due to their high surface area and capacity to be surface-modified. The preparation and characterization of these materials use a range of electrochemical techniques and other analytical methods. Nanoporous gold is being used for the development of electrochemical sensors for pollutants, hormones and endotoxins. He has published 130 articles, reviews, and book chapters.

processes

MDPI

Editorial

Special Issue: Synthesis and Applications of Nanomaterials

Keith J. Stine

Department of Chemistry and Biochemistry, University of Missouri–Saint Louis, Saint Louis, MO 63121, USA; kstine@umsl.edu

1. Introduction

The synthesis and application of new nanomaterials has been one of the most active fields of science since interest in these materials started growing about 30 years ago, when researchers discovered that these new materials with nanoscale dimensions or features could impart entirely unique or improved properties. The range of materials prepared and investigated has expanded to include nanomaterials of metals, alloys, semiconductors, metal oxides, various carbon nanostructures, layered structures, polymers, and anything else that the imaginative scientists in this field can create. All dimensionalities are being explored, from nanoparticles with two-dimensional structures to three-dimensional nanoporous or composite materials [1]. The range of synthesis methods introduced is broad and falls generally into top-down or bottom-up approaches [2]. Nanoparticles especially have been developed with many compositions [3], and the possibilities of gold nanoparticles, among the first introduced and investigated, continue to grow [4]. Every area of technology can potentially be transformed by the introduction of nanomaterials. The 10 papers in this Special Issue report on the preparation of nanomaterials, including nanoparticles, layered nanomaterials, and nanostructured coatings, with applications including water treatment, wear and resistance, drug release, and chemical analysis.

2. Overview of Contributions

In the article by Thiam et al., the synthesis of Zinc oxide nanoparticles was achieved using Licania tomentosa leaf extract, serving as an example of a green approach to nanoparticle synthesis [5]. In these methods based on plant extracts, phytochemicals serve as both reducing and stabilizing agents. Zinc oxide, a II–V semiconductor, is a highly useful type of nanoparticle that has photocatalytic properties and is nontoxic. In this study, the authors demonstrate the antimicrobial activity of ZnO nanoparticles against a wide range of bacteria. The photocatalytic properties of these nanoparticles are exploited to carry out the photodegradation of two dye molecules often found as pollutants in water. Both the antimicrobial and photocatalytic properties of these particles are largely due to the generation of reactive oxygen species upon irradiation of the nanoparticles in water, in addition to other contributing mechanisms. This paper uses a green method to make nontoxic nanoparticles useful for two aspects of water treatment. In its nanoparticle form, ZnO has a bandgap reported as 3.0 eV, which makes it useful as a photocatalyst. The authors also emphasize how the structural details of nanoparticles depend on the synthesis method used, and how their behavior depends on subtle structural details, a key point to remember about many types of nanoparticles. There is thematic overlap with the paper by Castro et al., who report a green chemistry synthesis of alumina nanoparticles.

In the paper by Batakliev et al., a green nanotechnology theme is also found in their effort to make a biodegradable nanocomposite material and study its micromechanical properties and self-healing of scratches by heating [6]. The authors use 3D printing

and melt extrusion to make flat nanocomposites of graphene-reinforced polylactic acid (PLA)/polycaprolactone (PCL). The material showed resistance to scratching, and its heterogeneous structure of hard and soft phase-separated domains allowed for the healing of scratches by heating, as polymer chains could return to their original conformations. In this study, graphene nanoplatelets of superior mechanical strength and high surface area impart valuable new mechanical properties to a biodegradable polymer composite.

The paper by Kim et al. focuses on a significant problem related to the ecological impact of the semiconductor industry [7]. Chemical mechanical planarization (CMP) is required for the production of ever smaller semiconductor devices. The traditional SiO_2 nanoparticle slurries used for CMP are difficult to recover and result in a significant amount of waste. In this study, the authors optimize the SiO_2 shell thickness of γ-Fe_2O_3@SiO_2 core–shell nanoparticles and apply them to the CMP of tungsten films, achieving a low surface roughness and a high magnetic recovery rate. The study again emphasizes the positive impact of nanomaterials on the environment, a theme that has emerged from more papers in the Special Issue than anticipated.

The removal of toxic metals and of organic pollutants by adsorption onto nanomaterials is an emerging strategy for environmental remediation. Hence, improved models for understanding adsorption behavior onto particles surfaces is the topic of the paper by de Sousa et al. [8]. In this paper, the authors improve the well-known Langmuir adsorption isotherm model by incorporating a temperature-dependent term in order to predict adsorption isotherms at different temperatures. The model is validated using literature data and experiments on the adsorption of copper ion by a zeolite.

The paper by Castro et al. focuses on a green synthesis method for aluminum oxide nanoparticles using lemongrass extract as a reducing agent [9]. The resulting particle size was found to depend on the choice of precursor. The plant extract contains many components and, while some act as reducing agents, others act as chelating ions, while some stabilize particles against agglomeration. Al_2O_3 nanoparticles can be applied as antimicrobial agents, as additives in coating, as active elements in gas sensors, and in other applications. The studies in this Special Issue emphasize how careful attention must be given to preparation conditions to tune the size and morphology of the resulting nanoparticles. Once a nanoparticle of a given material is synthesized, it can possibly be used in many different applications that make use of the different properties unique to its nanoscale dimensions.

Spherical nanoparticles of $Bi(C_6N_7O_3)$ were formed from potassium cyanurate—$K_3[C_6N_7O_3]$—nanorods through ion exchange in an autoclave in the paper by Jia et al. for use in the photocatalytic degradation of an antibiotic in water [10]. The spherical nanoparticles provided a greatly enhanced efficiency in the photodegradation of tetracycline, an antibiotic that is polluting natural waters, as compared to potassium cyanurate or graphitic carbon nitride. Emerging contaminants, of which antibiotics are a major class, and their detection using nanomaterials is also an active field [11]. The sensitivity of nanoparticle activity to composition and shape is effectively revealed by this study.

Fisher and Liu incorporate cellulose nanocrystals to stabilize oil-in-water nanoemulsions where the oil is lemongrass essential oil [12]. These natural essential oils are eco-friendly and also have antifungal and antimicrobial properties, while cellulose nanocrystals are a green stabilizer. Compared to standard emulsions, nanoemulsions have droplet sizes around 100 nm. The effects of freeze drying and storage on the nanoemulsion and its activity are studied in detail in this contribution.

Carbajal Arizaga and coworkers study the use of layered double hydroxides for the delivery of the anticancer drug doxorubicin (DOX) [13]. Three different methods of loading the drug into LDH nanoparticles are compared: incubation with DOX, co-precipitation, and

https://doi.org/10.3390/pr14121896

mechanochemical reaction. Magnesium/aluminum double hydroxide was stable under all three DOX loading processes, and the mechanochemical reaction loaded the most DOX. X-ray diffraction (XRD) and FTIR are used to provide characterization data for the particles.

In the contribution by Muniyappan et al., laser surface texturing is applied to the titanium alloy Ti_6Al_4V, which is then coated with a layer of TiN through physical vapor deposition [14]. The wear properties of the coating were studied, and a laser-textured sample with TiN coating was found to have a lower wear rate. These titanium alloys are important in medical implants. In this study, the authors reveal that the nanostructuring of surfaces can have a large impact on their mechanical behavior.

The review article by Adeniji et al. examines the growing application of nanomaterials in solid phase microextraction (SPME) through the modification of SPME fibers by nanomaterials to improve their specificity and capacity for the adsorption of volatile organic compounds, many of which are emerging pollutants [15]. The introduction of nanomaterials into SPME technology has the potential to advance environmental monitoring.

3. Future Prospects

One theme that has emerged from this Special Issue is that nanomaterials can be produced using methods that are environmentally friendly and can be applied to technologies for monitoring and remediating the environment. This suggests a strong motivation for future work along these directions. Another theme that emerges is that nanomaterials and nanostructured surfaces are complex, with morphologies and nanoscale features that depend strongly on preparation, compositional details, and processing conditions. It is clear from these contributions that applying detailed characterization using multiple methods after the preparation of a nanomaterial is essential, including, as applicable, diffraction, nanoscale microscopy, and thermal and spectroscopic methods. Furthermore, the performance characteristics of nanomaterials and nanostructured surfaces are critically dependent on these details, and much remains to be understood through further investigation. The possibilities for new nanomaterials and new applications are limited only by the imagination.

Conflicts of Interest: The author declares no conflicts of interest.

References

1. Paras, N.; Yadav, K.; Kumar, P.; Teja, D.R.; Chakraborty, S.; Chakraborty, M.; Mohapatra, S.S.; Sahoo, A.; Chou, M.M.; Liang, C.T.; et al. A Review on Low-Dimensional Nanomaterials: Nanofabrication, Characterization and Applications. *Nanomaterials* **2023**, *13*, 160. [CrossRef] [PubMed]
2. Baig, N.; Kammakakam, I.; Falath, W. Nanomaterials: A review of synthesis methods, properties, recent progress, and challenges. *Mater. Adv.* **2021**, *2*, 1821–1871. [CrossRef]
3. Khan, Y.; Sadia, H.; Ali Shah, S.Z.; Khan, M.N.; Shah, A.A.; Ullah, N.; Ullah, M.F.; Bibi, H.; Bafakeeh, O.T.; Khedher, N.B.; et al. Classification, Synthetic, and Characterization Approaches to Nanoparticles, and Their Applications in Various Fields of Nanotechnology: A Review. *Catalysts* **2022**, *12*, 1386. [CrossRef]
4. Karwal, A.; Samir, R.; Sachan, K.; Devgonm, I.; Devgon, J.; Pant, G.; Panchpuri, M.; Ahmad, A.; Alshammari, M.B.; Hossain, K.; et al. Gold Nanoparticles in Nanobiotechnology: From Synthesis to Biosensing Applications. *ACS Omega* **2024**, *9*, 29966–29982. [CrossRef] [PubMed]
5. Thiam, M.; Pellegrini, V.O.A.; Mamani, R.C.C.; Cassieri, F.; Furtado, H.L.A.; Ribeiro, M.S.; Pinheiro, A.J.M.C.R.; Silva, L.C.N.d.; Ngom, B.D.; Oliveira Neto, M.d.; et al. Antibacterial Activity and Photocatalytic Properties of Zinc Oxide Nanoparticles Biosynthesized Using *Licania tomentosa* Leaf Extract: Optimization and Kinetic Studies. *Processes* **2026**, *14*, 1334. [CrossRef]
6. Batakliev, T.; Ivanov, E.; Georgiev, V.; Angelov, V.; Kotsilkova, R. Design of Carbon Nanocomposites Based on PLA and PCL—From Microscratch Testing to Self-Healing Behavior. *Processes* **2026**, *14*, 956. [CrossRef]
7. Kim, Y.S.; An, G.S. Tailored Shell Engineering of γ-Fe_2O_3@SiO_2 Nanoparticles for High-Performance and Recyclable Chemical Mechanical Planarization. *Processes* **2026**, *14*, 902. [CrossRef]

https://doi.org/10.3390/pr14121896

8. de Sousa, A.P.S.; Lima, H.B.S.; da Costa, D.S.; Rodrigues, E.C.; Agustini, C.B.; Féris, L.A.; Estumano, D.C. A Proposal for the Incorporation of Temperature into the Langmuir Model in Adsorption Isotherms. *Processes* **2025**, *13*, 4036. [CrossRef]
9. Castro, M.; Tous, L.; Herrera, A.; Martinez-Bernett, D.; Saba, M. Effect of Aluminum Salt Precursor on the Crystalline Structure of Alumina Nanoparticles (Al_2O_3) Synthesized by Green Chemistry Using *Cymbopogon citratus* Extract. *Processes* **2025**, *13*, 3876. [CrossRef]
10. Jia, R.; Tang, M.; Hou, M.; Xing, H.; Cai, Y.; Wu, J.; Wang, X.; Chen, J.; Li, L.; Jin, C.; et al. Bi($C_6N_7O_3$) Nanospheres: A Novel Homogenous Photocatalyst for Efficient Treatment of Antibiotic in Water. *Processes* **2025**, *13*, 3535. [CrossRef]
11. Adeniji, T.M.; Stine, K.J. Nanostructure Modified Electrodes for Electrochemical Detection of Contaminants of Emerging Concern. *Coatings* **2023**, *13*, 381. [CrossRef]
12. Fisher, K.D.; Liu, L. Effect of Storage Conditions on the Composition and Bioactivity of Freeze-Dried Lemongrass Oil Nanoemulsions Stabilized by Salt-Sensitive Cellulose Nanocrystals and Tween 80. *Processes* **2025**, *13*, 2752. [CrossRef]
13. Ventura Muñoz, M.G.; Lara Cerón, J.A.; Gallegos Saucedo, M.d.J.; Carbajal Arizaga, G.G. Mechanochemical Loading of Doxorubicin on the Surface of Magnesium and Zinc-Based Layered Double Hydroxides. *Processes* **2025**, *13*, 931. [CrossRef]
14. Muniyappan, A.; Muthuvel, P.A.; Sanmugam, A.; Wadaan, M.A.; Baabbad, A.; Muthuchamy, N.; Park, K.H. Enhanced Tribological Performance of Laser-Textured TiN-Coated Ti_6Al_4V Alloy Surfaces: A Comparative Study with Untextured Surfaces. *Processes* **2025**, *13*, 204. [CrossRef]
15. Adeniji, T.M.; Haroon, N.; Stine, K.J. Applications of Nanomaterial Coatings in Solid-Phase Microextraction (SPME). *Processes* **2025**, *13*, 244. [CrossRef]

Disclaimer/Publisher's Note: The statements, opinions and data contained in all publications are solely those of the individual author(s) and contributor(s) and not of MDPI and/or the editor(s). MDPI and/or the editor(s) disclaim responsibility for any injury to people or property resulting from any ideas, methods, instructions or products referred to in the content.

https://doi.org/10.3390/pr14121896

processes

MDPI

Article

Antibacterial Activity and Photocatalytic Properties of Zinc Oxide Nanoparticles Biosynthesized Using *Licania tomentosa* Leaf Extract: Optimization and Kinetic Studies

Moudo Thiam [1], Vanessa O. Arnoldi Pellegrini [1], Ruth Celestina Condori Mamani [1], Fernanda Cassieri [1], Haryne Lizandrey Azevedo Furtado [2], Michael Santos Ribeiro [2], Aruanã Joaquim Matheus Costa Rodrigues Pinheiro [2], Luís Cláudio Nascimento da Silva [2], Balla D. Ngom [3], Mario de Oliveira Neto [4] and Igor Polikarpov [1,*]

[1] Institute of Physics, University of São Paulo, Avenida Joao Dagnone, 1100, Jardim Santa Angelina, São Carlos 13563-120, SP, Brazil; moudothiam_.167@usp.br (M.T.); varnoldi@yahoo.com.br (V.O.A.P.); ruthcondori20@gmail.com (R.C.C.M.); fernandacassieri@hotmail.com (F.C.)
[2] Laboratório de Patogencidade Microbiana, Universidade Ceuma, Rua Josué Montello, No. 1, Renascença II, São Luís 65075-120, MA, Brazil; haryne.lizandrey@gmail.com (H.L.A.F.); michaelribeiro99@hotmail.com (M.S.R.); aruana.pinheiro@ceuma.br (A.J.M.C.R.P.); luiscn.silva@ceuma.br (L.C.N.d.S.)
[3] Faculté des Sciences et Techniques, Université Cheikh Anta Diop de Dakar (UCAD), Fann, Dakar B.P. 5005, Senegal; balla.ngom@ucad.edu.sn
[4] Institute of Biosciences, Sao Paulo State University, District of Rubiao Jr., Botucatu 18618-970, SP, Brazil; mario.oliveira@unesp.br
* Correspondence: ipolikarpov@ifsc.usp.br

Abstract

Licania tomentosa leaf extract was used to synthesize zinc oxide nanoparticles (ZnO NPs) which were systematically analyzed by X-ray diffraction (XRD), scanning electron microscopy (SEM), UV-Visible (UV-Vis) and Fourier transform infrared (FT-IR) spectroscopies and energy-dispersion X-ray spectroscopy (EDS) methods. Based on XRD scans, the green NPs have an average crystallite size of 15.9 nm as estimated using the Scherrer equation and have a roughly spherical shape with an average diameter of 25.15 ± 1.2 nm as calculated from SEM data. As estimated from the Tauc plot based on UV-Vis absorption spectra, ZnO NPs have a small band gap of 3.0 eV. The biosynthesized ZnO NPs were effectively utilized for the photodegradation of methylene blue (MB) and crystal violet (CV) dyes under UV illumination with resulting MB and CV degradation efficiencies of ~94% and ~81% after 60 min and 70 min, with pH = 12 and pH = 10, respectively. Different experimental parameters such as NPs quantity, experimental pH, light intensity and initial concentration of dyes were varied to test the performance of the catalyst. Furthermore, efficient recycling of the catalyst was demonstrated. We also undertook antimicrobial studies of the green ZnO NPs. The ZnO NPs demonstrated broad-spectrum antimicrobial efficacy against *Escherichia coli* ATCC 35218, *Enterococcus faecalis* ATCC 29737, *Klebsiella pneumoniae* ATCC 700603, *Pseudomonas aeruginosa* ATCC 27853, *P. aeruginosa* B3, *Staphylococcus aureus* ATCC 29213, and *S. aureus* SA01, with the minimum inhibitory concentration (MIC) and the inhibitory concentrations associated with 50% effect (IC50) values ranging from 250 to 2000 μg/mL and 7.74 to 283.14 μg/mL, respectively. The nanoparticles also significantly inhibited biofilm formation by *E. faecalis* ATCC 29737, *P. aeruginosa* ATCC 27856, and *S. aureus* SA03. The antimicrobial efficiency of the ZnO NPs against *Escherichia coli* ATCC 25922 and *Staphylococcus aureus* SA03 isolates was also assessed using the disk diffusion assays. Taken together, our results reveal that the biosynthesized ZnO NPs are promising multifunctional materials with potential applications in antimicrobial treatments, biofilm control, and photocatalytic remediation.

Keywords: biosynthesized ZnO nanoparticles; antimicrobial activity; photocatalytic degradation; *Licania tomentosa* leaf

1. Introduction

Water is an invaluable vital resource, but clean sources are becoming more and more scarce due to human carelessness and manufacturing activities leading to elevated levels of pollution [1]. Organic pollutants, such as dyes, antibiotics, and pesticides, constitute the most concerning category of contaminants [2]. Furthermore, microbial contamination poses a major global health risk, causing serious diseases like dysentery, typhoid fever, and cholera [3].

ZnO NPs have diverse applications in fields such as anticancer, antidiabetic, antibacterial, BioReRAM, antifungal treatments, drug delivery, CO_2 photoreduction and agricultural technologies [4–7]. The application of NPs in water sanitation is an actively developing area. The most advanced materials in this field are the ones that combine photocatalytic and antimicrobial properties. These nanomaterials offer the potential to simultaneously achieve the degradation of organic pollutants and the eradication of pathogenic microorganisms in a single step under visible/UV light irradiation. Zinc oxide (ZnO), a Group II-V semiconductor compound, frequently crystallizes in a wurtzite structure. ZnO possesses remarkable qualities, such as a wide, direct band gap (approximatively 3.36 eV), strong absorption in the ultraviolet region, high room-temperature exciton binding energy (around 60 meV), a large electrochemical coupling coefficient, excellent photostability, biocompatibility and low toxicity [8].

ZnO is a highly versatile material, considered an ideal candidate for water treatment process thanks to its two main properties: ZnO exhibits strong photocatalytic activity, not only under ultraviolet (UV), but also visible radiation due to its lower band gap energy compared to TiO_2. When irradiated, ZnO NPs produce reactive oxygen species (ROS), which are responsible for both the photocatalytic activity (pollutant degradation) and the antimicrobial activity. The antimicrobial activity of ZnO NPs is generally higher for smaller NPs. This effect relies on two primary mechanisms [9]: (i). light-related mechanisms (ROS production), and (ii). morphology-related mechanisms including mechanical damage (physical destruction of microbial cell membranes) and/or ion release (diffusion of Zn^{2+} ions, which interact with essential cell components) [10]. Furthermore, ZnO is non-toxic to humans, water insoluble, reusable, and combines elevated photocatalytic and antimicrobial activities. However, all these characteristics strongly depend on the size, shape, surface morphology, and defects of the ZnO NPs, which are themselves determined by the synthesis method.

The preparation of ZnO NPs can follow various chemical and physical routes (sol–gel, pulsed laser deposition, thermal evaporation, etc.) [11,12]. However, most of these traditional methods are expensive, intensive in terms of energy and time, require critical conditions (temperature and pressure), and use hazardous chemicals that negatively affect the environment. Given environmental concerns, biosynthesis, or "green synthesis", has arisen as a very promising approach. This method is favored because it is simple and low-cost, environmentally friendly, suitable for large-scale production, results in more stable and biocompatible NPs [13]. At the same time, ZnO NPs might exhibit significant ecotoxicity to aquatic and terrestrial organisms, primarily driven by the release of Zn^{2+} ions and reactive oxygen production [14,15] and cause considerable oxidative stress, metabolic inhibition, and structural damage to algae, bacteria, and invertebrates [16]. Therefore, ZnO NPs applications have to be investigated in each specific case and applied with caution.

https://doi.org/10.3390/pr14091334

For practical large-scale implementation, improvements are required in synthesis reproducibility, photocatalytic efficiency, and NP recovery or reuse. Furthermore, pilot studies in real wastewater conditions, cost–benefit analyses, and adherence to industrial standards remain essential to ensure feasibility and efficiency at an industrial scale [17]. Green biosynthesis methods further enhance the environmental value of ZnO NPs by producing non-toxic and biodegradable materials. Using biological agents such as plant extracts, bacteria, or fungi, this approach avoids hazardous chemicals while yielding nanoparticles with enhanced photocatalytic and antimicrobial performance [18]. Several recent studies focus on ZnO NPs' capacity to act simultaneously as a photocatalyst (e.g., for organic dye degradation) and as an antimicrobial agent, optimizing both functionalities within the single nanostructures [19–22]. The composition of biological materials used in green synthesis, including plant extracts and microorganisms, can vary significantly depending on factors such as plant species, extraction techniques, seasonal conditions, and geographic origin. These variations can affect the consistency of NPs' characteristics, making it crucial to systematically evaluate NP production in particular pilot settings [23,24].

The most promising biosynthetic route utilizes plant extract (from fruits, leaves and seeds). Plants are rich in phytochemical compounds (flavonoids, tannins, alkaloids, etc.). These compounds can be extracted using eco-friendly solvents, such as distilled water, for example. The phytochemicals (especially polyphenols) serve as reducing agents, transforming the precursor metal ions into metal oxide NPs. They also serve as stabilizing agents, partially preventing the formed NPs from agglomeration.

There have been numerous reports on the ZnO NPs synthesis of with leaf extract from *Lemon peel* [23], *Camellia sinensis* [24], *Annato tree* [25], *Hibiscus subdariffa* [26], *Coffea arabica* L. [4], *Aloe vera* [27], *Ficus carica* [28], *Lupinus pilosus* [29], to name a few, and their antibacterial and photocatalytic activities have been evaluated [30]. *Licania tomentosa* Benth (Oiti) belongs to the *Chrysobalanaceae* family and is native to the Caatinga region of Brazil [31]. It is commonly used in public gardens to provide shade [32] and its seed oil can be used as ink drying oil [33]. *L. tomentosa* Benth leaves are readily available in Brazil, reducing raw material costs. The leaves are rich in active phytochemical compounds, such as betulinic acid, flavonoids, phenolics, and various triterpenic and fatty acids [34–36]. *Licania tomentosa* leaf extracts have demonstrated antioxidant [36], anticholinesterase [37], antibacterial, and antiviral activities [38]. Here, we report the biosynthesis of ZnO NPs with *L. tomentosa* leaf extract and their characterization with various techniques, such as UV-Vis, SEM, XRD, EDX, and FT-IR. The NPs were subsequently utilized as photocatalysts in organic dye photodegradation. The ZnO NPs were also shown to inhibit the biofilm formation and to eliminate planktonic cells of clinically relevant pathogenic microorganisms.

2. Material and Methods

2.1. Original Materials

Licania tomentosa Benth fresh leaves were collected at the Sao Carlos Campus 2 of the University of Sao Paulo (USP) (geolocation: −21.999041, −47.932830) in January 2025. The analytical quality zinc nitrate hexahydrate, ethylenediaminetetraacetic (EDTA), Isopropyl alcohol (IPA, P-Benzoquinone (BQ, and DMSO (purity $\geq$ 99.0%) were bought from Sigma-Aldrich (Burlington, MS, USA) and used as received. Origin 2018 64 Bit was used to plot graphs.

2.2. Licania Tomentosa Leaf Extracts

The *L. tomentosa* leaves were extensively rinsed with distilled water to clean them up. The leaves were dried at 50 °C for 5 days and milled. A total of 3.25 g of the milled powder was added to 150 mL of deionized water and stirred using a magnetic stirrer at room

https://doi.org/10.3390/pr14091334

temperature for 3 h to optimize the extraction of the soluble bioactive compounds. Well enclosed with an aluminum foil, the mixture was allowed to settle at room temperature for 21 h. Next, it was passed through a Whatman No. 1 filter paper (produced in Germany and packaged in Brazil) to get rid of the residual solids (Graphical abstract).

2.3. ZnO NPs Biosynthesis

ZnO NPs synthesis used 100 mL of the filtered extract in which 1 g of Zn $(NO_3)_2 \cdot 6H_2O$ was dissolved and stirred for 3 h at room temperature. The resultant solution was partially evaporated at 70–80 °C using a magnetic stirrer. The process was stopped when the mixture was reduced to 1/10th of the volume. The resulting solids were dried in the air oven at 70 °C overnight and thermally treated at 500 °C for 2 h. The obtained white powder was thoroughly washed to remove impurities and dried overnight at 70 °C (see Graphical abstract). The output efficiency was found to be 266.6 mg NPs/g using Equation (1):

$$efficiency = \frac{Masse\ of\ prepared\ NPs\ (\mathrm{mg})}{Mass\ of\ dried\ extract(\mathrm{g})} = \frac{800\ \mathrm{mg}}{3\ \mathrm{g}} = 266.6\ \mathrm{mg\ NPs/g} \quad (1)$$

2.4. Analytical Characterization of the Obtained NPs

XRD measurements were conducted using Cu Kα radiation (λ = 1.5406 Å) on a Miniflex 600 X-ray diffractometer (Rigaku, Tokyo, Japan), which was operating at 40 kV and 15 mA. Detection was performed in the 2θ range between 5° and 70°, with an angular step of 0.02° and an exposure time of 15 s per step. The observed diffraction peaks were extracted from the measured diffractograms. Peak fitting program (PeakFit Version 13; www.systat.com, accessed on 15 April 2026) was used to adjust Gaussian functions for each peak and the NPs' average crystallite sizes were estimated using the modified Scherrer equation [39,40]. For comparison, an average crystallite size (D), dislocation density (δ), and micro strain (ε) were also estimated using the Williamson–Hall method [41] from the following Equations (2) and (3):

$$\delta = \frac{1}{D^2} \quad (2)$$

$$\varepsilon = \frac{\beta}{4\ \tan\theta} \quad (3)$$

Here, D is the crystallite average dimension, β is the full width at half maximum (FWHM) in radians and θ is the scattering angle in degrees.

UV-Vis adsorption spectra were measured using Thermo Scientific (Waltham, MA, USA) Multiskan GO UV/Vis Microplate Reader Spectrophotometer between 200 and 1000 nm. For the measurements, the ZnO NPs were suspended in milli-Q water in a 1 cm quartz cuvette. Origin 8 software was used to analyze the adsorption spectra.

FT-IR data were obtained as follows: Pellets of the ZnO NPs samples were prepared using a hydraulic press. A Nicolet 6700 FT-IR spectrometer was used to collect spectra within a wave number range between 400 cm^{-1} and 4000 cm^{-1}.

Morphology and the average size of the synthesized green ZnO NPs were evaluated by scanning electron microscopy (SEM). The ZnO NPs powder was scattered on a sample holder, coated with gold and scanned using an electron beam. The element composition of the samples was analyzed by energy-dispersion X-ray spectroscopy (EDS) using an X-Max solid-state silicon detector (Oxford Instruments). Finally, the pHzpc of the ZnO NPs was determined.

Hydrodynamic radii and the NP size distribution were analyzed using the DLS technique (SpectroSize 300 instrument, XtalConcepts, Germany). DLS relies on the measurements of light intensity fluctuations as a function of time due to the particle's Brow-

https://doi.org/10.3390/pr14091334

nian motion [42]. Such measurements allow for the determination of the diffusion coefficient (D), which is related to the hydrodynamic radius (R_h) of the particle via the Stokes-Einstein equation,

$$D = \frac{k_b T}{6\pi\eta R_h} \quad (4)$$

where k_b is the Boltzmann constant (1.380×10^{-23} kg m^2 k^{-1}), T is the absolute temperature, and η is the viscosity of the solution [42].

2.5. Photocatalytic Activity Measurements

The photocatalytic activity of the ZnO NPs biosynthesized using *L. tomentosa* leaf extract was studied using MB and CV as model dyes. MB and CV are extensively applied in the textile and paper industries and are components of navy blue and black inks, respectively. In a typical photocatalytic experiment, 25 mgs of the ZnO NPs were dispersed in 100 mL of 5 mg/L MB dissolved in water. The mixture was first stirred in the dark for 30 min. After this period, a mixture containing dyes and the photocatalyst was submitted to UV-A light using eight (8) UV-A 6W T-5-BL Lucmat lamps (LUCMAT, São Paulo, SP, Brazil), with a maximum emission wavelength of 368 nm. After that, 1.5 mL aliquots were periodically taken. The supernatant was obtained by centrifugation at 13,300 rpm for 10 min. The dye degradation was monitored by measuring the fall in the maximum absorbance of MB and CV dyes in the supernatant, with absorption peaks centered at λ = 663 nm and 583 nm, respectively, using Thermo Scientific Multiskan GO UV/Vis Microplate Reader Spectrophotometer over a wavelength range 200–1000 nm (Figure 1).

The degradation was quantified using the equation:

$$Degradation\ (\%) = \frac{C_0 - C_t}{C_0} \times 100\% = \frac{A_0 - A_t}{A_0} \times 100\% \quad (5)$$

Here, A_0 is the initial absorbance of dyes at the initial concentration C_0, and A_t is the absorbance of the dye with concentration C_t at time interval t.

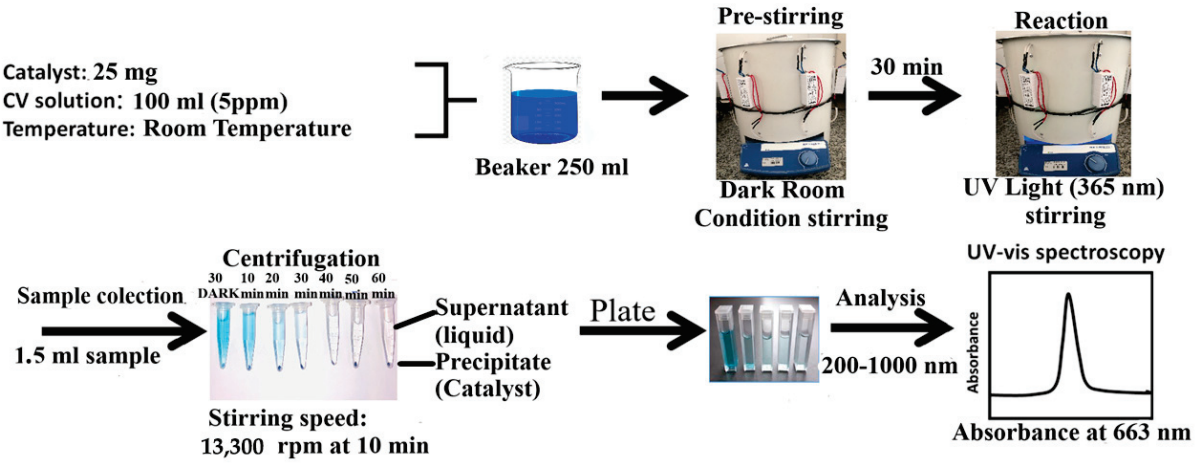


Figure 1. Schematic representation of the experimental steps for MB decomposition.

2.6. Antimicrobial Activity Measurements

The antimicrobial activity of the green-synthesized ZnO nanoparticles was evaluated using the broth microdilution method in 96-well microplates. The bacterial isolates (*Escherichia coli* ATCC 35218, *Enterococcus faecalis* ATCC 29737, *Klebsiella pneumoniae* ATCC 700603, *Pseudomonas aeruginosa* ATCC 27853, *P. aeruginosa* B3, *Staphylococcus aureus* ATCC 29213, and *S. aureus* SA01) were suspended in sterile saline and adjusted to an optical density of 0.1 at 600 nm (≈1.5×10^8 CFU/mL; McFarland 0.5 standard). A stock suspension

https://doi.org/10.3390/pr14091334

of ZnO NPs (4000 μg/mL) was prepared in Milli-Q water and subjected to twofold serial dilutions in Mueller–Hinton (MH) broth to obtain final concentrations ranging from 1.95 to 2000 μg/mL. Each well received 10 μL of the bacterial inoculum and 90 μL of MH broth containing the corresponding ZnO nanoparticle dilution. Following incubation at 37 °C for 24 h, 30 μL of 0.03% resazurin solution (Sigma-Aldrich®) was added to each well and plates were incubated for an additional 4 h [28]. Minimum inhibitory concentration (MIC) was defined as the lowest concentration capable of inhibiting the colorimetric changes from blue (no reduction in resazurin to resorufin) to pink. The bacterial growth was determined from measurements of the optical density at 600 nm (OD_{600}). The percentage of bacterial growth inhibition at each nanoparticle concentration was calculated relative to the positive growth control (bacteria without nanoparticles) using Formula (6):

$$\text{Growth Inhibition } (\%) = \left[1 - \frac{(\text{A}_{\text{test}} - \text{A}_{\text{NP blank}})}{\text{A}_{\text{control}}}\right] \times 100\% \quad (6)$$

Here, A_{test} is the absorbance of NPs in MH broth with bacteria, $A_{NP\ blank}$ is the absorbance of NPs in MH broth without bacteria, and $A_{control}$ is the absorbance of bacteria in MH broth without nanoparticles.

Nonlinear regression using a four-parameter logistic model ([inhibitor] vs. response, 4PL) was performed in GraphPad Prism (v. 10) to determine the IC_{50}, defined as the concentration of nanoparticles required to inhibit 50% of bacterial growth.

Minimum bactericidal concentrations (MBCs) were determined as follows: aliquots of 10 μL from wells showing no detectable bacterial growth after 24 h of incubation were streaked onto Mueller–Hinton agar plates and incubated at 37 °C for 24 h. The MBC was defined as the lowest concentration of ZnO NPs yielding no detectable bacterial colonies on the agar surface [43].

2.7. Biofilm Inhibition Assay

Further, the ZnO NPs were assessed for their ability to inhibit bacterial biofilm formation. For this assay, *E. faecalis* ATCC 29737, *P. aeruginosa* ATCC 27856 and *S. aureus* SA03 were used as test organisms. Bacterial cultures were initially grown in Mueller–Hinton broth and adjusted to a final density of approximately 1×10^6 CFU/mL. Aliquots of the standardized bacterial suspensions (10 μL) were then inoculated into sterile 96-well microplates together with 90 μL of ZnO NPs at different concentrations (0.25 × MIC, 0.5 × MIC, 1 × MIC) and 100 μL of MH broth. Following incubation, the solutions from the wells were gently aspirated, and each well was washed carefully with phosphate-buffered saline (PBS) to remove non-adherent cells. The remaining attached biofilms were then fixed using methanol and stained with 1% (w/v) CV for 20 min at room temperature. Excess stain was eliminated by repeated rinsing with PBS. The stained biofilm biomass was subsequently solubilized with 70% (v/v) ethanol and allowed to rest for 15 min. The OD of the solubilized crystal violet was analyzed at 590 nm using a microplate spectrophotometer. The measured absorbance was used to quantify biofilm formation and to calculate the percentage of biofilm inhibition induced by nanoparticle treatment relative to the untreated control [44].

$$\text{Biofilm formation } (\%) = \frac{(A_{\,test} - \text{A}_{\text{ blank}})}{(A_{\,control} - \text{A}_{\text{ blank}})} \times 100\% \quad (7)$$

2.8. Disk Diffusion Assays

The disk diffusion assay (Kirby–Bauer method) was adapted to evaluate the ZnO NPs antibacterial activity against *Staphylococcus aureus* SA03 and *Escherichia coli* ATCC 25922 isolates. Under sterile conditions, suspensions of the NPs were prepared using serial

https://doi.org/10.3390/pr14091334

dilutions. All suspensions were subjected to sonication for 10 min to ensure homogenous dispersion and subsequently kept at rest for 24 h to favor solubilization. The bacterial cultures were adjusted to an optical density of O.D. = 0.1 in LB medium. Next, 20 µL of each NPs suspension was applied to the plates previously seeded with the bacteria. Each assay was performed in duplicate. As a positive control (+), 10 µL of ampicillin (10 mg/mL) was used, and as a negative control, 10 µL of sterile water was applied. After that, the plates were incubated at 35 °C for 24 h. Finally, the inhibition zones formed were evaluated, and the results were recorded in millimeters (mm). All measurements were performed in duplicate.

2.9. Statistical Analysis

Statistical analyses were undertaken using the software GraphPad Prism version 10.01 (GraphPad Software Inc., La Jolla, CA, USA). The data were analyzed by one-way analysis of variance (ANOVA) followed by the Tukey test. A p-value of <0.05 was considered statistically significant. All experiments, excluding photocatalytic degradation and antimicrobial assays, were performed in triplicate (n = 3). The data are presented as the mean ± standard deviation.

3. Results and Discussion

3.1. SEM Analysis

The SEM was used to evaluate morphology of the biogenic ZnO NPs and to estimate their particle size (Figure 2a,b). The green ZnO NPs have a homogeneously spherical morphology and are grouped together in aggregates. To analyze the chemical composition of the NPs sample, energy dispersive X-ray (EDS) data were obtained, as depicted in Figure 2d. The EDS spectrum showed the presence of three main elements (zinc, oxygen and silicon) in the samples. The silicon signal originates from the Si grids used for the sample loading, whereas Zn and O signals support successful ZnO NP synthesis. In Figure 2c, the histogram of particle size distribution shows that the mean diameter of ZnO nanoparticles is 25.15 ± 1.2 nm.

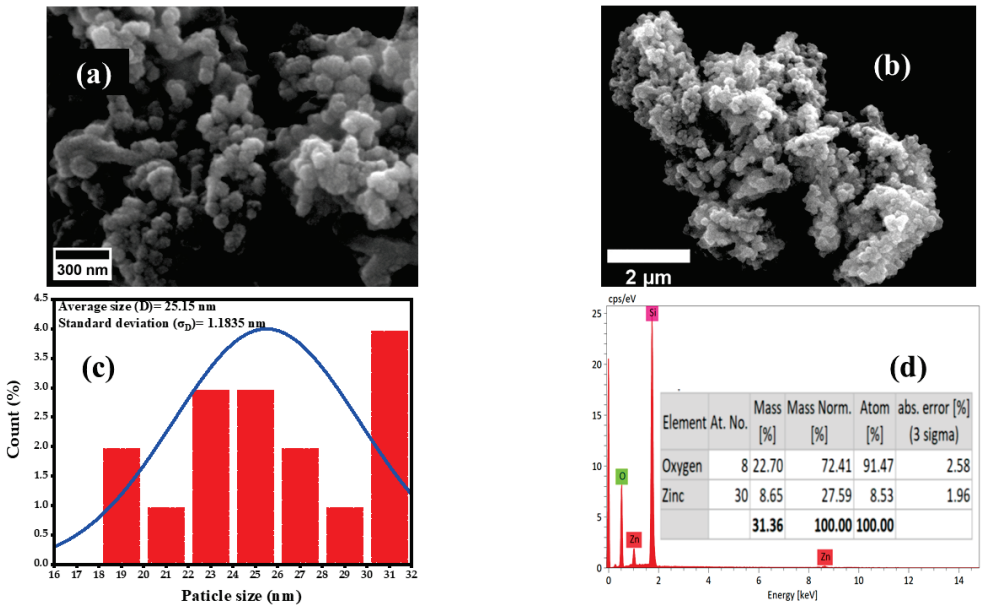


Figure 2. Structural and morphological characterization of ZnO NPs synthesized using *Licania tomentosa* leaves. (**a**,**b**) ZnO NPs as observed by SEM at two different amplifications; (**c**) distribution of the particle sizes; and (**d**) EDS of ZnO NPs: the detected Si (silicon) signal originates from the Si grids used for the sample loading.

https://doi.org/10.3390/pr14091334

3.2. XRD Analysis and Average Crystallite Size

X-ray diffraction (XRD) analysis of the biogenic ZnO NPs obtained using *L. tomentosa* leaf extract shows well-defined strong diffraction peaks (Figure 3a), with 2θ values of 31.65°, 34.33°, 36.12°, 47.44°, 56.50°, 62.78°, 66.40°, 67.87 and 69.0°. The peaks correspond to the crystallographic planes (100), (002), (101), (102), (110), (103), (200), (112) and (201) of ZnO NPs in a polycrystalline hexagonal wurtzite structure (JCPDS 5-0664). The XRD data exclude the presence of a secondary phase (Figure 3a). Out of all existing ZnO NPs structures, the hexagonal wurtzite structure is one of the most frequently observed [45].

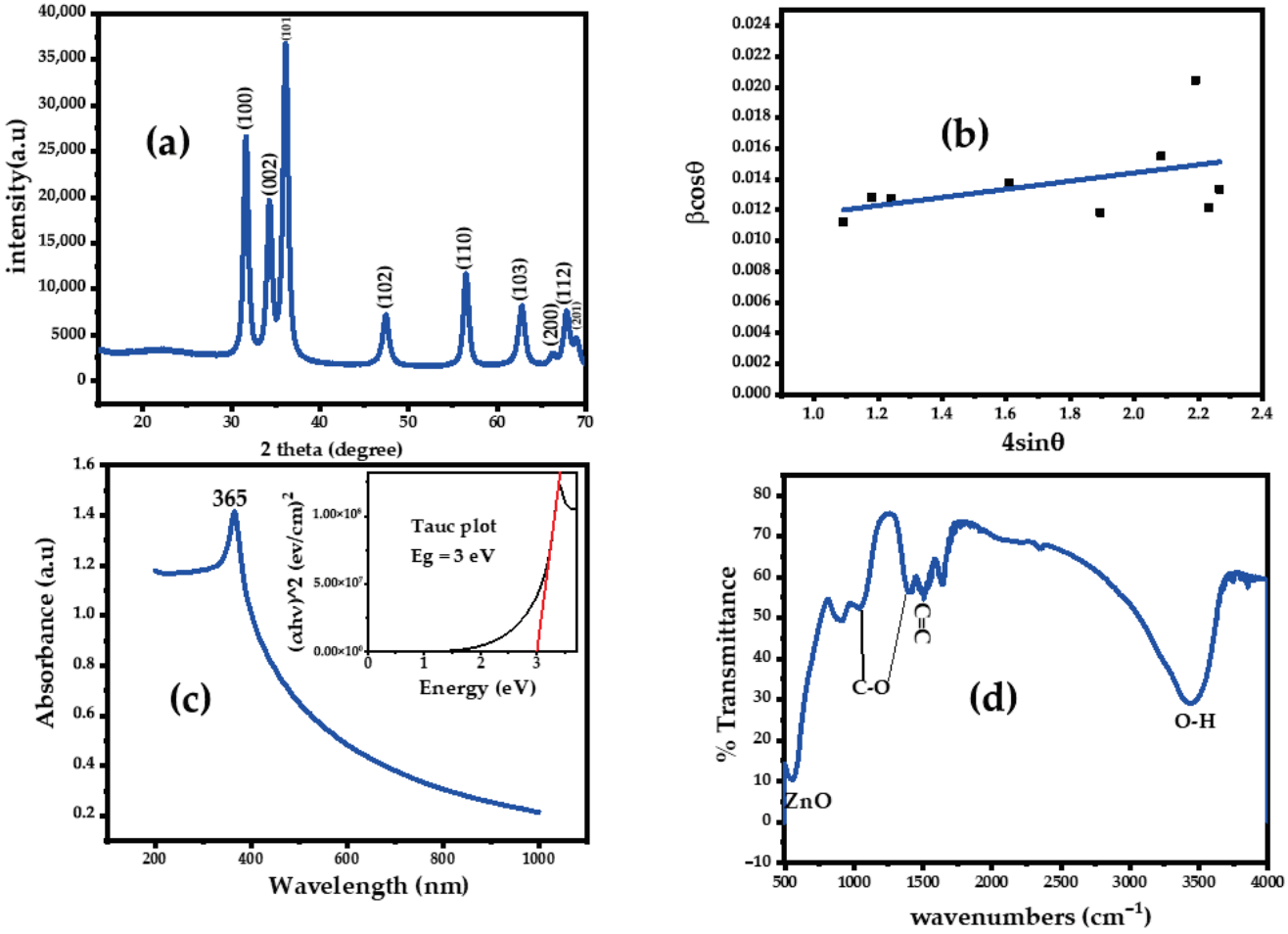


Figure 3. (**a**) X-ray diffraction data obtained from the green ZnO NPs produced using *Licania tomentosa* leaves extract. (**b**) The Williamson–Hall plot. (**c**) UV-Vis spectrum with the Tauc plot of $(\alpha h\upsilon)^2$ vs. hυ for ZnO NPs: experimental data (black) and linear fit (red) used to estimate the optical band gap. (**d**) The ZnO NPs FT-IR spectrum.

The average crystallite size was calculated using the Scherrer equation resulting in an estimate of about 15.9 nm. At the same time, using the Williamson–Hall approach (Figure 3b) the average crystallite size was estimated to be about 10.8 nm. In addition, the dislocation density (δ) and micro-strain (ε) can be evaluated as 2.55×10^{-3} nm and 3.94×10^{-3}. Comparison of the average crystallize sizes with the average particle size (Figure 3c) shows that each of the ZnO NPs is made of several crystallites, i.e., is polycrystalline.

3.3. UV-Vis Spectroscopy Data

The optical properties of the ZnO NPs were analyzed using UV-Vis adsorption spectroscopy (Figure 3c). A clear absorption peak at 365 nm is characteristic of ZnO NPs.

https://doi.org/10.3390/pr14091334

The ZnO NPs band gap was estimated from the experimental UV-Vis data based on Equation (8) [46].

$$(\alpha h\upsilon)^2 = B(h\upsilon - Eg)^{1/2} \quad (8)$$

Here, B is a constant, h = 6.626 × 10^{-34} J Hz^{-1} is the Planck constant, υ is the frequency of light, Eg is the optical band gap energy and α is the adsorption coefficient. The specific band gap was determined using the extrapolation of the linear part of the $(\alpha h\upsilon)^2$ versus (hυ) function to the *x*-axis. The band gap of the ZnO NPs was estimated to be equal to 3 eV (see the insert in Figure 3c). This band gap is considerably smaller than a typical band gap of bulk ZnO (EG = 3.37 eV) [47]. A decrease in the band gap is a consequence of nanoscopic NP dimensions as well as the plant extract reduction [48], which can result in even more catalytically active NPs than the similar NPs prepared by other methods [49,50].

3.4. FT-IR Measurements

The ZnO NPs FT-IR spectra reveal various peaks centered at 3400 cm^{-1}, 1550 cm^{-1}, 1400 cm^{-1}, 1050 cm^{-1} and 550 cm^{-1} (Figure 3d). The peak at 550 cm^{-1} corresponds to the Zn-O bond, which further corroborates the idea of ZnO NP synthesis [51]. A strong peak at 3400 cm^{-1} could be ascribed to the O-H stretching vibrations of the bound OH group and/or the moisture adsorbed on the ZnO NP surface, whereas a less intense peak at 1550 cm^{-1} stems from the deformation vibrations of the same chemical moieties [52,53]. At the same time, the peaks at 1400 cm^{-1} and 1050 cm^{-1} can be linked to the C-O stretching modes [54,55].

3.5. Dynamic Light Scattering (DLS) Measurements

DLS measurements (Figure 4) are highly sensitive to NP aggregation. The biosynthesized ZnO NPs particle size distribution (Figure 4) is a bimodal function (Figure 4a,b) with roughly half of the particles having a smaller average hydrodynamic radius of 217 ± 16 nm with a relatively narrow polydispersity index (PDI) of 12.9%. The other half of the particles form much larger aggregates with an average hydrodynamic radius of 6883 ± 1232 nm and a much broader distribution, reflected in PDI = 42%. This is broadly consistent with SEM images of the ZnO NPs (Section 3.1) which reveal significant NP aggregation (Figure 2). If one assumes that both modes in particle size distributions in solution as made of tightly packed rigid spheres with as average diameter of 25 nm (Figure 2c), the smaller size well-defined distribution with an average radius of 217 nm represents clusters with several hundreds to a few thousands individual NPs, although the upper limit might be overestimated, since an influence of the hydration sphere of water molecules tightly bound to the surface of NPs has not been taken into account. The second part of the distribution reflects much larger aggregates. Nevertheless, the suspension reveals good temporal stability, with only minor fluctuation in hydrodynamic radius over time (Figure 4c).

3.6. Point of Zero Charge (pH_{zpc})

The pH_{zpc} is the pH value for which the surface net charge of the NP is zero. This value is very important in photodegradation processes. To determine pH_{zpc}, a suspension with 25 mg of the catalyst was added to 10 mL of NaCl (C = 0.0125 molar) with an initial pH of 2, 4, 6, 8, 10, and 12 and stirred for 24h when the final pH was measured. Next, a curve of the pH change as a function of the initial pH was plotted, and the pHzpc was determined as the value of pH in which the pH change does not occur [56]. From Figure 5, it is clear that the pH_{zpc} = 8. The pH above pHzpc makes the surface of ZnO NPs negative while pH below pHzpc makes the ZnO NP surface positive [57,58].

https://doi.org/10.3390/pr14091334

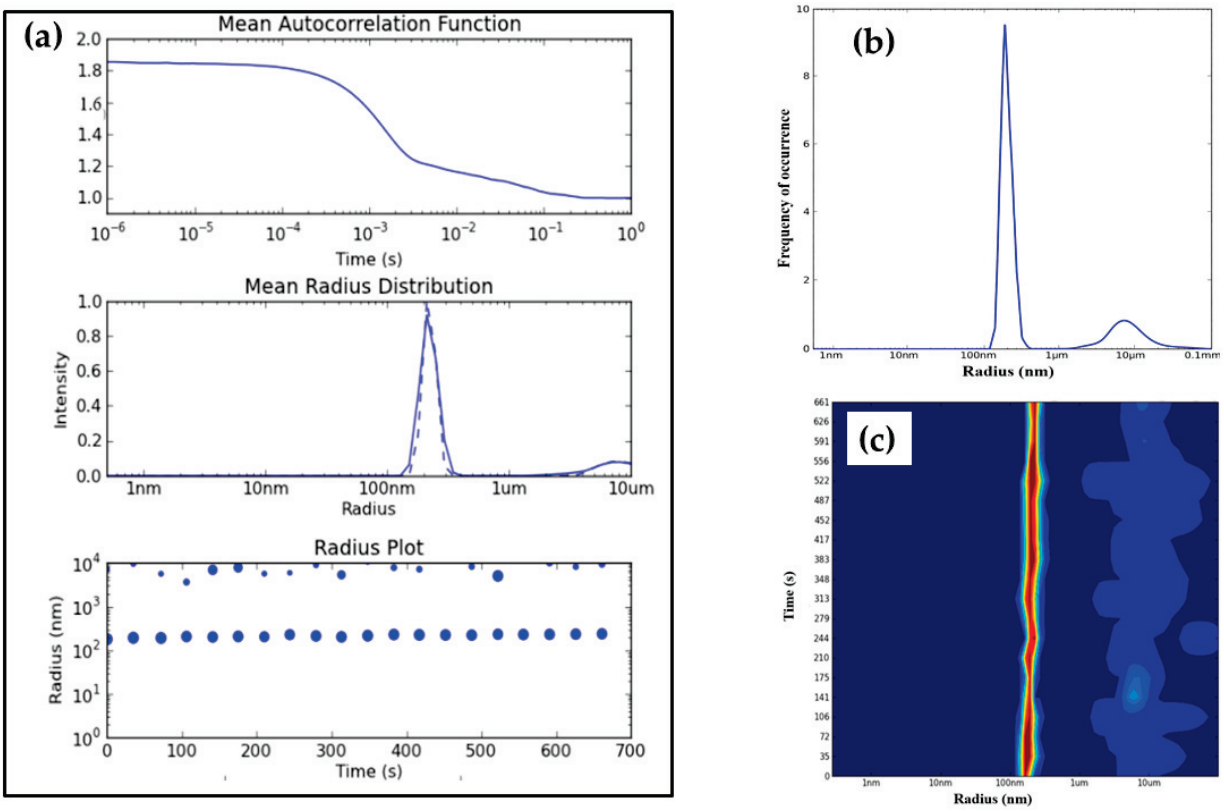


Figure 4. DLS analysis of ZnO NPs biosynthesized with the use of *Licania tomentosa* leaf extract. (**a**) Mean autocorrelation funcion, Mean radius distribution (solid line) and Gaussian peak fit in dashed line, Radii of the particles; (**b**) Size distribution of the NPs; (**c**) Time-dependent size distribution.

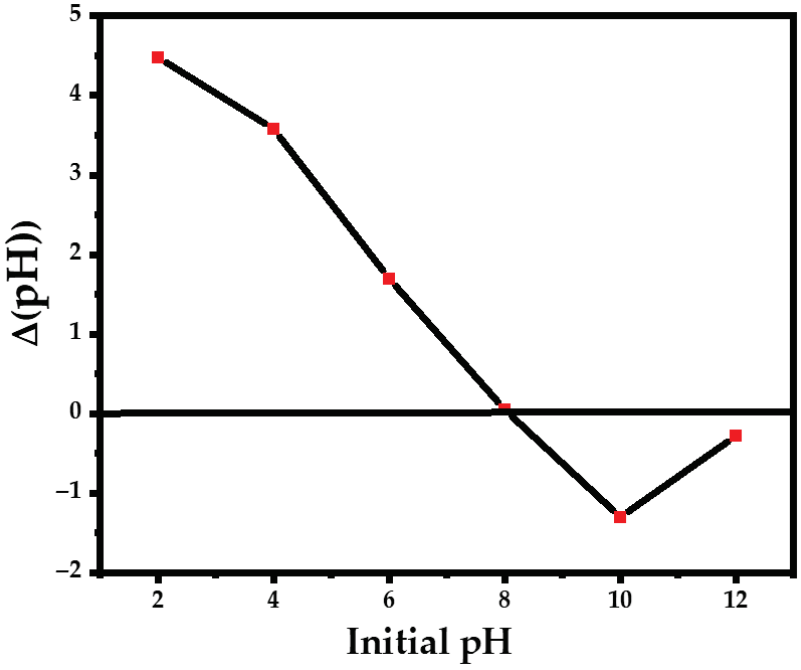


Figure 5. pH_{zpc} of the ZnO NPs biosynthesized with *Licania tomentosa* leaf. The black horizontal line at y = 0 represents the line of zero pH change. The black line with red squares plots the difference ((Δ (pH)) between the final pH and the initial pH of the solution after the addition of the ZnO NPs. The point where this data line crosses the zero-charge line (approximately at pH 8) indicate the point of zero charge for the ZnO NPs.

https://doi.org/10.3390/pr14091334

3.7. Photocatalytic Activity

One of the main objectives of our research was to assess the photocatalytic potential of the green ZnO NPs in degrading MB and CV dyes. The photocatalytic activity of the NPs was tested using a binary dye-catalyst system subjected to UV irradiation. The photocatalytic degradation was performed at an initial pH of MB and CV dyes (initial concentration of 5 ppm) and 25 mg of the respective photocatalyst. Figure 6a,b show the optical absorption spectra of the binary solution shifted significantly over time. A consistent decline in peak intensity for both MB (Figure 6a) and CV (Figure 6b) was observed as a function of the irradiation time. The application of ZnO NPs resulted in remarkable degradation efficiencies of 93.54% for MB (Figure 6c) and 79% for CV (Figure 6d) after seven and two hours of photocatalytic reactions, respectively.

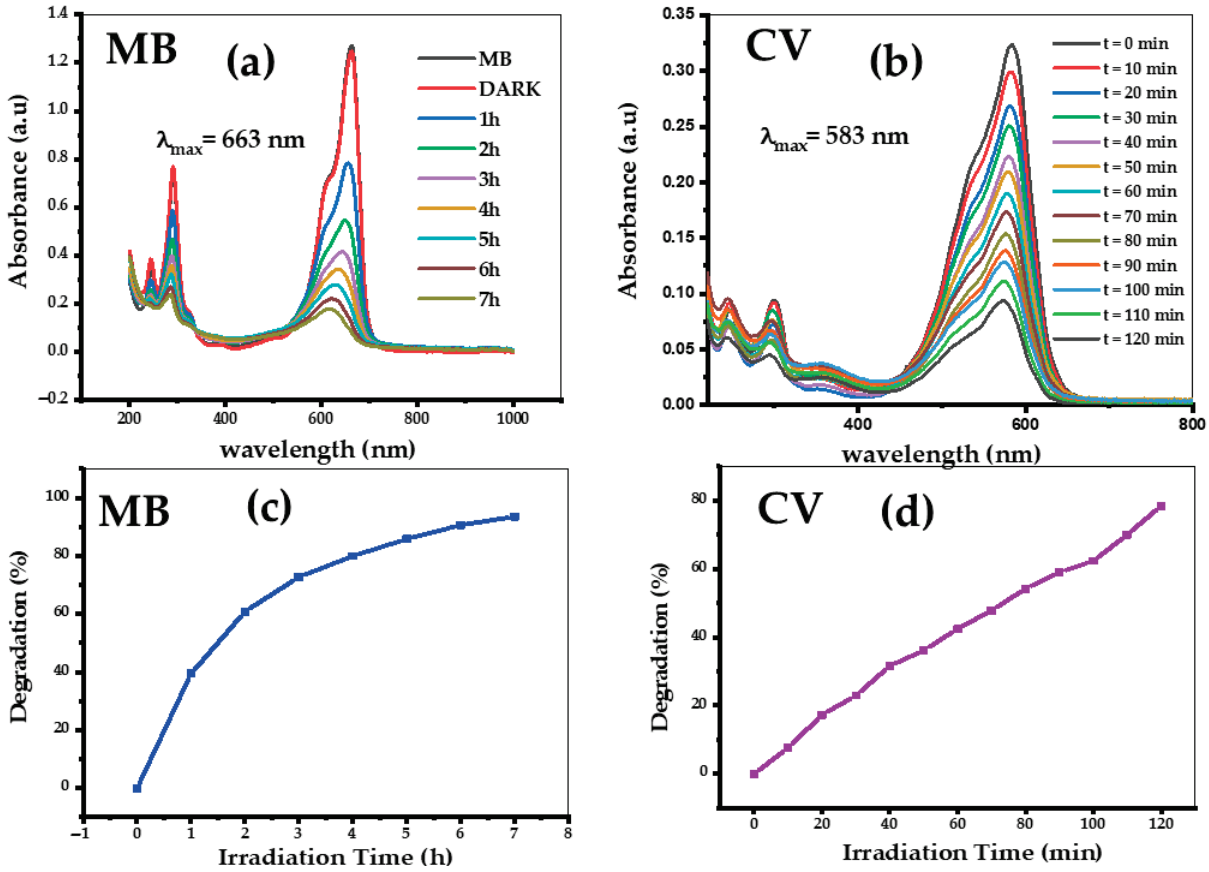


Figure 6. Photocatalytic performance of ZnO nanoparticles synthesized using *Licania tomentosa* leaves toward methylene blue and crystal violet degradation. (**a**,**b**) Changes in the absorption spectra of MB and CV dyes, respectively, as a function of irradiation time in the presence of ZnO NP photocatalyst; (**c**,**d**) the degradation efficiencies of MB and CV dyes solution by the ZnO NPs.

3.8. Kinetic of Photodegradation

The pseudo-first-order kinetics with respect to the substrate concentration is frequently applied to evaluate photocatalytic reactions [59,60]. The kinetic studies of photocatalytic degradation of both MB and CV dyes (Figure 7a,b) show that the photocatalytic degradation process occurs via the Langmuir–Hinshelwood pseudo-first-order reaction which can be described by Equation (9) [61–64]. The pseudo-second-order model was examined in parallel with the first-order model according to Equation (10). However, the R^2-values of the pseudo-first-order model were much better than those of the pseudo-second-order

https://doi.org/10.3390/pr14091334

model. For this reason, we have not included these data in the final text to avoid potentially cluttering the manuscript.

$$\ln\frac{C}{C_0} = -k_1 t \quad (9)$$

$$\frac{1}{C} = \frac{1}{C_0} + k_2\, t \quad (10)$$

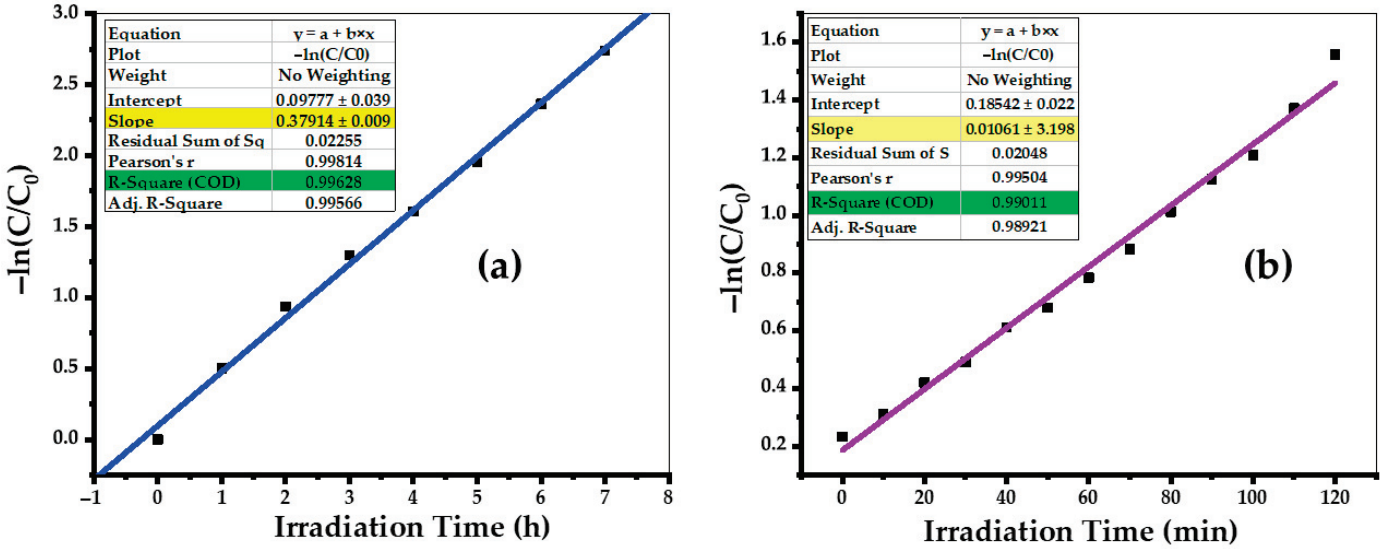


Figure 7. (**a**,**b**) Pseudo-first-order kinetics data for MB and CV dyes photodegradation using the ZnO NPs catalyst.

Here C_0, C, k_1 and k_2 represent the initial concentration of dyes, the concentration of dyes at time t, and the estimated pseudo-first- and second-order rate coefficients, respectively. The plots of $\ln(C/C_0)$ for the pseudo-first-order are given in Figure 7a,b. The rate constants and the corresponding coefficients (R^2) were calculated from the plots. From the results obtained, the pseudo-first-order equation describes well the experimental data as confirmed by the obtained parameters [65]. The MB and CV photodegradation rate constants of 0.37914 h^{-1} and 0.01061 min^{-1} have accomplished under UV light respectively.

3.9. Optimization of Photocatalytic Degradation Parameter

3.9.1. pH Optimization

The influence of the initial pH was evaluated within a pH range from 2 to 12 and 4 to 10 for MB and CV dyes. A 5 ppm dye concentration and 25 mg of the ZnO catalyst dosage were kept constant and the mixture was exposed to UV light (48 W) (Figure 8a,b). It is clear that the dye removal efficiency increases with an increase in the initial pH of MB (Figure 8). The photocatalytic efficiency of MB and CV dyes reached ~94% and ~81% with pH = 12 and pH = 10 after 60 min and 70 min, respectively, against only ~1% and 3% degradation in a weakly acidic medium at pH = 2 and pH = 4. As a result, their first-order rate constant increased with increasing pH values for both dyes, reaching a maximum of 0.051 min^{-1} and 0.0238 min^{-1} for MB and CV dyes, respectively, at pH = 12 and pH = 10 (Figure 8c,d). The pHzpc for the ZnO NPs is 8 (Figure 5). The pH above pHzpc makes the surface of ZnO negative and while pH below pHzpc makes the surface of ZnO positive [65,66]. As demonstrated in Figure 8c,d the highest rate of MB and CV degradation on the ZnO NPs occurs at pH 12 and 10, respectively. This can be explained by an electrostatic attraction of cationic, positively charged dyes to negatively charged NP surfaces. Additionally, a higher amount of OH· radical ions are absorbed on the photocatalyst surface at high pH values, further assisting the efficiency of the photodegradation process [67].

https://doi.org/10.3390/pr14091334

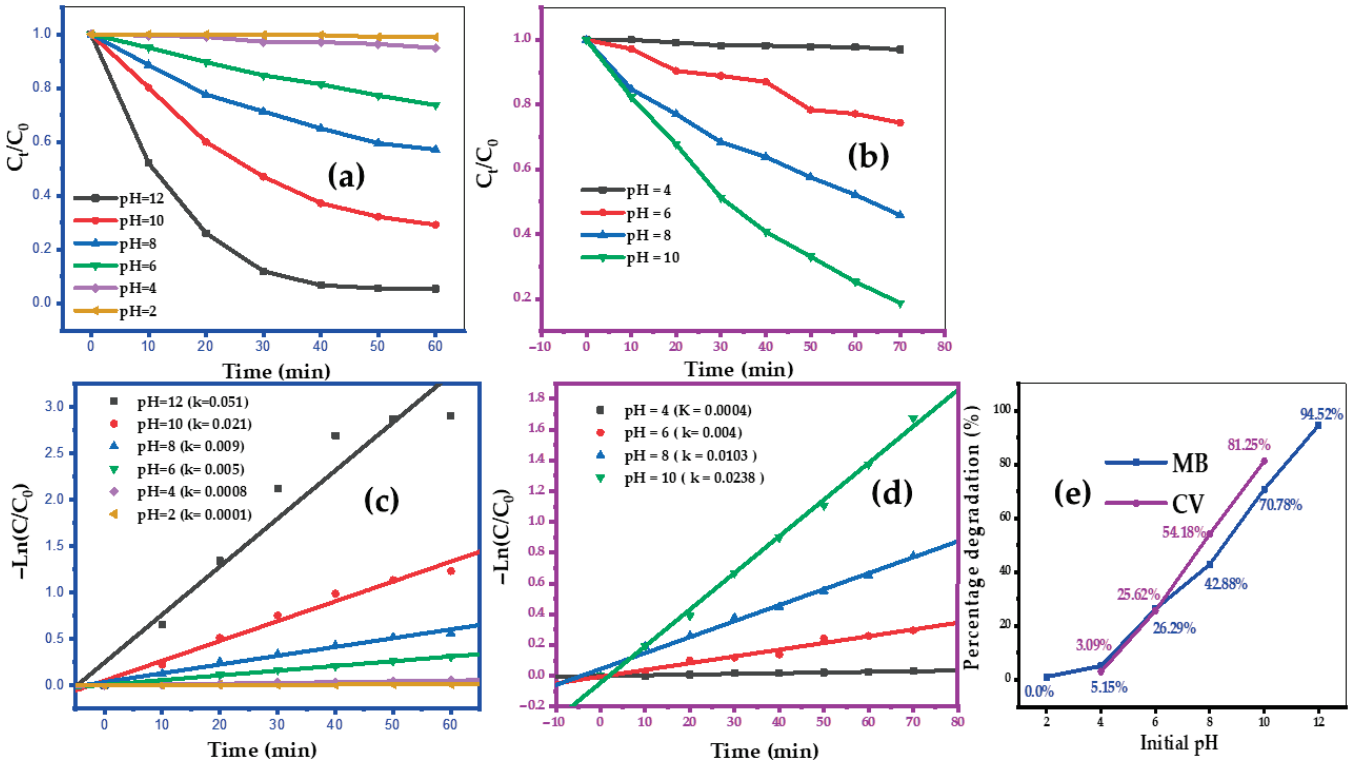


Figure 8. Photocatalyst degradation of MB and CV dye solutions using biosynthesized ZnO NPs under UV light illumination at different pHs. (**a**,**b**) (C/C_0) ratios for, respectively, MB and CV; (**c**,**d**) the plots of $\ln(C/C_0)$ as a function of irradiation time for MB and CV, respectively, and (**e**) the degradation efficiencies.

3.9.2. Optimization of the Catalyst Dosage

The optimal photocatalyst dosage for MB and CV dyes elimination was assessed by altering the quantity of ZnO NPs while maintaining constant dye concentrations and reaction pH. The results show that the efficacies of MB and CV dyes removal are impacted by the dosage of the photocatalyst (Figure 9a,b). When the photocatalyst dosage increased from 6.25 mg to 12.5 mg, ~92% and ~94% degradation of MB was detected, respectively. In parallel, the degradation of the CV dye increased from 13.76% to 79% when the ZnO NPs loading increased from 6.25 mg to 25 mg (Figure 9e). This enhancement in the degradation based on the amount of catalyst dosage is probably due to the availability of highly reactive surface area, which in turn increases the number of active sites as the ZnO NPs concentration increases [67,68]. Notwithstanding this, further increase in the dosage of photocatalyst from 25 mg to 50 mg led to a decrease in the photodegradation efficiency for both dyes. When the photocatalyst dosage exceeds a critical range when there will not be enough room for the NPs to disperse in the solution and the particles tend to stick to each other and become aggregated. In this situation most of the photocatalyst active sites will become blocked and unavailable and the degradation efficiency of the system is expected to decrease [69]. As illustrated in Figure 9e MB and CV dyes show the optimum photodegradation performance at photocatalyst dosages of 12.5 mg and 25 mg, respectively. Therefore, 12.5 mg and 25 mg were chosen as the optimal photocatalyst dosage and were utilized in subsequent experiments.

https://doi.org/10.3390/pr14091334

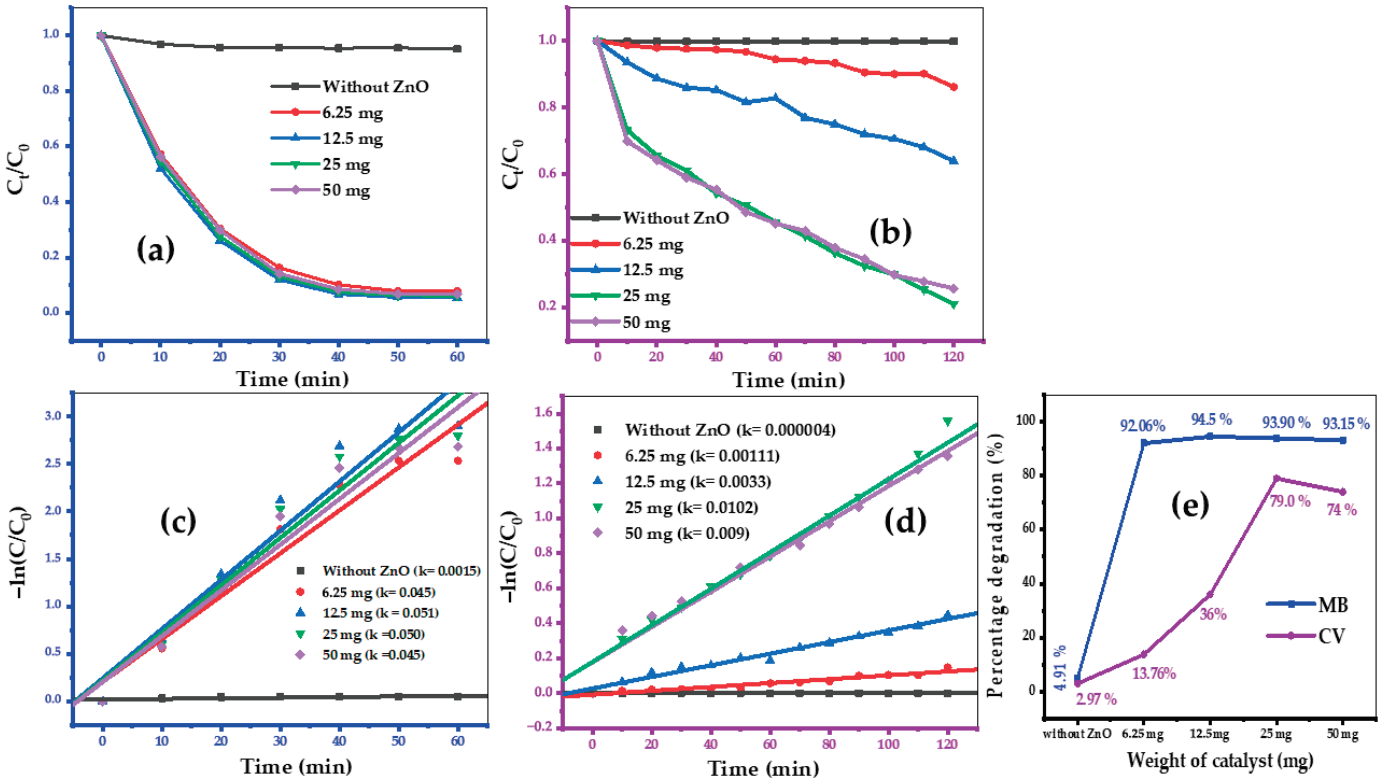


Figure 9. Photocatalyst degradation of MB and CV dye solutions with green-synthesized ZnO NPs under UV light illumination at different catalyst loadings. (**a**,**b**) Ratios (C/C_0) for MB and CV, respectively, (**c**,**d**) the plots of $\ln(C/C_0)$ as a function of irradiation time for, respectively, MB and CV and (**e**) the degradation efficiencies.

In addition, the photocatalytic degradation kinetics were analyzed using a pseudo-first-order kinetic model and the reaction rate constants (k) were calculated for each ZnO NPs dosage. The kinetics data (Figure 9c,d) revealed a similar trend to that of the photocatalytic degradation efficiencies. The k value increases from 0.045 min^{-1} to 0.051 min^{-1} when ZnO dosage is raised from 6.25 mg to 12.5 mg for MB and 0.001 min^{-1} to 0.0102 min^{-1} when photocatalyst dosage is increased from 6.25 mg to 25 mg for CV, confirming enhanced photocatalytic degradation rate at increased ZnO NPs dosages. This increase in the reaction kinetics reflects a larger quantity of active catalytic sites and higher ROS generation at optimal photocatalyst dosage. At 25 mg and 50 mg of ZnO NPs, however, the reaction rate constant for MB and CV declined from 0.050 min^{-1} to 0.045 min^{-1} and 0.0102 min^{-1} to 0.009 min^{-1} respectively, reinforcing the observation that excessive ZnO NPs concentrations are deleterious for its photocatalytic activity.

3.9.3. Optimization of the Initial Dye Concentration

The dye concentration impact on photocatalytic activity is very important for practical applications. Thus, the photocatalytic activity of the biosynthesized ZnO NPs for degradation of MB and CV dyes was investigated by changing the dye concentrations from 5.0 ppm to 15 ppm while maintaining the photocatalyst amount and reaction pH constants (12.5 mg at pH 12 for MB, 25 mg at initial pH of CV) and using UV light irradiation (48 W) (Figure 10a,b). The experimental results reveal that the photocatalytic efficiency of the ZnO NPs is inversely proportional to the concentration of both dyes under similar conditions and maximum catalytic efficacy corresponds to a minimum dye concentration (5 ppm). When the dye concentrations were increased from 5 to 15 ppm, the dye photodegradation fell from 94.5% to 37.0% and 79% to 25.35%, respectively, for MB and CV (Figure 10e). This

https://doi.org/10.3390/pr14091334

decrease is presumably related to lower light absorption on the ZnO photocatalyst surface caused by increased dye concentration in solution, which in turn reduces the production of ROS [70]. Thus, a 5 ppm dye concentration has been chosen in the following optimization experiments for both dyes.

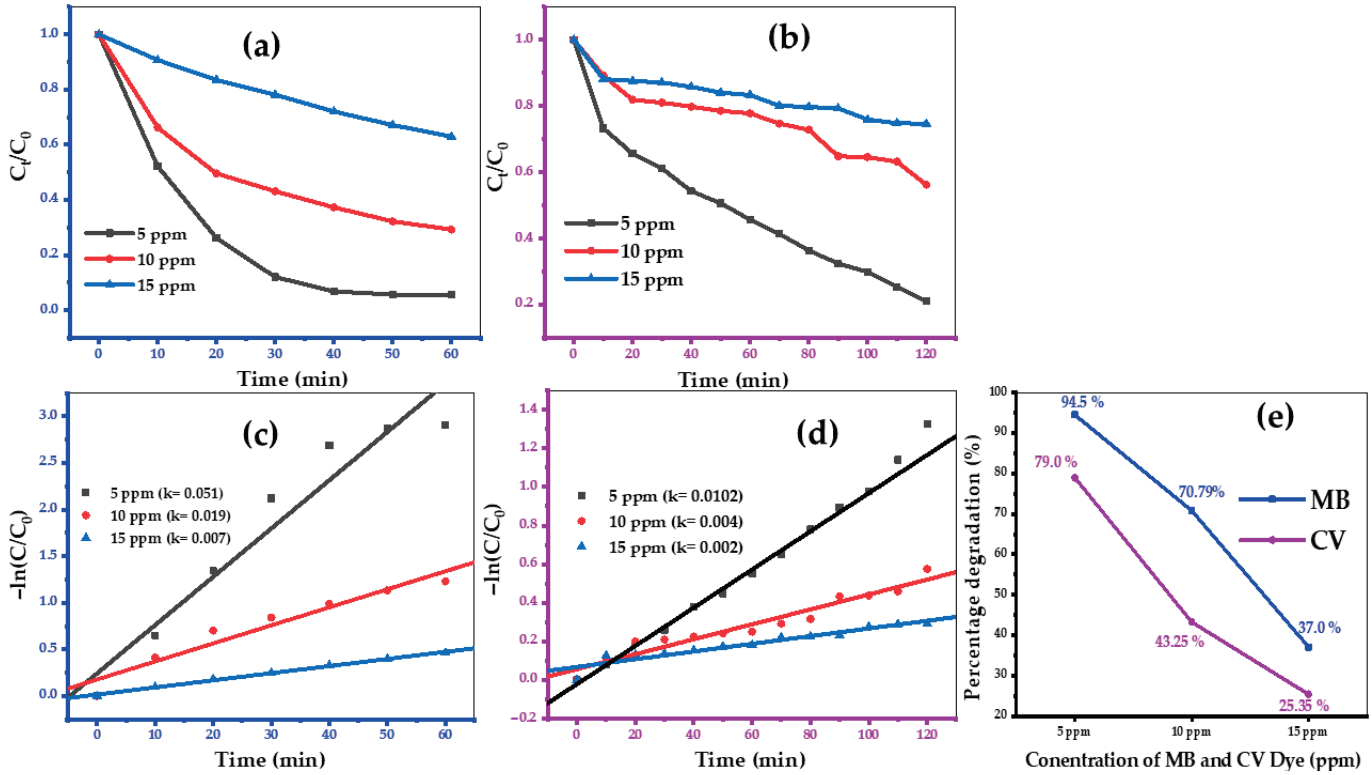


Figure 10. Photocatalyst degradation of MB and CV dyes solutions using biosynthesized ZnO NPs under UV illumination at different concentrations of dyes. (**a**,**b**) Ratios (C/C_0) for, respectively, MB and CV; (**c**,**d**) the plots of $\ln(C/C_0)$ as a function of irradiation time for MB and CV, respectively and (**e**) the degradation efficiencies.

Photocatalytic degradation kinetics were analyzed (Figure 10c,d) and the trend in rate constant closely follows the degradation efficiencies: at 5 ppm concentration of dyes, reaction rate constants were highest (0.051 min^{-1} for MB and 0.0102 min^{-1} for CV), reflecting efficient photocatalytic degradation due to the high amounts of ROS and minimal light attenuation. At 10 ppm dye concentrations, rate constants decreased (0.019 min^{-1} for MB and 0.004 min^{-1} for CV), indicating a slight reduction in degradation rate, whereas at 15 ppm dye concentrations, rate constants dropped sharply (0.007 min^{-1} for MB and 0.002 min^{-1} for CV). These results highlight the importance of matching the initial dye concentration with the catalyst dosage to maximize the photocatalytic activity. Excessive dye concentrations not only limit the availability of ROS but also impede light penetration, which ultimately hinders the overall photocatalytic reaction. Photocatalytic degradation at varying dye concentrations can be understood as a competition between the availability of ROS and the quantity of dye molecules. At low concentrations of dyes, ZnO NPs photogenerated ROS are abundant, enabling rapid and efficient degradation of the dye molecules. However, as the dye concentrations increase, ROS concentration becomes suboptimum, leading to a decrease in the photocatalytic degradation efficiencies and reaction rates. Dye concentration of 5 ppm represents a point of equilibrium at which the ROS production matches the dye molecule concentration. Beyond this concentration, the degradation process becomes diffusion- and light-limited, further underscoring a need for optimization for particular applications [71].

https://doi.org/10.3390/pr14091334

3.9.4. Intensity of Light Optimization

To investigate the influence of UV light intensity levels on the ZnO NP catalyzed photodegradation of MB and CV, the UV lamps with a total power of 34 W and 48 W were employed while the initial MB and CV dyes concentration, catalyst loading and pH were set to 5 ppm: 25 mg for CV, 12.5 mg for MB and (12 for MB and initial pH of CV, respectively. The experiments were conducted under light illumination and in the absence of light (Figure 11a,b). It is clear that the photodegradation efficiency is impacted by the light intensity. Indeed, when UV light intensity was increased from 24 W to 48 W, both the rate and percentage of dye degradations increased from 0.029 min^{-1} to 0.051 min^{-1} and 82.62% to 94.52%, respectively, for MB. In parallel, the same parameters grow from 0.004 min^{-1} to 0.0102 min^{-1} and 50% to 79% for CV (Figure 11c–e). Since the ZnO NPs suspension is stirred in solution, the light intensity directly affects the light intensity, which illuminates the surface of the catalyst. The increase in degradation rates and efficiencies can be explained by the higher generation of ROS on the ZnO NP surface under stronger light illumination. As expected, in the dark, the ZnO NPs were unable to efficiently eliminate the dyes (Figure 11) [72,73].

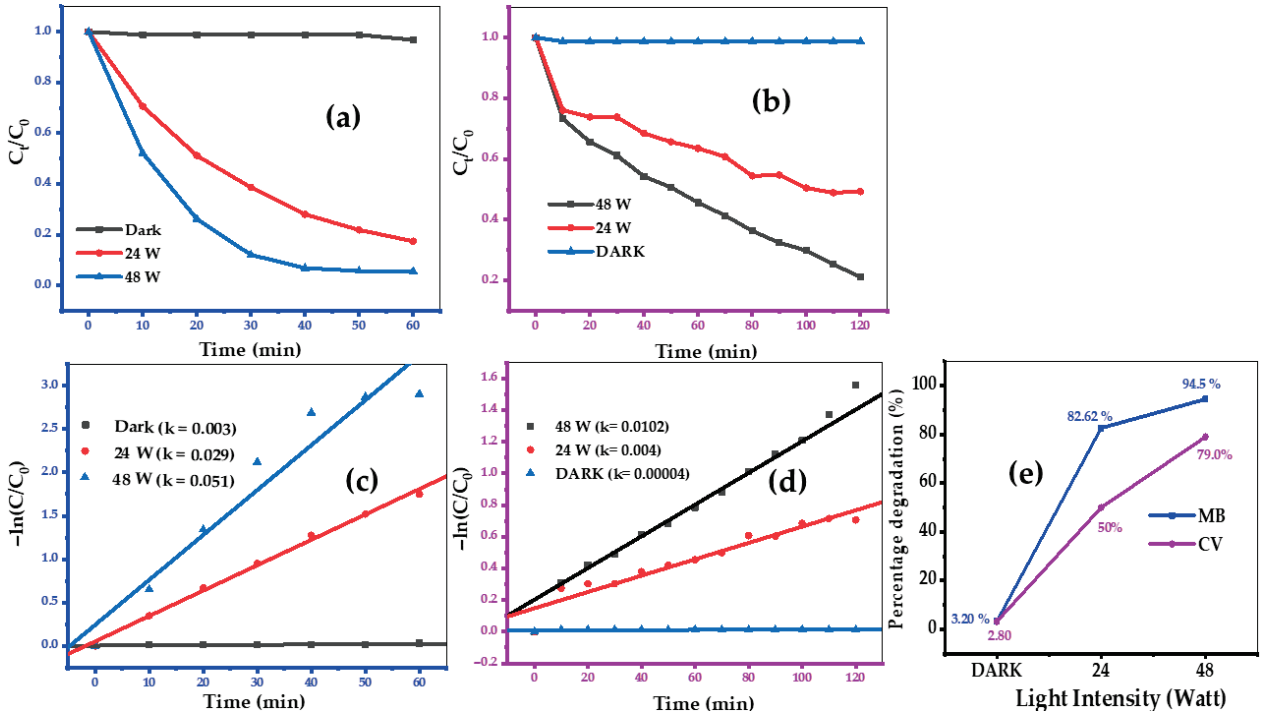


Figure 11. Photocatalyst degradation of MB and CV dye solutions using green-synthesized ZnO NPs under UV light illumination of different intensities. (**a**,**b**) Ratios (C/C_0) for MB and CV, respectively; (**c**,**d**) the plots of $\ln(C/C_0)$ as a function of illumination time for MB and CV, respectively, and (**e**) the degradation efficiencies.

3.10. Identification of Main Reaction Oxygen Species

To understand the photocatalytic process in molecular detail it is important to identify the ROS involved in the breakdown of dyes. When MB is photodegraded using ZnO, four different radical scavengers, EDTA, DMSO, BQ and IPA were separately added to the reactions to capture holes (h^+), electrons (e^-), superoxide ($^{\bullet}O_2^-$) and hydroxyl radicals ($^{\bullet}OH$) respectively [74–76]. All scavengers were tested at the same concentration (1.0 mM) but BQ (0.5 mM). A total of 5 ppm of aqueous MB solution at pH = 12 and 12.5 mg of ZnO catalyst were used. The plots (C/C_0) and the percentage of dye degradation in the presence and absence of scavengers are given in Figure 12a,b. The photodegradation

https://doi.org/10.3390/pr14091334

efficiency of MB was significantly reduced upon addition of BQ (40.1%), DMSO (61.7%) and EDTA (60.2%), while the addition of IPA (86.9%) had relatively little effect. According to the effects of scavengers on the efficiency of MB removal, their inhibitor effect can be ranked as BQ > DMSO > EDTA > IPA > No scavenger. This means that $^{\bullet}OH$ can have a certain influence on the reaction, whereas h^+, e^- and $^{\bullet}O_2^-$ radicals play crucial roles in the photocatalysis of MB dye. Although it is known that DMSO, particularly at high concentrations and high pHs, is capable of also capturing $^{\bullet}OH$ radicals [77,78], and the influence of DMSO can be partially ascribed to this effect, the fact that IPA has modestly affected the photocatalytic activity practically rules out a predominant role of hydroxyl radicals under the studied conditions. The impact of the scavengers on the efficiency of photocatalytic degradation of CV is represented in Figure 12c [69]. The strongest suppression of the photocatalytic reaction was observed for acid ascorbic (AA), revealing that superoxide plays a leading role in the CV photodegradation. IPA and EDTA also caused suppression of the rate of the CV photocatalytic degradation, but their impacts were somewhat more limited. This indicates that H^+ and $^{\bullet}OH$ also play important roles but they are less important than superoxide ions for this particular photocatalytic reaction.

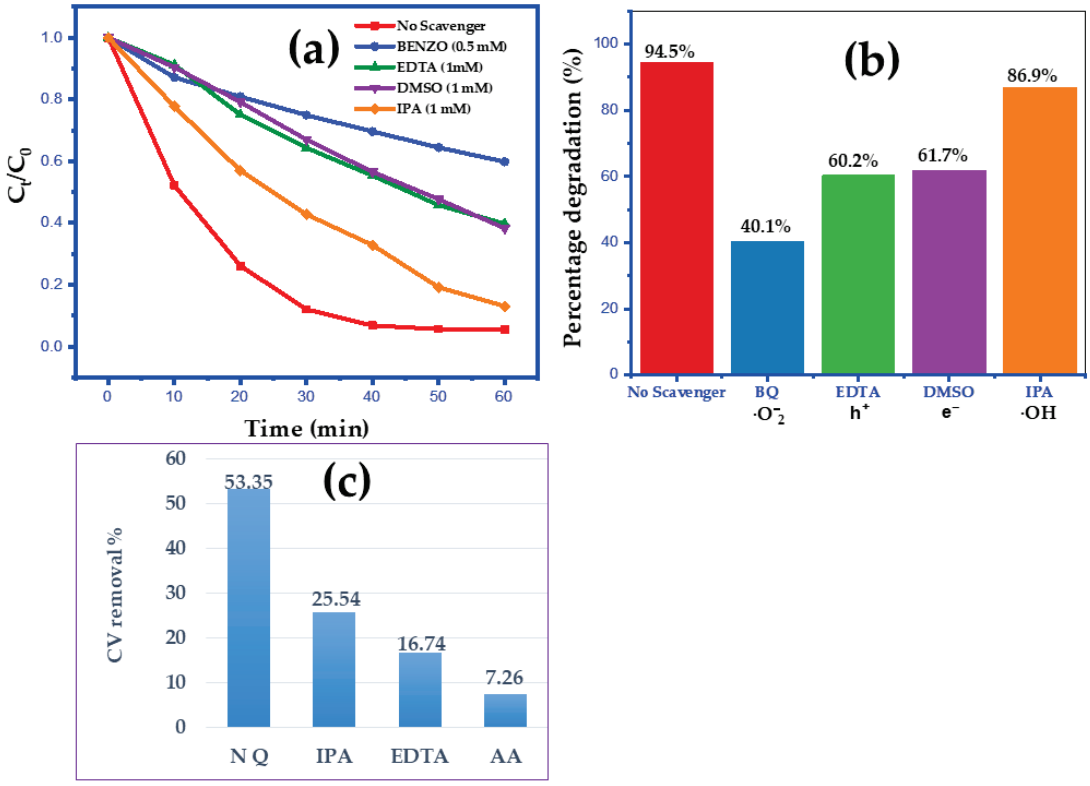


Figure 12. (**a**) Impacts of BQ, DMSO, EDTA, AA and IPA addition during the ZnO-mediated photocatalytic degradation of MB; (**b**) the maximum percentage of observed degradation in the presence of different scavenging agents; (**b**,**c**) the corresponding degradation efficiencies.

3.11. Mechanism of MB Dye Degradation

Based on the experiment data the following mechanism may be proposed for the degradation of MB dye (Figure 13). Upon exposure to UV irradiation, photons having energy equal to or greater than the band gap energy of the ZnO NPs (3 eV) excite e^- from the valence band (VB) to the conduction band (CB), creating electron–hole pairs. The electrons and photogenerated holes on the surface of the NPs react with O_2 and H_2O, leading to the formation of radicals with high oxidative power, such as superoxide ($^-O_2$)

https://doi.org/10.3390/pr14091334

and hydroxyl ($^{-}$OH) that degrade dyes down to the final H_2O and CO_2 molecules and other non-polluting sub-products [75,79,80].

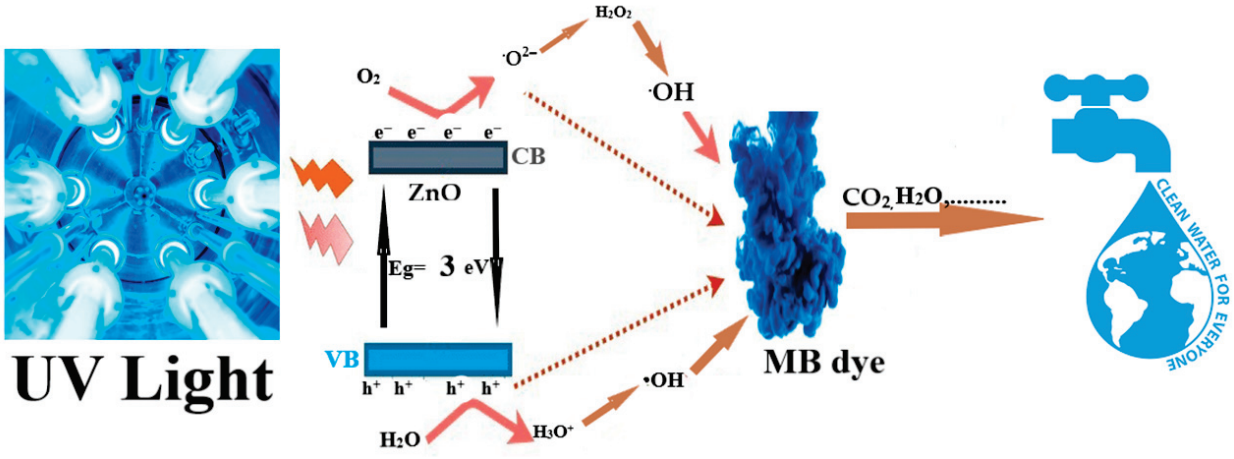


Figure 13. Schema of the photocatalytic degradation routes: Schematic illustration of the photocatalytic degradation mechanism of MB dye using ZnO under UV light irradiation. Upon UV exposure, electrons (e^{-}) are excited from the valence band (VB) to the conduction band (CB), leaving behind holes (h^{+}). These charge carriers generate reactive oxygen species such as •OH and $O_2{}^{-}$•, which contribute to dye degradation. Solid arrows indicate the primary charge transfer and redox reactions, while dotted arrows represent the diffusion and interaction of reactive species with MB dye molecules. Different colored arrows distinguish between oxidation (red) and reduction (brown) pathways involved in the photocatalytic process.

In this study, we decided to directly measure the availability of particular ROS produced by the ZnO NPs. We have chosen to measure H_2O_2 because it is the most biologically stable ROS and also the most quantifiable by biochemical means. To measure H_2O_2 release, we used the samples of ZnO NPs biosynthesized using *Licania tomentosa* and *Annato* tree leaves [25] suspended at 0.25 mg/mL in a solution of water exposed to 24 W UVA light for 4 h with continuous stirring. During the experiment, 1 mL aliquots were taken every one hour in duplicate. The supernatant was obtained by centrifugation at 13,300 rpm for 10 min. To measure the production of H_2O_2, a 49 µL kit consisting of a mixture of 200 µM Ampliflu red 5 U/mL of horseradish peroxidase and 50 mM Bis-Tris buffer pH = 6, was mixed with 51 µL of each type of nanoparticle, followed by an absorbance measurement at λ = 560 nm using spectrophotometer M200 Pro (TECAN) (Figure 14a).

Figure 14a indicates a steady increase in H_2O_2 content over time, with a production of 39.96 µM and 27.08 µM of H_2O_2, respectively, with ZnO NPs from Oiti (*Licania tomentosa*) and *Annatto* tree leaves extract.

ROS are inherently unstable and degrade over time. Some, such as hydroxyl radical (·OH), are highly reactive and consequently short-lived, having only an in vivo half-life of 10^{-9} s^{-1} [81]. H_2O_2 is the most stable of the ROS making it more suitable for quantification. ZnO NPs frequently have a number of crystalline defects at the surface allowing electron hole pairs (e^{-} h^{+}) to form upon excitation in the UV or visible spectrum [82,83]. Water suspending these particles can be split forming H_2O_2 and other ROS through the following possible reactions [82,84]:

$$ZnO + h\upsilon \rightarrow e^{-} + h^{+} \quad (11)$$

$$h^{+}H_2O \rightarrow OH^{\cdot} + H^{+} \quad (12)$$

$$e^{-} + O_2 \rightarrow O_2^{\cdot -} \quad (13)$$

https://doi.org/10.3390/pr14091334

$$O_2^{\cdot -} + H^+ \rightarrow HO_2^{\cdot} \quad (14)$$

$$HO_2^{\cdot} + H^+ + e^- + \rightarrow H_2O_2 \quad (15)$$

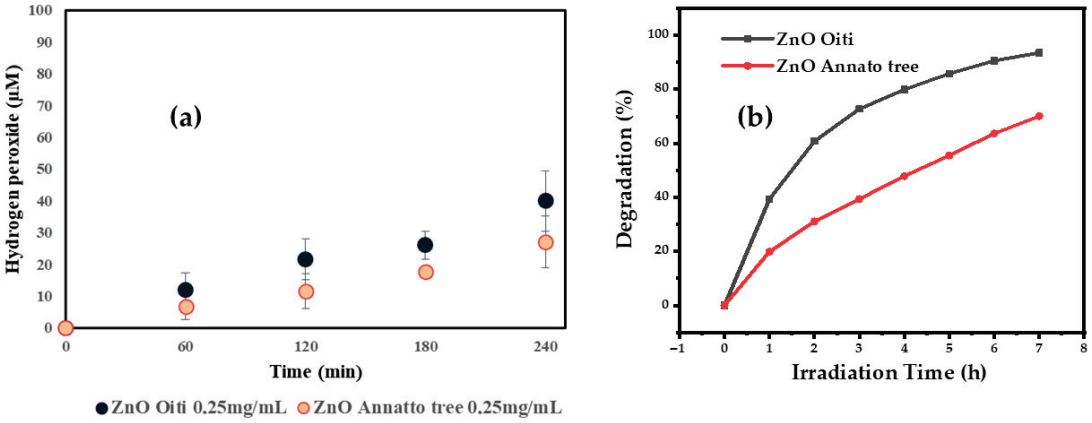


Figure 14. (**a**) H_2O_2 generated and (**b**) degradation efficiencies of MB dye by the ZnO NPs synthesized using *Licania tomentosa* and *Annatto* tree leaves extract during UV irradiation.

Moreover, the quantity of H_2O_2 generated by the ZnO NPs synthesized using *Licania tomentosa* leaf is greater than that produced by *Annatto* tree leaf extract. This could explain the difference in the photocatalytic performance obtained by these two types of ZnO NPs (Figure 14b). Indeed, Figure 14b shows that the ZnO NPs biosynthesized using *Licania tomentosa* leaves, which produce a higher amount of H_2O_2, offer superior degradation efficiency compared to the NPs biosynthesized with *Annatto* tree leaves (93.54% vs. 70.07%, respectively) under the same conditions (25 mg of ZnO NPs catalyst, 100 mL of 5 ppm MB in initial pH, 48 W UVA light during 7 h). This is consistent with the results obtained by Yangsi Liu et al. [85].

Under UV light, H_2O_2 supports the generation of hydroxyl radicals leading to improved treatment efficiency. This occurs either by interaction of H_2O_2 with radiation, superoxide anion (formed by the reaction of dissolved oxygen with the catalyst under irradiation) or by accepting the electron from the catalyst conduction band, according to the reactions shown below [86,87]. In general, an increase in H_2O_2 concentration leads to improved color removal [88–90].

$$H_2O_2 + h\upsilon \rightarrow 2HO^{\cdot} \quad (16)$$

$$H_2O_2 + O_2^{\cdot -} \rightarrow OH^{\cdot} + OH^- + O_2 \quad (17)$$

$$H_2O_2 + e^- \rightarrow OH^- + OH^{\cdot} \quad (18)$$

3.12. Reusability of Photocatalyst

The recyclability of ZnO nanoparticles for the photodegradation of MB was investigated to check the practical application of the catalysts in photocatalytic applications. In our experiments, the photocatalyst can be recycled up to four cycles and their photocatalytic results are shown in Figure 15a. After each photocatalysis experiment, the catalyst was thoroughly rinsed with ethanol and water then vacuum dried at 100° C and reused another time. The efficiency of photodegradation of MB by ZnO NPs has been observed to be intact for at least four cycles.

https://doi.org/10.3390/pr14091334

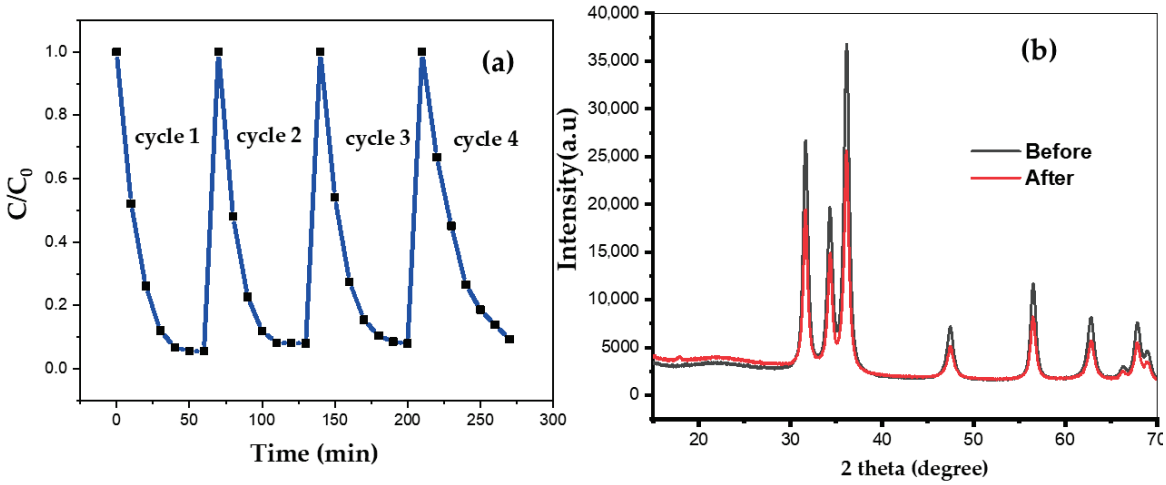


Figure 15. (**a**) The reusability of the ZnO NPs and (**b**) XRD before and after 4 photodegradation cycles.

To investigate what happens with the photocatalyst in the course of the photocatalytic process, the ZnO NPs after four photocatalytic cycles were subjected to XRD analysis. The XRD profile demonstrated a well-defined crystalline order (Figure 15b). Structural parameters of the biosynthesized ZnO NPs prior to and post four cycles of the photocatalytic degradation process are given in Table 1. Our results demonstrate that continuous UV illumination led to an increase in the average crystallite size (from 15.9 to 23.8 nm) and a significant decrease in the dislocation density (Table 1), consistent with the previous studies [4]. One possible explanation of this phenomenon is the heating up of the NPs in the process of UV irradiation during photocatalytic cycles and cooling them down between the cycles. This might lead to an annealing effect, which would promote the collapse of the individual crystallites leading to a bigger crystallite formation, accompanied by partial elimination of dislocations. This could impact parameters of the NPs, such as, for example, the nature and concentration of electronic defects which are known to have significant impacts on the NP photocatalytic performances [91]. However, additional studies of the structural parameters of photocatalytic NPs will be needed to fully confirm this hypothesis.

Table 1. Structural parameters of the ZnO NPs before and after 4 photocatalytic cycles.

	Average Crystallite Size (nm)	Dislocation Density (δ) (nm^{-2})	Strain
Before	15.9	3.94×10^{-3}	2.55×10^{-3}
After	23.8	1.76×10^{-3}	4.75×10^{-3}

4. Antimicrobial Activity

The antimicrobial activity of the biosynthesized ZnO NPs was evaluated through the determination of their MIC, MBC and IC_{50} (Table 2; Figure 16). The NPs exhibited broad-spectrum inhibitory effects against all tested species, although with variable potency depending on the microorganism. Among Gram-negative bacteria, *E. coli* ATCC 35218 showed the lowest IC_{50} value (7.74 μg/mL), indicating high susceptibility to ZnO NPs. *K. pneumoniae* ATCC 700603 exhibited an intermediate response (IC_{50} = 128.91 μg/mL). *P. aeruginosa* ATCC 27853 also demonstrated strong sensitivity to ZnO NPs (IC_{50} = 12.57 μg/mL), whereas the clinical isolate *P. aeruginosa* B3 displayed a markedly higher IC_{50} (283.14 μg/mL). The MIC values for Gram-negative strains were in the range from 1000 to 2000 μg/mL, and MBC values were ≥1000 μg/mL, suggesting that high nanoparticle concentrations are required to achieve bactericidal activity.

https://doi.org/10.3390/pr14091334

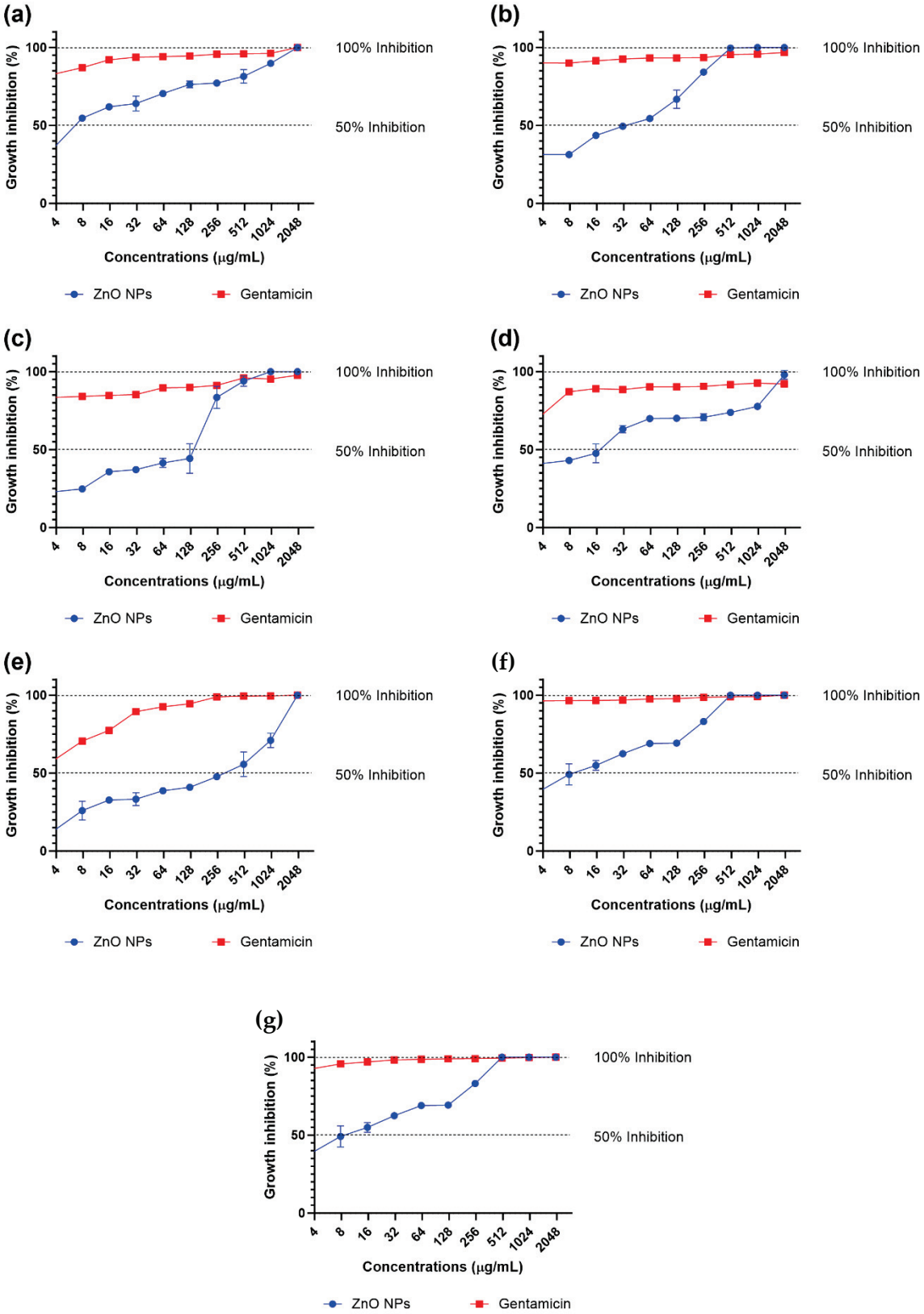


Figure 16. Dose–response inhibition curves of ZnO nanoparticles against Gram-negative and Gram-positive bacterial strains. (**a**) *E. coli* ATCC 35218, (**b**) *E. faecalis* ATCC 29737, (**c**) *K. pneumoniae* ATCC 700603, (**d**) *P. aeruginosa* ATCC 27853, (**e**) *P. aeruginosa* B3, (**f**) *S. aureus* ATCC 29213, and (**g**) *S. aureus* SA01. Data represent the mean inhibition percentage relative to untreated controls.

https://doi.org/10.3390/pr14091334

Table 2. Antimicrobial activity of green-synthesized ZnO nanoparticles against clinical and reference bacterial strains.

Bacteria	IC50 (μg/mL)	MIC (μg/mL)	MBC (μg/mL)
E. coli ATCC 35218	7.74	1000	2000
E. faecalis ATCC 29737	41.86	250	2000
K. pneumoniae ATCC 700603	128.91	1000	1000
P. aeruginosa ATCC 27853	12.56	1000	1000
P. aeruginosa B3	283.14	2000	>2000
S. aureus SA01	130.53	1000	2000
S. aureus ATCC 29213	10.98	1000	2000

IC_{50}: half maximal inhibitory concentration; MIC: minimum inhibitory concentration; MBC: minimum bactericidal concentration.

Among Gram-positive bacteria, *S. aureus* ATCC 29213 showed a low IC_{50} value (12.56 μg/mL), comparable to the more susceptible Gram-negative strains. In contrast, *S. aureus* SA01, a multidrug-resistant bloodstream isolate [92], showed reduced susceptibility (IC_{50} = 130.53 μg/mL). This strains *E. faecalis* ATCC 29737 exhibited moderate susceptibility with an IC_{50} of 41.86 μg/mL and an MIC of 250 μg/mL, the lowest MIC observed among all tested species. Consistent with the behavior of other strains, bactericidal activity required elevated concentrations (MBC = 2000 μg/mL).

These results demonstrate that ZnO NPs possess measurable antimicrobial activity; however, complete growth inhibition and bactericidal effects required higher doses. This is a typical behavior of metal–oxide nanoparticles, whose antimicrobial action is known to involve multiple mechanisms, including ROS generation, membrane disruption, and Zn^{2+} ion release. Indeed, evidence from mechanistic studies confirms that ZnO NPs induce oxidative stress, damage cytoplasmic membranes, and release Zn^{2+} ions, three central pathways contributing to their bactericidal activity [93–95].

Unlike previous studies with the use of the biosynthesized NPs, most works use the agar diffusion method based on halo formation, whereas the results of this study were obtained using the microdilution method. Furthermore, differences in the chemical composition of the extracts used, the synthesis conditions, or the particle morphology can significantly influence the antimicrobial response. Considering these factors, Gharbia et al. [96] observed strong antimicrobial activity of ZnO nanorods produced from Olea europaea leaf extract, with inhibition zones $\geq$ 30 mm against *S. aureus*, *Streptococcus mutans*, and *E. coli*. Similarly, Manojkumar et al. [30] and Francis et al. [90] synthesized ZnO nanoparticles from *Brassica oleracea* var. *botrytis* (BO) leaf extract and reported inhibition zones against *S. aureus* (13 mm), K. pneumoniae (13 mm), and *E. coli* (9 mm). Francis et al. [97], using the microdilution method, report MICs between 125 and 250 ng/μL (equivalent to 125–250 μg/mL) for biogenic ZnO NPs, with microbicidal activity equal to these MICs. These values are lower than those obtained in this study (250–2000 μg/mL). This difference could be related to partial aggregation of the nanoparticles in the liquid medium, reducing their specific surface area, or to the specific physicochemical characteristics of the extract used, which influence their bioavailability and their ability to interact with bacterial cells.

5. Antibiofilm Activity

The antibiofilm effects of ZnO nanoparticles were evaluated against *E. faecalis* ATCC 29737, *P. aeruginosa* ATCC 27856, and *S. aureus* SA01 using crystal violet staining to quantify biofilm biomass. ZnO NPs inhibited biofilm formation in a concentration-dependent fashion, although the magnitude and pattern of inhibition varied across species (Figure 17). For *E. faecalis*, ZnO NPs achieved 84.80 $\pm$ 4.74% inhibition at MIC, with inhibition decreas-

https://doi.org/10.3390/pr14091334

ing to 64.91 ± 6.30% at 0.5 × MIC and 22.82 ± 4.62% at 0.25 × MIC, indicating a clear dose-dependent response.

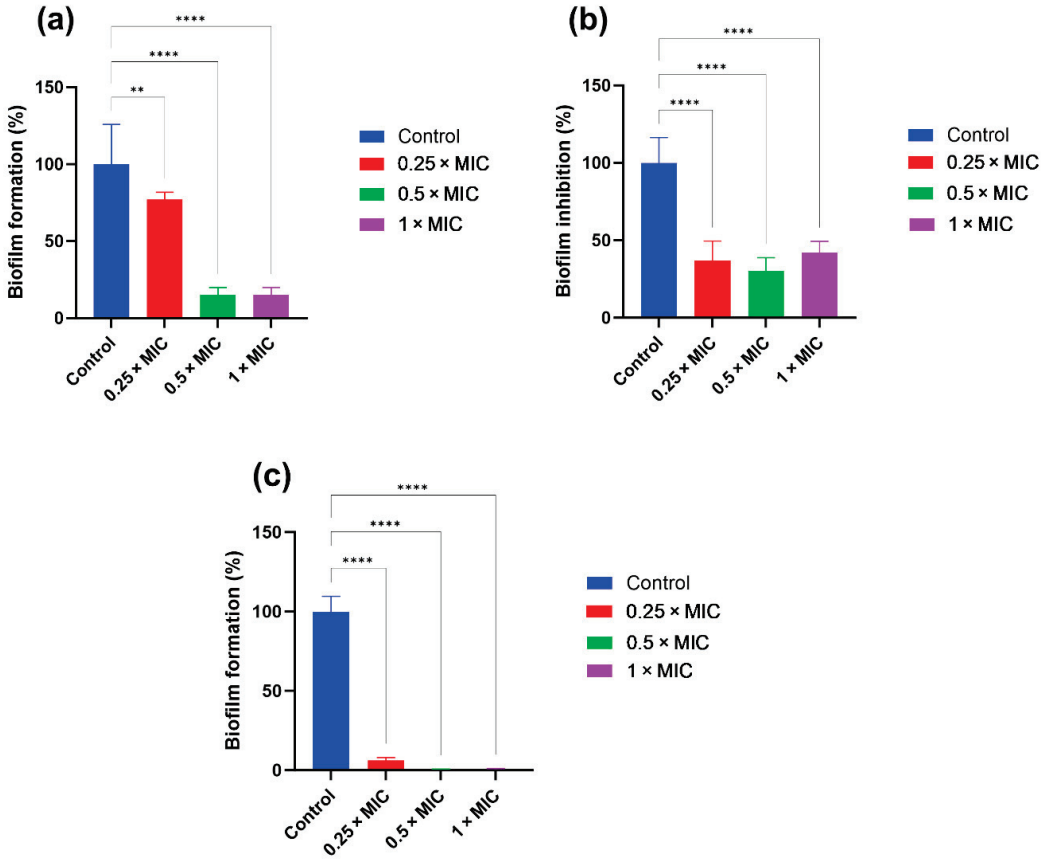


Figure 17. Inhibition of biofilm formation by green-synthesized ZnO nanoparticles. (**a**) *Enterococcus faecalis* ATCC 29737, (**b**) *Pseudomonas aeruginosa* ATCC 27856, and (**c**) *Staphylococcus aureus* SA01. The percentage of inhibition was calculated relative to untreated biofilm controls. ** $p < 0.01$; **** $p < 0.0001$. MIC: minimum inhibitory concentration.

Importantly, the biofilm of *S. aureus* SA01 was completely inhibited by all tested concentrations. In contrast, *P. aeruginosa* ATCC 27856 displayed similar levels of biofilm inhibition across all three concentrations tested. No statistically significant differences in the resulting values ($p > 0.05$) have been observed, which ranged from 57.75 ± 7.13% to 69.62 ± 12.63%. Comparable behavior has been described in other nanoparticle–biofilm systems, particularly under sub-inhibitory NP concentrations, where bacterial stress responses, extracellular polymeric substance (EPS) reorganization, or enhanced NP penetration into the biofilm matrix may modulate the extent of inhibition [92].

The green ZnO NPs characterized in this research demonstrated enhanced CV and MB dyes degradations under UV irradiation and antimicrobial MIC values as compared to other ZnO NPs (Table 3). The recent studies on green-synthesized ZnO NPs are compared in Table 3. While bulk ZnO has a band gap of about 3.37 eV, green-synthesized nanoparticles often show slightly reduced value (~2.9 eV, likely due to lattice defects such as oxygen vacancies formed during synthesis). This band gap narrowing enables activation under UV and visible light and improves photodegradation efficiency. Additionally, the nanoscale morphology of ZnO NPs enhances their interaction with bacterial cells, while defect-induced reactive oxygen species contribute to their antimicrobial activity [98,99].

https://doi.org/10.3390/pr14091334

Table 3. MB and CV dyes degradation efficiencies by biogenic ZnO NPs.

Source of Nanomaterials	Extract Mass	Temperature of Calcination	Band Bap (eV)	Composition	Catalyst Load (mg)	Light Source	Removal Efficiency (%)	Initial Dye Concentration (ppm)	pH of Solution	Rate Constant k (min^{-1})	Dye	Ref.
Cow dung	1 g in 100 mL water	400 °C, 3 h	3.19	Zn and O	18	UV	87.5 (100 min)	5	10	0.05675	MB	[100]
Delonix elata leaf	20 g in 100 mL water	400 °C, 2 h	2.7	Zn and O	20	UV	86 (90 min)	10	Initial pH	0.01598	CV	[101]
Acalypha indica leaf	20 mg in 50 mL	400 °C, 4 h	3.34	Zn and O	100	Sunlight	96 (90 min)	16.67	Initial pH	1.04476	MB	[102]
Litchi chinensis leaf	50 g in 200 mL	500 °C, 3 h	3.33	Zn and O	5	UV	98 (120)	5	Initial pH	0.0295	MB	[103]
Equisetum diffusum D	5 g in 100 mL	450 °C	2.79	Zn, O, S, C	20	UV	85.61 (120)	10	Initial pH	0.152	MB	[104]
Licania tomentosa leaf	3 g in 150 mL	500 °C	3	Zn and O	12.5	UV	94.5 (60 min)	5	12	0.051	MB	This work
Licania tomentosa leaf	3 g in 150 mL	500 °C	3	Zn and O	25	UV	81 (70 min)	5	10	0.0102	CV	This work

Zone of inhibition (mm) and MIC as demonstrated by green ZnO NPs

Plant	Extract mass	Temperature of calcination	Morphology structure	Composition	Bacterial strains	MIC (μg/mL)	Ref.
Equisetum diffusum D	5 g in 100 mL	450 °C	Spherical	Zn, O, S, C	*Listeria monocytogenes*, *Staphylococcus epidermidis*, *Escherichia coli* and *Bordetella bronchiseptica*	30, 20, 70 and 90	[104]
M. oleifera	50 g in 200 mL	80 °C	Agglomerated shape	Zn and O	*C. albicans*, *E. coli*, *K. paneumoniae*, *P. aeruginosa*, *S. aureus* and *A. baumannii*	18.89, 16.56, 10.85, 4.11, 5.42, and 6.23	[105]
Pomegranate Leaf and Flower	10 g in 100 mL	80 °C	Spherical	Zn and O	*B. cereus*, *P. aeruginosa*, *E. faecalis*, *A. hydrophila*, *S. pneumoniae*, *E. faecium*, *S. aureus*. *E. coli*, *L. monocytogenes*, *M. catarrhalis*, *S. typhi and K. pneumoniae*	0.93, 0.88, 1.25, 0.85, 0.93, 0.816, 1250, 1250, 0.71, 1250, 0.6, and 1250	[106]
Licania tomentosa leaf	3 g in 150 mL	500 °C	Spherical	Zn and O	*E. coli* ATCC 35218, *E. faecalis* ATCC 29737, *K. pneumoniae* ATCC 700603, *P. aeruginosa* ATCC 27853, *P. aeruginosa* B3, *S. aureus* SA01 and *S. aureus* ATCC 29213	1000, 250, 1000, 1000,2000, 1000 and 1000	This work

https://doi.org/10.3390/pr14091334

6. Disk Diffusion

We also conducted additional studies of antimicrobial activities of the green ZnO NPs using disk diffusion assays using representative Gram-positive and Gram-negative bacterial strains. Table 4. presents the results obtained in the disk diffusion assay for *Staphylococcus aureus* 03 and *Escherichia coli* 1TCC 25922.

Table 4. Antibacterial activity of ZnO NPs against *Staphylococcus aureus* (03) and *Escherichia coli* 1TCC 25922, expressed in inhibition zones (mm).

Zone of Inhibition (ZOI) (mm)					
Bacteria	**Controle (+) 10 mg/mL**	**Concentration of ZnO NPs**			
		10 mg/mL	**5 mg/mL**	**2.5 mg/mL**	**1.25 mg/mL**
Staphylococcus aureus 03 (24 h)	20 ± 0.8	13.5 ± 0.5	12 ± 0.8	9.7 ± 0.5	8 ± 0.5
Escherichia coli 25922 (24 h)	18 ± 1.1	5 ± 1	3 ± 1	No	No
Escherichia coli 25922 (48 h)	19 ± 1	6 ± 0.5	4 ± 0.5	No	No
		30 mg/mL	15 mg/mL	7.5 mg/mL	3.75 mg/mL
Escherichia coli 25922 (24 h)	18 ± 1.1	8 ± 1.1	5 ± 0.5	4.6 ± 0.5	1 ± 1.7

The ZnO NPs synthesized demonstrated an inhibitory effect on the bacterial growth, with greater antibacterial activity observed at a concentration of 10 mg/mL and 30 mg/mL, which resulted in inhibition zones of 13.5 mm and 8 mm, respectively, for *Staphylococcus aureus* SA03 (Figure 18A) and *Escherichia coli* 1TCC 25922 (Figure 18C). On the other hand, the concentration of 2.5 mg/mL and 1.25 mg/mL NPs did not produce any inhibition zones (Figure 18B) for *Escherichia coli* 1TCC 25922 indicating a directly proportional relationship between the concentration of the NPs and antibacterial activity [107–109]. The positive control (ampicillin, 10 mg/mL) produced an inhibition zone of 19 mm, confirming the sensitivity of the strain to the standard antibiotic, while negative controls showed no inhibition activity for either bacterium. These results are consistent with early studies [83,110], which reported that Gram-positive bacteria tend to be more susceptible to ZnO NPs, likely due to structural differences in their cell walls that facilitate NP penetration. The higher concentration of NPs required to inhibit *E.coli* can be attributed to the structural composition of this bacterium's cell walls, which consists of a thin layer of peptidoglycan associated with an outer membrane rich in lipopolysaccharides [111,112]. This can reduce the penetration and action of the nanoparticles.

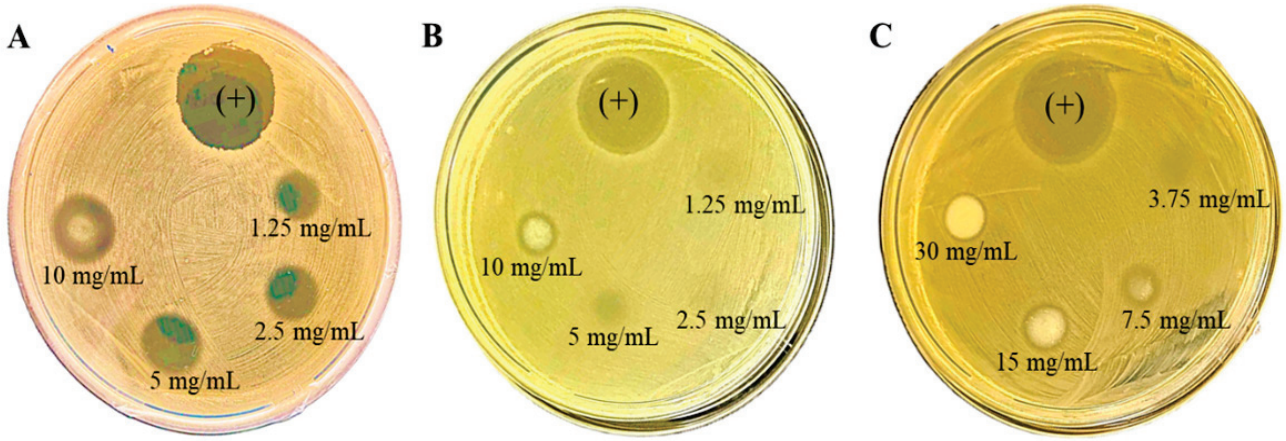


Figure 18. (**A**) Inhibition zones produced by the ZnO NPs against *Staphylococcus aureus* SA03. (**B**,**C**) Inhibition zones produced by ZnO NPs against *Escherichia coli* ATCC 25922.

https://doi.org/10.3390/pr14091334

7. Conclusions

Here, the ZnO NPs have been produced in an efficient, uncomplicated and environmentally friendly way utilizing *Licania Tomentosa* Benth leaf extracts. The Tauc plot, based on UV-Vis spectra of the ZnO NPs, reveals a relatively small band gap of 3.0 eV. EDX analysis demonstrated only Zn and O in the NPs' elementary composition. X-ray diffraction studies showed that the biosynthesized ZnO NPs have a hexagonal wurtzite structure. Scanning electron microscopy confirmed that the ZnO NPs have a spherical shape with an average diameter of 25.5 $\pm$ 1.1 nm. An average crystallite size of 15.9 nm was estimated, based on X-ray diffraction data using the Scherrer equation and 10.83 using the Williamson–Hall approach. Moreover, the ZnO NPs exhibited elevated antimicrobial activity against all tested strains, including isolates with multidrug resistance phenotypes. Their MICs range from 250 to 2000 μg/mL, notably demonstrating efficacy against *E. faecalis* ATCC 29737 (MIC = 250 μg/mL). The nanoparticles also exhibited significant antibiofilm activity, effectively inhibiting biofilm formation in *E. faecalis* ATCC 29737, *P. aeruginosa* ATCC 27856, and *S. aureus* SA01. In addition, photodegradation experiments showed that 12.5 mg and 25 mg of green ZnO NPs at pH 12 and 10 resulted in the highest equilibrium elimination of MB and CV (94.52% and 81%, respectively). Collectively, the biosynthesized ZnO NPs using *Licania tomentosa* Benth leaf extracts show a great promise as multifunctional material with applications in antimicrobial treatments, biofilm control, and photocatalytic remediation, making them potentially attractive for medical, environmental, and wastewater management technologies.

Author Contributions: M.T., R.C.C.M., F.C., L.C.N.d.S., V.O.A.P. and I.P. designed the experiments; M.T. synthesized and conducted characterization of the NPs; B.D.N. and M.d.O.N. contributed with scientific discussions and further characterization of the NPs; M.T. and F.C. conducted photodegradation studies; R.C.C.M., H.L.A.F., M.S.R., A.J.M.C.R.P. and L.C.N.d.S. conducted antimicrobial and antibiofilm investigations, M.T., V.O.A.P. and I.P. wrote the manuscript with the input from all the other authors; I.P., L.C.N.d.S. and M.d.O.N. secured funding, and I.P., M.d.O.N. and L.C.N.d.S. supervised the project. All authors have read and agreed to the published version of the manuscript.

Funding: This work was supported by the Fundação de Amparo à Pesquisa do Estado de São Paulo (FAPESP, grants #2021/08780-1 and 2024/00533-3 to I.P.), by the Conselho Nacional de Desenvolvimento Científico e Tecnológico (CNPq, grants #306852/2021-7 and 440180/2022-8 to I.P.) and by Federal Deputy Tiririca (to M.d.O.N.).

Data Availability Statement: The original contributions presented in this study are included in the article. Further inquiries can be directed to the corresponding author.

Acknowledgments: We acknowledge support of multiuser facilities of IQSC/USP to allow for SEM and EDS measurements.

Conflicts of Interest: The author declares no conflicts of interest.

References

1. Zolkefli, N.; Sharuddin, S.S.; Yusoff, M.Z.M.; Hassan, M.A.; Maeda, T.; Ramli, N. A review of current and emerging approaches for water pollution monitoring. *Water* **2020**, *12*, 3417. [CrossRef]
2. Arman, N.Z.; Salmiati, S.; Aris, A.; Salim, M.R.; Nazifa, T.H.; Muhamad, M.S.; Marpongahtun, M. A review on emerging pollutants in the water environment: Existences, health effects and treatment processes. *Water* **2021**, *13*, 3258. [CrossRef]
3. Ferreira, V.; Magalhães, R.; Teixeira, P.; Castro, P.M.L.; Calheiros, C.S.C. Occurrence of fecal bacteria and zoonotic pathogens in different water bodies: Supporting water quality management. *Water* **2022**, *14*, 780. [CrossRef]
4. de Oliveira Arnoldi Pellegrini, V.; de Jesus Bernardo, A.; Rossi, B.R.; Leite, R.R.; Possatto, J.F.; Dabul, A.N.G.; Fontana, C.R.; Dlamini, Z.W.; Mahule, T.S.; Mosepele, B.Q.; et al. Antimicrobial, photodegradation and BioReRAM applications of multifaceted green zinc oxide nanoparticles synthesized using coffee leaves extract. *Sci. Rep.* **2025**, *15*, 29054. [CrossRef] [PubMed]

https://doi.org/10.3390/pr14091334

5. Venkatachalam, P.; Jayaraj, M.; Manikandan, R.; Geetha, N.; Rene, E.R.; Sharma, N.; Sahi, S. Zinc oxide nanoparticles (ZnONPs) alleviate heavy metal-induced toxicity in Leucaena leucocephala seedlings: A physiochemical analysis. *Plant Physiol. Biochem.* **2017**, *110*, 59–69. [CrossRef] [PubMed]
6. Vimala, K.; Sundarraj, S.; Paulpandi, M.; Vengatesan, S.; Kannan, S. Green synthesized doxorubicin loaded zinc oxide nanoparticles regulates the Bax and Bcl-2 expression in breast and colon carcinoma. *Process Biochem.* **2014**, *49*, 160–172. [CrossRef]
7. Huang, J.; Zong, Z.; Wang, P.; Zhou, H.; Zhang, Y.; Li, Z. Atomic-level steering of charge flow from type-II to S-scheme in In_2O_3/BiOCl via vacancy–metal pairs for CO_2 photoreduction. *Chem. Eng. J.* **2026**, *528*, 172537. [CrossRef]
8. Sharma, S.; Devi, M.; Kumar, P.; Thakur, N.; Kumar, K.; Jeet, K.; Sharma, A.; Kumar, S.; Kumar, A.; Thakur, N. Photocatalytic, antibacterial and antioxidant study of Vitex negundo mediated green synthesized nickel and neodymium doped zinc oxide nanoparticles. *Toxicol. Environ. Chem.* **2025**, *107*, 178–206. [CrossRef]
9. Khan, A.K.; Renouard, S.; Drouet, S.; Blondeau, J.-P.; Anjum, I.; Hano, C.; Abbasi, B.H.; Anjum, S. Effect of UV irradiation (A and C) on Casuarina equisetifolia-mediated biosynthesis and characterization of antimicrobial and anticancer activity of biocompatible zinc oxide nanoparticles. *Pharmaceutics* **2021**, *13*, 1977. [CrossRef]
10. Joseph, J.A.; Nair, S.B.; John, S.S.; Remillard, S.K.; Shaji, S.; Philip, R.R. Zinc-doped iron oxide nanostructures for enhanced photocatalytic and antimicrobial applications. *J. Appl. Electrochem.* **2021**, *51*, 521–538. [CrossRef]
11. Ikhmayies, S.J. Synthesis of ZnO microrods by the spray pyrolysis technique. *J. Electron. Mater.* **2016**, *45*, 3964–3969. [CrossRef]
12. Manikandan, E.; Kavitha, G.; Kennedy, J. Epitaxial zinc oxide, graphene oxide composite thin-films by laser technique for micro-Raman and enhanced field emission study. *Ceram. Int.* **2014**, *40*, 16065–16070. [CrossRef]
13. Singh, J.; Dutta, T.; Kim, K.-H.; Rawat, M.; Samddar, P.; Kumar, P. 'Green' synthesis of metals and their oxide nanoparticles: Applications for environmental remediation. *J. Nanobiotechnol.* **2018**, *16*, 84. [CrossRef]
14. Roopa, M.; Thirumala, S.; Kallimani, S.; Manohara, B.; Basavarajaiah, S. Green synthesis of nanoparticles for enhanced wastewater treatment and other applications: A review and future perspectives. *Next Mater.* **2025**, *8*, 100664. [CrossRef]
15. Sanpradit, P.; Byeon, E.; Lee, J.-S.; Peerakietkhajorn, S. Ecotoxicological, ecophysiological, and mechanistic studies on zinc oxide (ZnO) toxicity in freshwater environment. *Comp. Biochem. Physiol. Part C Toxicol. Pharmacol.* **2023**, *273*, 109720. [CrossRef]
16. Raha, S.; Ahmaruzzaman, M. ZnO nanostructured materials and their potential applications: Progress, challenges and perspectives. *Nanoscale Adv.* **2022**, *4*, 1868–1925. [CrossRef]
17. Dunston, A.K.; Marimuthu, V.; Murugesan, S.; Sivasamy, N. Effective utilization of green synthesized zinc oxide nanoparticles for sequestering methylene blue dye from pharmaceutical industry. *Matéria* **2025**, *30*, e20240654. [CrossRef]
18. Nguyen, L.; Roth, D.M.; Shanewise, J.S.; Kaplan, J.A. Discontinuing cardiopulmonary bypass. In *Kaplan's Essentials of Cardiac Anesthesia*; Elsevier: Amsterdam, The Netherlands, 2018; pp. 715–740. [CrossRef]
19. Abou Zeid, S.; Perez, A.; Bastide, S.; Le Pivert, M.; Rossano, S.; Remita, H.; Hautière, N.; Leprince-Wang, Y. Antibacterial and photocatalytic properties of ZnO nanostructure decorated coatings. *Coatings* **2023**, *14*, 41. [CrossRef]
20. Xin, Z.; He, Q.; Wang, S.; Han, X.; Fu, Z.; Xu, X.; Zhao, X. Recent progress in ZnO-based nanostructures for photocatalytic antimicrobial in water treatment: A review. *Appl. Sci.* **2022**, *12*, 7910. [CrossRef]
21. Samadi, H.; Mohgadam, R.Z.; Shahraki, M.G. Green synthesis of ZnO nanoparticles, photocatalyst activity and its biomedical applications: A review. *Mater. Chem. Phys.* **2025**, *345*, 131161. [CrossRef]
22. Aldeen, T.S.; Mohamed, H.E.A.; Maaza, M. ZnO nanoparticles prepared via a green synthesis approach: Physical properties, photocatalytic and antibacterial activity. *J. Phys. Chem. Solids* **2022**, *160*, 110313. [CrossRef]
23. Duarte, F.S.; Melo, A.; Oliveira, L.; Duarte, J.; Oliveira, R. Green Synthesis for Antibiotic Photodegradation: Recent Advances and Future Trends. *Water* **2025**, *18*, 39. [CrossRef]
24. Vieira, I.R.S.; Mirres, A.C.d.M.; Conte-Junior, C.A. Zinc Oxide Nanomaterials: Green Synthesis, Properties, and Potentials in Active Food Packaging, Edible Coatings, and Nanomedicine Applications. *ChemistrySelect* **2026**, *11*, e04228. [CrossRef]
25. Bernardo, A.d.J.; Dabul, A.N.; Thiam, M.; Pellegrini, V.O.; Silva, M.A.; Vallabhapurapu, S.; Desarada, S.; Vallabhapurapu, V.S.; Fontana, C.R.; Polikarpov, I. Dye Photocatalytic Degradation and Water Treatment Using Biosynthetic ZnO Nanoparticles Produced Using Annatto Tree Leaf Extract. *Processes* **2026**, *14*, 459. [CrossRef]
26. Bala, N.; Saha, S.; Chakraborty, M.; Maiti, M.; Das, S.; Basu, R.; Nandy, P. Green synthesis of zinc oxide nanoparticles using Hibiscus subdariffa leaf extract: Effect of temperature on synthesis, anti-bacterial activity and anti-diabetic activity. *RSC Adv.* **2015**, *5*, 4993–5003. [CrossRef]
27. Sharma, S.; Kumar, K.; Thakur, N.; Chauhan, S.; Chauhan, M. The effect of shape and size of ZnO nanoparticles on their antimicrobial and photocatalytic activities: A green approach. *Bull. Mater. Sci.* **2020**, *43*, 20. [CrossRef]
28. Arumugam, J.; Thambidurai, S.; Suresh, S.; Selvapandiyan, M.; Kandasamy, M.; Pugazhenthiran, N.; Kumar, S.K.; Muneeswaran, T.; Quero, F. Green synthesis of zinc oxide nanoparticles using Ficus carica leaf extract and their bactericidal and photocatalytic performance evaluation. *Chem. Phys. Lett.* **2021**, *783*, 139040. [CrossRef]

https://doi.org/10.3390/pr14091334

29. Mirza, S.; Hussaini, A.A.; Öztürk, G.; Turgut, M.; Öztürk, T.; Tugay, O.; Ulukuş, D.; Yıldırım, M. Photocatalytic and antibacterial activities of ZnO nanoparticles synthesized from Lupinus albus and Lupinus pilosus plant extracts via green synthesis approach. *Inorg. Chem. Commun.* **2023**, *155*, 111124. [CrossRef]
30. Manojkumar, U.; Kaliannan, D.; Srinivasan, V.; Balasubramanian, B.; Kamyab, H.; Mussa, Z.H.; Palaniyappan, J.; Mesbah, M.; Chelliapan, S.; Palaninaicker, S. Green synthesis of zinc oxide nanoparticles using *Brassica oleracea* var. botrytis leaf extract: Photocatalytic, antimicrobial and larvicidal activity. *Chemosphere* **2023**, *323*, 138263. [CrossRef]
31. Carnevale Neto, F.; Pilon, A.C.; da Silva Bolzani, V.; Castro-Gamboa, I. Chrysobalanaceae: Secondary metabolites, ethnopharmacology and pharmacological potential. *Phytochem. Rev.* **2013**, *12*, 121–146. [CrossRef]
32. Zamproni, K.; Biondi, D.; de Carvalho Maria, T.R.B.; Almeida Louveira, F. Diagnóstico Quali-Quantitativo da Arborização Viária de Bonito, Mato Grosso do Sul. *Floresta* **2018**, *48*, 235–244. [CrossRef]
33. Andrade, E.H.A.; Zoghbi, M.d.G.B.; Maia, J.G.S. Constituintes voláteis dos frutos de *Licania tomentosa* Benth. *Acta Amaz.* **1998**, *28*, 55. [CrossRef]
34. Monteiro, K.L.; Oliveira, C.d.; Silva, B.M.d.S.; Môro, F.V.; Carvalho, D.A.d. Caracterização morfológica de frutos, de sementes e do desenvolvimento pós-seminal de *Licania tomentosa* (Benth.) Fritsch. *Ciência Rural* **2012**, *42*, 90–97. [CrossRef]
35. Castilho, R.O.; Kaplan, M.A.C. Constituintes químicos de *Licania tomentosa* Benth. (Chrysobalanaceae). *Química Nova* **2008**, *31*, 66–69. [CrossRef]
36. Macedo, J.B.M. *Capacidade Antioxidante In Vitro e Avaliação da Toxicidade Aguda In Vivo de Extratos de Folhas de Licania rigida Benth., Licania tomentosa (Benth.) Fritsch e Couepia impressa Prance (Chrysobalanaceae)*; Federal University of Rio Grande do Norte: Natal, Brazil, 2011. Available online: https://repositorio.ufrn.br/jspui/handle/123456789/13510 (accessed on 15 April 2026).
37. Farias, D.F.; Souza, T.M.; Viana, M.P.; Soares, B.M.; Cunha, A.P.; Vasconcelos, I.M.; Ricardo, N.M.P.S.; Ferreira, P.M.P.; Melo, V.M.M.; Carvalho, A.F.U. Antibacterial, antioxidant, and anticholinesterase activities of plant seed extracts from Brazilian semiarid region. *BioMed Res. Int.* **2013**, *2013*, 510736. [CrossRef] [PubMed]
38. Agra, M.d.F.; Freitas, P.F.d.; Barbosa-Filho, J.M. Synopsis of the plants known as medicinal and poisonous in Northeast of Brazil. *Rev. Bras. Farmacogn.* **2007**, *17*, 114–140. [CrossRef]
39. Nasiri, S.; Rabiei, M.; Palevicius, A.; Janusas, G.; Vilkauskas, A.; Nutalapati, V.; Monshi, A. Modified Scherrer equation to calculate crystal size by XRD with high accuracy, examples Fe_2O_3, TiO_2 and V_2O_5. *Nano Trends* **2023**, *3*, 100015. [CrossRef]
40. Monshi, A.; Foroughi, M.R.; Monshi, M.R. Modified Scherrer equation to estimate more accurately nano-crystallite size using XRD. *World J. Nano sci. Eng* **2012**, *2*, 154–160. [CrossRef]
41. Zak, A.K.; Majid, W.A.; Abrishami, M.E.; Yousefi, R. X-ray analysis of ZnO nanoparticles by Williamson–Hall and size–strain plot methods. *Solid State Sci.* **2011**, *13*, 251–256. [CrossRef]
42. Hameed, H.; Waheed, A.; Sharif, M.S.; Saleem, M.; Afreen, A.; Tariq, M.; Kamal, A.; Al-Onazi, W.A.; Al Farraj, D.A.; Ahmad, S.; et al. Green synthesis of zinc oxide (ZnO) nanoparticles from green algae and their assessment in various biological applications. *Micromachines* **2023**, *14*, 928. [CrossRef]
43. Figueiredo, C.S.S.e.S.; Branco Santos, J.C.; Castro Junior, J.A.d.A.; Wakui, V.G.; Rodrigues, J.F.; Arruda, M.O.; Monteiro, A.d.S.; Monteiro-Neto, V.; Bomfim, M.R.Q.; Kato, L. Himatanthus drasticus leaves: Chemical characterization and evaluation of their antimicrobial, antibiofilm, antiproliferative activities. *Molecules* **2017**, *22*, 910. [CrossRef]
44. Wahab, S.; Asmare, M.M.; Khan, A.; Khan, T.; Ahmad, R.; Sunghwan, K.; Yun, S.-I. Green synthesis of silver nanoparticles using salvia rosmarinus extract: Characterization, mechanistic antibacterial, antibiofilm, and in silico evaluation. *Ind. Crops Prod.* **2025**, *236*, 122033. [CrossRef]
45. Morkoç, H.; Özgür, Ü. *Zinc Oxide: Fundamentals, Materials and Device Technology*; John Wiley & Sons: Hoboken, NJ, USA, 2008. [CrossRef]
46. Theivarasu, C.; Indumathi, T. Effect of rare earth metal ion Ce^{3+} on the structural, optical and magnetic properties of ZnO nanoparticles synthesized by the co-precipitation method. *J. Mater. Sci. Mater. Electron.* **2017**, *28*, 3664–3671. [CrossRef]
47. Borysiewicz, M.A. ZnO as a functional material, a review. *Crystals* **2019**, *9*, 505. [CrossRef]
48. Koch, U.; Fojtik, A.; Weller, H.; Henglein, A. Photochemistry of semiconductor colloids. Preparation of extremely small ZnO particles, fluorescence phenomena and size quantization effects. *Chem. Phys. Lett.* **1985**, *122*, 507–510. [CrossRef]
49. Khan, M.M.; Saadah, N.H.; Khan, M.E.; Harunsani, M.H.; Tan, A.L.; Cho, M.H. Potentials of Costus woodsonii leaf extract in producing narrow band gap ZnO nanoparticles. *Mater. Sci. Semicond. Process.* **2019**, *91*, 194–200. [CrossRef]
50. Pantidos, N.; Horsfall, L.E. Biological synthesis of metallic nanoparticles by bacteria, fungi and plants. *J. Nanomed. Nanotechnol.* **2014**, *5*, 1. [CrossRef]
51. Alharthi, F.A.; Alghamdi, A.A.; Alothman, A.A.; Almarhoon, Z.M.; Alsulaiman, M.F.; Al-Zaqri, N. Green synthesis of ZnO nanostructures using Salvadora Persica leaf extract: Applications for photocatalytic degradation of methylene blue dye. *Crystals* **2020**, *10*, 441. [CrossRef]
52. Ayyanusamy, P.; Alphonse, R.; Minakshi, M.; Sivasubramanian, R. Synthesis of Amorphous Nickel-Cobalt Hydroxides for Ni−Zn Batteries. *Chem. Eur. J.* **2024**, *30*, e202402325. [CrossRef]

https://doi.org/10.3390/pr14091334

53. Minakshi, M.; Samayamanthry, A.; Whale, J.; Aughterson, R.; Shinde, P.A.; Ariga, K.; Kumar Shrestha, L. Phosphorous–containing activated carbon derived from natural honeydew peel powers aqueous supercapacitors. *Chem. Asian J.* **2024**, *19*, e202400622. [CrossRef]
54. Ragunathan, R.; Velusamy, S.; Nallasamy, J.L.; Shanmugamoorthy, M.; Johney, J.; Veerasamy, S.; Gopalakrishnan, D.; Nithyanandham, M.; Balamoorthy, D.; Velusamy, P. Synthesis and Enhanced Photocatalytic Activity of Zinc Oxide-Based Nanoparticles and Its Antibacterial Activity. *J. Nanomater.* **2022**, *2022*, 3863184. [CrossRef]
55. Álvarez-Chimal, R.; García-Pérez, V.I.; Álvarez-Pérez, M.A.; Arenas-Alatorre, J.Á. Green synthesis of ZnO nanoparticles using a Dysphania ambrosioides extract. Structural characterization and antibacterial properties. *Mater. Sci. Eng. C* **2021**, *118*, 111540. [CrossRef]
56. Souza, R.P.; Freitas, T.K.; Domingues, F.S.; Pezoti, O.; Ambrosio, E.; Ferrari-Lima, A.M.; Garcia, J.C. Photocatalytic activity of TiO_2, ZnO and Nb2O5 applied to degradation of textile wastewater. *J. Photochem. Photobiol. A Chem.* **2016**, *329*, 9–17. [CrossRef]
57. Humelnicu, D.; Dinu, M.V.; Drăgan, E.S. Adsorption characteristics of UO_2^{2+} and Th^{4+} ions from simulated radioactive solutions onto chitosan/clinoptilolite sorbents. *J. Hazard. Mater.* **2011**, *185*, 447–455. [CrossRef]
58. Belaid, K.D.; Kacha, S. Étude cinétique et thermodynamique de l'adsorption d'un colorant basique sur la sciure de bois. *Rev. Sci. L'eau* **2011**, *24*, 131–144. [CrossRef]
59. Daneshvar, N.; Rasoulifard, M.; Khataee, A.; Hosseinzadeh, F. Removal of CI Acid Orange 7 from aqueous solution by UV irradiation in the presence of ZnO nanopowder. *J. Hazard. Mater.* **2007**, *143*, 95–101. [CrossRef]
60. Saien, J.; Khezrianjoo, S. Degradation of the fungicide carbendazim in aqueous solutions with UV/TiO_2 process: Optimization, kinetics and toxicity studies. *J. Hazard. Mater.* **2008**, *157*, 269–276. [CrossRef]
61. Adeel, M.; Saeed, M.; Khan, I.; Muneer, M.; Akram, N. Synthesis and characterization of Co–ZnO and evaluation of its photocatalytic activity for photodegradation of methyl orange. *ACS Omega* **2021**, *6*, 1426–1435. [CrossRef]
62. Karthikeyan, S.; Boopathy, R.; Sekaran, G. In situ generation of hydroxyl radical by cobalt oxide supported porous carbon enhance removal of refractory organics in tannery dyeing wastewater. *J. Colloid Interface Sci.* **2015**, *448*, 163–174. [CrossRef] [PubMed]
63. Marques, J.O.; Bellato, C.R.; Souza, C.H.d.; Silva, R.C.d.; Rocha, P.A. Synthesis, characterization and enhanced photocatalytic activity of iron oxide/carbon nanotube/Ag-doped TiO_2 nanocomposites. *J. Braz. Chem. Soc.* **2017**, *28*, 2301–2312. [CrossRef]
64. Pham, X.N.; Nguyen, H.T.; Pham, T.N.; Nguyen, T.-T.-B.; Nguyen, M.B.; Tran, V.T.-T.; Doan, H.V. Green synthesis of H-ZSM-5 zeolite-anchored O-doped g–C3N4 for photodegradation of Reactive Red 195 (RR 195) under solar light. *J. Taiwan Inst. Chem. Eng.* **2020**, *114*, 91–102. [CrossRef]
65. Chen, C.; Liu, J.; Liu, P.; Yu, B. Investigation of photocatalytic degradation of methyl orange by using nano-sized ZnO catalysts. *Adv. Chem. Eng. Sci.* **2011**, *1*, 9–14. [CrossRef]
66. Chamjangali, M.A.; Boroumand, S. Synthesis of flower-like Ag-ZnO nanostructure and its application in the photodegradation of methyl orange. *J. Braz. Chem. Soc.* **2013**, *24*, 1329–1338. [CrossRef]
67. Farzana, M.H.; Meenakshi, S. Synergistic effect of chitosan and titanium dioxide on the removal of toxic dyes by the photodegradation technique. *Ind. Eng. Chem. Res.* **2014**, *53*, 55–63. [CrossRef]
68. Kuriechen, S.K.; Murugesan, S.; Raj, S.P.; Maruthamuthu, P. Visible light assisted photocatalytic mineralization of Reactive Red 180 using colloidal TiO_2 and oxone. *Chem. Eng. J.* **2011**, *174*, 530–538. [CrossRef]
69. Thiam, M.; Bernardo, A.d.J.; Pellegrini, V.d.O.A.; Possatto, J.F.; Dlamini, Z.W.; Mahule, T.S.; Ngom, B.D.; Mosepele, B.Q.; Thema, F.T.; Mamba, B.B.; et al. Green synthesis of ZnO nanoparticles using *Licania tomentosa* Benth (Oiti) leaf extract: Characterization and applications for the photocatalytic degradation of crystal Violet dye. *Processes* **2025**, *13*, 880. [CrossRef]
70. Pugazhenthiran, N.; Murugesan, S.; Sathishkumar, P.; Anandan, S. Photocatalytic degradation of ceftiofur sodium in the presence of gold nanoparticles loaded TiO_2 under UV–visible light. *Chem. Eng. J.* **2014**, *241*, 401–409. [CrossRef]
71. Sakthivel, S.; Neppolian, B.; Shankar, M.; Arabindoo, B.; Palanichamy, M.; Murugesan, V. Solar photocatalytic degradation of azo dye: Comparison of photocatalytic efficiency of ZnO and TiO_2. *Sol. Energy Mater. Sol. Cells* **2003**, *77*, 65–82. [CrossRef]
72. Debnath, S.; Ballav, N.; Nyoni, H.; Maity, A.; Pillay, K. Optimization and mechanism elucidation of the catalytic photo-degradation of the dyes Eosin Yellow (EY) and Naphthol blue black (NBB) by a polyaniline-coated titanium dioxide nanocomposite. *Appl. Catal. B Environ.* **2015**, *163*, 330–342. [CrossRef]
73. Mancuso, A.; Mottola, S.; Sacco, O.; Vaiano, V.; De Marco, I. Photocatalytic degradation of ceftriaxone using TiO_2 coupled with ZnO micronized by supercritical antisolvent route. *Nanomaterials* **2023**, *13*, 3130. [CrossRef]
74. Alamzeb, M.; Faryad, S.; Ullah, I.; Hussain, J.; Setzer, W.N. Photocatalytic degradation of brilliant blue dye under solar light irradiation: An insight into mechanistic, kinetics, mineralization and scavenging studies. *J. Fluoresc.* **2025**, *35*, 9093–9111. [CrossRef] [PubMed]
75. Younis, S.A.; Kim, K.-H. Heterogeneous photocatalysis scalability for environmental remediation: Opportunities and challenges. *Catalysts* **2020**, *10*, 1109. [CrossRef]
76. Huang, J.; Rasouli, K.; Zong, Z.; Wang, P.; Zhang, Y.; Li, Z. Engineering a high-performance $ZnFe_2O_4$/BiOBr/MXene S-scheme heterostructure for CO_2 photoreduction and wastewater treatment. *Chem. Eng. J.* **2026**, *530*, 173675. [CrossRef]

https://doi.org/10.3390/pr14091334

77. Hyland, K.; Auclair, C. The formation of superoxide radical anions by a reaction between O_2, OH^- and dimethyl sulfoxide. *Biochem. Biophys. Res. Commun.* **1981**, *102*, 531–537. [CrossRef]
78. Steiner, M.G.; Babbs, C.F. Quantitation of the hydroxyl radical by reaction with dimethyl sulfoxide. *Arch. Biochem. Biophys.* **1990**, *278*, 478–481. [CrossRef]
79. Shikuku, V.O.; Nyairo, W.N. Advanced oxidation processes for dye removal from wastewater. In *Impact of Textile Dyes on Public Health and the Environment*; IGI Global Scientific Publishing: Hershey, PA, USA, 2020; pp. 205–238. [CrossRef]
80. Masuleh, M.T.; Hasheminiasari, M.; Ashiri, R. Enhanced photocatalytic efficiency of eco-friendly synthesized ZnO for rapid full degradation of methylene blue dye. *Mater. Adv.* **2025**, *6*, 2611–2621. [CrossRef]
81. Pryor, W.A. Oxy-radicals and related species: Their formation, lifetimes, and reactions. *Annu. Rev. Physiol.* **1986**, *48*, 657–667. [CrossRef]
82. Hanley, C.; Thurber, A.; Hanna, C.; Punnoose, A.; Zhang, J.; Wingett, D.G. The influences of cell type and ZnO nanoparticle size on immune cell cytotoxicity and cytokine induction. *Nanoscale Res. Lett.* **2009**, *4*, 1409. [CrossRef]
83. Padmavathy, N.; Vijayaraghavan, R. Enhanced bioactivity of ZnO nanoparticles—An antimicrobial study. *Sci. Technol. Adv. Mater.* **2008**, *9*, 035004. [CrossRef]
84. Fang, M.; Chen, J.-H.; Xu, X.-L.; Yang, P.-H.; Hildebrand, H.F. Antibacterial activities of inorganic agents on six bacteria associated with oral infections by two susceptibility tests. *Int. J. Antimicrob. Agents* **2006**, *27*, 513–517. [CrossRef]
85. Liu, Y.; Han, J.; Qiu, W.; Gao, W. Hydrogen peroxide generation and photocatalytic degradation of estrone by microstructural controlled ZnO nanorod arrays. *Appl. Surf. Sci.* **2012**, *263*, 389–396. [CrossRef]
86. Freire, R.S.; Pelegrini, R.; Kubota, L.T.; Durán, N.; Peralta-Zamora, P. New trends for treatment of industrial effluents containing organochloride species. *Química Nova* **2000**, *23*, 504–511. [CrossRef]
87. Garcia, J.C.; Takashima, K. Photocatalytic degradation of imazaquin in an aqueous suspension of titanium dioxide. *J. Photochem. Photobiol. A Chem.* **2003**, *155*, 215–222. [CrossRef]
88. Taj-Aldeen, R.A.; Alqaraguly, M.B.; Salah, O.H.; Abdulwahid, A.S.; Hanoon, T.; Alzahraa, Z.A.; Omran, A.A. Enhanced photocatalytic performance of ZnO NPs in the presence of solar light and H_2O_2 for degradation of Tetracycline from wastewater: Optimal conditions for green products. *Adv. J. Chem. Sect. A* **2024**, *7*, 396–405. [CrossRef]
89. Mohammadzadeh, A.; Khoshghadam-Pireyousefan, M.; Shokrianfard-Ravasjan, B.; Azadbeh, M.; Rashedi, H.; Dibazar, M.; Mostafaei, A. Synergetic photocatalytic effect of high purity ZnO pod shaped nanostructures with H_2O_2 on methylene blue dye degradation. *J. Alloys Compd.* **2020**, *845*, 156333. [CrossRef]
90. Saridewi, N.; Rustanti, S.; Zulys, A.; Nurbayti, S.; Aziz, I.; Adawiah, A. Synthesis of ZnO nanoparticle using Lidah Mertua (*Sansevieria trifasciata*) extract through sol-gel method and its application for methylene blue photodegradation. *Bull. Chem. React. Eng. Catal.* **2023**, *18*, 375–385. [CrossRef]
91. Flores, N.M.; Pal, U.; Galeazzi, R.; Sandoval, A. Effects of morphology, surface area, and defect content on the photocatalytic dye degradation performance of ZnO nanostructures. *RSC Adv.* **2014**, *4*, 41099–41110. [CrossRef]
92. Ferreira, R.M.; dos Santos Silva, D.H.; Silva, K.F.; de Melo Monteiro, J.; Ferreira, G.F.; Silva, M.R.C.; da Silva, L.C.N.; de Castro Oliveira, L.; Monteiro, A.S. Draft genome sequence of Staphylococcus aureus sequence type 5 SA01 isolated from bloodstream infection and comparative analysis with reference strains. *Funct. Integr. Genom.* **2023**, *23*, 288. [CrossRef]
93. Mendes, C.R.; Dilarri, G.; Forsan, C.F.; Sapata, V.d.M.R.; Lopes, P.R.M.; de Moraes, P.B.; Montagnolli, R.N.; Ferreira, H.; Bidoia, E.D. Antibacterial action and target mechanisms of zinc oxide nanoparticles against bacterial pathogens. *Sci. Rep.* **2022**, *12*, 2658. [CrossRef]
94. Sirelkhatim, A.; Mahmud, S.; Seeni, A.; Kaus, N.H.M.; Ann, L.C.; Bakhori, S.K.M.; Hasan, H.; Mohamad, D. Review on zinc oxide nanoparticles: Antibacterial activity and toxicity mechanism. *Nano-Micro Lett.* **2015**, *7*, 219–242. [CrossRef] [PubMed]
95. Lallo da Silva, B.; Abuçafy, M.P.; Berbel Manaia, E.; Oshiro Junior, J.A.; Chiari-Andréo, B.G.; Pietro, R.C.R.; Chiavacci, L.A. Relationship between structure and antimicrobial activity of zinc oxide nanoparticles: An overview. *Int. J. Nanomed.* **2019**, *14*, 9395–9410. [CrossRef]
96. Abu-Gharbia, M.; Salem, J.; Al-Arabi, G. Biosynthesis of zinc oxide nanoparticles using Aloe vera leaves extract and their antibacterial impact. *Bull. Pharm. Sci. Assiut Univ.* **2024**, *47*, 499–517. [CrossRef]
97. Francis, D.V.; Jayakumar, M.N.; Ahmad, H.; Gokhale, T. Antimicrobial activity of biogenic metal oxide nanoparticles and their synergistic effect on clinical pathogens. *Int. J. Mol. Sci.* **2023**, *24*, 9998. [CrossRef] [PubMed]
98. Freire, P.G.; Montes, R.H.; Romeiro, F.C.; Lemos, S.C.; Lima, R.C.; Richter, E.M.; Munoz, R.A. Morphology of ZnO nanoparticles bound to carbon nanotubes affects electrocatalytic oxidation of phenolic compounds. *Sens. Actuators B Chem.* **2016**, *223*, 557–565. [CrossRef]
99. Pavithra, N.; Lingaraju, K.; Raghu, G.; Nagaraju, G. *Citrus maxima* (Pomelo) juice mediated eco-friendly synthesis of ZnO nanoparticles: Applications to photocatalytic, electrochemical sensor and antibacterial activities. *Spectrochim. Acta Part A Mol. Biomol. Spectrosc.* **2017**, *185*, 11–19. [CrossRef]

https://doi.org/10.3390/pr14091334

100. Shubha, J.P.; Kavalli, K.; Adil, S.F.; Assal, M.E.; Hatshan, M.R.; Dubasi, N. Facile green synthesis of semiconductive ZnO nanoparticles for photocatalytic degradation of dyes from the textile industry: A kinetic approach. *J. King Saud Univ.-Sci.* **2022**, *34*, 102047. [CrossRef]
101. Karthik, P.; Ravichandran, S.; Mukkannan, A.; Rajesh, J. Plant-mediated biosynthesis of zinc oxide nanoparticles from Delonix Elata: A promising photocatalyst for crystal violet degradation. *Inorg. Chem. Commun.* **2022**, *146*, 110122. [CrossRef]
102. Kamarajan, G.; Anburaj, D.B.; Porkalai, V.; Muthuvel, A.; Nedunchezhian, G. Green synthesis of ZnO nanoparticles using Acalypha indica leaf extract and their photocatalyst degradation and antibacterial activity. *J. Indian Chem. Soc.* **2022**, *99*, 100695. [CrossRef]
103. Akash, M.H.; Bhowmik, S.; Azad, M.A.S.; Sultana, N.; Alam, M.A. Microwave-assisted Green Synthesis of ZnO Nanoparticles Utilizing *Litchi chinensis* Leaf Waste for Efficient Photocatalytic degradation of Methylene Blue. *RSC Sustain.* **2026**, *4*, 1097–1112. [CrossRef]
104. Assad, N.; Abbas, A.; ur Rehman, M.F.; Naeem-ul-Hassan, M. Photo-catalytic and biological applications of phyto-functionalized zinc oxide nanoparticles synthesized using a polar extract of *Equisetum diffusum* D. *RSC Adv.* **2024**, *14*, 22344–22358. [CrossRef]
105. Elango, B.; Maghimaa, M.; Okram, G.S. Green Synthesis of Zinc Oxide Nanoparticles as a Therapeutic Approach for Antimicrobial, Antibiofilm and Cytotoxic Potentials Against Skin Cancer Cells. *Biomed. Mater. Devices* **2026**, 1–17. [CrossRef]
106. Ifeanyichukwu, U.L.; Fayemi, O.E.; Ateba, C.N. Green synthesis of zinc oxide nanoparticles from pomegranate (*Punica granatum*) extracts and characterization of their antibacterial activity. *Molecules* **2020**, *25*, 4521. [CrossRef]
107. Rezaei, F.Y.; Pircheraghi, G.; Nikbin, V.S. Antibacterial activity, cell wall damage, and cytotoxicity of zinc oxide nanospheres, nanorods, and nanoflowers. *ACS Appl. Nano Mater.* **2024**, *7*, 15242–15254. [CrossRef]
108. da Silva, B.L.; Caetano, B.L.; Chiari-Andréo, B.G.; Pietro, R.C.L.R.; Chiavacci, L.A. Increased antibacterial activity of ZnO nanoparticles: Influence of size and surface modification. *Colloids Surf. B Biointerfaces* **2019**, *177*, 440–447. [CrossRef] [PubMed]
109. Sharma, V.; Anderson, D.; Dhawan, A. Zinc oxide nanoparticles induce oxidative stress and genotoxicity in human liver cells (HepG2). *J. Biomed. Nanotechnol.* **2011**, *7*, 98–99. [CrossRef] [PubMed]
110. Raghupathi, K.R.; Koodali, R.T.; Manna, A.C. Size-dependent bacterial growth inhibition and mechanism of antibacterial activity of zinc oxide nanoparticles. *Langmuir* **2011**, *27*, 4020–4028. [CrossRef]
111. Li, W.-R.; Xie, X.-B.; Shi, Q.-S.; Zeng, H.-Y.; Ou-Yang, Y.-S.; Chen, Y.-B. Antibacterial activity and mechanism of silver nanoparticles on *Escherichia coli*. *Appl. Microbiol. Biotechnol.* **2010**, *85*, 1115–1122. [CrossRef]
112. Ullah, S.; Ahmad, A.; Ri, H.; Khan, A.U.; Khan, U.A.; Yuan, Q. Green synthesis of catalytic zinc oxide nano-flowers and their bacterial infection therapy. *Appl. Organomet. Chem.* **2020**, *34*, e5298. [CrossRef]

Disclaimer/Publisher's Note: The statements, opinions and data contained in all publications are solely those of the individual author(s) and contributor(s) and not of MDPI and/or the editor(s). MDPI and/or the editor(s) disclaim responsibility for any injury to people or property resulting from any ideas, methods, instructions or products referred to in the content.

https://doi.org/10.3390/pr14091334

processes

MDPI

Article

Design of Carbon Nanocomposites Based on PLA and PCL—From Microscratch Testing to Self-Healing Behavior

Todor Batakliev [1,2,*], Evgeni Ivanov [1,2], Vladimir Georgiev [1], Verislav Angelov [1,2] and Rumiana Kotsilkova [1]

[1] Open Laboratory on Experimental Micro and Nano Mechanics (OLEM), Institute of Mechanics, Bulgarian Academy of Sciences, Acad. G. Bonchev Str., Block 4, 1113 Sofia, Bulgaria; ivanov_evgeni@imbm.bas.bg (E.I.); vgeorgiev@imbm.bas.bg (V.G.); v.angelov@imbm.bas.bg (V.A.); kotsilkova@imbm.bas.bg (R.K.)

[2] Center of Competence for Mechatronics and Clean Technologies "Mechatronics, Innovation, Robotics, Automation and Clean Technologies"—MIRACle, 1113 Sofia, Bulgaria

* Correspondence: batakliev@imbm.bas.bg

Abstract

Biodegradable nanocomposite materials possessing self-healing behavior are emerging as an attractive option of being used in advanced mechatronic systems. The current study is focused on a thorough examination of the micromechanical properties of graphene–reinforced polylactic acid (PLA)/polycaprolactone (PCL) composite samples, followed by estimation of their self-healing behavior upon heating. Polymer blend–based nanocomposite materials were prepared using the green and reliable in terms of good nanofiller dispersion melt extrusion method. 3D printed nanocomposite specimens with impeccable flatness were subjected to fine microscratch testing by applying a constant force experimental mode. The surface resistance of the three-component polymer materials against the lateral movement of the stylus fulfilling the scratch and the impact of the dual-phase PLA/PCL ratio on the nanocomposite mechanical performance were estimated by calculation of the coefficient of friction (COF = F_x/F_z). COF values in the range of 0.8–1.4 indicated excellent nanocomposite resilience against scratch. Creating a heterogeneous polymer system that combines phase-separated soft and hard domains with close melt and glass transition temperatures, respectively, may facilitate the physical flow of macromolecular chains into voids or free volume areas. This aspect can be critical in the achievement of thermally–induced self-healing properties of the composite material. Scanning electron microscopy (SEM) imaging of the microscratches, made before and after Joule heating of the polymer samples, revealed a significant degree of surface recovery and a sensible reduction in the width of the adjusted scratch grooves.

Keywords: polymer nanocomposites; graphene nanoplatelets; microscratch testing; coefficient of friction; self-healing; SEM imaging

1. Introduction

Over the last decades, the tendency of development in self-healing polymer compositions, inspired by biological systems, woke up the interest of the scientific community. As a function of their specific physico-chemical properties, stimuli-responsive composite materials may play a key role in a wide range of technological innovations [1]. It could be summarized that the research activities on self-repairing synthetic materials are strictly motivated by the purpose of endowing them with sustainability and long service lifetime [2,3]. Self-healing polymers have the intrinsic capability to restore their conformation under certain external impact when altered by physical cut or any other mechanical damage [4–6]. The mobility of polymer chains taking part in the mechanism of self-repairing is highly

dependent on the presence of free volume [7]. This can be facilitated by designing a heterogeneous network consisting of well-dispersed hard and soft domains being able to rearrange upon superficial microscratch. The implementation of surface approach and the formation of a polymer–polymer interface, that would assist in filling the voids, are crucial in the achievement of diffusion of molecular segments or composite recovery in the wounded area [8]. Graphene nanoplatelets (GNPs) are well-known for their high mechanical strength, large specific surface area, and π-π conjugated structure [9], which makes them a good option to impart a reinforcing effect and integrated properties when used as a nanofiller in a polymer matrix [10]. The expected appearance of Van der Waals forces and π-π interactions amid graphene nanoparticles, entangled in a multi-component composite die, could have a positive role in the interfacial flow during self-healing of generated microscratches [11].

Polylactic acid (PLA) and polycaprolactone (PCL) are aliphatic polyesters susceptible to biodegradation, with increasing worldwide application as biomedical and packaging materials [12–14]. They are considered to be a green perspective for the replacement of petrochemical-based polymers [15]. It has been ascertained that melt mixing of PLA and PCL led to a phase-separated composite structure with excellent mechanical and shape memory behavior [16]. These properties of the polymer blend can make it capable, under definite conditions, to heal scratches by employing the conformational entropic energy storage [17] and the lack of chain slippage that is critical for getting a high efficiency of wound closure [18]. Thermally activated self-healing ability has been demonstrated with respect to 4D-printable smart material based on PCL containing a supramolecular structure whose surface was scratched by a razor blade [19]. Similar rough damaging approach has been applied regarding PLA-PCL-PLA triblock copolymers possessing properties of thermoplastic elastomers [20]. In both works, the self-repairing process has been observed by low-resolution optical microscopy at the sub-macroscopic scale. A dual-functional polymeric system based on the phase separation phenomenon between epoxy resin and polycaprolactone was found to possess a self-healing capacity when subjected to a single notched bending test upon temperature higher than the glass transition of the hard segment [21]. The effect of localized free volume at micro level, caused by mechanical scratch on the surface of polymer crosslinked networks, has been explored in the aspect of favoring chain rearrangements in the course of self-repairing process [22]. A common description of diffusion-driven rebonding by linear PCL chains interpenetrating a crosslinked PCL network [23] is being amplified by interface wound mending in a phase-separated polymer system consisting of electrospun PCL fibers locked in an amorphous epoxy matrix [24]. In these studies, the self-healing mechanism was enabled upon heating the damaged samples to 80 °C or above the PCL melting temperature.

The aim of the current paper is to demonstrate the effect of graphene nanofiller on the surface scratch resistance and self-repairing behavior of nanocomposite phase-separated polymer architectures with various PLA/PCL molecular ratios. Performing ultrafine microscratch grooves over a smooth composite sample, followed by their partial or complete removal through thermally-induced self-healing, could be of significant matter in the field of mechatronics and smart devices. The novelty in this study is completed by the use of Joule heating method, which was selected as an advanced physical approach to trigger and investigate the self-repair properties of the melt blended materials.

2. Materials and Methods

2.1. Materials

Polylactic acid (PLA) with formulated grade Ingeo™ 3D850, possessing a melt mass flow rate of 9–15 g/10 min (210 °C/2.16 kg), was delivered by Nature Works (Plymouth,

https://doi.org/10.3390/pr14060956

MN, USA). The second biodegradable polymer material, polycaprolactone (PCL), possessing a molecular weight Mn of 70,000–90,000 g/mol and a melt flow index of 2–4 g/10 min (160 °C/5.00 kg), was purchased from Sigma Aldrich (St. Louis, MI, USA). Both output biopolymers were obtained in the shape of pellets. Graphene nanoplatelets (GNPs) with purity >97 wt%, a particle size diameter of <50 μm, and a specific surface area (SSA) of 400–600 m^2/g, used as a 2D carbon nanofiller, were supplied by The Sixth Element (Changzhou, China).

2.2. Nanocomposite Samples Preparation Method

Graphene nanoplatelets-containing composite blends, based on PLA and PCL, were prepared by the reliable and low-cost melt extrusion method whose details were described in a previous article related to the topic [25]. In order to remove the adsorbed humidity that would have a negative effect on the extrusion process, all nanocomposite components were dried in advance for a couple of hours in a vacuum oven. Four PLA/PCL/GNPs compositions with different polymer ratio but the same graphene content of 4 wt% were received in the shape of a filament with a diameter suitable for 3D printing (see Table 1).

Table 1. List of melt-blended nanocomposite samples.

Nanocomposite Sample	PLA, wt%	PCL, wt%	GNPs, wt%
95PLA5PCL4GNP	95	5	4
70PLA30PCL4GNP	70	30	4
60PLA40PCL4GNP	60	40	4
30PLA70PCL4GNP	30	70	4

The flat upper-face side of each one 3D-printed nanocomposite specimen has been used for precise microscratch testing, whereat the wounded sample area has been observed by high-resolution SEM twice—before and after the self-healing process.

2.3. Methods

Microscratch experiments were performed using a universal mechanical tester (UMT-2, Bruker, Billerica, MA, USA) using a low-force sensor operating in the range of 5–500 mN. 3D-printed nanocomposite samples were scratched in constant load control mode by applying forces of 5 mN up to 200 mN. The microscratching tool was selected to be a diamond stylus with a diameter of 5 μm mounted to the sensor by means of soft suspension. Carefully designed experimental setup of the microscratch testing equipment can be seen in Figure S1.

SEM analysis of the superficial scratch grooves was carried out with the aid of a tabletop scanning electron microscope (SH 4000M, Hirox, Oradell, NJ, USA) employing a secondary electron detector at magnifications up to ×2.0 K. The instrumental software allowed the measurement of the width of the scratch tracks before and after the thermal treatment, which was critical for the right assessment of the nanocomposite's self-healing behavior.

Thermally-induced self-healing of the scratched polymer compositions was conducted in a vacuum oven for 60 min at a fixed temperature of 85 °C (T_h). The effectiveness of the self-healing process was considered by calculating the efficiency of the nanocomposite materials to repair the surface wounds made by the stylus, using the following equation:

$$Healing\ Ability\ (\%) = \frac{w_1 - w_2}{w_1} \times 100\% \quad (1)$$

where w_1 and w_2 are the widths of the scratch groove (in μm) measured before and after the self-repair heating process.

https://doi.org/10.3390/pr14060956

Another method to perform a self-healing procedure was held on rectangular specimens having dimensions of 30 × 10 × 1 mm whose ends were tentatively painted by silver paste prior to start an electrical heating. Then, each one microscratched composite sample was attentively connected to an external DC power source and subjected to Joule heating under constant voltage conditions. The applied voltage level was selected according to the initial electrical resistance of the nanocomposite formulation and was set in the range of 30 V–80 V, depending on the specific polymer composition. A GW-INSTEK PSW160-7.2 360 W DC power supply was used as the voltage source. In the course of electrical loading, the specimens were heated resistively until reaching of 100 °C surface temperature that took approximately 50 s of time. The accuracy of temperature evolution and the spatial heat distribution over the specimen surface were monitored in real time using a HighSense thermal imaging camera (Laserliner, Arnsberg, Germany). The Joule heating cycle was applied twice per specimen under identical conditions for all polymer compositions.

3. Results and Discussion

3.1. Microscratch Analysis

The microscratch testing of the graphene-containing polymer compositions was conducted in load controlled scratch mode by applying four distinct constant forces in the range of 50–200 mN. Plotting the received values of the coefficient of friction (COF) in function of the exerted scratch load revealed an intriguing surface mechanical behavior of the nanocomposite samples in two principal aspects—the weight content ratio between both polymers in the composite mixture and the normal force (F_z) set in the script during the movement of the stylus over the sample surface (see Figure 1). An apparent scatter of the COF values when the constant force of the microscratch was set to 50 mN can be seen. It means that the superficial scratch resistance of the samples is more sensitive to the PLA/PCL ratio in the polymer compositions when a 50 mN normal force was applied to the diamond stylus. In that case, the lower COF value of the nanocomposite containing 70 wt% polycaprolactone should be noted, which was reflected in a lower lateral force in the course of the scratch test, meaning easier penetration of the stylus into the material. Upon 100 mN and 150 mN microscratch constant loads, the mechanical behavior of the nanocomposite samples seemed to be similar except the COF of the polymer composition 60PLA40PCL4GNP, whose value was found to stand a little bit above the other coefficients. The increment of the normal force over the stylus up to 200 mN led to sensitively lower COF value of the specimen 95PLA5PCL4GNP. It could be explained with the sample's higher ultimate strength due to the combination of carbon nanofiller and uppermost weight content of the PLA [16]. This strength is likely to impede the formation of material pile-up, reducing the sinking of the stylus into the solid polymer nanocomposite and facilitating the lateral movement on the surface. Another experimental approach, closely related to the estimation of the self-healing ability of the samples, was the implementation of microscratch testing by setting extremely low constant forces of 5 mN and 10 mN. In order to better reproduce the received raw instrumental data, an exponential nonlinear fit of the COF vs. Time curves was performed (see Figures 2 and 3).

Apparently, when applying a 5 mN normal load of scratch over the surface of the polymer samples, the superficial mechanical response of the composite materials has slightly changed compared to the scratch behavior registered for the higher loads. The impact of the PLA content on the position of the curves depicting the ratio between the lateral and the constant forces during the time of the scratch test should be noted. The harder nature of the specimens with a higher weight percent of PLA in the composite matrix may be the reason for shallower penetration and easier motion of the stylus on the sample surface, resulting in a lower value of F_x, and, respectively, in a lower coefficient

https://doi.org/10.3390/pr14060956

of friction (Figure 2). In the opposite case, where the PCL as a soft segment is the main nanocomposite phase, the greater COF value suggested for a deeper subsidence of the diamond stylus in the material's upper layer, even at 5 mN exerted normal force.

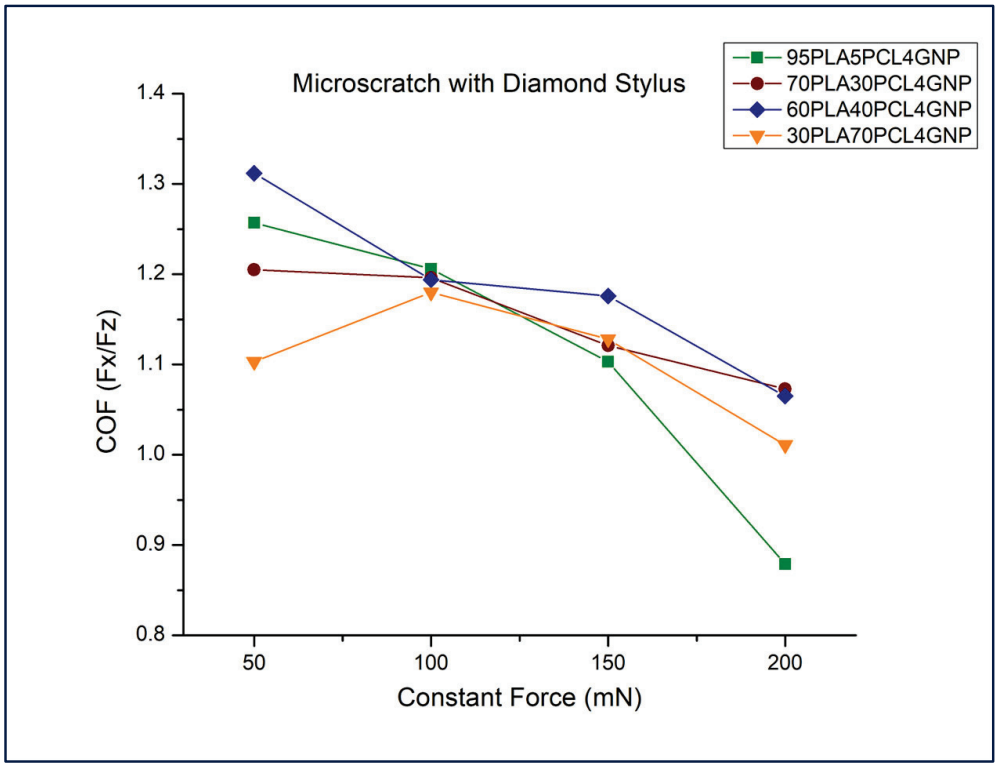


Figure 1. COF values of GNPs-containing polymer compositions as a function of the applied normal force (F_z).

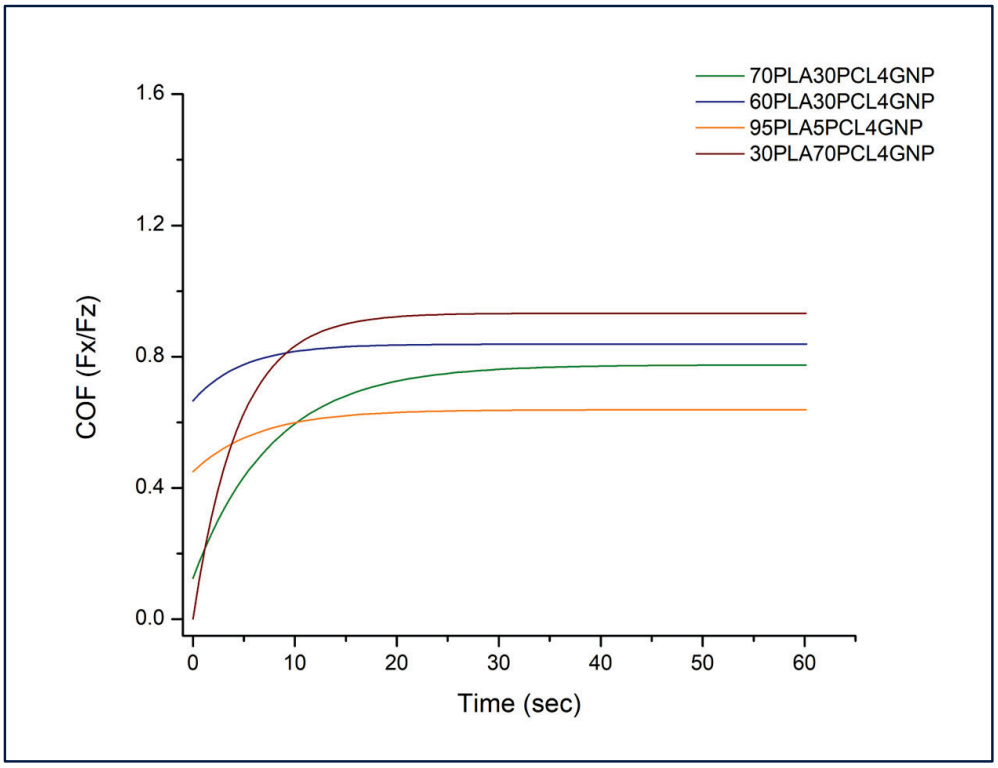


Figure 2. Exponential fit of COF vs. Time curves from microscratch testing of nanocomposite specimens by applying a constant force of 5 mN.

https://doi.org/10.3390/pr14060956

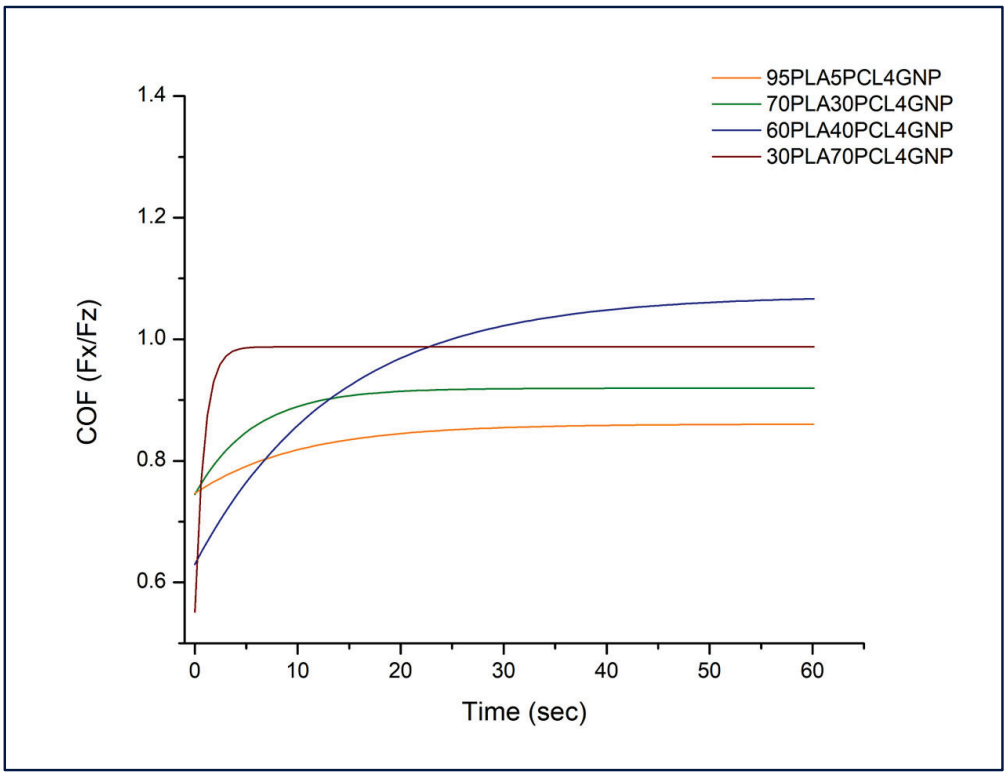


Figure 3. Exponential fit of COF vs. Time curves from microscratch testing of nanocomposite specimens by applying a constant force of 10 mN.

Similar tendency in the microscratch resistance of the graphene-reinforced polymer compositions can be noticed in Figure 3, where the curves outlining the coefficient of friction in function of the experimental time are obtained by setting 10 mN constant load over the conical tip of the stylus. A sharp transition of the initial linear part of the graph to the steady-state section of the coefficient of friction was observed with respect to the nanocomposite sample 30PLA70PCL4GNP. This distinct mechanical behavior could be unraveled with the ductility of the specimen, allowing the stylus to get in the material more rapidly, compared to the other samples, before to start its scratching move on the surface. Overall, the conducted microscratch analysis disclosed that the surface mechanical properties of the polymer composite materials depend on the applied constant force whose specific value may alter the friction resilience of the samples as a function of the variation in penetration depth during the scratch process.

3.2. Thermally-Induced Self-Healing

Self-healing investigation of the microscratched nanocomposite materials was conducted in few stages, encompassing SEM-assisted observation and fine measurement of the thin surface wounds, made before and after the thermal treatment. Representative SEM images of surface scratch grooves, serving to estimate with high accuracy the shrinking of the tracks as a result of the nanocomposite samples' heating, are presented in Figure 4. The focus in the thermally-induced self-healing was over the specimens possessing more than 30 wt% polycaprolactone in the nanocomposite matrix and subjected to microscratch with a constant force in the range of 50–200 mN. For statistical purposes and because of the presence of pile-up in some cut sections, the width of each one measured nick was taken at several points of the scan, whereafter the averaged values were employed in the estimation of the nanocomposite's healing ability (Equation (1)). Using this approach of measuring the reduction in the scratch width enabled the assessment of the nanocomposite's self-repairing behavior by calculating the healing efficiency of the polymer samples according

https://doi.org/10.3390/pr14060956

to Equation (1). The obtained values designate the importance of the PCL as a soft segment, ensuring the chain mobility within the nanocomposite structure at the achievement of high-level surface recovery, even in case of wounds caused by scratch constant loads of 150 mN and 200 mN (see Figure 5).

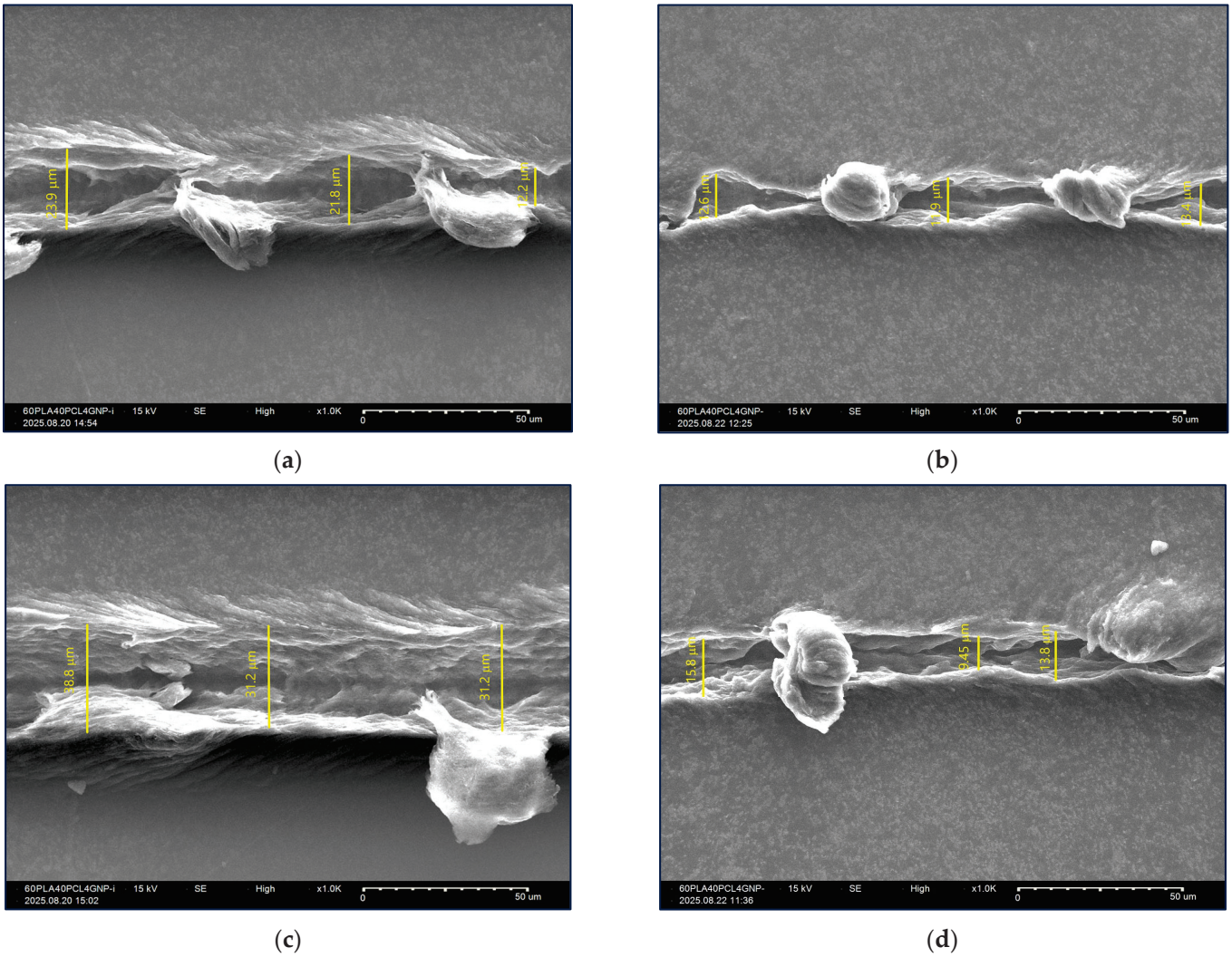


Figure 4. SEM images of scratch wounds measured by means of the instrumental software before (**a**,**c**), and after thermal treatment (**b**,**d**) of the specimen 60PLA40PCL4GNP.

It should be emphasized that the selected T_h, being more than 20 °C above the PCL melting temperature (T_m) [25], can be considered as a prerequisite for low viscosity and better liquidity of the PCL phase that is crucial in the process of self-healing [26]. This may be the reason of sensitively higher self-repairing properties of the sample 30PLA70PCL4GNP compared to the other two polymer compositions, especially with regard to the scratch tracks received by exerting a normal constant force of 50 mN (Figure 5). An interesting inference about the degree of surface recovery can be made by a more general look over the entire length of the microscratches, scanned with lower magnification before and after the thermal heating (Figure 6). The image in Figure 6a represents a scratch performed with a 100 mN constant load, while the scratch track shown in the SEM image in Figure 6c was made by applying a 50 mN constant force.

https://doi.org/10.3390/pr14060956

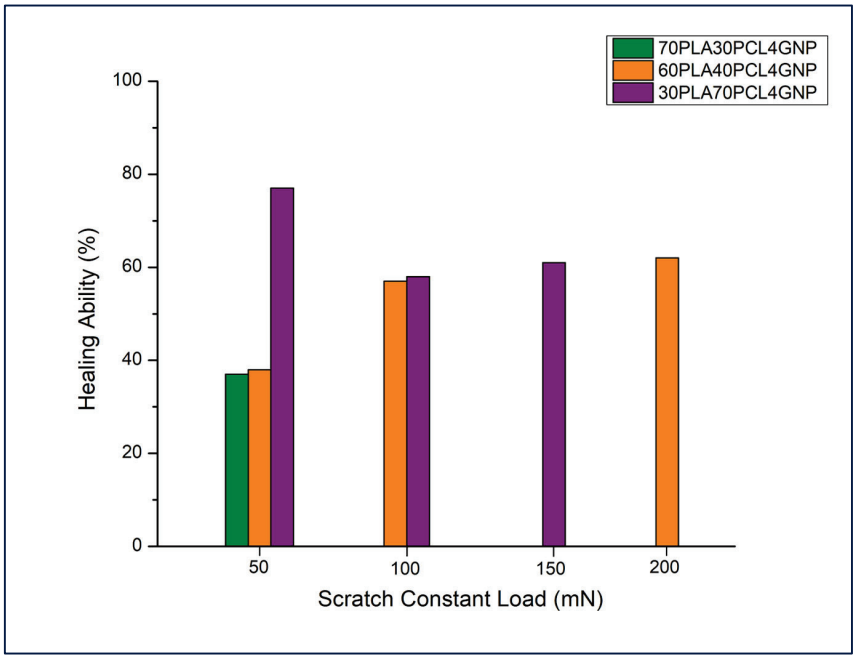


Figure 5. Healing ability of the nanocomposite samples being scratched with constant force in the range of 50–200 mN.

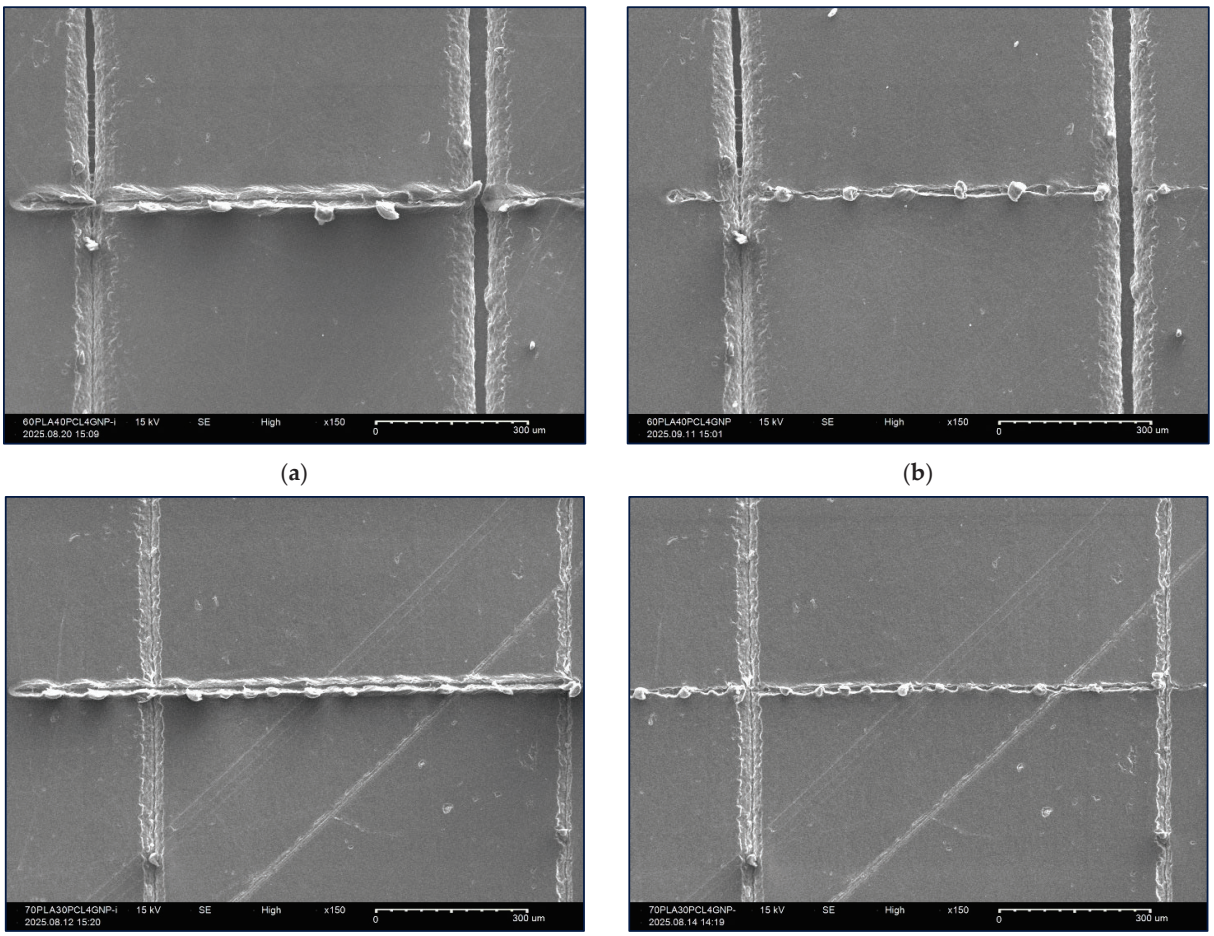


Figure 6. SEM micrographs of full-length microscratches over the polymer nanocomposites 60PLA40PCL4GNP and 70PLA30PCL4GNP, made before (**a**,**c**) and after (**b**,**d**) thermally-induced self-healing.

https://doi.org/10.3390/pr14060956

The established significant surface recovery, demonstrated by the noticeable pile-up reduction and the presence of spots in the wounds where the gap is almost fully closed, can be related as well to the interfacial regions in the nanocomposite structure where is the most probable location of the reinforcing graphene nanoparticles. Good dispersion of GNPs in the dual-phase polymer system may contribute to integrated properties of the nanocomposite material, facilitating key processes, such as polymer chain re-entanglement in the damaged interfaces and segmental surface rearrangements during self-repair activated by thermal heating [4,27].

3.3. Self-Healing of Nanocomposite Samples by Joule Effect

As an alternative method of self-healing estimation, the Joule heating effect on the self-repair capacity of low-force microscratched polymer nanocomposites has been studied. It turned out that the electrical heating allowed to trigger more efficiently the self-healing properties of the PLA/PCL/GNPs composites. This fact could be explained by the specific function of the carbon nanofiller in the improvement of the electrical and thermal conductivity of the samples, which is critical in terms of the diffusion of Joule energy into the nanocomposite matrix [28,29]. The calculated values of the nanocomposite healing efficiency, displaying the relative increment in self-repair capability of the specimens treated by Joule heating in comparison to those that underwent thermal treatment in an oven, are summarized in Table 2. There shouldn't be missed the ascertained fraught self-recovery of the surface of the sample 30PLA70PCL4GNP with respect to the scratch grooves formed by applying a 5 mN constant load. In practice, the trend of healing ability is headed upward for the whole set of polymer compositions as the weight content of the soft phase rendered a definite sway on the overall self-repair performance of the nanocomposite samples (see Figure S2).

Table 2. Self-healing properties of low-force microscratched nanocomposite samples subjected to Joule heating.

Nanocomposite Sample	Healing Efficiency at 5 mN Scratch Load, %	Healing Efficiency at 10 mN Scratch Load, %
95PLA5PCL4GNP	43.9	52.4
70PLA30PCL4GNP	62.2	50.1
60PLA40PCL4GNP	64.0	72.0
30PLA70PCL4GNP	100	69.0

Another factor influencing the boosted conversion of electrical energy into Joule heating is likely to be the presence of 4 wt% GNPs as nanofiller in the nanocomposite structure [30]. Selection of SEM images illustrating the Joule effect on the self-healing properties of the graphene-containing composite materials can be seen in Figure 7.

A substantial decrease is noticed not only with respect to the scratch width but as well regarding the depth of the grooves, though the latter can't be measured straight by the instrumental software. The observed fade off may signify good mobility and rearrangement of the polymer chains induced by the Joule energy when implemented in the nanocomposite matrix (Figure 7b,d). Apparently, the mechanism of Joule heating turned out to assign more effectiveness in the process of samples' self-repair contrasted to the thermal treatment committed in an oven.

https://doi.org/10.3390/pr14060956

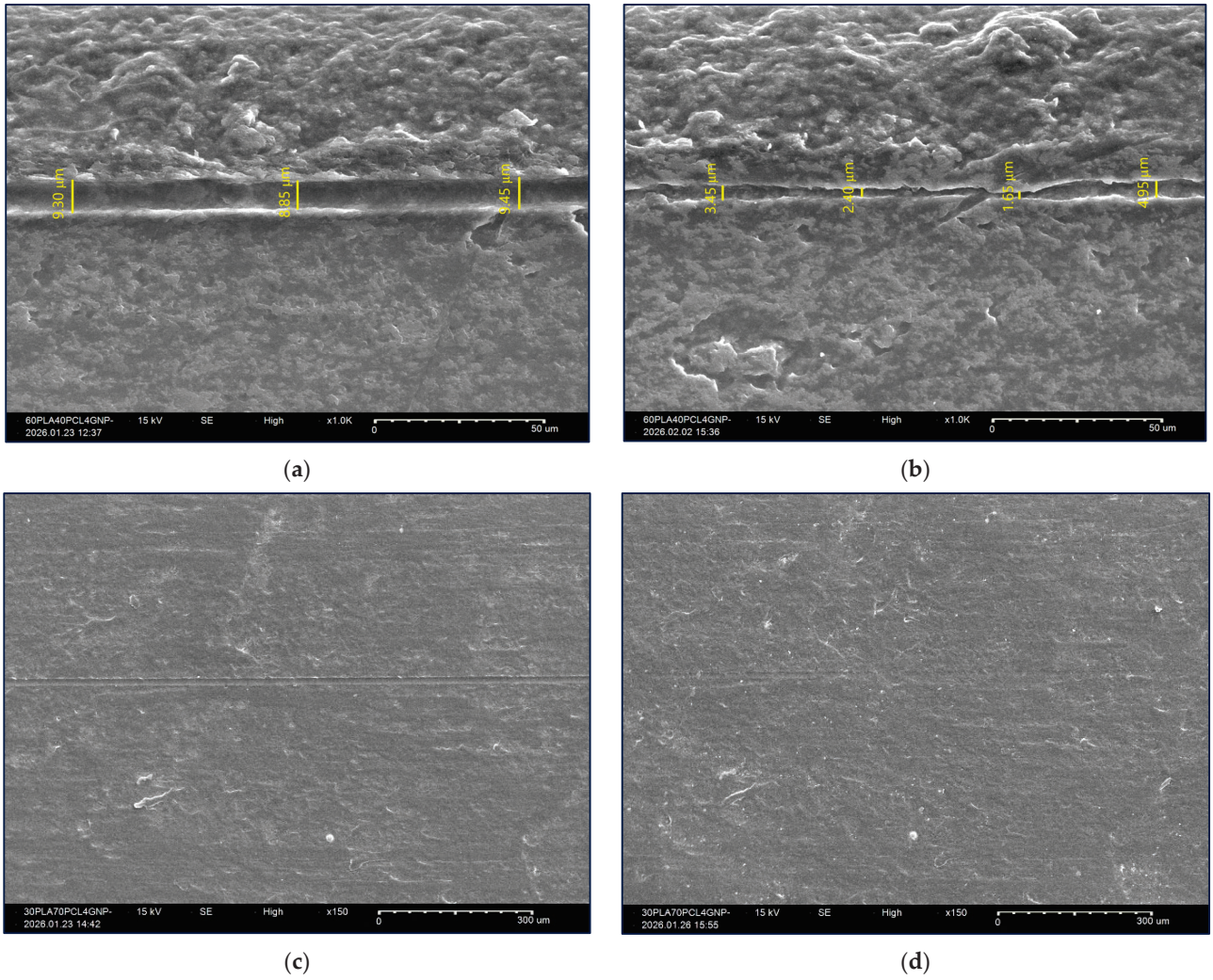


Figure 7. High-resolution SEM images of the sample 60PLA40PCL4GNP before (**a**) and after (**b**) performing Joule Heating on microscratches made with 10 mN constant force, and low-resolution SEM images of the sample 30PLA70PLA4GNP before (**c**) and after (**d**) performing Joule Heating on microscratches made with 5 mN constant force.

4. Conclusions

A novel nanocomposite material, based on PLA, PCL, and GNPs, was successfully designed and elaborated, forming a heterogeneous phase-separated polymer system containing interfacial regions whose presence is beneficial in the achievement of integrated mechanical and self-healing properties. Fine microscratch testing of the nanocomposite samples uncovered significant surface resistance against the lateral movement of the diamond stylus, which was found to be dependent on the weight content ratio between the hard and the soft polymer segments. High-resolution SEM images, focused on the surface wounds of thermally and electrically treated composite specimens, were used to designate the distinct impact of the PCL as a soft phase on the self-repair ability of the materials. The established healing efficiencies, especially upon low constant force microscratches, seemed as a potential overcoming of the substantial challenge to convert the molecular mobility on damaged solid surface during a self-healing process into microscopic volume changes. It should be underscored the role of the graphene nanoparticles which, being rather located at the interface between both polymer phases, may have facilitated the partial recovery of the heavily scratched sample surface where the geometry of the diamond stylus has left its imprint. Joule heating was found to be a promising physical method for fast and

https://doi.org/10.3390/pr14060956

effective healing of nanocomposite surface damages in a microscopic scale. The outstanding mechanical and self-repair behavior of the new composite material could open many technological options in the field of its future industrial application.

Supplementary Materials: The following supporting information can be downloaded at: https://www.mdpi.com/article/10.3390/pr14060956/s1, Figure S1: Experimental set-up of microscratch testing equipment; Figure S2: Healing ability of the nanocomposite samples subjected to scratch constant force in the range of 5–10 mN.

Author Contributions: Conceptualization, T.B. and R.K.; methodology, T.B., V.G., and E.I.; validation, T.B. and V.G.; formal analysis, T.B.; investigation, T.B. and V.G.; resources, V.A.; data curation, T.B. and E.I.; writing—original draft preparation, T.B.; writing—review and editing, T.B. and E.I.; visualization, T.B.; supervision, E.I.; project administration, R.K.; funding acquisition, R.K. All authors have read and agreed to the published version of the manuscript.

Funding: This study was done with the financial support of the European Union—Next GenerationEU within the Project No. BG-RRP-2.011-0001-C02.

Data Availability Statement: All raw data that are in the fundamental of the results presented in this study can be provided by the corresponding author on request.

Acknowledgments: Part of the present work was carried out using equipment included in the Center of Competence for Mechatronics and Clean Technologies "Mechatronics, Innovation, Robotics, Automation and Clean Technologies"—MIRACle, under contract No. BG16RFPR002-1.014-0019-C01, funded by the European Regional Development Fund (ERDF) through the Programme "Research, Innovation and Digitalization for Smart Transformation" (PRIDST) 2021–2027.

Conflicts of Interest: The authors declare no conflict of interest.

References

1. Hornat, C.C.; Urban, M.W. Shape memory effects in self-healing polymers. *Prog. Polym. Sci.* **2020**, *102*, 101208. [CrossRef]
2. Sumerlin, B.S. Next-generation self-healing materials. *Science* **2018**, *362*, 150–151. [CrossRef] [PubMed]
3. Mauldin, T.C.; Kessler, M.R. Self-healing polymers and composites. *Int. Mater. Rev.* **2010**, *55*, 317–346. [CrossRef]
4. Yang, Y.; Ding, X.; Urban, M.W. Chemical and physical aspects of self-healing materials. *Prog. Polym. Sci.* **2015**, *49*, 34–59. [CrossRef]
5. Yang, Y.; Urban, M.W. Self-healing of glucose-modified polyurethane networks facilitated by damage-induced primary amines. *Polym. Chem.* **2017**, *8*, 303–309. [CrossRef]
6. Yang, Y.; Davydovich, D.; Hornat, C.C.; Liu, X.; Urban, M.W. Leaf-inspired self-healing polymers. *Chem* **2018**, *4*, 1928–1936. [CrossRef]
7. Chen, Y.; Kushner, A.M.; Williams, G.A.; Guan, Z. Multiphase design of autonomic self-healing thermoplastic elastomers. *Nat. Chem.* **2012**, *4*, 467–472. [CrossRef]
8. Liu, F.; Urban, M.W. Recent advances and challenges in designing stimuli-responsive polymers. *Prog. Polym. Sci.* **2010**, *35*, 3–23. [CrossRef]
9. Kim, H.; Abdala, A.A.; Macosko, C.W. Graphene/Polymer Nanocomposites. *Macromolecules* **2010**, *43*, 6515–6530. [CrossRef]
10. Batakliev, T.; Ivanov, E.; Georgiev, V.; Angelov, V.; Ahuir-Torres, J.I.; Harvey, D.M.; Kotsilkova, R. New Insights in the Nanomechanical Study of Carbon-Containing Nanocomposite Materials Based on High-Density Polyethylene. *Appl. Sci.* **2024**, *14*, 9961. [CrossRef]
11. Huang, L.; Yi, N.; Wu, Y.; Zhang, Y.; Zhang, Q.; Huang, Y.; Ma, Y.; Chen, Y. Multichannel and repeatable self-healing of mechanical enhanced graphene–thermoplastic polyurethane composites. *Adv. Mater.* **2013**, *25*, 2224–2228. [CrossRef] [PubMed]
12. Kumar, R.; Singh, R.; Kumar, V.; Ranjan, N.; Gupta, J.; Bhura, N. On 3D printed thermoresponsive PCL-PLA nanofibers based architected smart nanoporous scaffolds for tissue reconstruction. *J. Manuf. Process.* **2024**, *119*, 666–681. [CrossRef]
13. Tatu, R.R.; Oria, M.; Rao, M.B.; Peiro, J.L.; Chia-Ying, L. Biodegradation of poly(L-lactic acid) and poly(ε-caprolactone) patches by human amniotic fluid in an in-vitro simulated fetal environment. *Sci. Rep.* **2022**, *12*, 3950. [CrossRef] [PubMed]
14. Rasal, R.M.; Janorkar, A.V.; Hirt, D.E. Poly(lactic acid) modifications. *Prog. Polym. Sci.* **2010**, *35*, 338–356. [CrossRef]
15. Nakajima, H.; Dijkstra, P.; Loos, K. The Recent Developments in Biobased Polymers toward General and Engineering Applications: Polymers that are Upgraded from Biodegradable Polymers, Analogous to Petroleum-Derived Polymers, and Newly Developed. *Polymers* **2017**, *9*, 523. [CrossRef]

https://doi.org/10.3390/pr14060956

16. Batakliev, T.; Georgiev, V.; Ivanov, E.; Angelov, V.; Kotsilkova, R. Tailored Polylactic Acid/Polycaprolactone Blends with Excellent Strength–Stiffness and Shape Memory Capacities. *Processes* **2025**, *13*, 1328. [CrossRef]
17. Xiao, X.; Xie, T.; Cheng, Y.T. Self-healable graphene polymer composites. *J. Mater. Chem.* **2010**, *20*, 3508–3514. [CrossRef]
18. Yang, Y.; Urban, M.W. Self-Healing of Polymers via Supramolecular Chemistry. *Adv. Mater. Interfaces* **2018**, *5*, 1800384. [CrossRef]
19. Invernizzi, M.; Turri, S.; Levi, M.; Suriano, R. 4D printed thermally activated self-healing and shape memory polycaprolactone-based polymers. *Eur. Polym. J.* **2018**, *101*, 169–176. [CrossRef]
20. Jing, Z.; Shi, X.; Zhang, G.; Gu, J. Synthesis and properties of poly(lactide)/poly(ε-caprolactone) multiblock supramolecular polymers bonded by the self-complementary quadruple hydrogen bonding. *Polymer* **2017**, *121*, 124–136. [CrossRef]
21. Wei, H.; Yao, Y.; Liu, Y.; Leng, J. A dual-functional polymeric system combining shape memory with self-healing properties. *Compos. Part B* **2015**, *83*, 7–13. [CrossRef]
22. Ghosh, B.; Chellappan, K.V.; Urban, M.W. Self-healing inside a scratch of oxetane-substituted chitosan-polyurethane (OXE–CHI–PUR) networks. *J. Mater. Chem.* **2011**, *21*, 14473–14486. [CrossRef]
23. Rodriguez, E.D.; Luo, X.; Mather, P.T. Linear/network poly(ε-caprolactone) blends exhibiting shape memory assisted self-healing (SMASH). *ACS Appl. Mater. Interfaces* **2011**, *3*, 152–161. [CrossRef] [PubMed]
24. Luo, X.; Mather, P.T. Shape memory assisted self-healing coating. *ACS Macro Lett.* **2013**, *2*, 152–156. [CrossRef] [PubMed]
25. Ivanov, E.; Kotsilkova, R.; Georgiev, V.; Batakliev, T.; Angelov, V. Advanced Rheological, Dynamic Mechanical and Thermal Characterization of Phase-Separation Behavior of PLA/PCL Blends. *J. Manuf. Mater. Process.* **2025**, *9*, 35. [CrossRef]
26. Burattini, S.; Greenland, B.W.; Chappell, D.; Colquhoun, H.M.; Hayes, W. Healable polymeric materials: A tutorial review. *Chem. Soc. Rev.* **2010**, *39*, 1973–1985. [CrossRef]
27. Stankovich, S.; Dikin, D.A.; Dommett, G.H.B.; Kohlhaas, K.M.; Zimney, E.J.; Stach, E.A.; Piner, R.D.; Nguyen, S.T.; Ruoff, R.S. Graphene-based composite materials. *Nature* **2006**, *442*, 282–286. [CrossRef]
28. Ren, D.; Chen, Y.; Li, H.; Rehman, H.U.; Cai, Y.; Liu, H. High-efficiency dual-responsive shape memory assisted self-healing of carbon nanotubes enhanced polycaprolactone/thermoplastic polyurethane composites. *Colloids Surf. A* **2019**, *580*, 123731. [CrossRef]
29. Orellana, J.; Moreno-Villoslada, I.; Bose, R.K.; Picchioni, F.; Flores, M.E.; Araya-Hermosilla, R. Self-Healing Polymer Nanocomposite Materials by Joule Effect. *Polymers* **2021**, *13*, 649. [CrossRef]
30. Wang, K.; Zhou, Z.; Zhang, J.; Tang, J.; Wu, P.; Wang, Y.; Zhao, Y.; Leng, Y. Electrical and Thermal and Self-Healing Properties of Graphene-Thermopolyurethane Flexible Conductive Films. *Nanomaterials* **2020**, *10*, 753. [CrossRef]

Disclaimer/Publisher's Note: The statements, opinions and data contained in all publications are solely those of the individual author(s) and contributor(s) and not of MDPI and/or the editor(s). MDPI and/or the editor(s) disclaim responsibility for any injury to people or property resulting from any ideas, methods, instructions or products referred to in the content.

https://doi.org/10.3390/pr14060956

processes

MDPI

Article

Tailored Shell Engineering of γ-Fe_2O_3@SiO_2 Nanoparticles for High-Performance and Recyclable Chemical Mechanical Planarization

Young Seo Kim and Gye Seok An *

Department of Advanced Material Engineering, Kyonggi University, 154-42 Gwanggyosan-ro, Yeongtong-gu, Suwon-si 16227, Republic of Korea; youngso7512@kyonggi.ac.kr
* Correspondence: gsmaroan@kyonggi.ac.kr; Tel.: +82-31-249-9763

Abstract

As semiconductor devices continue to scale down and integrate more densely, the atomic-level planarization of metal interconnects and dielectric layers is critical. Consequently, the development of chemical mechanical planarization (CMP) materials must address both high polishing performance and environmental sustainability. In this study, γ-Fe_2O_3@SiO_2 core–shell abrasive particles were designed to overcome the performance and recyclability limitations of conventional SiO_2 abrasives. The γ-Fe_2O_3 core enables an efficient magnetic separation from spent slurry, while the tunable SiO_2 shell enhances the dispersion stability and modulates the polishing characteristics. When applied to the CMP of tungsten (W) thin films, the optimized γ-Fe_2O_3@SiO_2 abrasives achieved a higher removal rate and lower surface roughness than commercial SiO_2-based slurries. Notably, the abrasives maintained a high performance even after 10 reuse cycles through simple magnetic recovery. This demonstrates a highly efficient and sustainable design strategy for next-generation CMP materials.

Keywords: chemical mechanical planarization; γ-Fe_2O_3; core–shell nanoparticles; synthesis; recycling

1. Introduction

With the continuous scaling and miniaturization of semiconductor devices, the optimization of surface planarization processes has become increasingly crucial. In particular, the linewidth of integrated circuits (ICs) is now approaching the nanometer scale. At this scale, even minor surface topographies can induce misalignments in subsequent photolithography or degrade electrical properties. Consequently, atomic-level surface flatness is essential for reliable device fabrication. To meet these stringent requirements, chemical mechanical planarization (CMP), a hybrid technique that combines mechanical abrasion and chemical reactions, has been established as a critical process in semiconductor manufacturing. CMP removes residual surface roughness and produces a uniformly flat surface, thereby ensuring both device performance and yield reliability [1].

A typical CMP slurry contains abrasive particles, oxidizers, complexing agents, dispersants, and pH adjusters. Among these components, the physicochemical properties of the abrasives play a decisive role in determining key process parameters such as the removal rate (RR), surface roughness, and polishing selectivity. Colloidal SiO_2 nanoparticles are currently the leading abrasives in commercial CMP. This is due to their excellent chemical

stability and high dispersibility in aqueous media [2]. However, conventional SiO_2 abrasives exhibit limitations in terms of post-processing slurry recovery, leading to significant waste generation. In fact, recent environmental impact assessments have emphasized that the production and disposal of CMP slurries contribute significantly to the semiconductor industry's ecological footprint [3]. Therefore, the development of advanced abrasive particles that ensure both a superior polishing performance and efficient reusability is critical [4].

To address the limitations of pure silica, which have been extensively documented over the past six decades [5], we propose a novel CMP abrasive system based on Fe_2O_3@SiO_2 core–shell nanoparticles, employing γ-Fe_2O_3 as the magnetic core. This superparamagnetic iron oxide allows for facile magnetic separation from spent slurries. Unlike Fe_3O_4, it exhibits enhanced chemical stability in oxidative environments, making it highly suitable for long-term CMP without significant degradation. Furthermore, the SiO_2 shell improves the surface stability and dispersibility of the particles by preventing agglomeration, while modulating the mechanical and chemical interactions during polishing.

In this study, Fe_2O_3@SiO_2 nanoparticles with various SiO_2 shell thicknesses were synthesized by controlling the dosage of tetraethyl orthosilicate (TEOS). The synthesized particles were evaluated for the planarization of tungsten (W) thin films, systematically investigating the effects of shell thickness on the removal rate and surface roughness. Alongside polishing performance, a comparative analysis with conventional SiO_2-based slurries was conducted to evaluate their magnetic recoverability and reuse efficiency. By tailoring the SiO_2 shell thickness, our design successfully fine-tunes the polishing characteristics while simultaneously reducing slurry waste. These findings highlight the potential of γ-Fe_2O_3@SiO_2 core–shell nanoparticles as next-generation CMP abrasives capable of meeting key industrial demands for process optimization and environmental sustainability.

2. Materials and Methods

2.1. Surface Modification of γ-Fe_2O_3 Nanoparticles

Maghemite nanoparticles (γ-Fe_2O_3, 99+%, Cosmo AM & T Co., Ltd., Chungju, Republic of Korea), 7.5 g total mass, were initially purified via ultrasonication in distilled water three times to remove residual impurities. Next, the superparamagnetic γ-Fe_2O_3 nanoparticles were magnetically separated from the solution using an external magnet. The collected nanoparticles were then transferred to a 3 L round-bottom flask containing 2 N ammonia solution (NH_4OH, 28–30 wt% stock solution, Junsei, Tokyo, Japan). The mixture was heated to 80 °C for 1 h with continuous stirring at 300 rpm. Subsequently, the mixture was allowed to cool naturally to room temperature under continuous stirring, and the nanoparticles were washed repeatedly to remove residual chemicals. This surface modification step was designed to introduce hydroxyl groups and enhance the hydrophilicity of γ-Fe_2O_3 nanoparticles, facilitating subsequent silica shell formation.

2.2. Fabrication of Core–Shell Structure of γ-Fe_2O_3@SiO_2 Nanoparticles

The surface-modified γ-Fe_2O_3 nanoparticles were dispersed in a 1:1 mixture of deionized water (DIW) and ethanol (500 mL total volume). To this dispersion, 75 mL of NH_4OH was added and the resulting mixture was homogenized by magnetic stirring at 300 rpm for 30 min. Subsequently, a solution of TEOS (95.0%, Samchun, Seoul, Republic of Korea) in ethanol was added dropwise using a syringe pump at a controlled rate of 0.08 mL/min. Upon completion of the TEOS/ethanol addition, the reaction mixture was stirred continuously for 18 h to facilitate the formation of Fe_2O_3@SiO_2 core–shell nanoparticles. The nanoparticles were magnetically separated from the reaction medium by applying an external magnetic field (5000× g) to the flask. To remove any residual reactants or by-products,

https://doi.org/10.3390/pr14060902

the separated nanoparticles were subjected to several cycles of magnetic washing with distilled water and ethanol. Finally, the purified Fe_2O_3@SiO_2 nanoparticles were dried in an oven at 80 °C for 6 h to remove residual solvents and obtain the dry powder form of core–shell particles.

2.3. Characterization of Fe_2O_3@SiO_2 Particles

The crystal structure of the Fe_2O_3@SiO_2 particles was analyzed using X-ray diffraction spectroscopy (XRD; UltimaIV, Rigaku, Tokyo, Japan). Fourier transform infrared spectroscopy (FT-IR; IRAffinity-1S, Shimadzu, Kyoto, Japan) was used to investigate the functional groups present on the particle surfaces after silica synthesis. The zeta potentials of the prepared samples were measured using dynamic light scattering (DLS; Zetasizer Nano ZSP, Malvern Instruments, Westborough, MA, USA) to estimate the surface charge changes. The morphology and shell thickness of the particles were studied using high-resolution transmission electron microscopy (HR-TEM; Tecnai G2 F30 S-Twin, FEI, Eindhoven, The Netherlands). The changes in the magnetic properties post-coating were quantified using a vibrating sample magnetometer (VSM; Lake Shore 7400, Lake Shore Cryotronics, Inc., Westerville, OH, USA) with an applied field range of $\pm$10 kOe to measure the magnetic hysteresis behavior.

2.4. Preparation of CMP Slurry Using Fe_2O_3@SiO_2 Particles

Fe_2O_3@SiO_2 core–shell nanoparticles with varying SiO_2 shell thicknesses were dispersed in 1 L of DIW at a concentration of 5 wt%, followed by ultrasonication for 20 min to ensure colloidal stability. To regulate the chemical interactions during polishing, 1 wt% 2-picolinic acid ($C_6H_5NO_2$, Sigma-Aldrich, St. Louis, MO, USA) was added as a corrosion inhibitor, and 1 wt% glycine (NH_2CH_2COOH, Sigma-Aldrich, St. Louis, MO, USA) was introduced as a dispersant. The pH of the slurry was adjusted to 2.5 using nitric acid (HNO_3, Sigma-Aldrich, St. Louis, MO, USA), and hydrogen peroxide (H_2O_2, Samchun Chemicals, Seoul, Republic of Korea) was added as an oxidizing agent to promote the oxidation of the W film surface. The prepared slurry was subsequently used for the CMP evaluation.

2.5. W CMP Evaluation

A 6-inch silicon wafer coated with a 5000 Å thick W film via chemical vapor deposition (CVD) was diced into 6 $\times$ 6 cm^2 coupons for polishing experiments. CMP performance was evaluated using a coupon-scale polisher (POLI-400, G&P Technology, Busan, Republic of Korea) equipped with an IC1010 polishing pad (Suba IV, Dupont, Wilmington, NC, USA). During the process, the platen and head rotation speeds were set to 89 rpm and 91 rpm, respectively, and a downward force of 2 psi was applied. The slurry was delivered at a flow rate of 100 mL/min for a polishing time of 60 s.

The material RR was calculated based on measurements at five different points using a four-point probe (CMT-SR5000, AIT Co., Ltd, Suwon, Republic of Korea), and the average was used to calculate the RR. To ensure data reliability, measurements were taken from five different positions on each coupon, and the average value was reported. The surface morphologies of the polished W films were further analyzed using field-emission scanning electron microscopy (FE-SEM; JSM-6330F, JEOL, Tokyo, Japan) and atomic force microscopy (AFM; XE-150, Park Systems, Suwon, Republic of Korea).

2.6. Recovery and Reuse of Fe_2O_3@SiO_2 Abrasive Particles

Immediately after the CMP process, the slurry was collected, and the Fe_2O_3@SiO_2 abrasive particles were separated from the waste slurry using an external magnetic field. The recovered particles were sequentially washed three times with ethanol (EtOH) and DIW

https://doi.org/10.3390/pr14060902

under ultrasonication to remove any remaining residues. After purification, the particles were reused to formulate fresh CMP slurries under identical preparation conditions, and subsequent polishing evaluations were conducted. The recovery efficiency of the abrasive particles was determined by comparing the initial mass of the particles used in the slurry with the mass of particles recovered from the post-CMP waste slurry.

3. Results and Discussion

XRD analysis (Figure 1) was carried out to evaluate the changes in the atomic and crystalline structures of as-received γ-Fe_2O_3, NH_4OH-treated γ-Fe_2O_3, and TEOS-modified γ-Fe_2O_3 nanoparticles. The TEOS-modified samples were synthesized at varying molar ratios of γ-Fe_2O_3 to TEOS (1:1, 1:3.5, and 1:7) and are hereafter referred to as FS_(1:1), FS_(1:3.5), and FS_(1:7), respectively.

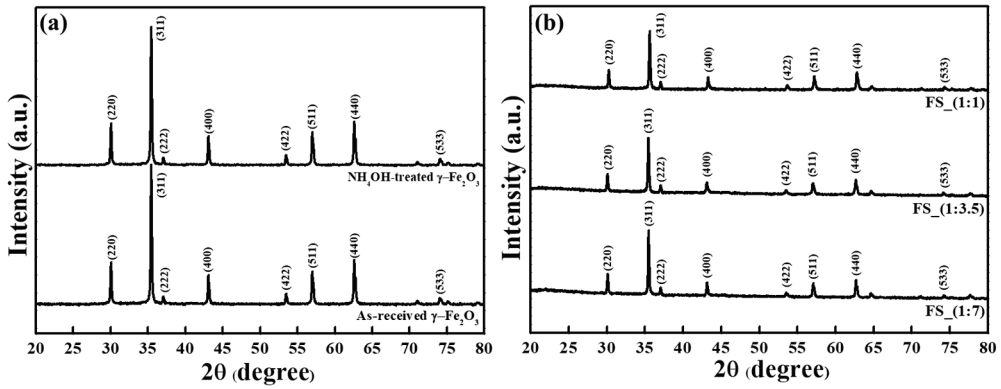


Figure 1. XRD spectra of (**a**) as-received γ-Fe_2O_3, NH_4OH-treated Fe_2O_3, (**b**) FS_(1:1), FS_(1:3.5) and FS_(1:7).

All samples exhibited diffraction peaks corresponding to the (220), (311), (400), (422), (511), and (440) planes at 2θ values of 30.36°, 35.64°, 43.36°, 53.84°, 57.34°, and 62.98°, respectively [6]. These peaks are characteristic of the inverse spinel structure of γ-Fe_2O_3, in accordance with the JCPDS Card No. 39-1346 [7]. It is known that γ-Fe_2O_3 consists solely of Fe^{3+} ions and possesses a defective spinel structure in which some Fe^{3+} ions are absent from octahedral sites, resulting in the formation of vacancies. This structural feature leads to a disordered distribution of Fe^{3+} ions and vacancies within the octahedral sites.

The XRD pattern of the NH_4OH-treated γ-Fe_2O_3 sample revealed no newly developed peaks or shifts in existing reflections, suggesting that the surface modification occurred without altering the crystalline structure or the internal crystalline framework.

In the case of the TEOS-modified γ-Fe_2O_3 nanoparticles, all major diffraction peaks associated with γ-Fe_2O_3 remained unchanged, suggesting that the core crystal structure was preserved regardless of the shell thickness. However, an increase in baseline intensity at low angles (2θ < 40°) was observed in the low-angle region (2θ < 40°), which is attributed to the presence of an amorphous SiO_2 phase generated via the hydrolysis and condensation of TEOS during shell formation [8]. The baseline shift and subtle slope changes in this region further corroborated the formation of an amorphous silica coating. This result confirms that the silica shell is amorphous and does not induce a phase transformation in the magnetic core.

Taken together, these results confirm that neither NH_4OH surface treatment nor TEOS-based silica coating induced any significant modifications to the crystalline structure of the γ-Fe_2O_3 core, while the presence of amorphous silica was clearly identified in TEOS-treated samples.

https://doi.org/10.3390/pr14060902

Figure 2 shows the FT-IR spectra of as-received γ-Fe_2O_3, NH_4OH-treated γ-Fe_2O_3, and TEOS-modified γ-Fe_2O_3 nanoparticles, highlighting the evolution of surface functional groups resulting from chemical treatments. A broad absorption band centered at approximately 600 cm^{-1} is observed in all samples and is attributed to the stretching vibration of the Me–O (Fe–O) bonds, which is a characteristic of the spinel ferrite framework.

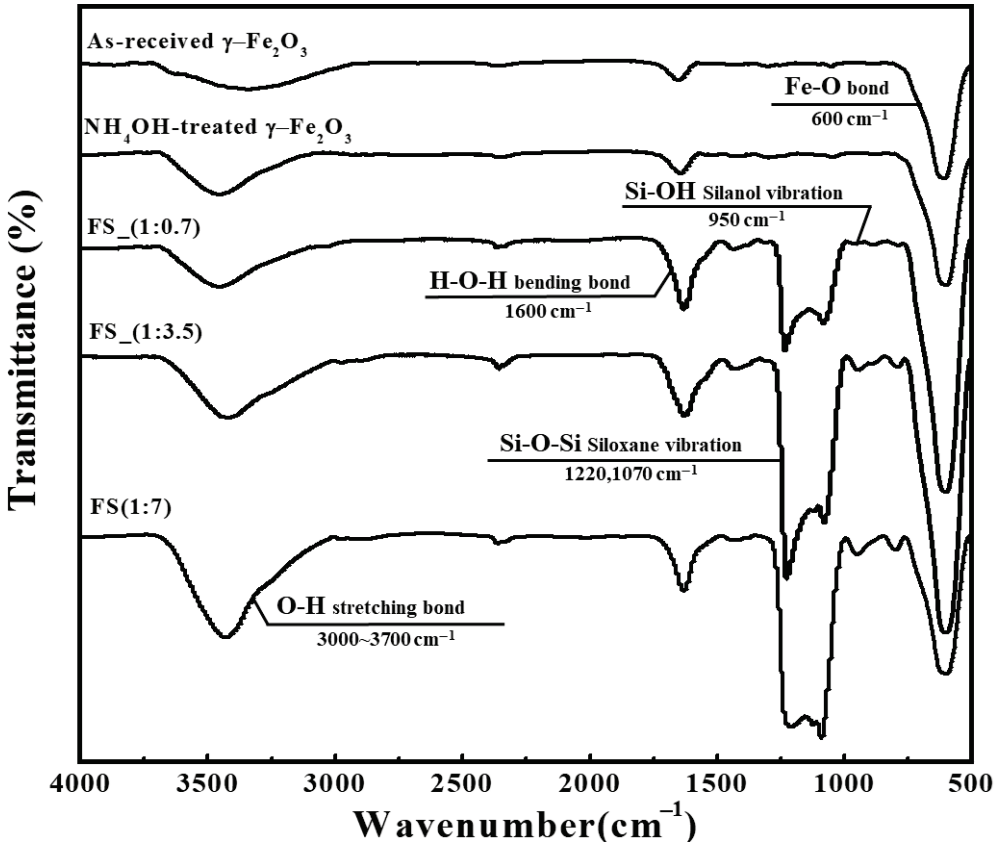


Figure 2. FT-IR spectra of as-received γ-Fe_2O_3, NH_4OH-treated γ-Fe_2O_3, FS_(1:1), FS_(1:3.5) and FS_(1:7).

The broad band appearing in the 3000–3700 cm^{-1} range corresponds to O–H stretching vibrations, indicative of surface hydroxyl groups, whereas the absorption peak near 1600 cm^{-1} is ascribed to the H–O–H bending mode of physisorbed water. Notably, both the O–H stretching and H–O–H bending vibration intensities progressively increased with increasing TEOS concentration, suggesting enhanced hydroxylation and water association on the particle surface.

This trend is attributed to the hydrolysis of the TEOS molecules, as described by the following reaction [9]:

$$Si(OC_2H_5)_4 + 4H_2O \rightarrow Si(OH)_4 + 4C_2H_5OH \quad (1)$$

Hydrolysis results in the formation of silanol groups (Si–OH), which exhibit vibrational characteristics similar to those of O–H bonds. As the TEOS content increases, the formation of silanol groups is promoted, leading to an increase in the intensity of the O–H-related absorption bands. Furthermore, because each TEOS molecule requires four water molecules for complete hydrolysis, a higher TEOS concentration inevitably alters the hydration environment, contributing to the amplification of the H–O–H bending peak.

In addition to hydroxyl-related features, two distinct absorption bands attributed to Si–O–Si stretching vibrations were observed at approximately 1220 cm^{-1} and 1070 cm^{-1} [10].

https://doi.org/10.3390/pr14060902

The intensities of these peaks increased with increasing TEOS concentration, indicating the progressive formation of siloxane (Si–O–Si) networks through the condensation of silanol groups. These results collectively confirm that increased TEOS content not only enhances surface hydroxylation but also facilitates the development of an amorphous silica network via siloxane bond formation [11].

TEM was employed to examine the correlation between TEOS concentration and the resulting thickness of the SiO_2 shell on γ-Fe_2O_3 nanoparticles. The as-received γ-Fe_2O_3 particles (Figure 3a) exhibited a spherical morphology with slightly uneven surfaces, and their average particle diameter was measured to be approximately 274 nm. Following surface treatment with aqueous ammonia, the particle size was slightly reduced to 259 nm (Figure 3b), which is attributed to surface etching or modification [12].

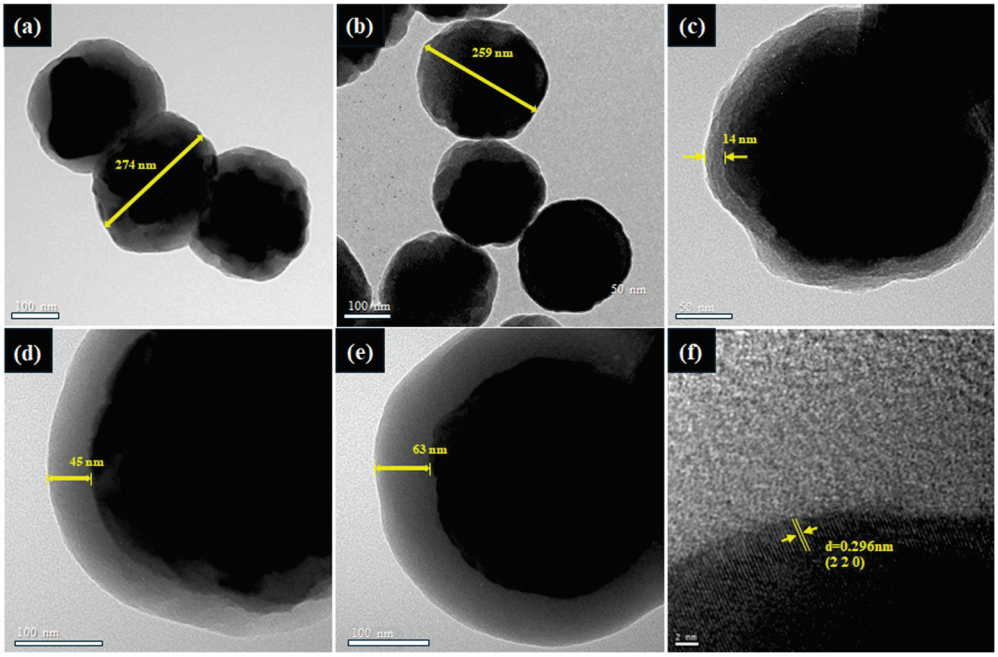


Figure 3. TEM images of (**a**) as-received Fe_2O_3, (**b**) NH_4OH-treated Fe_2O_3, (**c**) FS_(1:1), (**d**) FS_(1:3.5), (**e**) FS_(1:7) and (**f**) HR-TEM of FS_(1:3.5).

Representative TEM images of γ-Fe_2O_3@SiO_2 core–shell nanoparticles synthesized with varying amounts of TEOS (0.0369, 0.168, and 0.336 mol) are shown in Figure 3c–e. In all cases, successful and uniform shell formation was observed to encapsulate the γ-Fe_2O_3 core completely. The corresponding shell thicknesses were 14, 45, and 63 nm, respectively, confirming a clear trend of increasing shell thickness with increasing TEOS concentration [13].

This increase in shell thickness is attributed to the hydrolysis and condensation of TEOS in the presence of ammonia. Specifically, TEOS undergoes hydrolysis to form silanol (Si–OH) groups, which subsequently condense to form a Si–O–Si network comprising a silica shell. As the TEOS concentration increases, a higher concentration of silanol intermediates is generated, which accelerates the condensation reaction, resulting in a thicker SiO_2 layer.

Figure 3f presents a high-resolution TEM (HR-TEM) image of the γ-Fe_2O_3@SiO_2 nanoparticles synthesized with 0.168 mol of TEOS, corresponding to the sample in Figure 3d. The image clearly reveals the crystalline nature of the γ-Fe_2O_3 core, as evidenced by the visible lattice fringes and the amorphous character of the surrounding SiO_2 shell, which lacks long-range ordering. The interplanar distance of the observed lattice fringes was

https://doi.org/10.3390/pr14060902

measured to be 0.296 nm, corresponding to the (220) crystallographic plane of γ-Fe_2O_3, consistent with the XRD results presented in Figure 1.

These findings confirm that the thickness of the amorphous SiO_2 shell can be precisely modulated by controlling the TEOS precursor concentration during synthesis and that the γ-Fe_2O_3 core retains its crystalline structure throughout the coating process.

Figure 4 presents the zeta potential, particle size distribution (PSD), and polydispersity index (PDI) of as-received γ-Fe_2O_3, NH_4OH-treated γ-Fe_2O_3, and TEOS-modified γ-Fe_2O_3@SiO_2 nanoparticles to evaluate their dispersion stability and particle uniformity.

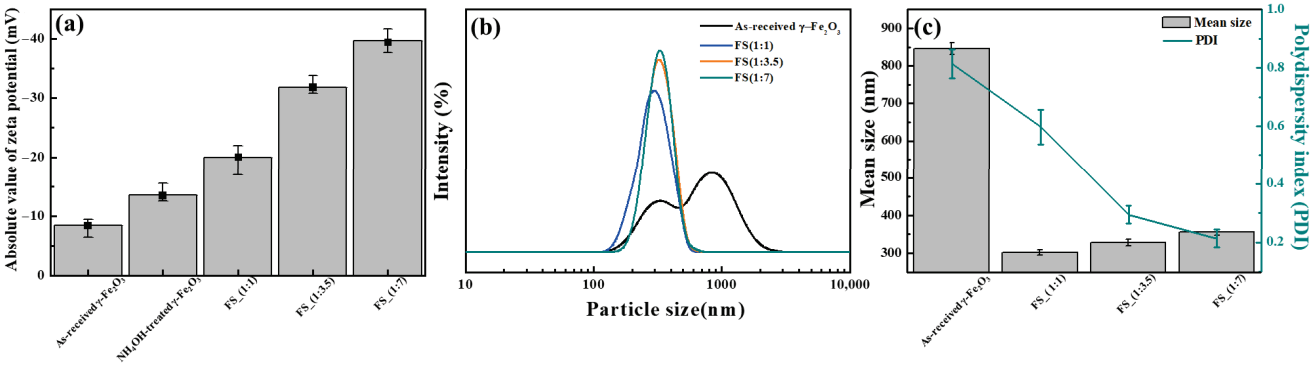


Figure 4. (**a**) Zeta potential, (**b**) particle size distribution (PSD), and (**c**) mean size and polydispersity (PDI) of as-received γ-Fe_2O_3, FS_(1:1), FS_(1:3.5) and FS_(1:7).

As shown in Figure 4a, the as-received γ-Fe_2O_3 nanoparticles exhibited a zeta potential of −8.46 mV, indicating a relatively low surface charge. Upon treatment with aqueous ammonia, the zeta potential decreased to −13.52 mV, implying an enhancement in surface charge density. This change is attributed to the increased presence of surface hydroxyl groups (–OH) introduced during the ammonia treatment. This trend is consistent with the FT-IR results (Figure 2), where an increase in the O–H stretching band was observed for NH_4OH-treated samples.

Further modification with TEOS resulted in a gradual increase in the absolute value of the zeta potential, which was positively correlated with the TEOS concentration. This behavior is attributed to the formation of silanol groups (Si–OH) via TEOS hydrolysis, which are chemically analogous to hydroxyl groups and contribute to an increase in the negative surface charge. Accordingly, the enhanced electrostatic repulsion between the particles led to improved dispersion stability, as reflected in the zeta potential values [14].

Figure 4b shows the PSD profiles of the nanoparticles. The as-received γ-Fe_2O_3 displays a bimodal distribution with peaks centered at approximately 368 nm and 995 nm and a mean hydrodynamic diameter of 845.7 ± 16.3 nm. This value is significantly larger than the particle diameter observed in the TEM images (Figure 3), which is attributed to the agglomeration of nanoparticles owing to van der Waals interactions and their high surface energies.

In contrast, the γ-Fe_2O_3@SiO_2 core–shell nanoparticles exhibited unimodal PSD curves, indicating that thicker SiO_2 shells improve colloidal stability by increasing surface charge repulsion. The average hydrodynamic diameters for the nanoparticles synthesized with 0.0369, 0.168, and 0.336 mol of TEOS were 301.4 ± 7.4 nm, 327.8 ± 9.3 nm, and 355.2 ± 8.5 nm, respectively.

As shown in Figure 4c, the corresponding PDI values are 0.597, 0.294, and 0.213. These results indicate that an increase in the TEOS concentration not only contributes to an increase in particle size due to shell thickening but also leads to a significant narrowing of the particle size distribution [15]. This is attributed to the enhanced colloidal stability arising

https://doi.org/10.3390/pr14060902

from the higher surface density of –OH groups, which generates stronger interparticle electrostatic repulsion and reduces aggregation.

Collectively, these findings demonstrate that both the hydrodynamic size and dispersity of γ-Fe_2O_3@SiO_2 nanoparticles can be modulated by controlling the TEOS concentration, with improved dispersion stability and size uniformity achieved at higher TEOS levels.

Figure 5 presents the magnetic hysteresis curves of γ-Fe_2O_3 and γ-Fe_2O_3@SiO_2 core–shell nanoparticles with varying shell thicknesses, measured using a vibrating sample magnetometer (VSM) to evaluate the effect of SiO_2 coating on their magnetic properties. All samples exhibited typical superparamagnetic behavior, as evidenced by the absence of remanent magnetization and coercivity in the hysteresis curves, indicating that the nanoparticles did not retain magnetization after removal of the external magnetic field [16].

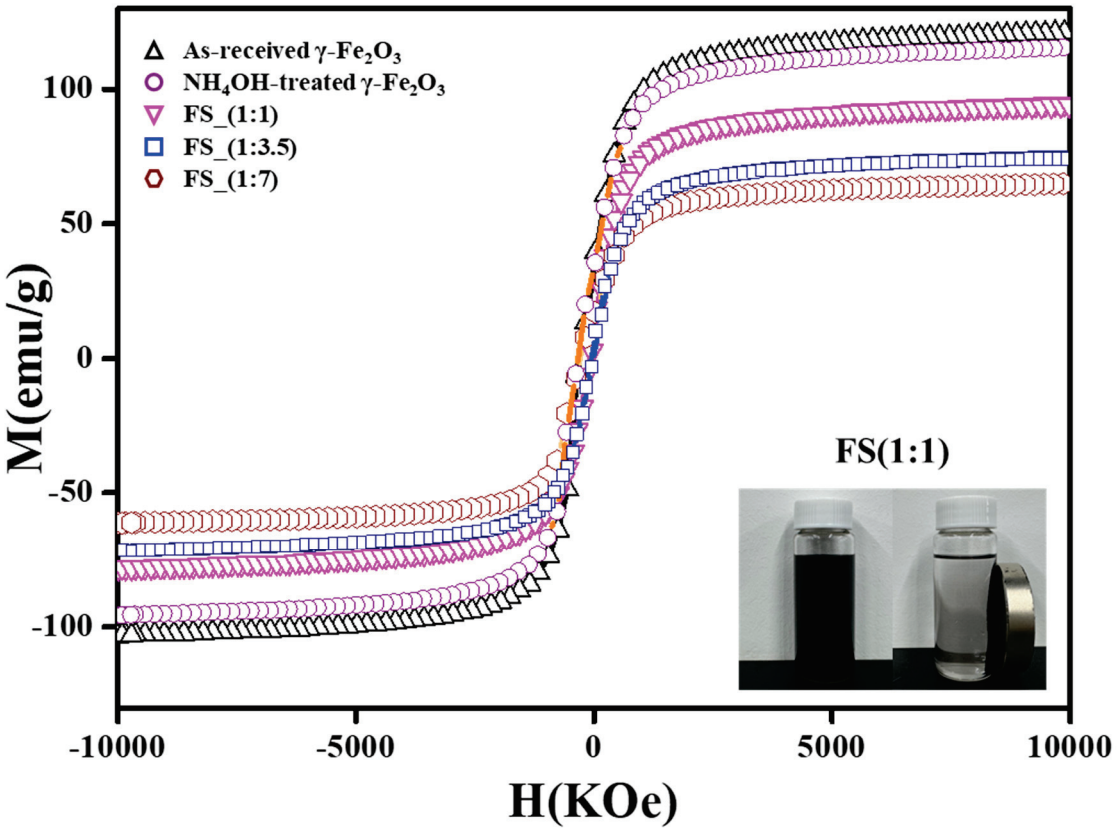


Figure 5. Magnetization curves of as-received γ-Fe_2O_3 and NH_4OH-treated γ-Fe_2O_3. FS_(1:1), FS_(1:3.5) and FS_(1:7).

The as-received γ-Fe_2O_3 nanoparticles exhibited a high saturation magnetization (M_s) value of 121.48 emu/g. Upon treatment with ammonia solution, the M_s value slightly decreased to 117.71 emu/g while retaining the superparamagnetic property, suggesting that the surface modification did not significantly affect the magnetic core [17].

In contrast, a noticeable decrease in M_s was observed as the SiO_2 shell thickness increased with increasing TEOS concentration. Specifically, when the TEOS-to-γ-Fe_2O_3 molar ratios were adjusted to 1:1, 1:3.5, and 1:7, the corresponding saturation magnetization values were reduced to 93.02, 74.15, and 62.48 emu/g, respectively. This reduction is primarily attributed to the increase in the nonmagnetic SiO_2 shell thickness, which leads to the dilution of the magnetic core content per unit mass of the composite particles [18].

These results confirm that, while the superparamagnetic behavior is preserved regardless of SiO_2 shell thickness, the saturation magnetization of γ-Fe_2O_3@SiO_2 nanoparticles is

https://doi.org/10.3390/pr14060902

inversely related to the volume fraction of the magnetic core, controlled by the TEOS concentration during synthesis. Furthermore, this result suggests that Fe_2O_3@SiO_2 abrasives can be effectively recovered using magnetic separation without residual magnetization, which is beneficial for repeated reuse.

Figure 6a illustrates the removal rates of W films polished using CMP slurries containing as-prepared SiO_2 particles and γ-Fe_2O_3@SiO_2 core–shell nanoparticles with different shell structures (FS_(1:1), FS_(1:3.5), and FS_(1:7)). All the slurries were formulated under identical chemical conditions, consisting of 5 wt% abrasive particles, 1 wt% 2-picolinic acid, 1 wt% glycine, and H_2O_2 as an oxidizing agent, with the pH adjusted to 2.5 [19]. A slurry containing the prepared SiO_2 abrasives exhibited a removal rate of 191 Å/min. In contrast, the γ-Fe_2O_3@SiO_2 abrasives demonstrated enhanced polishing performance, with removal rates of 277, 262, and 212 Å/min for FS_(1:1), FS_(1:3.5), and FS_(1:7), respectively. A clear decreasing trend in the removal rate is observed with increasing SiO_2 shell thickness, indicating that thinner shell particles are more effective for material removal during W CMP [20].

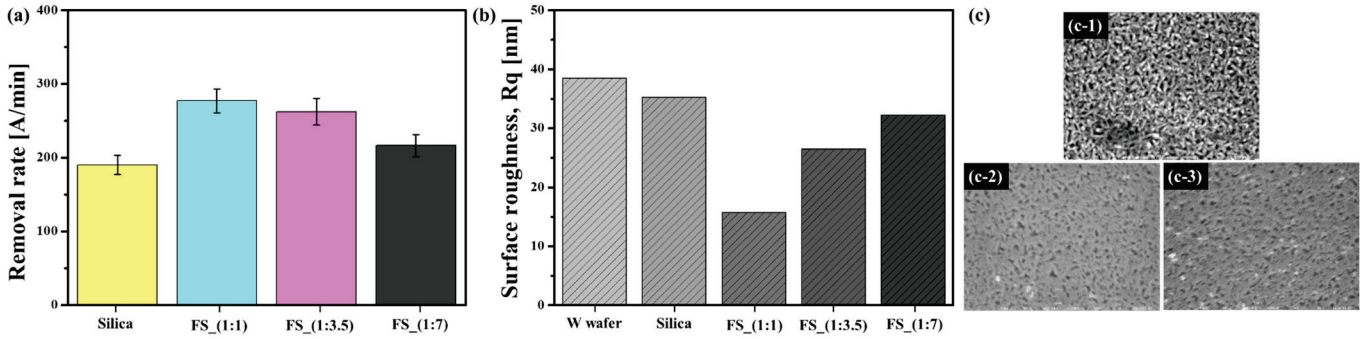


Figure 6. (**a**) W removal rates obtained using CMP slurries containing 5 wt% as-prepared SiO_2 and γ-Fe_2O_3@SiO_2 core–shell particles (FS_(1:1), FS_(1:3.5), and FS_(1:7)). (**b**) Surface roughness (Rq) of the bare (unpolished) W wafer and W films after CMP using different abrasive particles. (**c**) Top-view SEM images of W films: (**c-1**) bare W wafer before CMP, (**c-2**) W film polished with FS_(1:1), and (**c-3**) W film polished with FS_(1:7).

Figure 6b shows the surface roughness (Rq) of the W films after polishing, as measured by AFM, together with that of the bare (unpolished) W wafer for comparison. The bare W wafer exhibits a relatively high surface roughness of 38.52 Å. Polishing with as-prepared SiO_2 particles slightly reduced the roughness to 35.28 Å, indicating a limited planarization efficiency. In contrast, the use of γ-Fe_2O_3@SiO_2 core–shell abrasives led to a substantial reduction in surface roughness. The Rq values were measured to be 15.74 Å for FS_(1:1), 26.49 Å for FS_(1:3.5), and 32.26 Å for FS_(1:7), corresponding to roughness reductions of approximately 59%, 31%, and 16%, respectively, relative to the bare W wafer. Among the investigated samples, FS_(1:1) exhibits the most pronounced improvement in surface planarity, which is consistent with its superior removal rate.

Figure 6c presents top-view SEM images of the W films before and after CMP. The bare W wafer before CMP (c-1) exhibits a rough and heterogeneous surface morphology with clearly distinguishable grain structures, reflecting the inherent surface irregularities of the as-deposited W film. After polishing with γ-Fe_2O_3@SiO_2 abrasives, a marked improvement in surface uniformity is observed. In particular, the W film polished with FS_(1:1) (c-2) showed a significantly smoother and more homogeneous surface with suppressed grain contrast, indicating the effective removal of surface asperities. In contrast, the surface polished with FS_(1:7) (c-3) exhibits relatively less smoothing and discernible residual surface features. These SEM observations are in good agreement with the AFM roughness

https://doi.org/10.3390/pr14060902

results and removal rate trends shown in Figure 6a,b, confirming that thinner-shell γ-Fe_2O_3@SiO_2 abrasives provide superior surface planarization during W CMP.

To elucidate the origin of the observed dependence of CMP performance on the shell structure of γ-Fe_2O_3@SiO_2 nanoparticles, the relationship between particle mechanics and polishing behavior must be considered. CMP proceeds through cyclic processes involving surface oxidation, mechanical abrasion, and chemical dissolution. Because all the slurries in this study were prepared with identical chemical compositions, the differences in polishing performance can be primarily attributed to variations in the physical and mechanical properties of the abrasive particles.

The mechanical behavior of γ-Fe_2O_3@SiO_2 core–shell particles is strongly governed by the thickness of the amorphous SiO_2 shell, which modulates the effective stiffness of the composite particle. Crystalline γ-Fe_2O_3 cores possess a relatively high stiffness, with reported Young's modulus values of approximately 150–200 GPa, whereas amorphous SiO_2 shells exhibit lower Young's moduli in the range of ~60–75 GPa. As the SiO_2 shell becomes thicker, the overall stiffness of the particle decreases, leading to a reduced contact stress at the particle–wafer interface. Consequently, thicker shell particles tend to distribute the applied load over a larger contact area, thereby lowering the effective polishing pressure and reducing the removal rates.

Conversely, thinner shell particles, such as FS_(1:1), retained a higher effective stiffness and generated greater localized contact stress during polishing, thereby facilitating the efficient removal of surface asperities and enhanced surface planarization [21]. Although excessively thin shells may raise concerns regarding mechanical durability, the present results demonstrate that FS_(1:1) achieves an optimal balance between polishing efficiency and structural stability under the applied CMP conditions. These findings highlight the critical role of SiO_2 shell engineering in optimizing the CMP performance of magnetically recoverable γ-Fe_2O_3@SiO_2 abrasives.

Figure 7a illustrates the change in recovery rate of γ-Fe_2O_3@SiO_2 abrasive particles with varying SiO_2 shell thicknesses over multiple reuse cycles. Initially, all the samples exhibited similar recovery rates of approximately 99%. However, a gradual decrease was observed as the number of reuse cycles increased. Specifically, the particles with a 14 nm shell maintained a high recovery rate of 96.8% after 10 cycles, whereas those with 45 nm and 63 nm shells exhibited slightly lower rates of 95.1% and 94.6%, respectively. This trend is attributed to the weakening of the magnetic properties of the γ-Fe_2O_3 core as the SiO_2 shell becomes thicker, thereby reducing the separation efficiency under an external magnetic field. This observation is consistent with the magnetic characterization results shown in Figure 5, in which a decrease in magnetization is observed with increasing shell thickness. Nonetheless, the overall loss of recovery remained within 5.4% under all conditions, confirming that a high recovery efficiency was maintained even after repeated reuse.

Figure 7b shows the variations in the W removal rate and surface roughness (Ra) of the FS_(1:1) sample over ten reuse cycles. After each cycle, the used particles were recovered from the slurry using an external magnetic field, sequentially washed with EtOH and DIW, and then redispersed in a fresh slurry of identical composition. The removal rate decreased slightly from 277 Å/min to 262 Å/min after 10 cycles. This reduction is likely due to minor particle loss during recovery and microstructural damage, such as surface cracking induced by repeated polishing. Despite this, the overall removal rate remained consistently high with no statistically significant deterioration in performance. Similarly, the surface roughness showed a mild increase with repeated reuse, but no substantial degradation in the polishing quality was observed. These findings indicate that the γ-Fe_2O_3@SiO_2

https://doi.org/10.3390/pr14060902

abrasive particles exhibit excellent durability and performance stability under repeated use in the CMP process [22].

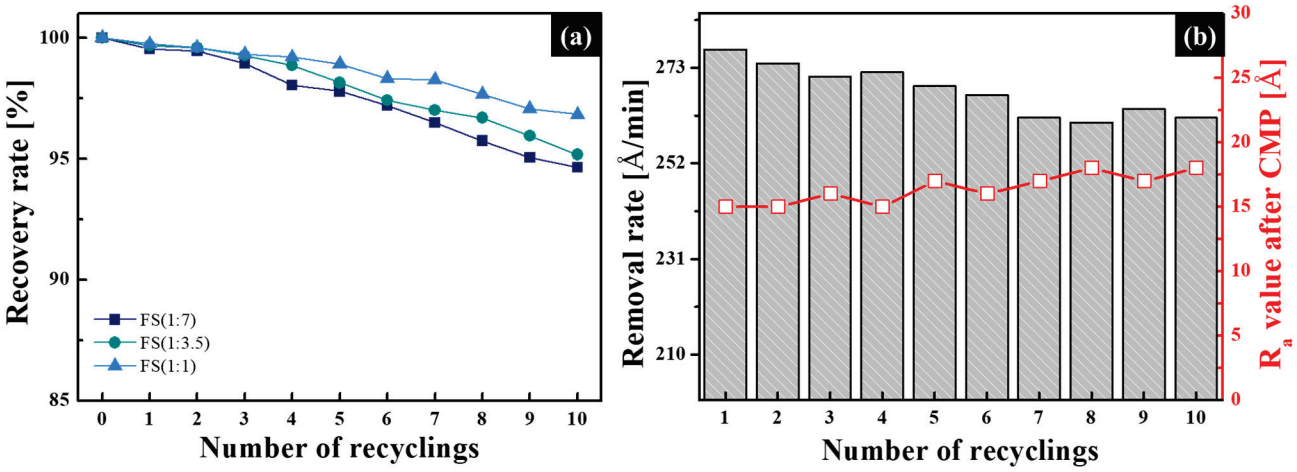


Figure 7. (**a**) Recovery rates of γ-Fe_2O_3@SiO_2 NPs after CMP evaluation, (**b**) W removal rates and roughness R_a values after CMP evaluation for varying reuse cycles of FS_(1:1) particles.

4. Conclusions

In this study, γ-Fe_2O_3@SiO_2 core–shell abrasive particles were synthesized and systematically evaluated for W CMP processes. The evaluation focused on how SiO_2 shell thickness influences physicochemical properties and polishing performance. The SiO_2 shell thickness was precisely controlled by varying the amount of the TEOS precursor during synthesis. FT-IR analysis confirmed the successful coating of silica through characteristic Si–O–Si and Si–OH bonding vibrations, whereas TEM imaging clearly revealed a distinct core–shell structure and uniform shell growth.

Zeta potential, PSD, and PDI measurements revealed that increasing shell thickness enhanced the surface negative charge due to additional –OH groups. This enhancement subsequently improved the dispersion stability. VSM analysis indicated that the superparamagnetic nature of the particles was retained, whereas the magnetic saturation decreased with thicker shells.

CMP performance tests demonstrated that the particles with a 14 nm thick SiO_2 shell achieved the highest W removal rate and lowest surface roughness among the tested samples. Furthermore, magnetic separation enabled the efficient recovery and reuse of the particles without noticeable degradation in the polishing performance over repeated cycles.

This study presents a promising design strategy for environmentally sustainable CMP abrasives by integrating superparamagnetic cores with tunable silica shells. These findings provide practical insights for the development of high-performance recyclable abrasive materials suitable for advanced semiconductor manufacturing.

Author Contributions: Conceptualization, methodology, validation, formal analysis, investigation, data curation, writing—original draft preparation, and visualization, Y.S.K.; writing—review and editing, resources, and supervision, G.S.A. All authors have read and agreed to the published version of the manuscript.

Funding: This work was supported by Kyonggi University Research Grant 2023.

Data Availability Statement: Data are contained within the article.

Conflicts of Interest: The authors declare no conflicts of interest.

https://doi.org/10.3390/pr14060902

Abbreviations

The following abbreviations are used in this manuscript:

CMP	Chemical mechanical planarization
IC	Integrated circuit
RR	Removal rate
TEOS	Tetraethyl orthosilicate
PSD	Particle size distribution
PDI	Polydispersity index

References

1. Luo, J.; Dornfeld, D.A. Material Removal Mechanism in Chemical Mechanical Polishing: Theory and Modeling. *IEEE Trans. Semicond. Manuf.* **2001**, *14*, 112–133. [CrossRef]
2. Laurent, S.; Forge, D.; Port, M.; Roch, A.; Robic, C.; Elst, L.V.; Muller, R.N. Magnetic Iron Oxide Nanoparticles: Synthesis, Stabilization, Vectorization, Physicochemical Characterizations, and Biological Applications. *Chem. Rev.* **2008**, *108*, 2064–2110. [CrossRef] [PubMed]
3. Venkataswamy, R.; Trimble, L.; McDonald, A.; Nevers, D.; Bengochea, L.V.; Carswell, A.; Rossner, A.; Seo, J. Environmental impact assessment of chemical mechanical planarization consumables: Challenges, future needs, and perspectives. *ACS Sustain. Chem. Eng.* **2024**, *12*, 11841–11855. [CrossRef]
4. Liu, L.; Zhang, Z.; Wu, B.; Hu, W.; Meng, F.; Li, Y. A review: Green chemical mechanical polishing for metals and brittle wafers. *J. Phys. D Appl. Phys.* **2021**, *54*, 373001. [CrossRef]
5. Wu, Z.; Cheng, J.; Yu, Z.; Zhou, W.; Li, Y.; Cao, J.; Sun, W.; Yuan, S.; Yang, D. Challenges, development and future of silica abrasives in chemical mechanical polishing derived from past six decades. *J. Semicond.* **2025**, *47*, 041301.
6. Bruce, I.J.; Sen, T. Surface Modification of Magnetic Nanoparticles with Alkoxysilanes and Their Application in Magnetic Bioseparations. *Langmuir* **2005**, *21*, 7029–7035. [CrossRef]
7. Itoh, H.; Sugimoto, T. Systematic control of size, shape, structure, and magnetic properties of uniform magnetite and maghemite particles. *J. Colloid Interface Sci.* **2003**, *265*, 283–295. [CrossRef]
8. Lu, A.-H.; Salabas, E.L.; Schüth, F. Magnetic Nanoparticles: Synthesis, Protection, Functionalization, and Application. *Angew. Chem. Int. Ed.* **2007**, *46*, 1222–1244. [CrossRef]
9. DeNardis, D.; Sorooshian, J.; Habiro, M.; Rogers, C.; Philipossian, A. Tribology and Removal Rate Characteristics of Abrasive-Free Slurries for Copper CMP Applications. *Jpn. J. Appl. Phys.* **2003**, *42*, 6809–6814. [CrossRef]
10. Seo, J.; Hur, J.U.; Kim, S.; Kim, Y.S.; Kim, Y.H.; Bae, K.; Lee, K.; An, G.S. Recovery and reuse of magnetic silica-coated iron oxide particles for eco-friendly chemical mechanical planarization. *Colloids Surf. A Physicochem. Eng. Asp.* **2024**, *694*, 134064. [CrossRef]
11. Stöber, W.; Fink, A.; Bohn, E. Controlled growth of monodisperse silica spheres in the micron size range. *J. Colloid Interface Sci.* **1968**, *26*, 62–69. [CrossRef]
12. Jung, J.H.; An, G.S. Fabrication of Core−Shell γ-Fe2O3@SiO2 Nanoparticles for Plasmid DNA Purification. *ACS Appl. Nano Mater.* **2023**, *6*, 19423–19430. [CrossRef]
13. Guerrero-Martínez, A.; Pérez-Juste, J.; Liz-Marzán, L.M. Recent Progress on Silica Coating of Nanoparticles and Related Nanomaterials. *Adv. Mater.* **2010**, *22*, 1182–1195. [CrossRef]
14. Ein-Eli, Y.; Starosvetsky, D. Review on copper chemical-mechanical polishing (CMP) and post-CMP cleaning in ultra large system integrated (ULSI)—An electrochemical perspective. *Electrochim. Acta* **2007**, *52*, 1825–1838. [CrossRef]
15. Tartaj, P.; del Puerto Morales, M.; Veintemillas-Verdaguer, S.; González-Carreño, T.; Serna, C.J. The preparation of magnetic nanoparticles for applications in biomedicine. *J. Phys. D Appl. Phys.* **2003**, *36*, R182–R197. [CrossRef]
16. Teja, A.S.; Koh, P.-Y. Synthesis, properties, and applications of magnetic iron oxide nanoparticles. *Prog. Cryst. Growth Charact. Mater.* **2009**, *55*, 22–45. [CrossRef]
17. Lu, Y.; Yin, Y.; Mayers, B.T.; Xia, Y. Modifying the Surface Properties of Superparamagnetic Iron Oxide Nanoparticles through A Sol-Gel Approach. *Nano Lett.* **2002**, *2*, 183–186. [CrossRef]
18. Mao, M.; Chen, W.; Liu, J.; Hu, Z.; Qin, C. Chemical mechanism of chemical mechanical polishing of tungsten cobalt cemented carbide inserts. *Int. J. Refract. Met. Hard Mater.* **2020**, *88*, 105179. [CrossRef]
19. Palla, B.J.; Shah, D.O. Stabilization of High Ionic Strength Slurries Using Surfactant Mixtures: Molecular Factors That Determine Optimal Stability. *J. Colloid Interface Sci.* **2002**, *256*, 143–152. [CrossRef]
20. Liu, J.; Niu, X.; Jia, Y.; Zhan, N.; Zou, Y.; Shi, Y.; Zhou, J. Chemical mechanical polishing for copper films in integrated circuit wiring layers using an advanced slurry. *Tribol. Int.* **2024**, *198*, 109832. [CrossRef]

https://doi.org/10.3390/pr14060902

21. Seo, Y.-J.; Lee, W.-S. Effects of different oxidizers on the W-CMP performance. *Mater. Sci. Eng. B* **2005**, *118*, 281–284. [CrossRef]
22. Du, T.; Vijayakumar, A.; Desai, V. Effect of hydrogen peroxide on oxidation of copper in CMP slurries containing glycine and Cu ions. *Electrochim. Acta* **2004**, *49*, 4505–4512. [CrossRef]

Disclaimer/Publisher's Note: The statements, opinions and data contained in all publications are solely those of the individual author(s) and contributor(s) and not of MDPI and/or the editor(s). MDPI and/or the editor(s) disclaim responsibility for any injury to people or property resulting from any ideas, methods, instructions or products referred to in the content.

https://doi.org/10.3390/pr14060902

processes

MDPI

Article

A Proposal for the Incorporation of Temperature into the Langmuir Model in Adsorption Isotherms

Ana Paula Souza de Sousa [1], Haianny Beatriz Saraiva Lima [1], Deibson Silva da Costa [2], Emerson Cardoso Rodrigues [3], Caroline Borges Agustini [4], Liliana Amaral Féris [4] and Diego Cardoso Estumano [5,*]

[1] Graduate Program in Chemical Engineering, Federal University of Pará, Belém 66075-110, PA, Brazil; anaps.souz@gmail.com (A.P.S.d.S.); hamylima@gmail.com (H.B.S.L.)
[2] Faculty of Materials Engineering, Federal University of Pará, Ananindeua 67130-660, PA, Brazil; deibson@ufpa.br
[3] Faculty of Chemical Engineering, Institute of Technology, Federal University of Pará, Belém 66075-110, PA, Brazil; ecr@ufpa.br
[4] Graduate Program in Chemical Engineering, Federal University of Rio Grande do Sul, Porto Alegre 90035-007, RS, Brazil; caroline.agustini@ufrgs.br (C.B.A.); liliana.feris@gmail.com (L.A.F.)
[5] Simulation and Computational Biology Laboratory, High Performance Computing Center, Federal University of Pará, Belém 66075-110, PA, Brazil
* Correspondence: dcestumano@ufpa.br

Abstract: Adsorption is a frequently used technique for pollutant removal due to its efficiency and versatility. Mathematical modeling of these processes enables understanding of adsorbent and adsorbate interactions and prediction of system dynamics, especially when experimental data are limited. Among adsorption isotherm models, the Langmuir model is one of the most applied; however, its formulation does not explicitly consider temperature variation, limiting predictive capability in practical applications. This article proposes an adaptation of the Langmuir model by incorporating temperature dependence, enabling inference of isotherms at temperatures without experimental data. The model was first validated using data from the literature at different temperatures, considering the adsorption of amoxicillin, phosphate, methylene blue, and caffeine. Subsequently, it was applied to experimental data of copper ion adsorption by 5A zeolite obtained in this work, allowing estimation of Q_{max} and K_L. Based on these estimates, hypotheses regarding their temperature dependence were formulated, and isotherms at 55 °C, 65 °C, and 75 °C were inferred and compared with experimental data. Finally, the model was applied to infer isotherms from 25 °C to 95 °C, demonstrating its ability to represent experimental dynamics and predict adsorption at temperatures without available data, contributing to the analysis and optimization of adsorption processes.

Keywords: batch adsorption; Bayesian inference; Markov Chain Monte Carlo; model proposal

1. Introduction

The removal of different types of organic and inorganic compounds, such as heavy metals and pharmaceuticals present in industrial and domestic effluents, represents a major environmental challenge due to the high toxicity of these compounds and their adverse impacts on both the environment and public health. From this perspective, there is a continuous pursuit of effective technologies for the removal of these contaminants. Among the different existing techniques, adsorption stands out as a viable method employed for the removal of various types of compounds, in which adsorbent solids retain

molecules on their surface through molecular interactions, enabling the separation of components [1–4].

In adsorption isotherms, knowledge of the mechanisms governing the interaction between adsorbent and adsorbate, such as monolayer formation, surface heterogeneity of the adsorbent, and the strength of interaction forces, is essential to understanding system performance and to determining ideal conditions for the process. In this context, the use of isotherm models becomes fundamental to describe these mechanisms, as they allow the interpretation of the process using experimental data [5,6]. Several studies have applied such models to estimate parameters in different systems; however, isotherms obtained at different temperatures are usually fitted independently, without explicitly considering temperature dependence in the equations [7–10].

Din et al. (2024) [7] and Gyawali et al. (2023) [8] applied parameter estimation of isotherm models to experimental data of arsenic adsorption with biochar and pomelo peel, respectively. Hung et al. (2023) [9] and Rasheed et al. (2024) [10] investigated the adsorption dynamics of metal ions (Co^{2+}, Sr^{2+}, and Cs^{2+}) and cobalt with Fe_3O_4 nanoparticles and quartz rock, respectively, by means of parameter estimation of the Langmuir, Freundlich, and Temkin models.

However, the isotherm models employed do not include temperature as a parameter in their equations, which prevents the prediction of isotherms at different temperatures based on the available data. A predictive model allows optimization of processes under different operational conditions [11,12]. In adsorption processes, estimating isotherms at different temperatures can contribute to greater efficiency in pollutant removal, facilitating the adaptation of effluent treatment systems to different environmental and industrial scenarios.

In this context, this study proposes an adaptation of the Langmuir isotherm model by incorporating a temperature term into the equation. This proposal consists of the formulation of hypotheses derived from isolated estimations of model parameters using experimental data from different adsorption dynamics, encompassing the stages of calibration, model validation, and inference of isotherms over a wide temperature range.

2. Methodology

The present study was developed through the following two main stages: the proposal and calibration of the model using experimental data from the literature (Table 1), followed by the application and validation of the model using experimental data of copper ion adsorption by zeolite 5A obtained in this work.

Table 1. Experimental data used in the proposal and calibration of the predictive model.

Adsorbate	Adsorbent	Temperature (°C)	References
Adsorption of Amoxicillin	Bentonite	30, 40 and 50	[13]
Adsorption of Phosphate	Dolomite	25, 35 and 45	[14]
Adsorption of Methylene Blue	Residue Char	30, 35 and 40	[15]
Adsorption of Caffeine	Activated Carbon	15, 25 and 40	[16]

The first stage consisted of the use of four sets of experimental data from the literature, whose isotherms, obtained at different temperatures, showed an increase in the amount adsorbed as a function of increasing temperature. These are presented in Table 1.

Subsequently, the parameters of the Langmuir model were estimated using the experimental isotherm data of each system (Table 1), considering the steps outlined in Figure 1.

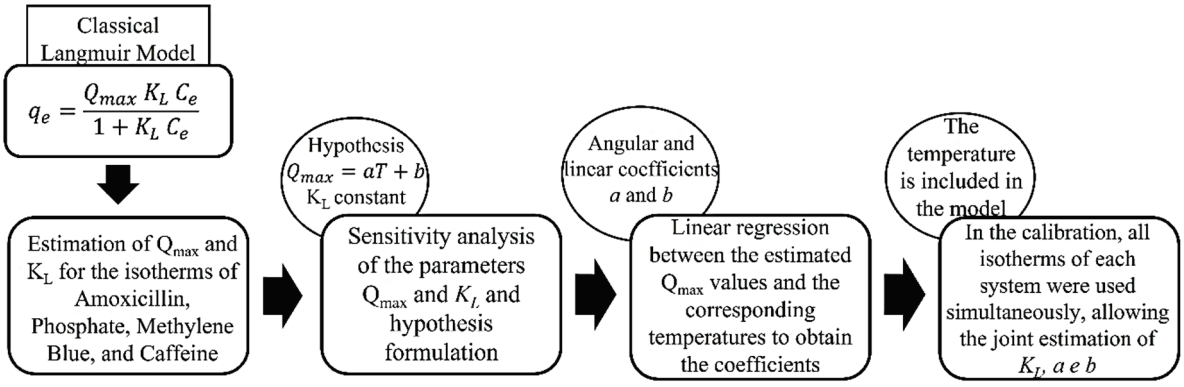


Figure 1. Steps performed for the Langmuir model adaptation.

For each system, the classical Langmuir model was considered, for which an initial estimate of the constant K_L was used, based on the order of magnitude of the original estimations. The maximum adsorption capacity (Q_{max}) was estimated for each temperature, restricted to a range between the highest experimentally adsorbed amount in each isotherm and up to 50% above this experimental limit. From these estimations, a sensitivity analysis of the model parameters was carried out, and the hypotheses that Q_{max} depends linearly on temperature while K_L is considered constant with respect to temperature were proposed. Subsequently, linear regression was applied between the estimated values of Q_{max} and the respective temperatures (in Kelvin) to obtain the coefficients of the proposed adaptation.

Thus, the parameters K_L, a, and b obtained were used as initial estimates in a new simulation via Markov Chain Monte Carlo (MCMC). In this stage, the calibration was conducted considering all the isotherms of each system simultaneously, since the incorporation of temperature into the model made it possible to perform the joint estimation of the parameters K_L, a, and b.

2.1. Proposed Adaptation of the Langmuir Model

The Langmuir model is based on principles involving the presence of a fixed number of adsorption sites, where the energy of the sites is uniform and the adsorbed molecules do not interact with each other, so each site has the same capacity to attract adsorbate molecules; adsorption occurs in a single layer, meaning that only one layer of adsorbed molecules can form on the adsorbent surface; and finally, each site accommodates only one molecule, with no interaction between already adsorbed molecules [17].

When a solution comes into contact with the adsorbent and the system reaches equilibrium, this state is characterized by the equality of the adsorption and desorption rates of molecules or ions on the adsorbent surface. This suggests that if the adsorption rate is directly proportional to the adsorbate concentration in the fluid and to the fraction of the adsorbent surface area that remains vacant, the adsorption and desorption rates can be defined [18–20], as follows:

$$Adsorption\ rate\ =\ K_1 C_e\ (1\ -\ \theta) \tag{1}$$

$$Desorption\ rate = K_2 \theta \tag{2}$$

where K_1 is the adsorption constant, K_2 is the desorption constant, C_e is the adsorbate concentration in the fluid, and θ is the fraction of the surface occupied.

Assuming that all sites on the adsorbent surface have the same energy, the parameter K_1 assumes a uniform value, and assuming that adsorption occurs in a monolayer, the adsorption rate is directly proportional to $1 - \theta$, indicating that adsorption will be complete

when θ = 1. Once the system is at equilibrium, the two rates can be equated according to Equation (3).

$$K_1 C_e\ (1 - \theta) = K_2 \theta \tag{3}$$

Isolating θ and considering K_L as the ratio between K_1 and K_2, Equation (4) is obtained.

$$\theta = \frac{K_L\ C_e}{1 + K_L C_e} \tag{4}$$

Since θ represents the fraction of the surface occupied by the adsorbate, q_e is the amount of adsorbate retained at equilibrium per unit mass of adsorbent, and Q_{max} is the maximum adsorption capacity (when all sites are occupied), the following relationship can be established:

$$\theta = \frac{q_e}{Q_{max}} \tag{5}$$

Finally, expressing the process in terms of the amount of solute adsorbed (q_e) per unit mass of adsorbent and considering that q and θ are proportional, the Langmuir equation is obtained, as follows:

$$q_e = \frac{Q_{max} K_L C_e}{1 + K_L C_e} \tag{6}$$

In Equation (6), q_e represents the amount of solute adsorbed per gram of adsorbent at equilibrium (mg/g), Q_{max} is the maximum adsorption capacity of the adsorbent (mg/g), K_L represents the adsorbate/adsorbent interaction constant (L/mg), and C_e is the equilibrium concentration of the adsorbate (mg/L).

In the Langmuir model, temperature is not included as a parameter in the equation, which hinders the prediction of isotherms at temperatures not experimentally studied. Therefore, considering the experimental data of the isotherms and based on the sensitivity analysis of the parameters K_L and Q_{max}, hypotheses were formulated within the temperature range in which experimental data were obtained: the parameter K_L was considered constant, that is, independent of temperature, and the maximum adsorption capacity was expressed as a linear equation as a function of temperature (Equation (7)).

$$Q_{max} = aT + b \tag{7}$$

where a is the angular coefficient (mg/g.K) and b (mg/g) is the linear coefficient, determined by linear regression of the estimated Q_{max} data as a function of temperature in Kelvin (K).

Sensitivity analysis is essential to evaluate how parameter variations influence the model response. In this context, sensitivity coefficients with large magnitudes indicate that small variations in the parameters lead to large changes in the response. On the other hand, coefficients with low magnitude suggest that the response variable is not significantly affected by parameter variations [21]. The sensitivity coefficient was calculated according to Equation (8), as follows:

$$X_{ij} = P_j \frac{\partial q_i^{exp}}{\partial P_j} \tag{8}$$

where X_{ij} represents the reduced sensitivity coefficient, P_j is the parameter, and q_i^{exp} is the observable state variable.

As part of the formulation of the proposed model, hypotheses of a linear dependence of the parameter Q_{max} on temperature and of a constant K_L throughout the thermal range were adopted based on the trends observed in the individual estimates obtained for each isotherm of each studied system, including both the literature datasets and the experimental data obtained in this work. These trends indicated systematic variations for Q_{max} and no

apparent trend for K_L. These hypotheses are later evaluated and confirmed in the Results and Discussion section, where the parameter sensitivity and the experimental dynamics reinforce their adequacy.

2.2. Bayesian Techniques—Markov Chain Monte Carlo (MCMC)

The Langmuir model is defined by two parameters, $P^T = [K_L, Q_{max}]$. Among these, the constant K_L cannot be determined directly through experimental observation, and if the system does not reach equilibrium or saturation, the value of Q_{max} will also not be experimentally obtained. Similarly, in the adaptation proposed in this work, the parameters $P^T = [K_L$ a b], inherent to the formulation that incorporates the dependence of Q_{max} on temperature, also cannot be determined directly by experimentation, and must be estimated using appropriate methods.

Due to the difficulty of direct observation of the parameters, the Bayesian technique Markov Chain Monte Carlo (MCMC) was chosen, as it is an approach capable of integrating prior information about the problem and because of the effectiveness of Bayes' theorem in updating the model with such information, resulting in a more accurate solution [22]. In Bayes' theorem, presented in Equation (9), $\pi(\boldsymbol{P}|q_{exp})$ is the posterior probability distribution, and the information from the experimental data is inserted into the likelihood function $\pi(q_{exp}|\boldsymbol{P})$, while π (**P**) represents the prior probability distribution of the parameters [22–25].

$$\pi(\boldsymbol{P}|q_{exp}) \propto \pi(q_{exp}|\boldsymbol{P})\ \pi(\boldsymbol{P}) \tag{9}$$

It is assumed that the likelihood follows a Gaussian distribution for the experimental data, under the assumption that the measurements are independent, as expressed in Equation (10). Thus, σ_T^2 represents the variance associated with measurement uncertainty; q_{sim} is the solution of the forward model calculated with the parameters to be estimated; q_{exp} is the measured value; and **P** is the value of the parameters of interest.

$$\pi(q_{exp}|\boldsymbol{P}) = \frac{1}{\left(2\pi\sigma_T^2\right)^{\frac{-n_{obs}}{2}}} exp\left(-\frac{\left(q_{exp}-q_{sim}(\boldsymbol{P})\right)^T\left(q_{exp}-q_{sim}(\boldsymbol{P})\right)}{2\sigma_T^2}\right) \tag{10}$$

In the application of the MCMC method, the Metropolis–Hastings algorithm proposed by Metropolis et al. (1953) [26] and Hastings (1970) [27] was used. This algorithm is based on the acceptance–rejection method and adheres to the following steps [28–30]:

1. The number of states of the Markov chain (n) is chosen, indicating the number of simulations;
2. The chain iteration counter is initialized (i = 0) and an initial value $P^{(0)}$ is chosen;
3. A candidate value **P*** is generated from the distribution $P(\mathbf{P}^* \mid \mathbf{P}^{(i)})$, obtained according to Equation (11), as follows:

$$\boldsymbol{P}^* = \boldsymbol{P}^{(i)}(1 + \boldsymbol{w}\varepsilon) \tag{11}$$

where **w** is the search step and ε is a random variable resulting from a Gaussian distribution N(0,1).

4. The acceptance probability $\alpha(\mathbf{P}^{(i)} \mid \mathbf{P}^*)$ of the candidate value is obtained using Hastings' equation (Equation (12)), as follows:

$$\alpha\left(\boldsymbol{P}^*\middle|\boldsymbol{P}^{(i)}\right) = \min\left[1, \frac{\pi\left(\boldsymbol{P}^*\middle|q_{sim}\right)\ p\left(\boldsymbol{P}^{(i)}\middle|\boldsymbol{P}^*\right)}{\pi\left(\boldsymbol{P}^{(i)}\middle|q_{sim}\right)\ p\left(\boldsymbol{P}^*\middle|\boldsymbol{P}^{(i)}\right)}\right] \tag{12}$$

where $\pi(P^*|q_{sim})$ is the posterior probability distribution.

5. An auxiliary random sample is generated from a uniform distribution u~U(0,1).
6. If u $\leq$ α ($P^{(i)}$ | P*), the new value is accepted and one sets $P^{(i+1)}$ = P*. Otherwise, P* is rejected and one sets $P^{(i+1)} = P^{(i)}$.
7. The counter is incremented (i to I + 1) and the procedure returns to step 3.

Figure 2 presents a flowchart illustrating the operation of the Metropolis–Hastings algorithm used in this study for the parameter estimation of the adapted Langmuir model.

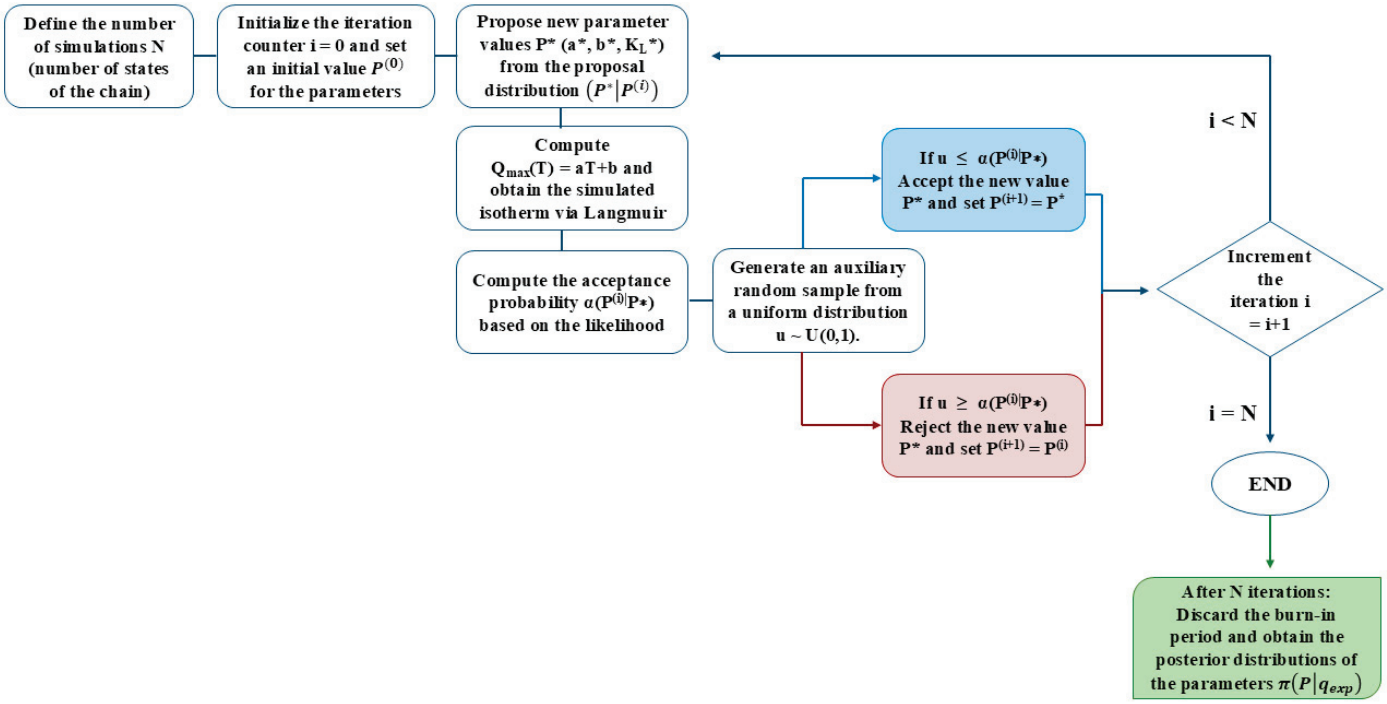


Figure 2. Metropolis–Hastings algorithm flowchart.

The quality of the simulated data relative to the experimental data was assessed using classical statistical metrics, such as the coefficient of determination (R^2) and the root mean square error (RMSE), as described in Equations (13) and (14). Accordingly, R^2 values close to 1 indicate a good agreement of the model in relation to the experimental data, while lower RMSE values reflect smaller residual dispersion and, therefore, better fit.

$$R^2 = 1 - \frac{SSE}{SST} = 1 - \frac{\sum_{i=1}^{n_{obs}} (q_{exp} - q_{sim})}{\sum_{i=1}^{n_{obs}} (q_{exp} - \overline{q_{exp}})^2} \quad (13)$$

$$RMSE = \sqrt{\left(\frac{1}{n_{obs}} \sum_{i=1}^{n_{obs}} (q_{exp} - q_{sim})^2 \right)} \quad (14)$$

In Equations (13) and (14), SSE represents the sum of squared errors, SST is the total sum of squares, q_{exp} is the observed data up to the number of sample observations (n_{obs}), q_{sim} is the estimated data, and q_{exp} is the mean of the observed data.

2.3. Application of the Model to Copper Ion Adsorption by Zeolite 5A

In this section, the same numerical methodology is applied to the process of copper ion adsorption by zeolite 5A, now using experimental data obtained in this study, complementing the previous stage in which data from the literature were employed. The isotherms were conducted at temperatures of 25 °C, 35 °C, 45 °C, 55 °C, 65 °C, 75 °C, 85 °C, and

95 °C. To obtain these experimental data, the adsorbent material was first produced, followed by the performance of experimental adsorption isotherm tests.

In the preparation of the adsorbent, zeolite 5A was obtained by ion exchange of zeolite 4A with a calcium chloride solution (2.6 N) for 8 h at a temperature of 100 °C, under constant stirring at 700 RPM. For the isotherm tests, the adsorbent was calcined in a muffle furnace at 400 °C for 2 h to release the sites and remove moisture.

The copper ion solution was prepared from a copper sulfate solution with a concentration of 2.5 g/L, with pH adjusted to 5 to prevent Cu^{2+} precipitation and to promote its interaction with the negatively charged sites of the adsorbent [31,32]. The solution was conditioned to obtain different concentrations ranging between 150 ppm and 2500 ppm, corresponding to the adsorption isotherm points, and for each adsorption test, standard solutions were prepared in the same concentration range. The batch experiments were carried out in 250 mL Erlenmeyer flasks containing 0.1 g of zeolite 5A and 100 mL of the copper sulfate solution, kept on a shaker table (at 150 RPM) for 2 h. After equilibrium was reached, the samples were filtered and analyzed by UV-Vis spectrophotometry, with copper absorbance readings taken at a wavelength of 800 nm.

Subsequently, the experimental data were used to estimate the model parameters following the same steps described previously (Figure 1), with the addition of validation and later prediction of isotherms at different temperatures, using the following steps:

(a) Step 1: Five experimental isotherms of copper ion adsorption (25 °C, 35 °C, 45 °C, 85 °C, and 95 °C) were selected for model calibration. Based on the estimated values of Q_{max} at these temperatures, a linear regression was performed to estimate the coefficients a and b. The parameter K_L was considered constant according to the previously performed sensitivity analysis.
(b) Step 2: Using the parameter estimates obtained in Step 1, isotherms at 55 °C, 65 °C, and 75 °C were simulated to evaluate the agreement between the simulated data from the calibrated model and the experimental data, noting that the simulated data did not include the experimental data in the inference process, being used only for later comparison.
(c) Step 3: The proposed model was used for the prediction of isotherms in the temperature range from 25 °C to 95 °C.

3. Results and Discussion

In this section, the results obtained from the calibration, validation, and application of the proposed model are presented. Four sets of experimental data were fitted to the Langmuir model, enabling the individual estimation of the parameters Q_{max} and K_L at different temperatures. Then, the hypotheses of K_L being constant and Q_{max} being a linear function of temperature were adopted. Taking these assumptions into account, an adaptation to the Langmuir model was proposed, explicitly incorporating temperature, which allowed the joint calibration of all isotherms of each system. Subsequently, this methodology was applied to the experimental data of copper ion adsorption by zeolite 5A, obtained at different temperatures in this work, integrating validation with data not used in calibration, as well as predictions for the studied temperature range, demonstrating the applicability of the model to simulate isotherms under untested conditions.

In the application of the parameter estimation method, a variance of 1% of the maximum experimental measurement (q_{exp}) was considered for the experimental uncertainty, related to the amount of adsorbate adsorbed in the isotherms. The number of states of the Markov chain (N) was set to 10,000, and the search step (**w**) used was 0.003, ensuring the stabilization of the chains.

Thus, for parameter estimation by the MCMC method using the Metropolis–Hastings algorithm, based on the acceptance/rejection method, a uniform prior probability distribution was employed. The lower bound was established at zero, since physically, all parameters must be positive, and for the upper bound, a value considered sufficiently high was chosen, where it is expected that the probability of the value lies within this interval.

The choice of a uniform prior probability distribution (Equation (15)) is justified by the lack of prior knowledge about the parameters, allowing all values to have an equal probability of being chosen.

$$Prior = Uniform\left(0, 10\boldsymbol{P}^{ref}\right) \tag{15}$$

The definition of the posterior probability distribution was carried out after verifying the convergence of the chains for the determination of the burn-in states. Thus, a burn-in period corresponding to 90% of the number of Markov chain states was considered, so that only the final 10% were used in the analysis of the posterior probability distributions. Moreover, the credibility interval, used to provide an estimate of the uncertainty in the adjusted parameters, indicating the probability that the true value of the parameters lies within this interval, was set at 95%. Table 2 presents the elements employed for the application of MCMC in parameter estimation.

Table 2. Fundamental elements employed in parameter estimation.

Parameter Estimation by MCMC	
Variance (Uncertainty)	1% max (q_{exp})
States of the Markov chain (N)	10,000
Search Step (w)	0.003
Credibility Interval	95%
Prior	$Prior = Uniform\left(0, 10\boldsymbol{P}^{ref}\right)$

The four datasets from the literature were initially fitted to the classical Langmuir model (Equation (6)) individually for each temperature. For each system (Table 1), an initial estimate of the K_L constant was adopted, based on the order of magnitude of the estimates originally reported in the respective studies. The maximum adsorption capacity (Q_{max}) at each temperature for each system was estimated using the Markov Chain Monte Carlo (MCMC) method, considering that this parameter is restricted to an interval between the value corresponding to the highest experimentally observed adsorbed amount in each isotherm and, at most, 50% above this value. This choice is justified because, in some systems, the experimental isotherms did not reach the saturation region, making it impossible to directly identify Q_{max}. Thus, defining an upper limit 50% above the highest experimental value ensures that the MCMC explores a physically plausible region, preventing estimates that are incompatible with the observed dynamics. This value proved to be sufficiently broad to allow variability in the estimates without compromising physical plausibility or the stability of the Markov chains.

In addition, a sensitivity analysis of the parameters Q_{max} and K_L was performed for each isotherm of each system. The graphs corresponding to the sensitivity coefficients (Equation (8)) are presented in the Supplementary Materials (Figure S1), allowing assessment of the influence of each model parameter.

In general, it was observed that Q_{max} presented a high magnitude in relation to the experimental data, evidencing a significant influence on the isotherm dynamics. On the other hand, the model constant (K_L) exhibited a low magnitude, indicating little influence on the response, which justifies the hypothesis of being considered constant. This behavior

was consistent across all datasets, supporting the hypothesis that K_L can be considered constant within the evaluated temperature range.

From the individual fittings of the isotherms and the sensitivity analyses, it was possible to establish the hypotheses adopted in the proposed model. For the parameter Q_{max}, the estimated values exhibited a monotonic and linear increase with temperature across all evaluated systems, including both the literature datasets and the experimental results obtained in this work. The linear regressions presented coefficients of determination confirming that this relationship is sufficient to represent the system dynamics within the studied temperature range.

Regarding the parameter K_L, its reduced sensitivity was low in all analyzed systems, as evidenced by the low magnitude of its reduced sensitivity coefficient, indicating minimal influence on the isotherm dynamics across the evaluated temperatures. Thus, no variation was observed that would justify formulating an explicit temperature dependence for this parameter. Therefore, the assumption of a constant K_L emerged directly from the experimental dynamics, providing consistency to the calibration process.

Table 3 presents the Q_{max} and K_L values estimated through MCMC for each system, while the equilibrium curve fittings obtained for the evaluated systems of amoxicillin, phosphate, methylene blue, and caffeine adsorption are shown in the Supplementary Materials (Figure S2). According to the studies used in the model proposal, and as reported by Wu et al. (2022) [33], Liu et al. (2024) [31], Hung et al. (2023) [9], and Rasheed et al. (2024) [10], the adsorption capacity (Q_{max}) estimated by the Langmuir model showed relevant variations as a function of temperature. This dynamic reinforces the importance of strategies that explicitly incorporate temperature into model equations, as a means to improve the descriptive and predictive capability of the model under different operational conditions.

Table 3. Estimates of Q_{max} and K_L obtained through MCMC for each system, with Q_{max} estimated individually for each temperature and the same K_L.

Adsorption of Amoxicillin				**Adsorption of Phosphate**				**Adsorption of Methylene Blue**				**Adsorption of Caffeine**			
Temp. (°C)	**Q_{max} (mg/g)**	**R^2**	**RMSE**	**Temp. (°C)**	**Q_{max} (mg/g)**	**R^2**	**RMSE**	**Temp. (°C)**	**Q_{max} (mg/g)**	**R^2**	**RMSE**	**Temp. (°C)**	**Q_{max} (mg/g)**	**R^2**	**RMSE**
30 °C	34.69	0.96	1.12	**25 °C**	2.12	0.99	0.07	**30 °C**	89.26	0.74	3.92	**15 °C**	13.24	0.96	0.82
40 °C	57.64	0.99	1.03	**35 °C**	2.22	0.98	0.09	**35 °C**	90.83	0.89	2.18	**25 °C**	19.95	0.95	1.42
50 °C	78.52	0.97	2.39	**45 °C**	2.29	0.96	0.13	**40 °C**	97.25	0.87	2.66	**40 °C**	24.11	0.93	1.77
K_L (L/mg) = 0.02				K_L (L/mg) = 0.14				K_L (L/mg) = 2.45				K_L (L/mg) = 0.03			

From the sensitivity analysis, in the first stage, it was established in the estimation process that the parameter K_L should remain constant for all isotherms at different temperatures. Furthermore, it was verified that the Q_{max} values estimated in this study were consistent with those reported experimentally in the original articles. For example, at higher temperatures, Jurado Davila et al. (2023) [14] observed about 2.3 mg/g (R^2 = 0.97) for phosphate, Cheng et al. (2020) [15] reported 95.24 mg/g (R^2 = 0.96) for methylene blue, and Oliveira et al. (2024) [16] indicated approximately 20.26 mg/g (R^2 = 0.98) for caffeine. This occurred partly due to the range defined for the estimates (between the experimental value and up to 50% above it), which provided flexibility to the model to accommodate variations arising from the stochastic nature of the MCMC process.

It is worth noting that the coefficients of determination (R^2) obtained in the individual fittings of each isotherm were, in some cases, lower than the values reported in the original studies. This difference was expected, since the present work imposed restrictions on the Q_{max} values to ensure physical consistency among the isotherms and reduce the risk

of inconsistencies, whereas in the original fittings, the models had complete freedom to fit exclusively to the experimental data. For instance, for the phosphate system, the R^2 values were 0.99 and 0.97 (25 and 45 °C), while in this study, they were close, ranging between 0.98 and 0.96. For methylene blue, the original values were 0.95 and 0.94 (30 and 35 °C), whereas the estimates obtained here presented lower values, such as 0.75 and 0.88, reflecting the greater dispersion in the experimental data of this system. In the case of caffeine, R^2 reached up to 0.988 (40 °C), while in this work, it ranged between 0.96 and 0.93.

After the initial estimates, based on the Q_{max} values estimated (Table 3), linear regression as a function of temperature (in Kelvin) was performed for each dataset ($Q_{max} = aT + b$), as presented in the Supplementary Materials (Figure S3), which shows the relationship between the individually estimated Q_{max} values and the line obtained by regression. The model proposed in this article was calibrated for each system, obtaining the coefficients a and b by regression, which are presented in Table 4.

Table 4. Estimates of parameters a, b, and K_L obtained through MCMC in the calibration step of the model with simultaneous fitting of the isotherms.

Adsorption of Amoxicillin			**Adsorption of Phosphate**			**Adsorption of Methylene Blue**			**Adsorption of Caffeine**		
K_L (L/mg) = 0.0182 **a (mg/g.K) = 2.2101** **b (mg/g) = −633.3110**			**K_L (L/mg) = 0.1440** **a (mg/g.K) = 0.0085** **b (mg/g) = −0.4208**			**K_L (L/mg) = 2.4718** **a (mg/g.K) = 0.7919** **b (mg/g) = −151.6459**			**K_L (L/mg) = 0.0313** **a (mg/g.K) = 0.4245** **b (mg/g) = −108.4988**		
Temp. (°C)	**R^2**	**RMSE**	**Temp. (°C)**	**R^2**	**RMSE**	**Temp. (°C)**	**R^2**	**RMSE**	**Temp. (°C)**	**R^2**	**RMSE**
30 °C	0.96	1.18	**25 °C**	0.99	0.07	**30 °C**	0.74	3.92	**15 °C**	0.94	1.02
40 °C	0.98	1.20	**35 °C**	0.98	0.09	**35 °C**	0.83	2.69	**25 °C**	0.92	1.77
50 °C	0.97	1.29	**45 °C**	0.96	0.13	**40 °C**	0.87	2.71	**40 °C**	0.94	1.71

The regressions showed coefficients of determination (R^2) ranging between 0.89 and 0.99, which indicates a good degree of fit to the experimental data. Even in cases where R^2 values were slightly lower (0.89 for methylene blue adsorption and 0.94 for caffeine adsorption), the linear function was considered adequate to represent the trend of Q_{max} variation as a function of temperature, maintaining physical consistency and coherence among the isotherms. In the study of Cheng et al. (2020) [15] (methylene blue adsorption), for example, the fittings reported in the original article already presented relatively modest R^2 values for each temperature (0.95 for 30 °C, 0.94 for 35 °C, and 0.96 for 40 °C), indicating that the experimental data already showed greater dispersion, which naturally influences the results of the joint regression of these data performed in this study.

Considering the adopted hypotheses and the coefficients a, b, and K_L previously obtained, the calibration step was performed for each dataset, aiming to infer prior knowledge of the process dynamics. In this step, the parameters were used as initial estimates in a new simulation using MCMC with the Metropolis–Hastings algorithm, allowing the posterior distributions to be obtained and the estimated values to be refined based on the simultaneous fitting of the isotherms at different temperatures. The simulated curves, presented in the Supplementary Materials (Figure S4), were then generated from this calibration, considering the dependence of Q_{max} on temperature and K_L as constant.

According to the comparison between the simulated and experimental curves (Figure S4), the results indicated a good fit of the adapted model to the isotherms, even with the adopted hypotheses. This reinforces the capability of the model to describe the system dynamics with a reduced number of parameters. The consideration of Q_{max} as a

linear function of temperature and K_L as constant enabled the simultaneous calibration of all evaluated isotherms, unlike the conventional approach, in which each isotherm is fitted individually. This strategy reduces the risk of inconsistencies and enhances the predictive capability of the model, since the influence of temperature is explicitly incorporated into the equation.

Furthermore, although the coefficients of determination (R^2) and the root mean square error (RMSE) obtained in the joint calibration step showed slightly lower and higher values, respectively, compared to the individual fittings, this is expected due to the constraints imposed on the model. While the isolated estimation of each isotherm provides greater freedom for the parameters to adjust to the experimental data, the adapted model introduces restrictions grounded in physically consistent hypotheses, promoting a more coherent representation of the overall system dynamics. These results demonstrate that the proposed methodology is potentially applicable to other adsorption systems that exhibit thermally dependent dynamics.

It is important to highlight that the differences between the R^2 values obtained in the individual fittings and those obtained in the joint fittings arise directly from the constraints introduced by the adapted model. In the individual fittings, the parameters have full freedom to be estimated and to adjust the simulation to the experimental data, which tends to result in higher R^2 values. In contrast, in the joint fitting, the parameters a and b, which describe the linear dependence of Q_{max} (T), are shared across all temperatures, reducing the model's degrees of freedom and consequently lowering the overall R^2. This reduction does not indicate inadequacy of the model, but is instead the natural consequence of imposing such restrictions and ensuring physical coherence among all evaluated isotherms, enabling the model to simultaneously represent the adsorptive dynamics of the system and provide predictive capability across the entire temperature range studied.

Application of the Model to Copper Ion Adsorption by Zeolite 5A

The same approach was applied to the experimental data obtained in the present work for copper ion adsorption by zeolite 5A. Initially, the Langmuir model parameters were estimated individually for each temperature, as is commonly addressed in the literature. Table 5 presents the estimates of the model parameters (Q_{max} and K_L), obtained individually, at temperatures of 25 °C, 45 °C, 55 °C, 65 °C, 75 °C, 85 °C, and 95 °C.

Table 5. Estimation of Langmuir isotherm parameters at different temperatures.

Parameter	25 °C	35 °C	45 °C	55 °C	65 °C	75 °C	85 °C	95 °C
Q_{max} (mg/g)	236.99	271.70	368.34	432.08	524.63	704.77	784.19	965.60
K_L (L/mg)	0.01	0.018	0.006	0.009	0.007	0.005	0.005	0.005
R^2	0.97	0.89	0.94	0.93	0.96	0.94	0.97	0.98
RMSE	7.81	16.06	21.96	26.74	24.11	36.61	30.19	36.09

According to Table 5, the Langmuir model exhibited good agreement with the experimental data, as most of the determination coefficients (R^2) assumed values above 0.9, indicating that the model represents more than 90% of the variability observed in the copper ion sorption isotherms under the established conditions. In parallel, the relatively low values of the root mean square error (RMSE), ranging between approximately 7.8 and 36.1 mg/g, reinforce the quality of the individual fittings. These results indicate that the average differences between the values predicted by the model and the experimental data were small, showing that the estimates of Q_{max} and K_L properly represented the system dynamics at all analyzed temperatures.

In addition, from the data in Table 5, an increase in the maximum sorption capacity was observed with an increasing temperature, indicating an endothermic process, which can be attributed to the greater kinetic energy of the molecules as temperature rises, facilitating the interaction between copper ions and the sorption sites [7,8].

The K_L constant represents the interaction between adsorbate and adsorbent, but it did not show a clear trend with respect to temperature, suggesting that the affinity between the ions and the sorption sites is not directly influenced by this parameter. Thus, due to the analysis of the dynamics and the sensitivity analysis of K_L and Q_{max} at the five temperatures (25 °C, 35 °C, 45 °C, 85 °C, and 95 °C), as shown in the Supplementary Materials (Figure S5), the premises for the predictive model of isotherms at temperatures not experimentally tested could be adopted.

According to the sensitivity coefficients (Figure S5), in general, it was observed that Q_{max} presented a high magnitude, evidencing a significant influence on the dynamics of the isotherms. On the other hand, the model constant (K_L) showed a low magnitude, indicating a minor influence on the response, which supports the same hypotheses previously adopted. Since the maximum adsorption capacity (Q_{max}) exhibits a linear dynamic with respect to temperature, the premise that the parameter is established by a linear equation (Equation (7)) to describe this dependence is justified.

Based on the definition of the hypotheses, a linear regression was applied to the Q_{max} data, once again estimated through MCMC (Table 6), respecting the previously adopted limits in which the parameter could not be lower than the experimental value observed for each isotherm nor greater than 50% above this value. Simultaneously, the K_L parameter was also estimated, using a value of the same order of magnitude as that obtained in the individual fittings of each isotherm as an initial guess (Table 5).

Table 6. Estimates of Q_{max} and K_L with Q_{max} of zeolite 5A estimated individually for each temperature.

25 °C	**Q_{max} (mg/g)**	262.00
	R^2	0.89
	RMSE	15.74
45 °C	**Q_{max} (mg/g)**	326.64
	R^2	0.71
	RMSE	45.06
55 °C	**Q_{max} (mg/g)**	376.95
	R^2	0.94
	RMSE	22.31
85 °C	**Q_{max} (mg/g)**	746.76
	R^2	0.96
	RMSE	32.49
95 °C	**Q_{max} (mg/g)**	921.90
	R^2	0.97
	RMSE	38.17
K_L = 0.059		

The regression was performed as a function of temperature (Figure 3), expressed in Kelvin (K), to obtain the angular (a) and linear (b) coefficients of Equation (7), which assumed the values of 9.15 mg/g.K and -2.54×10^3 mg/g, respectively, with K_L estimated at 0.006 L/mg. The determination coefficient (R^2) obtained was 0.98, indicating that the

linear regression adequately describes the dynamics of the adsorption capacity as a function of temperature. Thus, the determination of the coefficients made it possible to estimate Q_{max} at different temperatures.

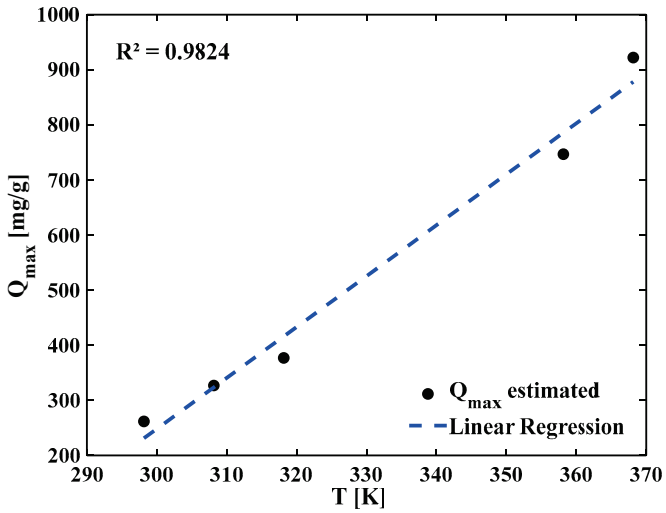


Figure 3. Linear regression of Q_{max} data as a function of temperature.

Considering the previously established hypotheses, a new joint estimation of the parameters a, b, and K_L was carried out through the Markov Chain Monte Carlo (MCMC) method. At this stage, the parameter values obtained in the previous steps were used as initial estimates. Figure 4a–e present the simultaneous fitting of the Langmuir model to the experimental isotherm data at 25 °C, 35 °C, 45 °C, 85 °C, and 95 °C, which were used for model calibration, adopting Q_{max} as a linear function of temperature and K_L as constant.

From the curves estimated individually and those obtained considering the model assumptions, a reduction in the determination coefficients (R^2) of the predicted curves with respect to the formulated hypotheses (Table 6) was observed, in comparison with the results estimated individually (Table 5). However, when Q_{max} was treated as a random variable without restrictions for estimation, the model tended to supply a better fit to the experimental data. From a physical standpoint, this may indicate an invalid result, since the hypothesis that Q_{max} depends on temperature was confirmed by the experimental data. By supplying this additional information to the model (incorporated into the prior probability distribution), the reliability of the response variable was increased, better reflecting the reality of the studied system.

In the model validation stage, assuming that Q_{max} varies linearly with temperature (Equation (7)), isotherms at intermediate temperatures of 55 °C, 65 °C, and 75 °C, which were not included in the fitting stage, were predicted to evaluate the predictive capability of the model. Figure 5 presents the experimental and simulated isotherms at the intermediate temperatures generated from the predictive model.

According to the validation estimates, the model proved effective in predicting isotherms, enabling the extension of predictions to temperatures not experimentally assessed. Figure 6 shows the adsorption equilibrium curves across the temperature range of 25 °C to 95 °C, including conditions not experimentally performed, in which the amount of adsorbate (copper) adsorbed per gram of zeolite (mg/g) is expressed as a function of temperature (°C) and equilibrium concentration (mg/L).

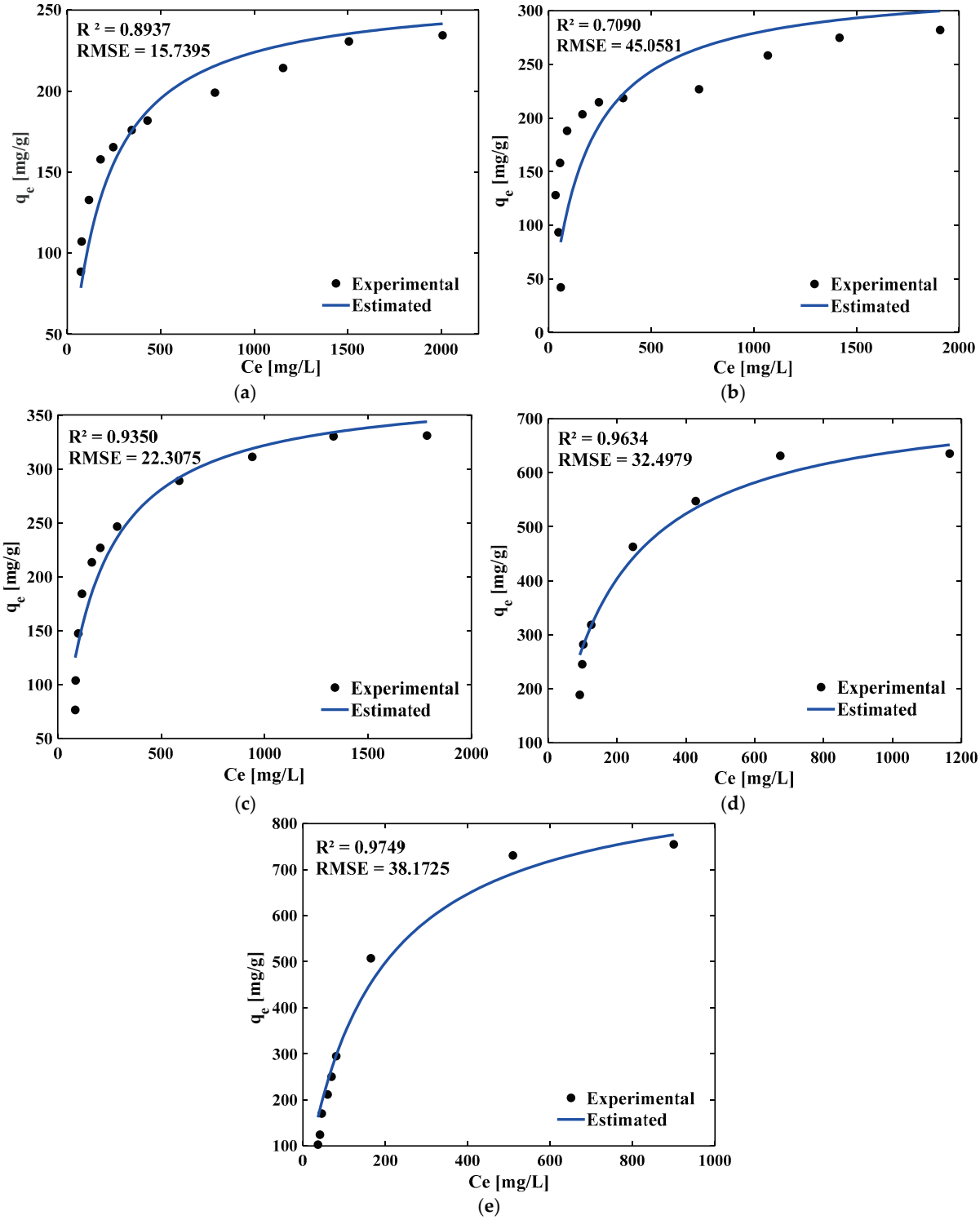


Figure 4. Fitting of the isotherms used for model calibration at temperatures of 25 °C (**a**), 35 °C (**b**), 45 °C (**c**), 85 °C (**d**), and 95 °C (**e**).

As shown in Figure 6, the proposed model allowed the estimation of adsorption capacity throughout the entire evaluated temperature range (25–95 °C), including intermediate isotherms not experimentally obtained. This approach enhances the understanding of system dynamics under different thermal conditions without the need to perform additional experiments for each temperature, which has practical implications, especially in industrial contexts, where it is often desirable to know adsorbent performance under varying operating conditions.

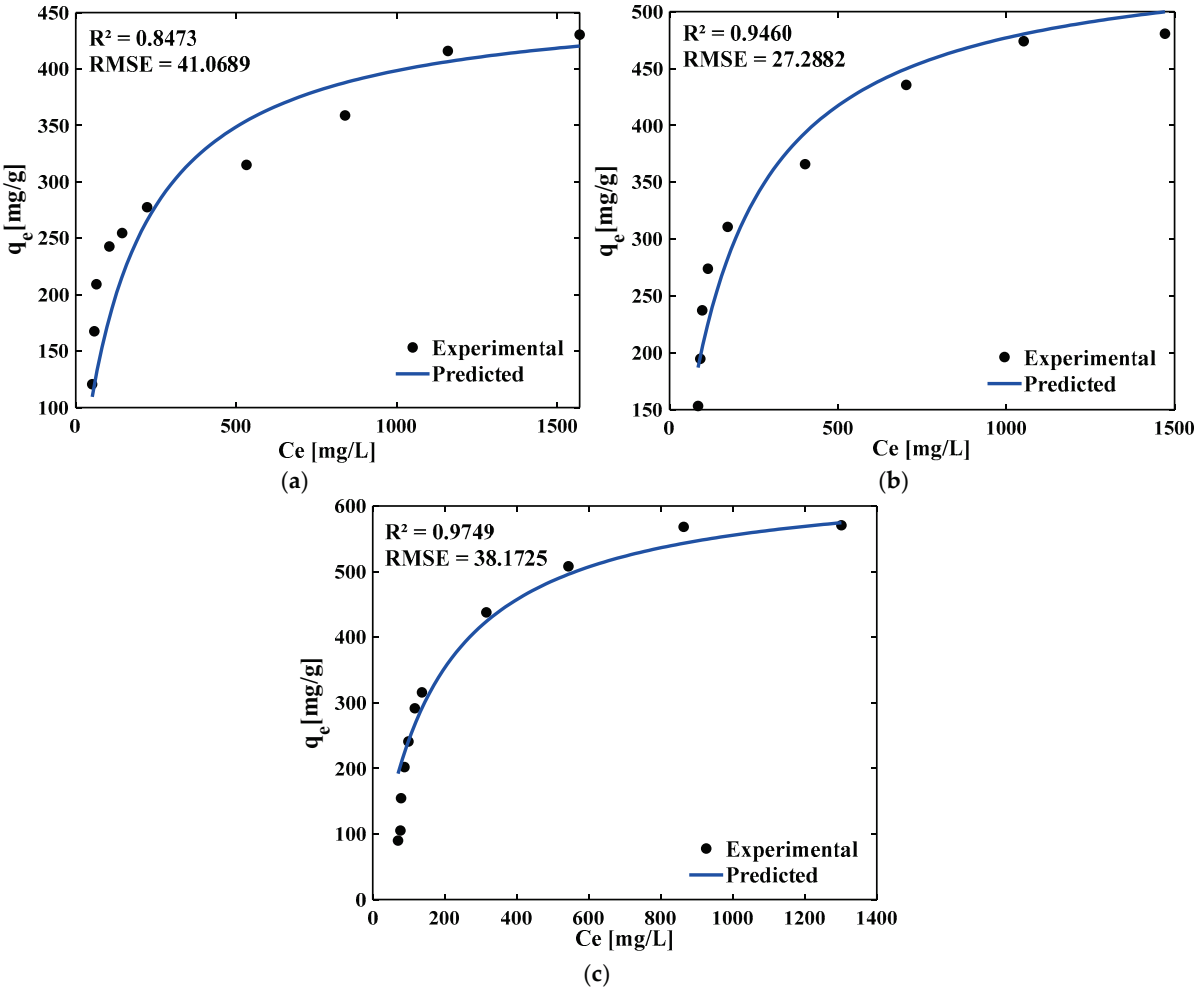


Figure 5. Estimation of the isotherms used for model validation at temperatures of 55 °C (**a**), 65 °C (**b**), and 75 °C (**c**).

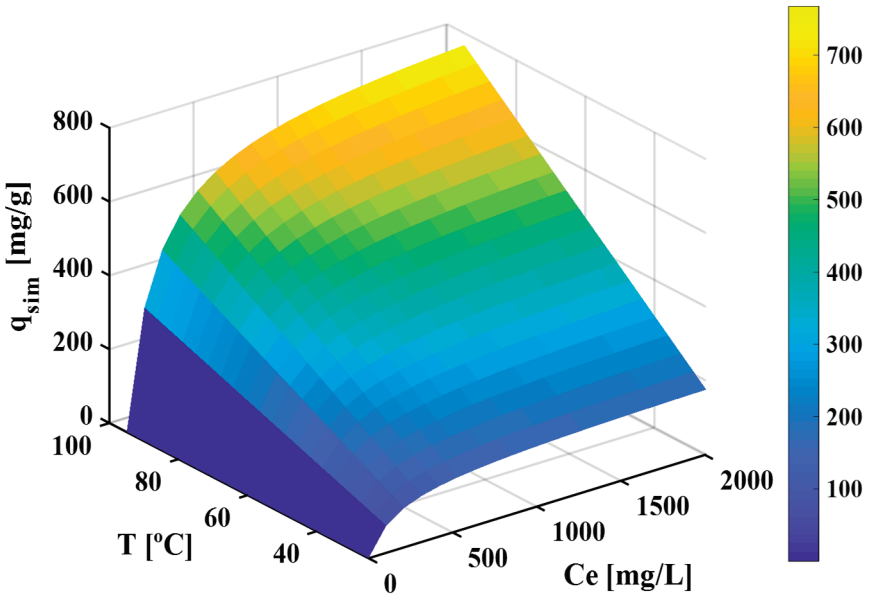


Figure 6. Prediction of adsorption isotherms at different temperatures.

Thus, the prediction provided by this model enables a continuous analysis of the process over a wide temperature range, enabling the practical application of the model

under different conditions, supporting the planning and optimization of processes in which thermal control is a critical factor.

The linear relationship proposed for Q_{max} (T) proved to be adequate within the temperature range studied, showing strong consistency with the individually generated experimental values for the different systems evaluated. This formulation reflects an empirical behavior consistently observed in the analyzed data, allowing the isotherms to be integrated into a single model representative of the adsorptive dynamics within the evaluated temperature interval. However, because this linearity does not derive from a fundamental relationship based on mass and energy balances, extending this trend to temperatures substantially different from those investigated is avoided, as additional effects related to adsorption energy and adsorbent behavior may become relevant outside the experimental range. Thus, the conclusions obtained with the model are valid for the temperature interval in which this trend was verified for the systems studied.

In parallel, the assumption of a constant K_L proved adequate within the temperature range studied, since the values individually estimated for the different systems exhibited low sensitivity, remaining within the same order of magnitude and showing no clear trend of variation with temperature. Thus, within the considered interval, no significant variation in K_L was observed that would allow for the development of a mathematical formulation incorporating temperature into this parameter. This behavior allowed K_L to be adopted as constant in the formulation of the proposed model, ensuring mathematical coherence without introducing unnecessary degrees of freedom.

However, because this constancy does not arise from a thermodynamic relationship but rather from a pattern observed in the experimental systems evaluated, its application to temperatures markedly different from those investigated should be approached with caution, making predictions within the studied temperature range more appropriate. Therefore, the validity of this hypothesis is restricted to the temperature range studied and to the systems for which this trend was experimentally verified.

4. Conclusions

The adaptation of the Langmuir isotherm model with the inclusion of temperature as a variable, developed through the computational methodology presented in this work, was initially formulated based on isotherms involving different adsorbent–adsorbate systems and subsequently applied to experimental data obtained from copper ion adsorption by zeolite 5A. This approach enabled the prediction of isotherms within a temperature range of 25 °C to 95 °C.

The assumptions formulated and the methodology employed to calibrate and validate the model were fundamental for the prediction stage. In this way, the predictive model contributed to the understanding of the adsorption process dynamics as a function of temperature, which is particularly important in scenarios where experimental data are limited. Thus, it is not only possible to assess the adequacy of an experiment to a model, but also to simulate conditions and optimize adsorption processes, highlighting the potential applicability of the methodology to different cases of isotherms under operating conditions for which no experimental data are available.

Supplementary Materials: The following supporting information can be downloaded at: https://www.mdpi.com/article/10.3390/pr13124036/s1, Figure S1: Sensitivity analysis of the parameters Q_{max} and K_L with respect to the adsorbed amount q_e for the systems: amoxicillin (S1.1), phosphate (S1.2), methylene blue (S1.3), and caffeine (S1.4); Figure S2: Langmuir model fittings to the experimental adsorption data for the evaluated systems: amoxicillin (S2.1), phosphate (S2.2), methylene blue (S2.3), and caffeine (S2.4); Figure S3: Linear regressions of the individually estimated Q_{max} values as a function of temperature (in Kelvin) for each experimental dataset: amoxicillin (a), phosphate (b),

methylene blue (c), and caffeine (d); Figure S4: Simulated curves generated from the calibration of the Langmuir model for the evaluated systems: amoxicillin (S4.1), phosphate (S4.2), methylene blue (S4.3), and caffeine (S4.4), considering Q_{max} as a linear function of temperature and K_L as constant. Figure S5: Sensitivity analysis of the parameters K_L and Q_{max} at temperatures of 25 °C (a), 35 °C (b), 45 °C (c), 85 °C (d), and 95 °C (e).

Author Contributions: Conceptualization, A.P.S.d.S. and H.B.S.L.; methodology, A.P.S.d.S., D.C.E., H.B.S.L. and E.C.R.; software, D.C.E.; validation, A.P.S.d.S., H.B.S.L. and D.C.E.; formal analysis, D.S.d.C., C.B.A. and L.A.F.; investigation, L.A.F. and D.C.E.; data curation, A.P.S.d.S., L.A.F. and D.C.E.; writing—original draft preparation, A.P.S.d.S.; writing—review and editing, L.A.F., D.S.d.C., C.B.A. and E.C.R.; visualization, A.P.S.d.S. and H.B.S.L. All authors have read and agreed to the published version of the manuscript.

Funding: This research was funded by Fundação Amazônia de Amparo a Estudos e Pesquisas (FAPESPA) and the Pró-Reitoria de Pesquisa e Pós-Graduação of the Universidade Federal do Pará (PROPESP/UFPA), through the project entitled "Adsorption of Gases in Fixed Bed: Use of Adsorbents Produced from Mining Waste in a Semi-Pilot Scale System", grant agreement No. 13/2022.

Data Availability Statement: The data presented in this study are available from the corresponding author upon reasonable request. Part of the material is temporarily restricted.

Acknowledgments: Thank FAPESPA and PROPESP (UFPA) for financial supporting research through financing the project entitled "Adsorção De Gases Em Leito Fixo: Uso De adsorventes Produzidos A Partir De Resíduos De Mineração Em Sistema Com escala Semi Piloto" agreement N°13/2022. Thank CNPq for financially supporting research through financing the project entitled "Adsorção de multicomponentes em colunas de Leito fixo: experimental, modelagem, scale-up" agreement MCTI/FNDCT N° 44/2024—UNIVERSAL and N° 18/2024—Bolsas de Produtividade em Pesquisa.

Conflicts of Interest: The authors declare no conflicts of interest.

References

1. Hong, Y.; Lee, I.; Lee, W.; Kim, H. Mass-Balance-Model-Based evaluation of sewage treatment plant contribution to residual pharmaceuticals in environmental waters. *Chemosphere* **2019**, *225*, 378–387. [CrossRef] [PubMed]
2. Sousa, G.C. Contaminação por Metais Pesados: A Ameaça dos Poluentes ao Oceano e à Saúde Humana. Jornal da USP. São Paulo. 2023. Available online: https://jornal.usp.br/atualidades/contaminacao-por-metais-pesados-a-ameaca-dos-poluentes-aos-oceanos-e-a-saude-humana/ (accessed on 9 July 2025).
3. Saleh, T.A. *Surface Science of Adsorbents and Nanoadsorbents: Properties and Applications in Environmental Remediation*; Academic Press: Cambridge, MA, USA, 2022.
4. Smart, L.E.; Moore, E.A. *Solid State Chemistry: An Introduction*, 5th ed.; CRC Press: Boca Raton, FL, USA, 2020.
5. Worch, E. *Adsorption Technology in Water Treatment: Fundamentals, Processes, and Modeling*, 2nd ed.; Walter de Gruyter GmbH: Berlin, Germany, 2021; 376p.
6. Sing, K.S.W. Reporting physisorption data for gas/solid systems with special reference to the determination of surface area and porosity (IUPAC Recommendations 1984). *Pure Appl. Chem.* **1985**, *57*, 603–619. [CrossRef]
7. Din, S.U.; Khaqan, U.; Imran, M.; Al-Ahmary, K.M.; Alshdoukhi, I.F.; Carabineiro, S.A.; Bakheet, A.M. Enhancing arsenic reoval using Cu-infused biochar: Unravelliing the influence of pH, temperature and kinectics. *Chem. Eng. Res. Des.* **2024**, *203*, 368–377. [CrossRef]
8. Gyawali, D.; Rijal, S.; Basnet, P.; Ghimire, K.N.; Pokhrel, M.R.; Paudyal, H. Effective biosorption of As (V) from polluted water using Fe (III)-modified Pomelo (Citrus maxima) peel: A batch, column, and thermodynamic study. *Heliyon* **2023**, *9*, e13465. [CrossRef]
9. Hung, D.Q.; Dinh, L.X.; Van Tung, N.; Huong, L.T.M.; Lien, N.T.; Minh, P.T.; Le, T.-H. The adsorption kinetic and isotherm studies of metal ions (Co^{2+}, Sr^{2+}, Cs^{+}) on Fe_3O_4 nanoparticle of radioactive importance. *Results Chem.* **2023**, *6*, 101095. [CrossRef]
10. Rasheed, F.A.; Sillanpää, M.; Moradi, M. Cobalt Adsorption by Ca $(OH)_2$ Modified Quartz Rock Particles Adsorbent: Equilibrium Isotherm, Kinetics, and Thermodynamic Studies. *Desalination Water Treat.* **2024**, *319*, 100477. [CrossRef]
11. Ma, K. Integrated hybrid modeling and SHAP (SHapley Additive exPlanations) to predict and explain the adsorption properties of thermoplastic polyurethane (TPU) porous materials. *RSC Adv.* **2024**, *14*, 10348–10357. [CrossRef]

12. Cao, X.; Luo, W.; Liu, H. A prediction model for CO_2/CO adsorption performance on binary alloys based on machine learning. *RSC Adv.* **2024**, *14*, 12235–12246. [CrossRef]
13. Yeo, J.Y.J.; Khaerudini, D.S.; Soetaredjo, F.E.; Waworuntu, G.L.; Ismadji, S.; Sunarso, J.; Liu, S. Isotherm data for adsorption of amoxicillin, ampicillin, and doripenem onto bentonite. *Data Brief* **2023**, *48*, 109159. [CrossRef]
14. Jurado-Davila, I.V.; Schneider, I.A.H.; Estumano, D.; Féris, L.A. Phosphate removal using dolomite modified with ultrasound: Mathematical and experimental analysis. *J. Environ. Sci. Health Part A* **2023**, *58*, 469–482. [CrossRef]
15. Cheng, G.; Li, Y.; Sun, L.; Luo, S.; Kyzas, G.Z.; Fu, J. Residue char derived from microwave-assisted pyrolysis of sludge as adsorbent for the removal of methylene blue from aqueous solutions. *Processes* **2020**, *8*, 979. [CrossRef]
16. Oliveira, J.T.; Nunes, K.G.P.; Estumano, D.C.; Féris, L.A. Applying the Bayesian technique, statistical analysis, and the maximum adsorption capacity in a deterministic way for caffeine removal by adsorption: Kinetic and isotherm modeling. *Ind. Eng. Chem. Res.* **2024**, *63*, 1530–1545. [CrossRef]
17. Langmuir, I. The dissociation of hydrogen into atoms. III. The mechanism of the reaction. *J. Am. Chem. Soc.* **1916**, *38*, 1145–1156. [CrossRef]
18. Sohn, S.; Kim, D. Modification of Langmuir isotherm in solution systems—Definition and utilization of concentration dependent factor. *Chemosphere* **2005**, *58*, 115–123. [CrossRef]
19. Nascimento, R.F.D.; Lima, A.C.A.D.; Vidal, C.B.; Melo, D.D.Q.; Raulino, G.S.C. *Adsorção: Aspectos Teóricos e Aplicações Ambientais*, 2nd ed.; Imprensa Universitária: Mozambique, Southern Africa, 2020; pp. 14–24.
20. Tien, C. *Introduction to Adsorption: Basics, Analysis and Applications*; Elsevier: Amsterdam, The Netherlands, 2019.
21. Orlande, H.R.B.; Colaço, M.J.; Cotta, C.P.; Guimarães, G.; Borges, V. Problemas inversos em transferência de calor. *São Carlos SBMAC (Soc. Bras. Matemática Apl. Comput.)* **2011**, *51*, 113.
22. Ito, K.; Jin, B. *Inverse Problems: Tikhonov Theory and Algorithms*; World Scientific: Singapore, 2015; Volume 22.
23. Ferreira, J.R.; Sena, A.P.; Coutinho, J.P.d.S.; Estumano, D.C.; Macêdo, E.N. Fluid dynamics characterization of stirred-tank reactors via approximate Bayesian computational (ABC) for parameter estimation and model selection. *Numer. Heat Transf. Part A Appl.* **2023**, *85*, 2579–2596. [CrossRef]
24. Tavares, R.; Santana, C.D.; Rodrigues, C.H.M.; Rodrigues, E.C.; Viegas, B.M.; Estumano, D.C. Parameter Estimation in Mass Balance Model Applied in Fixed Bed Adsorption Using the Markov Chain Monte Carlo Method. *J. Heat Mass Transf. Res.* **2022**, *9*, 219–232. [CrossRef]
25. Cardoso, A.C.; Dias, C.S.; de Moura, C.H.R.; Ferreira, J.L.; Rodrigues, E.C.; Macêdo, E.N.; Estumano, D.C.; Viegas, B.M. Use of Bayesian Methods in the Process of Uranium Bioleaching by *Acidithiobacillus ferrooxidans*. *Appl. Sci.* **2023**, *14*, 109. [CrossRef]
26. Metropolis, N.; Rosenbluth, A.W.; Rosenbluth, M.N.; Teller, A.H.; Teller, E. Equation of State Calculations by Fast Computing Machines. *J. Chem. Phys.* **1953**, *21*, 1087–1092. [CrossRef]
27. Hastings, W. Monte Carlo Sampling Methods using Markov Chains and their Applications. *Biometrika* **1970**, *57*, 97–109. [CrossRef]
28. Lima, H.B.S.; Sousa, A.P.S.; Silva, W.B.D.; Costa, D.S.D.; Rodrigues, E.C.; Estumano, D.C. Parameter estimation of breakthrough curve models in the adsorption process of H_2S and CO_2 using the Markov Chain Monte Carlo Method. *Appl. Sci.* **2024**, *14*, 6956. [CrossRef]
29. Dias, C.S.; Franco, M.A.E.; Rodrigues, E.C.; Ferreira, J.L.; Viegas, B.M.; Féris, L.A.; Estumano, D.C.; Macêdo, E.N. Diclofenac sodium adsorption on activated carbon: Experimental, modeling and bayesian statistics. *An. Acad. Bras. Cienc.* **2024**, *96* (Suppl. S1), e20231110. [CrossRef]
30. Jurado-Davila, V.; Reolon, L.S.; Nunes, K.G.P.; Estumano, D.C.; Féris, L.A. Classical and bayesian computational statistics applied to acetylsalicylic acid mitigation in aqueous solutions: Study of batch scale, kinetic modeling, and fixed-bed column adsorption. *Ind. Eng. Chem. Res.* **2024**, *63*, 9943–9954. [CrossRef]
31. Liu, C.; Yan, X.; Zhang, H.-X.; Yang, J.-M.; Yoon, K.-B. Silicone-Modified black peanut shell (BPS) biochar adsorbents: Preparation and their adsorptions for copper (II) from water. *Heliyon* **2024**, *10*, e35169. [CrossRef]
32. Huang, X.; Lang, L.; Li, J.-S.; Poon, C.S. Synthesis of Na-A zeolite loaded bentonite and its application for removal of Cu (II) from aqueous solutions. *J. Water Process Eng.* **2023**, *56*, 104359. [CrossRef]
33. Wu, X.; Song, Y.; Yin, P.; Xu, Q.; Yang, Z.; Xu, Y.; Liu, X.; Sun, W.; Cai, H. Efficient copper ions adsorption property of the composite sepiolite-based polyethyleneimine alginate microspheres in wastewater treatment. *Desalination Water Treat.* **2022**, *262*, 200–214. [CrossRef]

Disclaimer/Publisher's Note: The statements, opinions and data contained in all publications are solely those of the individual author(s) and contributor(s) and not of MDPI and/or the editor(s). MDPI and/or the editor(s) disclaim responsibility for any injury to people or property resulting from any ideas, methods, instructions or products referred to in the content.

processes

MDPI

Article

Effect of Aluminum Salt Precursor on the Crystalline Structure of Alumina Nanoparticles (Al_2O_3) Synthesized by Green Chemistry Using *Cymbopogon citratus* Extract

Miguel Castro [1], Laura Tous [1], Adriana Herrera [1], Dylan Martinez-Bernett [1,*] and Manuel Saba [2]

[1] Nanomaterials and Computer-Aided Process Engineering Research Group, Department of Chemical Engineering, College of Engineering, University of Cartagena, Cartagena 130015, Colombia; mcastroh@unicartagena.edu.co (M.C.); ltousm@unicartagena.edu.co (L.T.); aherrerab2@unicartagena.edu.co (A.H.)

[2] Structures, Construction and Heritage Research Group, Department of Civil Engineering, College of Engineering, University of Cartagena, Cartagena 130015, Colombia; msaba@unicartagena.edu.co

* Correspondence: dmartinezb5@unicartagena.edu.co

Abstract: Alumina nanoparticles have broad applications in catalysis, electronics, and the construction sector, and are widely incorporated as additives in coating formulations to enhance mechanical durability and functional performance. This work focuses on the green synthesis of aluminum oxide (Al_2O_3) nanoparticles using lemongrass (*Cymbopogon citratus*) extract. Aluminum nitrate [$Al(NO_3)_3$] and aluminum chloride ($AlCl_3$) were used with extract. The reaction was carried out at 70 °C for 1 h at 250 rpm and then thermal treatments at 700 °C and 900 °C were applied. The results showed that nanoparticles synthesized from the $AlCl_3$ and calcined at 700 °C exhibited a smaller particle size (36 ± 14 nm) as compared with those synthesized from the [$Al(NO_3)_3$] and calcined at 700 °C (49 ± 25 nm). Despite both precursors yielding nanoparticles, the peaks related to the γ-Al_2O_3 crystal phase were observed in the $AlCl_3$ at 700 °C calcination. Conversely, the nanoparticles synthesized from the [$Al(NO_3)_3$] required a high temperature treatment at 900 °C to display this stable crystal phase. This study reports an easy and cost-effective green chemistry route to obtain γ-Al_2O_3 nanoparticles, highlighting the importance of the selection of precursors as a critical step to achieve a sustainable and low-energy process, suggesting the potential applications in paints with multifunctional properties.

Keywords: green synthesis; nanoparticles; aluminum nitrate; aluminum chloride; coatings

1. Introduction

Metal oxide nanomaterials stand out for their remarkable physicochemical properties, such as high catalytic activity, thermal stability, and adsorption capacity [1]. Their reduced size (10–100 nanometers) and high surface-to-volume ratio mainly account for these features. Moreover, they can be used to improve mechanical and thermal resistance in ceramic materials; to fabricate semiconductors and electronic devices [2] due to their dielectric nature; to provide protective coatings against friction and high temperatures in the aerospace industry; to serve as antimicrobial agents and drug carriers in medicine; to enable the controlled release of nutrients in agriculture; and to develop chemical sensors for gas detection [3]. Among all known metal oxide nanomaterials, aluminum oxide (Al_2O_3) nanoparticles have attracted considerable interest in the design and formulation of antimicrobial agents for sustainable biomedical applications, since they are chemically bio-inert and exhibit good hydrolytic stability [4]. Additionally, the Al_2O_3 nanoparticles

can be used as additives for paints and coating materials to provide functional properties, such as antifungal activity [5,6], self-cleaning [7,8], and UV protection by generating a reflective effect [4].

The synthesis of nanoparticles through green chemistry [9] has become a sustainable alternative to traditional methods, which often require the use of toxic reagents and high energy consumption. In this green approach, plant extracts containing active components such as flavonoids, polyphenols, enzymes, and terpenes are used as ion chelators, reducing agents, and stabilizers during the nanoparticle formation [10].

Several studies have reported the green synthesis of alumina nanoparticles using plant extracts such as Coffea (coffee), *Camellia sinensis* (tea), and *Triphala* (Indian gooseberry), under microwave irradiation, producing nanoparticles with spherical or oval morphologies and sizes ranging from 50 to 100 nm [11]. Lemongrass (*Cymbopogon citratus*) is an herbaceous plant rich in phytocomponents such as terpenoids, flavonoids, and phenolic acids. These secondary metabolites exhibit high chelating and antioxidant capacities, which are useful for the nucleation and stabilization of nanomaterials when a green synthesis approach is applied. Ansari and coworkers [12] reported the effectiveness of lemongrass extract for the synthesis of spherical Al_2O_3 nanoparticles with an average size of 34.5 nm and a strong antibacterial activity against Pseudomonas aeruginosa by using a minimal inhibitory concentration of nanoparticles ranging from 1600 to 3200 μg/mL [12], in contrast with the current study, we employ a simpler and energy-efficient method that does not require microwave-assisted equipment. This approach improves scalability and reproducibility, while also underscoring the critical role of precursor selection in nanoparticle production. In other work, Rashid and coworkers evaluated the synthesis of Al_2O_3 nanoparticles using red onion peel extract and aluminum chloride as the precursor. They observed the formation of spherical to rod-like nanoparticles with a hexagonal crystal phase after calcination at 450 °C [13].

Several recent studies have demonstrated that the choice of aluminum precursor plays a decisive role in determining the final structure of alumina as well as the temperature required for the formation of specific crystalline phases. Wen et al. compared different aluminum precursors including chlorides, nitrates, and sulfates and showed that the anion type governs the thermal decomposition pathway and, consequently, the formation of phases such as γ-Al_2O_3. Their results indicated that nitrates decompose rapidly and violently, leading to materials with lower crystallinity, whereas chlorides promote a more defined formation of the gamma phase at relatively lower temperatures. These findings highlight the relevance of comparing $AlCl_3$ and $Al(NO_3)_3$ in our synthesis, as they explain the marked differences in crystallinity observed between both precursors [14]. Complementary evidence was provided by Zheng et al. who demonstrated that the chemical nature of the precursor or catalyst can modify nucleation kinetics and the final structural order of alumina. In their study, the presence of anhydrous aluminum chloride during the hydrolysis of aluminum isopropoxide acted as a nucleation modulator, producing more uniform particles and better-ordered phases after calcination. This reinforces that even subtle variations in precursor chemistry directly affect the structural quality of the resulting alumina [15].

This research was focused on synthesizing aluminum oxide (Al_2O_3) nanoparticles prepared by green chemistry using lemongrass (*Cymbopogon citratus*) extract as a reducing and stabilizing agent. Moreover, the influence of the aluminum precursor on size distribution and crystal structure was analyzed. For this purpose, two different inorganic aluminum salts were evaluated: aluminum nitrate nonahydrate [$Al(NO_3)_3.9H_2O$] and aluminum chloride hexahydrate [$AlCl_3.6H_2O$]. Additionally, the synthesized Al_2O_3 nanoparticles were submitted to thermal treatments at 700 °C and 900 °C to encourage the gamma crys-

tal phase, which is desirable for innovative paint-type coatings; thus, this study aims to contribute to the development of suitable methods for obtaining nanomaterials applicable to multifunctional coatings.

2. Materials and Methods

2.1. Materials

Lemongrass leaves (*Cymbopogon citratus*) were collected at Gambote, Bolivar, Colombia. Aluminum nitrate nonahydrate [$Al(NO_3)_3.9H_2O$, 99%] and ethyl alcohol (C_2H_5OH, 99.5%) were purchased from Merck KGaA (Darmstadt, Germany). Aluminum chloride hexahydrate [$AlCl_3.6H_2O$, 99%] and sodium hydroxide (NaOH, 99%) were acquired from Loba Chemie (Mumbai, India) and Sigma-Aldrich (Burlington, MA, USA).

2.2. Extract Preparation of Cymbopogon citratus

Lemongrass extract was prepared using fresh biomass, as illustrated in Figure 1. In a typical procedure, the lemongrass leaves were washed with distilled water and then placed in an oven at 60 °C for 6 h. The dried biomass was ground, and 100 g of this biomaterial was used to prepare the lemongrass extract in 600 mL of distilled water at 80 °C for 20 min. Afterward, the aqueous extract was filtered and stored in a glass bottle at 4 °C [16]

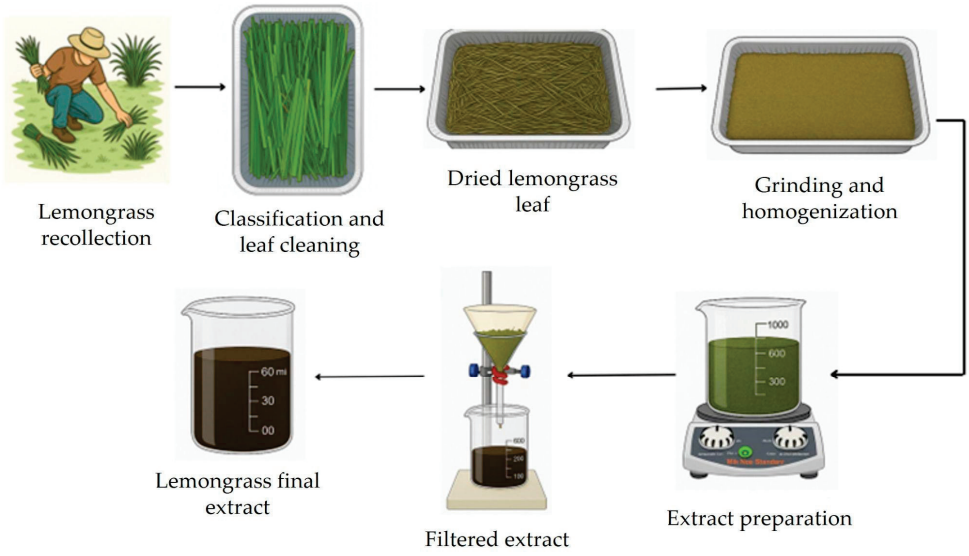


Figure 1. Preparation of the lemongrass aqueous extract.

2.3. Synthesis of Al_2O_3 Nanoparticles

Figure 2 shows the methodology employed to obtain aluminum oxide (Al_2O_3) nanoparticles using lemongrass extract. The presence of terpenes and terpenoids in the extract prevents uncontrolled agglomeration of the aluminum hydroxide formed during synthesis. These phytochemicals as *6-Methyl-5-hepten-2-one* and *β-Myrcene* could interact through their functional groups, effectively contributing to size control. This extract has also proven effective in the green synthesis of TiO_2 nanoparticles in previous studies of this group [17]. Initially, 10 g of the inorganic aluminum salt precursor (aluminum nitrate or aluminum chloride) was dissolved in 100 mL of the lemongrass extract. This mixture was heated at 70 °C for 1 h at 250 rpm, with a 6 M NaOH solution added dropwise; the total volume added was 14 mL for the aluminum nitrate precursor and 21 mL for the aluminum chloride, corresponding to addition rates of 0.22 $mL \cdot min^{-1}$ and 0.35 $mL \cdot min^{-1}$, respectively. The resulting nanoparticles were washed twice with deionized water and once with ethanol

via centrifugation at 5800 rpm for 10 min. Finally, the nanomaterials were calcined at 700 °C and 900 °C for 4 h [3,18]. Samples were labelled according to the precursor and the calcination temperature, as follows: for aluminum nitrate (N-Al_2O_3-700, N-Al_2O_3-900) and for aluminum chloride (C-Al_2O_3-700, C-Al_2O_3-900).

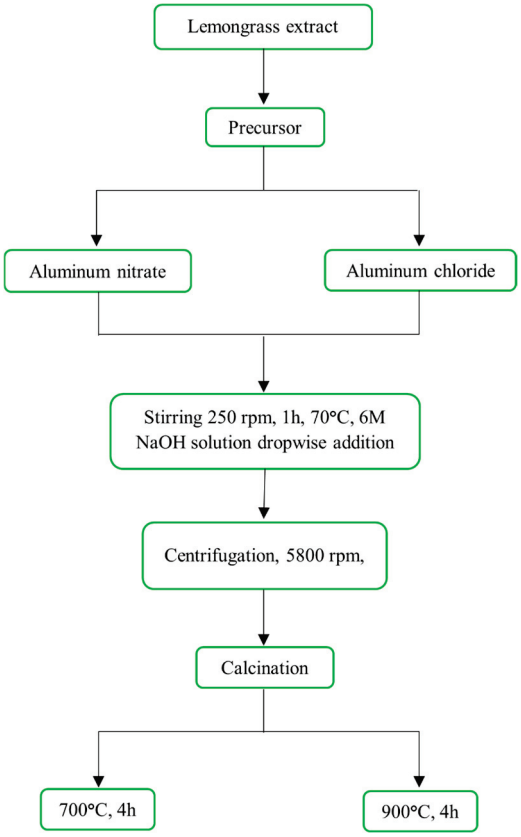


Figure 2. Schematic representation of alumina oxide nanoparticles synthesized in the presence of lemongrass extract and two aluminum salt precursors.

Compared with conventional chemical synthesis, green nanoparticle production offers a lower environmental footprint. Studies report substantial reductions in emissions and toxicity based on the use of green routes under mild heating instead of the high-temperature stages of chemical methods, which may exceed 800–1500 °C [19]. Life Cycle Assessment data shows that green synthesis eliminates carcinogenic impacts and significantly decreases air-pollution-related indicators, largely due to the absence of corrosive precursors and hazardous reducing agents [20]. Additionally, the use of plant extracts and renewable biomass aligns with the principles of safer and less toxic industrial chemical processing [21].

2.4. Characterizations

Aluminum oxide nanoparticles were characterized by scanning electron microscopy (SEM) coupled with energy-dispersive X-ray spectroscopy (EDS) using a Thermo Fisher Scientific (ThermoFisher Scientific, Waltham, MA, USA) Scios 2 LoVac Dual Beam Field Emission Electron Microscope equipped with an UltraDry 129 eV 30 mm2 EDS microanalysis system (SDBX-30PM-B). Samples were analyzed at a resolution of 0.7 nm, 30 kV in STEM mode, and 1.4 nm at 1 kV in FESEM mode [22,23]. Furthermore, X-ray diffraction (XRD) was used to analyze the crystal structure of the synthesized nanoparticles. For these measurements, a Malvern-PANalytical Empyrean 2012 diffractometer (Malvern Panalytical, Malvern, UK) was used with a Cu-Kα radiation (λ = 1.541 Å) at 45 kV and 40 mA. Measurements were performed in a 2θ range between 10° and 80°, with a step of 0.05° and

a counting time of 50 s per step [24,25]. This technique allows for the identification of the crystalline phases present in the samples.

3. Results and Discussion

3.1. SEM–EDS

Figure 3 presents SEM images of the Al_2O_3 nanoparticles, in which the presence of agglomerated nanoparticles with an irregular spherical shape can be observed. Particle size distribution is displayed in Figure 4. Although a broad size distribution was observed for all samples, the largest population of nanoparticles had a size smaller than 50 nm, suggesting that for both precursors, aluminum chloride or aluminum nitrate, the phytocomponents present in the lemongrass extract prevented the growth of the nanomaterials, acting as capping and stabilizing agents. These results agree with the values reported in scientific literature. Gharbi and coworkers obtained aluminum oxide nanoparticles with an average size of 33 nm using a plant extract prepared from fire bush (*Calligonum comosum* L.) leaves and aluminum nitrate as the precursor reagent [18]. Additionally, Ali and coworkers reported the preparation of aluminum oxide nanoparticles by the coprecipitation method, using aluminum chloride to obtain nanoparticles with a size ranging from 30 to 50 nm [26].

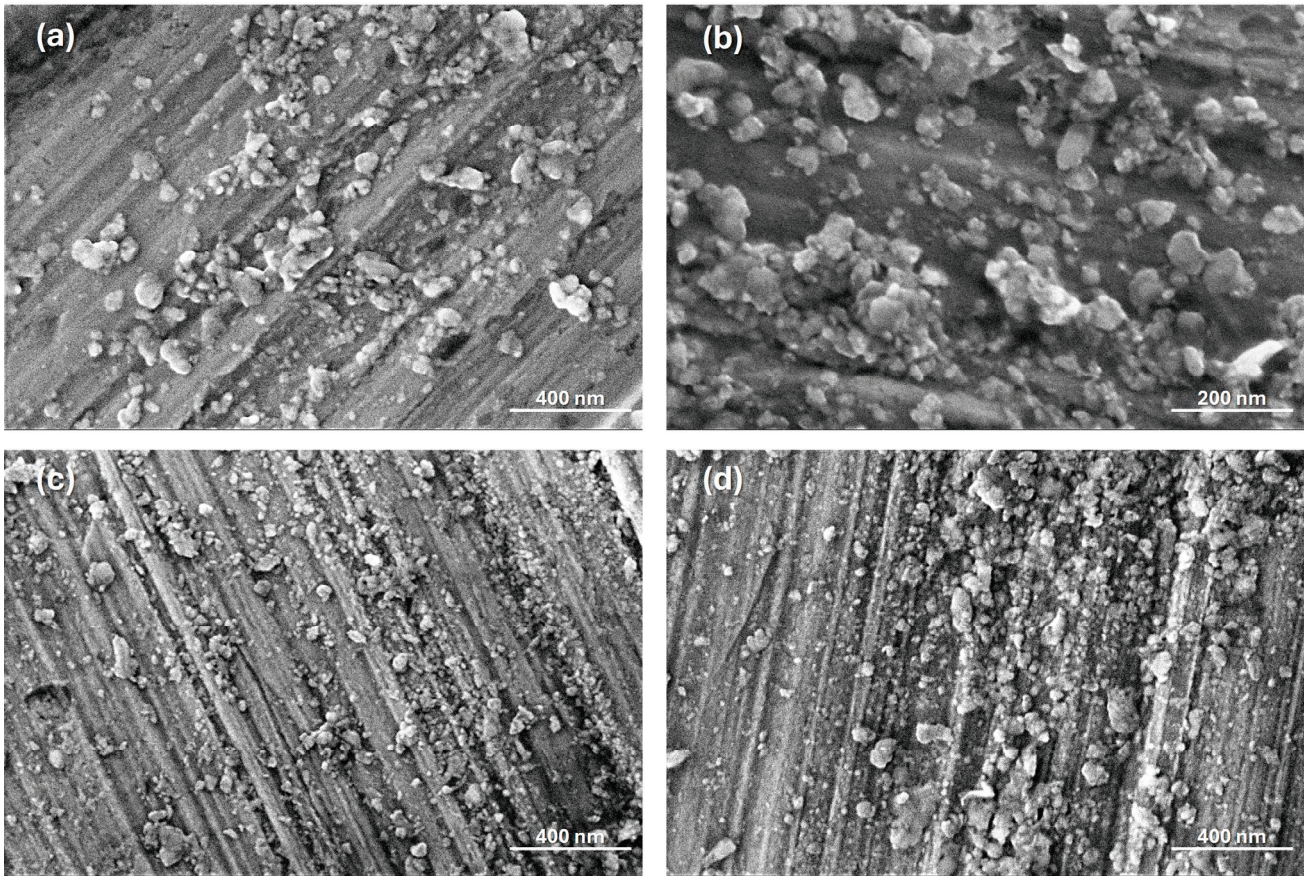


Figure 3. SEM images of the synthesized nanoparticles: (**a**) N-Al_2O_3-700; (**b**) N-Al_2O_3-900; (**c**) C-Al_2O_3-700, and (**d**) C-Al_2O_3-900.

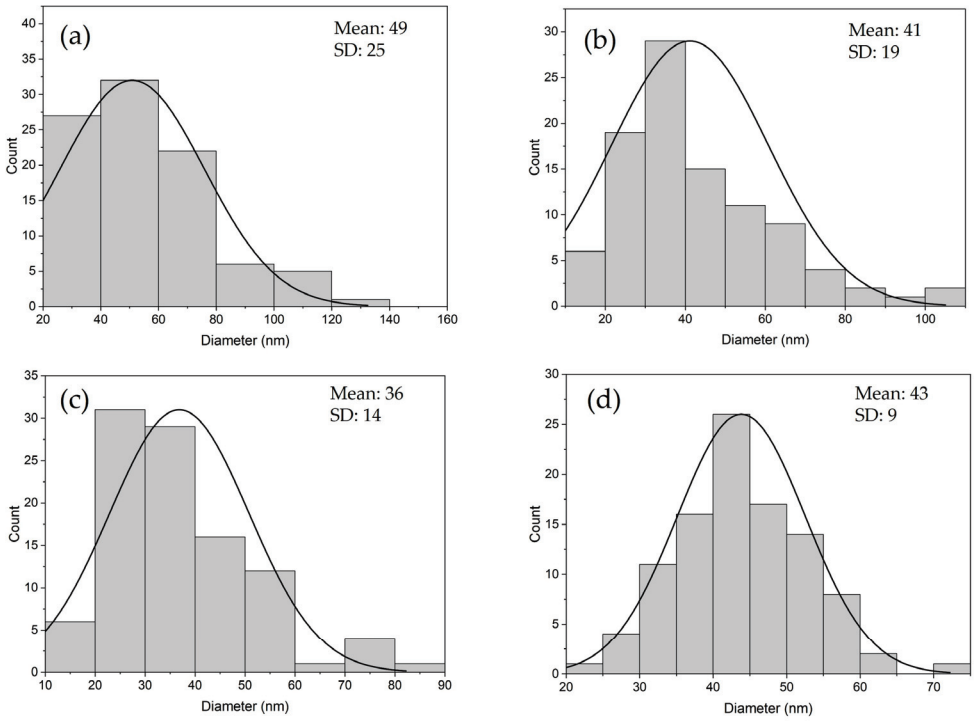


Figure 4. Particle size distribution of the synthesized nanoparticles: (**a**) N-Al_2O_3-700; (**b**) N-Al_2O_3-900; (**c**) C-Al_2O_3-700; and (**d**) C-Al_2O_3-900.

It is important to note that nanoparticles synthesized from the $AlCl_3$ precursor and calcined at 700 °C exhibited a smaller particle size (36 ± 14 nm) as compared with the nanoparticles obtained from the [$Al(NO_3)_3$] precursor at the same calcination temperature (49 ± 25 nm). Moreover, no significant increase in particle size was determined after thermal treatment at 900 °C for both aluminum precursors, despite slight evidence of sintering initiation being observed in Figure 3b,d, reflected in partial particle agglomeration. Suaebah and coworkers reported a relevant size increase of Al_2O_3 nanoparticles synthesized by the Sol–gel method from 374 nm up to 754 nm after submitting the nanoparticles to a calcination temperature of 800 °C and 1000 °C, respectively. This size increase was totally attributed to a sintering process due to grain boundary movements and material densification at the higher temperature of 1000 °C, desirable for the formation of the α- Al_2O_3 crystal phase [27].

The elemental composition of the Al_2O_3 nanoparticles was analyzed from X-ray energy dispersive spectroscopy (EDS). Figure 5 presents these results, from which it was observed that all samples exhibited a high concentration of aluminum (Al) and oxygen (O), being more notable this composition at the sample C- Al_2O_3-900, which displays an aluminum content of 58.97% with an oxygen content of 37.5%. In addition, minimal traces of sodium (Na) were detected in all samples, derived from the precipitating agent (NaOH) used in the synthesis process. Similar results were reported by Manyasree and coworkers, who prepared Al_2O_3 nanoparticles by the coprecipitation of the aluminum sulfate precursor with sodium hydroxide [28].

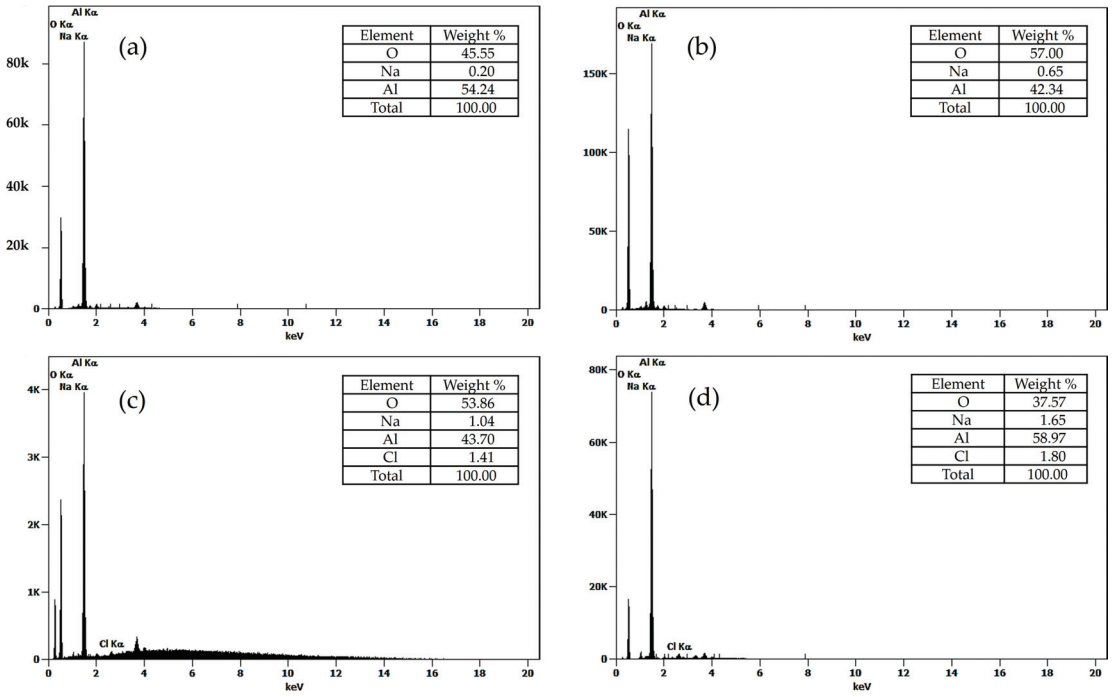


Figure 5. Elemental analysis by X-ray energy dispersive spectroscopy (EDS) for Al_2O_3 nanoparticles: (**a**) N-Al_2O_3-700, (**b**) N-Al_2O_3-900, (**c**) C-Al_2O_3-700, and (**d**) C-Al_2O_3-900.

The results showed traces of Na and Cl in the nanoparticles. These species originated from residual products formed during the synthesis with NaOH, a phenomenon also reported by Khine et al. [29], where NaCl may remain entrapped within hydroxide surfaces of the nanoparticles or adsorbed on metal oxide nanoparticles after washing. The detected levels are minimal, and their presence indicates that precursor and after synthesis conditions influence its surfaces.

3.2. X-Ray Diffraction

The synthesized Al_2O_3 nanomaterials exhibited X-ray diffraction patterns characteristic of the γ- Al_2O_3 phase (Figure 6), being more notable for the samples C-Al_2O_3-700 and C-Al_2O_3-900. These samples presented peaks at 32°, 38°, 46°, and 67° (Figure 6c,d), which are associated with the Miller indices (220), (311), (400), and (440), representatives of the γ-Al_2O_3 crystal phase (JCPDS card No. 10-0425) [18,30,31], confirming the formation of this stable crystal phase for the nanoparticles prepared with the $AlCl_3$ precursor.

For the nanoparticles prepared from the aluminum nitrate precursor, the γ-Al_2O_3 crystalline phase was only observed after calcination at 900 °C for 4 h (Figure 6b). In the N-Al_2O_3-700 sample, no diffraction peaks corresponding to the gamma phase were detected, indicating a predominantly amorphous material. Moreover, the diffraction peaks of the N-Al_2O_3-900 sample were less intense and broader than those observed for the C-Al_2O_3-700 and C-Al_2O_3-900 samples, suggesting lower crystallinity or a higher content of amorphous material in the nanoparticles obtained from the [$Al(NO_3)_3$] precursor.

The average crystallite size was estimated using the Debye–Scherrer equation, where D represents the crystallite size, θ is the Bragg angle (0.5824 rad), λ is the wavelength of the Cu Kα radiation (1.541 Å), β is the full width at half maximum of the diffraction peak (FWHM = 0.0332 rad), and k is the shape factor (0.9) [18]. For the calculation, the diffraction peaks with the highest intensities corresponding to the (311), (400), and (440) planes were selected. It is important to note that no instrumental broadening correction was applied in this analysis; therefore, the calculated values should be considered approximate estimates

of the crystallite size. The values obtained for the synthesized nanomaterials are presented in Table 1, observing a crystal size of approximately 4 nm for these samples, independent of the aluminum precursor or thermal treatment applied. This result agrees very well with the values reported by Ali and coworkers in their study on the synthesis of γ-Al_2O_3 nanoparticles from the hydrothermal method, in which crystal size values from 4 to 6.5 nm were determined for the aluminum oxide nanoparticles prepared from aluminum nitrate precursor and with a calcination temperature of 600 °C [32].

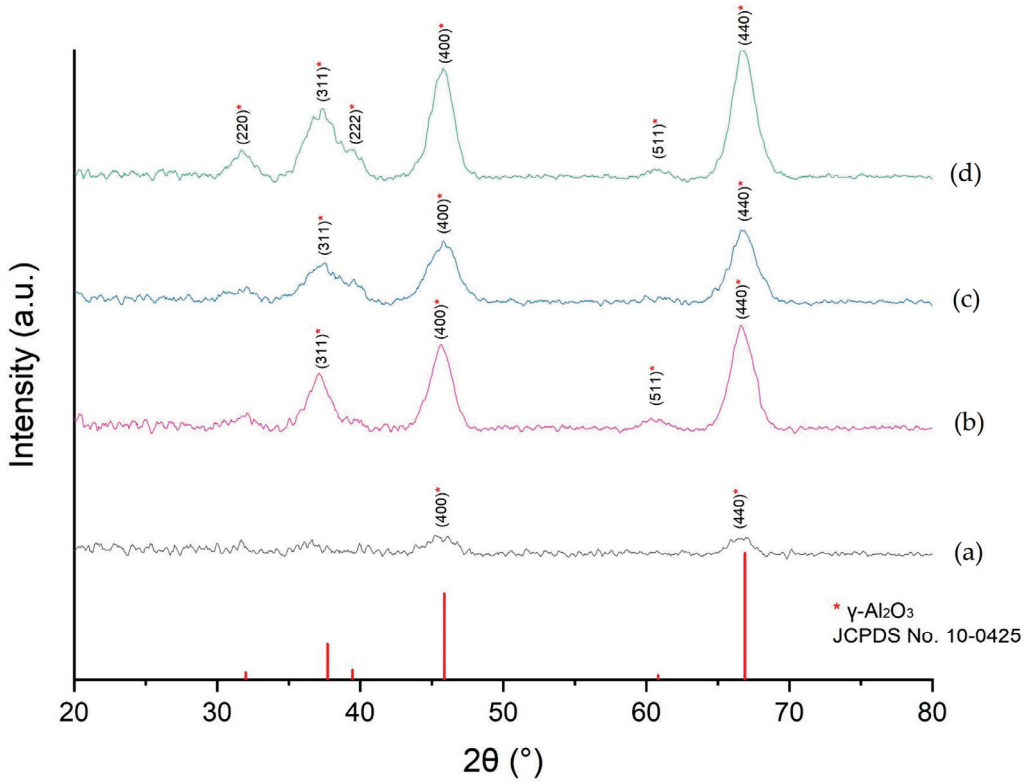


Figure 6. X-ray diffraction patterns of the samples (a) N-Al_2O_3-700; (b) N-Al_2O_3-900; (c) C-Al_2O_3-700; and (d) C-Al_2O_3-900.

Table 1. Crystal size of the Al_2O_3 nanoparticles.

Sample	Crystal Size (nm)
N-Al_2O_3-700	3.87
N-Al_2O_3-900	4.61
C-Al_2O_3-700	4.05
C-Al_2O_3-900	4.03

4. Conclusions

The main objective of this study was to develop a green synthesis route for aluminum oxide (Al_2O_3) nanoparticles using lemongrass (*Cymbopogon citratus*) extract and to evaluate the influence of different aluminum precursors and thermal treatments on their structural and morphological properties. The aluminum precursor and thermal treatment significantly influenced the size and crystal structure of the Al_2O_3 nanoparticles prepared by green synthesis using lemongrass extract. In particular, the samples derived from $AlCl_3$ exhibited more defined diffraction peaks and a more uniform morphology, as compared to those obtained from the $Al(NO_3)_3$ precursor. These observations highlight that the choice of aluminum precursor not only affects crystallinity and particle uniformity, but also governs

the interaction between Al^{3+} ions and the bioactive metabolites in the lemongrass extract, influencing nucleation, growth, and stabilization processes. Consequently, precursor selection is a key factor for optimizing the structural quality and performance of γ-Al_2O_3 nanoparticles synthesized via green routes.

Additionally, the presence of bioactive metabolites in the lemongrass (*Cymbopogon citratus*) extract (phenols, flavonoids, and aldehydes) might have reinforced these differences. The Cl^- ions released from the aluminum chloride precursor appear to play an active role in stabilizing the transient complex between Al^{+3} and the functional groups of the extract, thereby favoring the formation of more stable nanoparticles with higher crystallinity. In contrast, the $NO_3{}^-$ ions from the aluminum nitrate precursor appear to compete with the bioactive metabolites for coordination to aluminum, thereby limiting the efficiency of the stabilization process and contributing to the irregular shape and poor crystallinity of the aluminum oxide nanoparticles. These results are consistent with reports on the synthesis of boehmite and alumina, which show that the type of precursor directly affects the structure and properties of the nanoparticles [33–35]. In conclusion, the $AlCl_3$ precursor combined with the lemongrass extract provided a better route for synthesizing γ-Al_2O_3 nanoparticles by promoting crystallization at 700 °C, resulting in a lower energy cost than the thermal treatments at 900 °C required for the alumina nanoparticles obtained with the $Al(NO_3)_3$ reagent.

The green γ-Al_2O_3 nanoparticles synthesized in this study show promising potential for use as functional additives in advanced coating systems. Beyond their capacity to enhance wear resistance and UV protection, these nanomaterials represent a prospective solution for future applications in asbestos-cement products and protective coatings designed to reduce fiber release from aging asbestos surfaces. Such applications are particularly relevant in developing countries—such as Colombia—where asbestos has been recently banned, and efforts are underway to identify effective mitigation strategies that limit environmental dispersion while improving thermal comfort in housing. Accordingly, future research by the authors will focus on exploring the integration of these green-synthesized alumina nanoparticles into asbestos-cement rehabilitation systems and related coating technologies to improve thermal comfort.

Author Contributions: Conceptualization, A.H. and M.S.; methodology, M.C., L.T. and D.M.-B.; validation, A.H. and M.S.; formal analysis, M.C. and L.T.; investigation, M.C., L.T. and D.M.-B.; resources, M.S.; data curation, M.C. and D.M.-B.; writing—original draft preparation, M.C., L.T. and D.M.-B.; writing—review and editing, A.H. and M.S.; supervision, A.H. and M.S.; project administration, M.S.; funding acquisition, M.S. All authors have read and agreed to the published version of the manuscript.

Funding: The authors are grateful for funding from the University of Cartagena through the project "Plan de Fortalecimiento del grupo NIPAC. Acta No. 008-2023". Furthermore, this article forms part of the outcomes of the project "Formulation of a Comprehensive Strategy to Reduce the Impact of Asbestos on Public and Environmental Health in the Department of Bolívar", funded by the General System of Royalties of the Republic of Colombia (SGR), under project code BPIN 2020000100366. The project was implemented by the University of Cartagena in partnership with the Asbestos-Free Colombia Foundation (FundClas).

Data Availability Statement: The original contributions presented in this study are included in the article. Further inquiries can be directed to the corresponding author.

Conflicts of Interest: The authors declare no conflicts of interest.

References

1. Kam, O.R.; Bakouan, C.; Zongo, I.; Guel, B. Removal of Thallium from Aqueous Solutions by Adsorption onto Alumina Nanoparticles. *Processes* **2022**, *10*, 1826. [CrossRef]
2. Masemola, C.M.; Moloto, N.; Tetana, Z.; Linganiso, L.Z.; Motaung, T.E.; Linganiso-Dziike, E.C. Advances in Polyaniline-Based Composites for Room-Temperature Chemiresistor Gas Sensors. *Processes* **2025**, *13*, 401. [CrossRef]
3. Babiker, M.E.M. Eco-Environmentally Friendly Green Synthesis and Characterization of Aluminum Oxide Nanoparticles Using Leaf Extract of Mentha Pulegium. *Int. J. Chem. Biochem. Sci.* **2024**, *25*, 958–965. [CrossRef]
4. Ghotekar, S. Plant extract mediated biosynthesis of Al_2O_3 nanoparticles—A review on plant parts involved, characterization and applications. *Nanochem. Res.* **2019**, *4*, 163–169. [CrossRef]
5. Phrompet, C.; Sriwong, C.; Ruttanapun, C. Mechanical, dielectric, thermal and antibacterial properties of reduced graphene oxide (rGO)-nanosized C_3AH_6 cement nanocomposites for smart cement-based materials. *Compos. Part B* **2019**, *175*, 107128. [CrossRef]
6. Panda, A.; Gopikishan, S.; Mahapatra, S.; Barhai, P.; Das, A.; Banerjee, I. Bactericidal efficiency of nanostructured Al–O/Ti–O composite thin films prepared by dual magnetron reactive co-sputtering technique. *Ceram. Int.* **2014**, *40*, 4681–4690. [CrossRef]
7. Yuan, X.; Zhou, R.; Hu, M.; Wu, X.; Du, Y.; Ge, Y.; Yang, C.; Jiang, B.; Yang, R. Self-cleaning Al_2O_3-PTFE composite coatings on aluminum alloy with enhanced superhydrophobicity, corrosion and wear resistance. *Ceram. Int.* **2025**, *51*, 35483–35495. [CrossRef]
8. Zhu, D.; Xu, T.; Li, C.; Xu, D.; Liu, G.; Zhu, H.; Guo, Y. PES/Fe_3S_4@Al_2O_3 self-cleaning membrane with rapid catalysis for effective emulsion separation and dye degradation. *Process. Saf. Environ. Prot.* **2024**, *194*, 337–349. [CrossRef]
9. Ashour, M.; Mansour, A.T.; Abdelwahab, A.M.; Alprol, A.E. Metal Oxide Nanoparticles' Green Synthesis by Plants: Prospects in Phyto- and Bioremediation and Photocatalytic Degradation of Organic Pollutants. *Processes* **2023**, *11*, 3356. [CrossRef]
10. Gligor, O.; Mocan, A.; Moldovan, C.; Locatelli, M.; Crișan, G.; Ferreira, I.C. Enzyme-assisted extractions of polyphenols—A comprehensive review. *Trends Food Sci. Technol.* **2019**, *88*, 302–315. [CrossRef]
11. Sutradhar, P.; Debnath, N.; Saha, M. Microwave-assisted rapid synthesis of alumina nanoparticles using tea, coffee and triphala extracts. *Adv. Manuf.* **2013**, *1*, 357–361. [CrossRef]
12. Ansari, M.A.; Khan, H.M.; Alzohairy, M.A.; Jalal, M.; Ali, S.G.; Pal, R.; Musarrat, J. Green synthesis of Al_2O_3 nanoparticles and their bactericidal potential against clinical isolates of multi-drug resistant *Pseudomonas aeruginosa*. *World J. Microbiol. Biotechnol.* **2015**, *31*, 153–164. [CrossRef]
13. Rashid, S.N.; Bdewi, S.F.; Alshammary, E.T.; Hammad, R.T. Characterization of Alumina Nanoparticles Prepared Via Green Synthesis Method. *J. Univ. Anbar Pure Sci.* **2023**, *17*, 184–189. [CrossRef]
14. Wen, W.; Bai, Y.; Xu, M.; Gao, Y.; Yan, P.; Xu, H. Mechanistic Study of the Influence of Reactant Type and Addition Sequence on the Microscopic Morphology of α-Al_2O_3. *Appl. Sci.* **2024**, *14*, 2438. [CrossRef]
15. Zheng, S.; Lu, Y.; Zhao, H. Green Synthesis and Particle Size Control of High-Purity Alumina Based on Hydrolysis of Alkyl Aluminum. *Materials* **2025**, *18*, 2100. [CrossRef] [PubMed]
16. Solano, R.A.; Herrera, A.P.; Maestre, D.; Cremades, A. Fe-TiO_2 Nanoparticles Synthesized by Green Chemistry for Potential Application in Waste Water Photocatalytic Treatment. *J. Nanotechnol.* **2019**, *2019*, 4571848. [CrossRef]
17. Solano, R.; Patiño-Ruiz, D.; Herrera, A. Preparation of modified paints with nano-structured additives and its potential applications. *Nanomater. Nanotechnol.* **2020**, *10*, 1847980420909188. [CrossRef]
18. Gharbi, A.H.; Laouini, S.E.; Hemmami, H.; Bouafia, A.; Gherbi, M.T.; Ben Amor, I.; Hasan, G.G.; Abdullah, M.M.S.; Trzepieciński, T.; Abdullah, J.A.A. Eco-Friendly Synthesis of Al_2O_3 Nanoparticles: Comprehensive Characterization Properties, Mechanics, and Photocatalytic Dye Adsorption Study. *Coatings* **2024**, *14*, 848. [CrossRef]
19. Ying, S.; Guan, Z.; Ofoegbu, P.C.; Clubb, P.; Rico, C.; He, F.; Hong, J. Green synthesis of nanoparticles: Current developments and limitations. *Environ. Technol. Innov.* **2022**, *26*, 102336. [CrossRef]
20. Rodríguez-Rojas, M.d.P.; Bustos-Terrones, V.; Díaz-Cárdenas, M.Y.; Vázquez-Vélez, E.; Martínez, H. Life Cycle Assessment of Green Synthesis of TiO_2 Nanoparticles vs. Chemical Synthesis. *Sustainability* **2024**, *16*, 7751. [CrossRef]
21. Abady, M.M.; Mohammed, D.M.; Soliman, T.N.; Shalaby, R.A.; Sakr, F.A. Sustainable synthesis of nanomaterials using different renewable sources. *Bull. Natl. Res. Cent.* **2025**, *49*, 24. [CrossRef]
22. Al-Byati, M.K.A.A.; Al-Duhaidahawi, A.M.J. Synthesis of Aluminum Oxide Nanoparticles and Their Applications in Dye-Sensitized Solar Cells as a Clean Energy. *Biomed. Chem. Sci.* **2023**, *2*, 48–52. [CrossRef]
23. Anandgaonker, P.; Kulkarni, G.; Gaikwad, S.; Rajbhoj, A. Synthesis of TiO_2 nanoparticles by electrochemical method and their antibacterial application. *Arab. J. Chem.* **2019**, *12*, 1815–1822. [CrossRef]
24. Yang, H.; Han, R.; Li, F. Synthesis of mesoporous γ-alumina and its catalytic performance in dichloropropanol cyclization. *Quim. Nova* **2019**, *42*, 851–858. [CrossRef]
25. Praveen, P.; Viruthagiri, G.; Mugundan, S.; Shanmugam, N. Structural, optical and morphological analyses of pristine titanium di-oxide nanoparticles—Synthesized via sol–gel route. *Spectrochim. Acta Part A Mol. Biomol. Spectrosc.* **2014**, *117*, 622–629. [CrossRef]

26. Ali, S.; Abbas, Y.; Zuhra, Z.; Butler, I.S. Synthesis of γ-alumina (Al_2O_3) nanoparticles and their potential for use as an adsorbent in the removal of methylene blue dye from industrial wastewater. *Nanoscale Adv.* **2019**, *1*, 213–218. [CrossRef] [PubMed]
27. Suaebah, E.; Yunata, E.E.; Wijaya, A.S.N. The sintering temperature effect of Alumina (Al_2O_3) ceramic using the sol-gel method. *J. Phys. Conf. Ser.* **2024**, *2900*, 012044. [CrossRef]
28. Manyasree, D.; Kiranmayi, P.; Kumar, R. Synthesis, characterization and antibacterial activity of aluminium oxide nanoparticles. *Int. J. Pharm. Pharm. Sci.* **2018**, *10*, 32–35. [CrossRef]
29. Khine, E.E.; Kaptay, G. Identification of Nano-Metal Oxides That Can Be Synthesized by Precipitation-Calcination Method Reacting Their Chloride Solutions with NaOH Solution and Their Application for Carbon Dioxide Capture from Air—A Thermodynamic Analysis. *Materials* **2023**, *16*, 776. [CrossRef]
30. Li, Z.; Wang, D.; Shen, J.; Chen, J.; Wu, C.; Qu, Z.; Luo, K.; Meng, Z.; Li, Y. Study on the Synthesis of High-Purity γ-Phase Mesoporous Alumina with Excellent CO_2 Adsorption Performance via a Simple Method Using Industrial Aluminum Oxide as Raw Material. *Materials* **2021**, *14*, 5465. [CrossRef]
31. Liu, Y.; Ma, D.; Han, X.; Bao, X.; Frandsen, W.; Wang, D.; Su, D. Hydrothermal synthesis of microscale boehmite and gamma nanoleaves alumina. *Mater. Lett.* **2008**, *62*, 1297–1301. Available online: www.fhi-berlin.mpg.de/ac (accessed on 27 May 2025). [CrossRef]
32. Buwono, H.P.; Adiwidodo, S.; Wicaksono, H.; Firmansyah, H.I. Hydrothermal synthesis and characterization of nano-particles γ-Al_2O_3. *IOP Conf. Ser. Mater. Sci. Eng.* **2021**, *1073*, 012011. [CrossRef]
33. Xiao, J.; Qin, Q.; Wan, Y.; Zhou, F.; Chen, Y.-B.; Li, J.; Liu, Y.-X. Effect of anions on preparation of ultrafine α-Al_2O_3 powder. *J. Cent. South Univ. Technol.* **2007**, *14*, 773–778. [CrossRef]
34. Abdollahifar, M.M.; Hidaryan, M.; Jafari, P. The role anions on the synthesis of AlOOH nanoparticles using simple solvothermal method. *Bol. Soc. Esp. Ceram. Vidr.* **2018**, *57*, 66–72. [CrossRef]
35. Toledo, R.R.; Santoyo, V.R.; Sánchez, C.D.M.; Rosales, M.M. Effect of aluminum precursor on physicochemical properties of Al_2O_3 by hydrolysis/precipitation method. *Nova Sci.* **2018**, *10*, 83–99. [CrossRef]

Disclaimer/Publisher's Note: The statements, opinions and data contained in all publications are solely those of the individual author(s) and contributor(s) and not of MDPI and/or the editor(s). MDPI and/or the editor(s) disclaim responsibility for any injury to people or property resulting from any ideas, methods, instructions or products referred to in the content.

processes

MDPI

Article

$Bi(C_6N_7O_3)$ Nanospheres: A Novel Homogenous Photocatalyst for Efficient Treatment of Antibiotic in Water

Rongrong Jia [1], Mingchuan Tang [1], Mengshan Hou [1], Haiheng Xing [1], Yuxing Cai [1], Jianhao Wu [1], Xiaozhuo Wang [1], Jinchao Chen [1], Lan Li [1], Chengchao Jin [1], Zhi Chen [1,*] and Xiaojing Wang [2,*]

[1] College of Materials and Chemistry, China Jiliang University, 258 Xueyuan Street, Xiasha Higher Education Zone, Hangzhou 310018, China; rongrongjia@cjlu.edu.cn (R.J.)
[2] School of Electronic and Electrical Engineering, Wuhan Textile University, Wuhan 430074, China
* Correspondence: zchen@cjlu.edu.cn (Z.C.); xj_wang@wtu.edu.cn (X.W.); Tel./Fax: +86-571-86835738 (Z.C.)

Abstract: The development of photocatalyst material is vital for the practical application of environmental purification, solar energy conversion, and chemical production. In this work, a spherical $Bi(C_6N_7O_3)$ photocatalyst is successfully prepared by replacing K^+ of rod-shaped $K_3[C_6N_7O_3]$ with Bi^{3+} ions through the ion exchange method, which demonstrates an improved homogeneous photodegradation efficiency over antibiotics in water compared to pristine $K_3[C_6N_7O_3]$. Under visible light irradiation, $Bi(C_6N_7O_3)$ degraded 81% of tetracycline hydrochloride within 60 min, and the rate constant was 1.8 and 79.1 times greater than $K_3[C_6N_7O_3]$ and bulk g-C_3N_4, respectively. Scavenger experiments revealed that superoxide radicals and holes are the primary active species in the photocatalytic process. This study presents a promising route for designing high-performance visible-light photocatalysts by a simple ion-exchange approach for environmental applications.

Keywords: antibiotic degradation; $Bi(C_6N_7O_3)$ sphere; visible-light photocatalysis; homogeneous photocatalysis

1. Introduction

Environmental pollution caused by antibiotic misuse directly threatens human life and health [1], which is one of the key problems around the world and needs to be addressed urgently [2–6]. The traditional methods dealing with antibiotic pollution are mainly physical adsorption and microbiological treatment [7]. However, these methods have been labeled as insufficient due to the unconquerable drawbacks such as limited choice of adsorbents, potential for secondary contamination, high cost, long treatment time, and ineffective removal. Developing a green approach is vital for the efficient control of antibiotic pollution. Photocatalytic oxidation directly employs solar energy as a light source to drive catalysis [8], which has become a green and ideal approach to monitor the antibiotic pollutants [9–13].

Graphitic phase carbon nitride (g-C_3N_4) is a prospective polymer photocatalyst with the advantages of strong visible-light response, ease of preparation, and chemical stability, which has been intensively studied and broadly applied in visible-light photocatalysis, such as hydrogen production via water splitting and degradation of the emerging pollutant [14]. However, the practical application is severely restricted due to the drawbacks, such as a lack of active sites and a faint visible-light response. Great efforts have been made to overcome these defects, and strategies such as constructing hollow or porous structures have been developed to enlarge the specific area recently [15]. Nevertheless, most of the currently reported g-C_3N_4 photocatalysts are heterogeneous phases. They are still suffering

from the main insufficiencies such as limited specific surface area and active sites, which hinder the practical applications of g-C_3N_4-type photocatalyst [14,16].

On the contrary, homogeneous photocatalysis deals with a photocatalytic reaction where the catalyst and reactants exist in the same phase, facilitating the complete access of reactants toward the active sites, which may be an alternative approach to optimize the photocatalytic performance. The construction of homogeneous photocatalysts has thrived in recent years. In 2018, Huang et al. successfully synthesized a homogeneous CN-based photocatalyst, which demonstrated an improved photocatalytic activity in comparison with that of the heterogeneous counterpart [17]. However, the prepared photocatalyst is solely soluble in certain corrosive solvents, including CH_3SO_2OH and H_2SO_4, which limits its wide application in water. Given the urgent demand for water purification and pollutant decomposition, the fabrication of water-soluble photocatalysts remains challenging. Recently, a series of CN derivatives such as basic cyanurate of $K_3[C_6N_7(NCN)_3]$ and $C_6N_7O_3H_3$ with distinct optical properties have been developed via alkali treatment, which are water-soluble compounds [18,19]. In 2021, Yang et al. successfully prepared rod-shaped $K_3[C_6N_7O_3]$ compounds from top to bottom by reacting melon polymer with a hot strong base and applied it as a homogeneous photocatalyst in removing antibiotic residues in water for the first time [20]. The obtained photocatalyst showed 10-fold higher photocatalytic activity than that of bulk g-C_3N_4. However, a further improvement of activity is necessary for the practical application of homogeneous photocatalysis.

In this study, $Bi(C_6N_7O_3)$ was successfully synthesized by replacing the K^+ ion in $K_3[C_6N_7O_3]$ with the Bi^{3+} ion from an ion-exchange process under solvothermal conditions, which showed improved photocatalytic activity and excellent stability toward the visible-light degradation of antibiotic residue in aqueous solutions. The substitution of K^+ with Bi^{3+} may introduce a high-valence metal center, effectively modulating the electronic structure and facilitating charge carrier separation, which promotes the photocatalytic behaviors. The as-prepared $Bi(C_6N_7O_3)$ shows 79.1 and 1.8-fold greater activity than those of g-C_3N_4 and $K_3[C_6N_7O_3]$, respectively. Several techniques have been utilized to explore the factors contributing to the enhanced properties and stability. The active species are identified, and a reaction mechanism is proposed in the end. This work offers an easy strategy of ion exchange to manipulate the photocatalytic properties, which may spur the development and application of homogeneous photocatalysis.

2. Experimental

2.1. Chemicals and Materials

Melamine ($C_3N_3(NH_2)_3$, 99%) was bought from Sinopharm Chemical Reagent Co., Ltd. (Shanghai, China). Potassium hydroxide (KOH, 85%) was obtained from Aladdin Industrial Corporation. (Shanghai, China). N,N-dimethylformamide ($HCON(CH_3)_2$, 99.5%) and bismuth nitrate pentahydrate ($Bi(NO_3)_3{\cdot}5H_2O$, 99%) were obtained from Hangzhou Mick Chemical Reagent Co., Ltd. (Hangzhou, China). Methanol (CH_3OH, 99.7%) was obtained from Hangzhou Gaojing Fine Chemical Industry Co., Ltd. (Hangzhou, China). All the reagents were directly used after purchase.

2.2. Preparation

Preparation of rod-shaped $K_3[C_6N_7O_3]$. The preparation of $K_3[C_6N_7O_3]$ is followed by the previous report [20]. Typically, 14.0 g of KOH and 5.0 g of melon powder were added to 50.0 mL of aqueous solution, mixed thoroughly, and transferred to a 150 mL round-bottom flask. Subsequently, the flask was positioned in an oil bath and refluxed at 130 °C for 2 h under magnetic stirring until the yellow-colored solution turned transparent. The hot solution was filtered, and the filtrate was stored in a refrigerator for 12 h. Finally,

the precipitated solid was separated via vacuum filtration and washed repeatedly with absolute ethanol, and then dried under vacuum at 70 °C for 6 h to yield the product of potassium cyanurate $K_3[C_6N_7O_3]$.

Preparation of $Bi(C_6N_7O_3)$ nanospheres. 1.455 g $Bi(NO_3)_3 \cdot 5H_2O$ and 1.005 gas-prepared $K_3[C_6N_7O_3]$ were dispersed in 50 mL of mixed solution (DMF:CH_3OH = 3:1) and stirred for 30 min to form a homogeneous solution. Subsequently, the solution was sealed in an autoclave equipped with polytetrafluoroethylene and heated at 120 °C for 16 h at a rate of 1 °C per minute. After that, the synthesized $Bi(C_6N_7O_3)$ was washed with absolute ethyl alcohol multiple times and dried at 70 °C for 12 h under vacuum.

2.3. Characterization

X-ray diffraction (XRD) pattern was detected on the a Panalytical X'Pert'3 Powder instrument (Malvern Panalytical, Almelo, The Netherlands) applying Cu Kα (λ = 1.5406 Å) as the source. Fourier transform infrared spectroscopy (FTIR) was performed on a Bruker Tensor 27 spectrometer (Bruker Corporation, Billerica, MA, USA). Scanning electron microscopy (SEM) pictures and energy dispersive X-ray (EDX) patterns were carried out on a ZEISS Sigma 300 microscope (Carl Zeiss AG, Oberkochen, Germany). X-ray photoelectron spectroscopy (XPS) was recorded on a Thermo Scientific K-Alpha instrument (Thermo Fisher Scientific, Waltham, MA, USA). UV-visible diffuse spectrum (UV-vis DRS) was performed on a Shimadzu UV-3600 UV-visible spectrophotometer (Shimadzu Corporation, Kyoto, Japan). Full-wavelength UV-visible absorption spectra were recorded on the UV-2600 UV-visible spectrophotometer (Shanghai Sunny Hengping Scientific Instrument Co., Ltd., Shanghai, China).

2.4. Photocatalytic Degradation Measurements

TC-HCl was employed as the typical antibiotic residue to evaluate the photocatalytic activities of the prepared samples. For simulated visible light, a 300 W Xenon lamp equipped with a 420-nm cut-off filter was employed, with a spectral irradiance of 272.0 mW/cm^2. Moreover, a circulating cooling system was applied to maintain the reaction temperature at around 20 °C. Briefly, 20.0 mg of the prepared photocatalyst was dispersed in 100 mL of TC-HCl solution (10, 20, and 50 mg/L) using a 150 mL beaker as the reactor. The solution was stirred in the dark for 30 min to reach adsorption–desorption equilibrium. Then, the solution was positioned under the simulated light source, with the bottom of the reactor positioned at a vertical distance of 13 cm from the lamp, and the lamp was turned on for illumination with constant magnetic stirring (550 rpm). The initial pH of the solution before the photocatalytic reaction was measured to be 6.76. 5.0 mL of solution was collected every 10 min, and the supernatant after centrifugation was taken for measurement on a UV-2600 spectrophotometer. All experiments were repeated at least three times to ensure reproducibility.

3. Results and Discussion

The crystal structure of $Bi(C_6N_7O_3)$ was analyzed using XRD, as shown in Figure 1a. The diffraction pattern was compared to that of $K_3[C_6N_7O_3]$, considering the absence of a reference XRD pattern for $Bi(C_6N_7O_3)$. The prominent peak at 28.12° corresponded to the interlayer stacking of aromatic units, while the diffraction peak at approximately 14.02° was characteristic of the melon structure, which was ascribed to the cohesive and ordered arrangement of cyanuric acid units [21]. A notable rightward shift in the diffraction peak positions for $Bi(C_6N_7O_3)$ was observed when compared to the JCPDS pattern of $K_3[C_6N_7O_3]$. This shift is attributed to the substitution of Bi^{3+} ions, which have a smaller ionic radius than K^+ ions. The introduction of smaller dopant atoms into the lattice leads

to a reduction in the unit cell parameters, thereby causing the rightward shift of the XRD peaks.

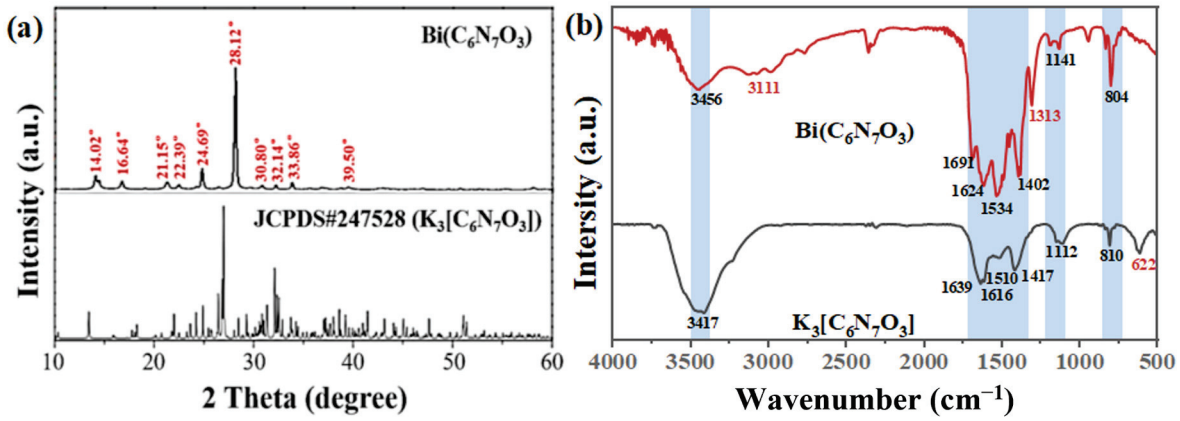


Figure 1. (**a**) XRD patterns of $Bi(C_6N_7O_3)$ and $K_3[C_6N_7O_3]$, (**b**) Recorded FTIR spectra of $K_3[C_6N_7O_3]$ and $Bi(C_6N_7O_3)$. The black and red lines correspond to the $K_3[C_6N_7O_3]$ and $Bi(C_6N_7O_3)$ samples, respectively.

As displayed in Figure 1b, the FTIR spectra of $K_3[C_6N_7O_3]$ and $Bi(C_6N_7O_3)$ were consistent with previous studies [18]. The peak at 804 cm^{-1} corresponded to the bending vibration associated with the S-triazine unit. In the range of 1000–1600 cm^{-1}, the observed band was attributed to the stretching vibration of the C-N heterocyclic ring [22]. The peaks at 1624, 1534, and 1402 cm^{-1} were associated with the stretching vibration of heptazine-derived repeating units, respectively [23]. Additionally, the broad band between 3111 and 3456 cm^{-1} was attributed to the stretching vibration of N-H bonds and the presence of absorbed water [24]. These characteristic features collectively confirm the identity of the prepared sample as $Bi(C_6N_7O_3)$.

The chemical composition and valence states of $Bi(C_6N_7O_3)$ were investigated using XPS measurement. As shown in Figure 2a, the presence of all constituent elements, including carbon (C), nitrogen (N), oxygen (O), and bismuth (Bi), corroborated the above discussion. No peak belonging to potassium (K) was observed, indicating the complete substitution of K by Bi. The fine C 1s spectrum and its deconvoluted peaks, presented in Figure 2b, revealed two principal peaks at 284.8 eV (C-C) and 288.6 eV (N-C=N), corresponding to different carbon environments within $Bi(C_6N_7O_3)$ [25]. In addition, the peak at 286.5 eV is likely ascribed to the presence of C-O-Bi groups. Figure 2c displayed the N 1s spectrum with a peak at 398.4 eV, characteristic of the sp2 hybridized N atom in C=N-C bonds [26]. The peaks at 400.0 eV and 401.1 eV are tentatively assigned to N atoms in N-(C)3 and N-H configurations, respectively [27]. The faint peak at 404.8 eV was related to π-excitation [28]. The O 1s (Figure 2d) exhibited a peak at 531.2 eV, which corresponded to C-O-Bi bonds in $Bi(C_6N_7O_3)$ [29]. Figure 2e revealed two distinct peaks at 159.4 eV (Bi $4f_{7/2}$) and 164.7 eV (Bi $4f_{5/2}$), which were indicative of the bismuth species present within the compound. These XPS results confirm that the prepared $Bi(C_6N_7O_3)$ has an aromatic skeleton composed of heptazine units, suggesting the successful synthesis of the target compound.

Figure 3a shows the SEM image of the $Bi(C_6N_7O_3)$ sample. The prepared $Bi(C_6N_7O_3)$ had an irregular spherical shape with diameters close to 5 μm. As seen in Figure 3b, the chemical composition of Bi was via EDS and peaks at ~0.3, ~0.4, ~0.5, and ~2.4 keV were detected in the EDS spectra, assigned to the elements C, N, O, and Bi, respectively, indicating that C, N, O, and Bi atoms coexisted in $Bi(C_6N_7O_3)$ [30]. According to the EDS analysis, the atomic contents of C and N were 31.53% and 36.28%, respectively. The

ratio of C to N atoms was 0.87, which is consistent with the structural formula. The EDS elemental mappings of $Bi(C_6N_7O_3)$, as demonstrated in Figure 3c–f confirmed the uniform distribution of all the elements within $Bi(C_6N_7O_3)$. These results further confirm the successful preparation of $Bi(C_6N_7O_3)$.

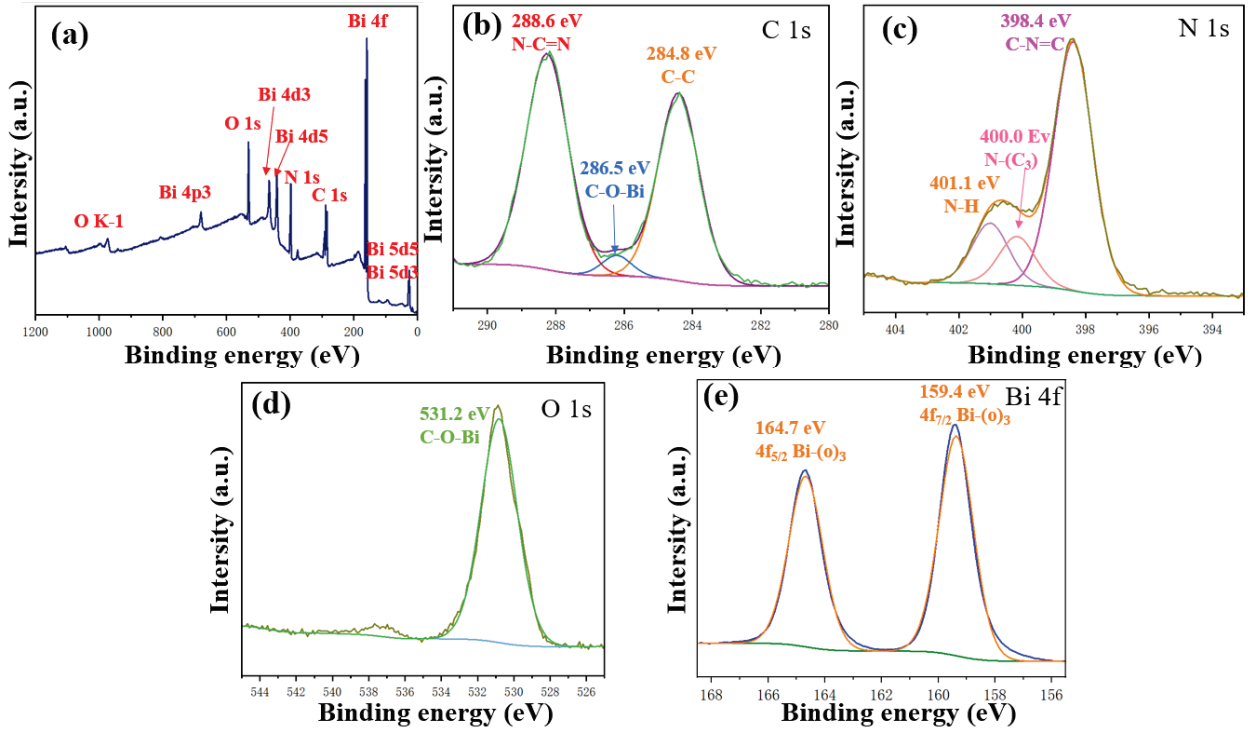


Figure 2. XPS spectra of $Bi(C_6N_7O_3)$: (**a**) survey spectrum, (**b**) C 1s spectrum, (**c**) N 1s spectrum, (**d**) O 1s spectrum, and (**e**) Bi 4f spectrum.

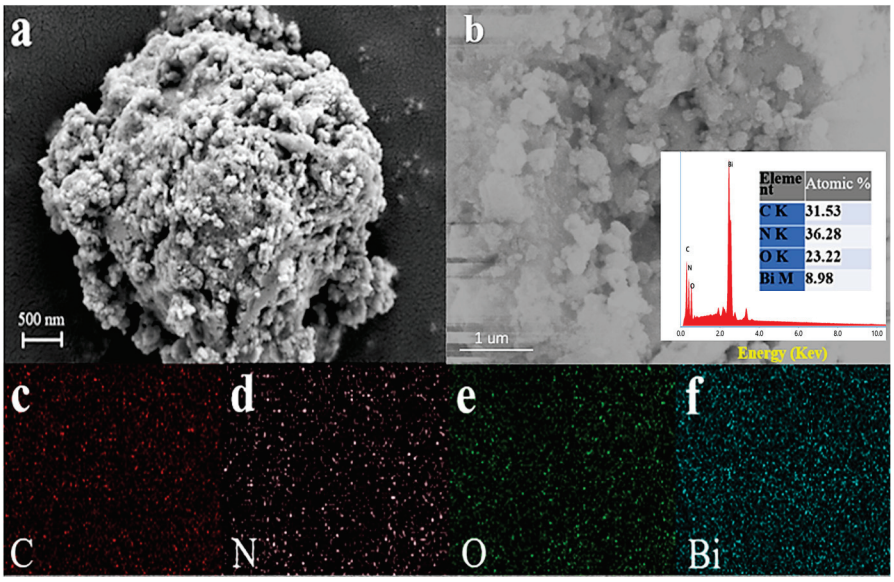


Figure 3. (**a**) SEM image of $Bi(C_6N_7O_3)$, (**b**–**f**) EDS elemental mappings of $Bi(C_6N_7O_3)$.

Figure 4 presents the homogeneous degradation profiles of tetracycline hydrochloride (TC-HCl) in aqueous solution under visible-light irradiation using different dosages of photocatalysts. As depicted in Figure 4a, g-C_3N_4 exhibited minimal degradation of TC-HCl under visible light, with only a 2.4% reduction observed. In contrast, significant degradation was achieved with $K_3[C_6N_7O_3]$ and $Bi(C_6N_7O_3)$ as photocatalysts, resulting

in efficiencies of 63% and 81%, respectively, within 60 min. Further investigation into the photocatalytic degradation efficiency of $Bi(C_6N_7O_3)$ on TC-HCl solutions with different concentrations was shown in Figure 4b. Photocatalytic degradation efficiencies of TC-HCl solutions with initial concentrations of 20, 30, and 50 mg/L were 81%, 75%, and 55%, respectively. These results confirm that the synthesized $Bi(C_6N_7O_3)$ is an effective photocatalyst for homogeneous processes, demonstrating its potential for practical applications in water treatment.

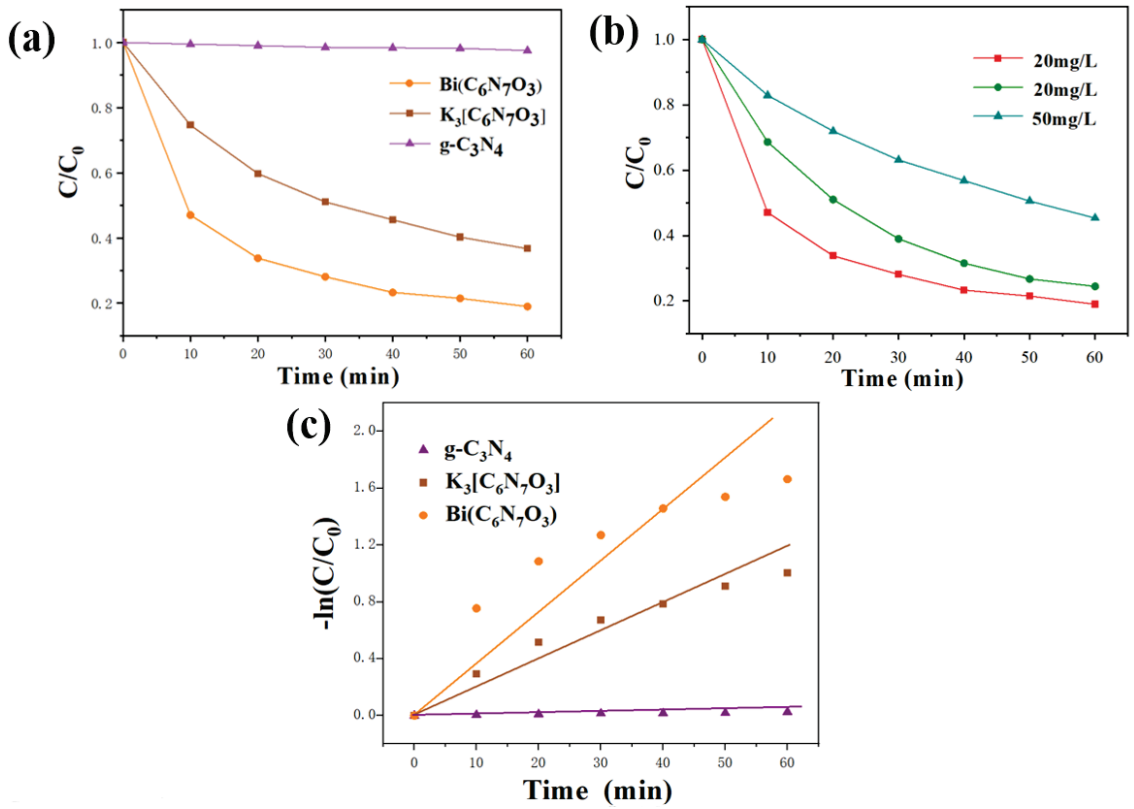


Figure 4. (**a**) Photocatalytic degradation efficiency of TC-HCl under the visible light irradiation using g-C_3N_4, $K_3[C_6N_7O_3]$, and $Bi(C_6N_7O_3)$; (**b**) Degradation efficiency of TC-HCl solutions with different concentrations (20, 30, and 50 mg/L) using $Bi(C_6N_7O_3)$; (**c**) Pseudo-first-order kinetic fitting of TC-HCl degradation over the three photocatalysts.

The photocatalytic activity of the obtained samples was quantified using a pseudo-first-order model, Equation (1).

$$k = \frac{-ln(C_t/C_0)}{t} \quad (1)$$

where C_0 represented the initial TC-HCl concentration, and C_t represented the TC-HCl concentration following t min of irradiation. The optimum slope, corresponding to the apparent rate constant k_{app}, was obtained by the method of least squares [28]. In Figure 4c, the calculated k_{app} values for g-C_3N_4, $K_3[C_6N_7O_3]$, and $Bi(C_6N_7O_3)$ photocatalysts were 0.00042 min^{-1}, 0.01873 min^{-1}, and 0.03323 min^{-1}, respectively. Obviously, the k_{app} value of $Bi(C_6N_7O_3)$ is 79.1 and 1.8-fold higher than that of g-C_3N_4 and $K_3[C_6N_7O_3]$, demonstrating the superior photocatalytic activity of $Bi(C_6N_7O_3)$.

The photocatalytic performance of $Bi(C_6N_7O_3)$ was compared with that of the recently reported photocatalysts. As summarized in Table 1, the $Bi(C_6N_7O_3)$ catalyst exhibits a notably higher k_{app} than most of the compared materials, underscoring its superior activity and reinforcing the advancement presented in this study.

Table 1. Comparison of the k_{app} for various photocatalysts reported in recent studies.

Year	Photocatalyst	k_{app} (min^{-1})
2025	$Bi(C_6N_7O_3)$	0.033
2025	$ZnO_2/Bi_2O_2CO_3$ [31]	0.012
2025	20SA-CN [32]	0.012
2025	2% Ni-decorated melem hydrate/g-C_3N_5 [33]	0.032
2025	EG-BiOCl [34]	0.019
2025	$Fe_{0.1}Co_{0.05}Ni_{0.05}$/CdS [35]	0.031

The reusability and sustainability of photocatalysts are crucial for their practical applications. The $Bi(C_6N_7O_3)$ photocatalyst in ethanol was collected and washed after the initial photocatalytic run and then subjected to an additional three cycles of the same procedure, as illustrated in Figure 5. A decline in photocatalytic activity with each cycle was observed, which could be attributed to the gradual leaching of Bi^{3+} from the $(C_6N_7O_3)^{3-}$ framework as the cycles progress. Additionally, $Bi(C_6N_7O_3)$ has good solubility, readily soluble in water, leading to noticeable mass loss during the recovery process in ethanol, considering that ethanol contains a small amount of water.

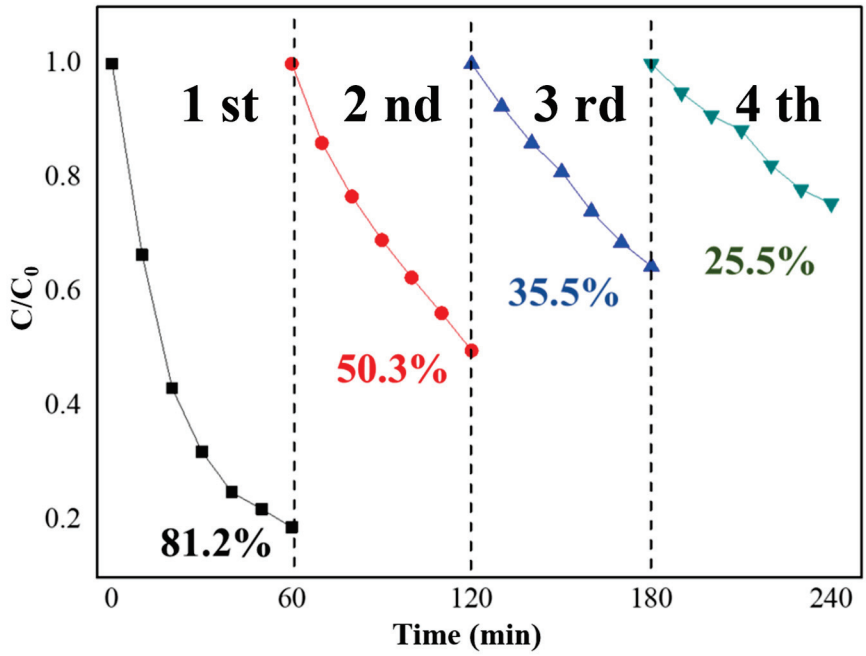


Figure 5. Cyclic stability tests of $Bi(C_6N_7O_3)$ for TC-HCl photodegradation.

The underlying mechanism of the enhanced photocatalytic property of $Bi(C_6N_7O_3)$ was investigated. The UV-Vis diffuse reflection absorption spectra for the synthesized photocatalysts were measured, as depicted in Figure 6a. Both $K_3[C_6N_7O_3]$ and $Bi(C_6N_7O_3)$ demonstrated strong absorption across the UV-visible spectrum, with distinct absorption edges observed at 438 and 486 nm. These edges suggest that the samples can capture a fraction of the visible light. The bandgap of the $K_3[C_6N_7O_3]$ and $Bi(C_6N_7O_3)$ was calculated using the Tauc plot, as shown in Figure 6b, yielding bandgap values of 2.8 eV for $K_3[C_6N_7O_3]$ and 2.2 eV for $Bi(C_6N_7O_3)$. Compared to $K_3[C_6N_7O_3]$, the band gap of $Bi(C_6N_7O_3)$ was reduced, allowing it to absorb more light energy and generate more electron-hole pairs, increasing its photosensitivity and photovoltaic effect.

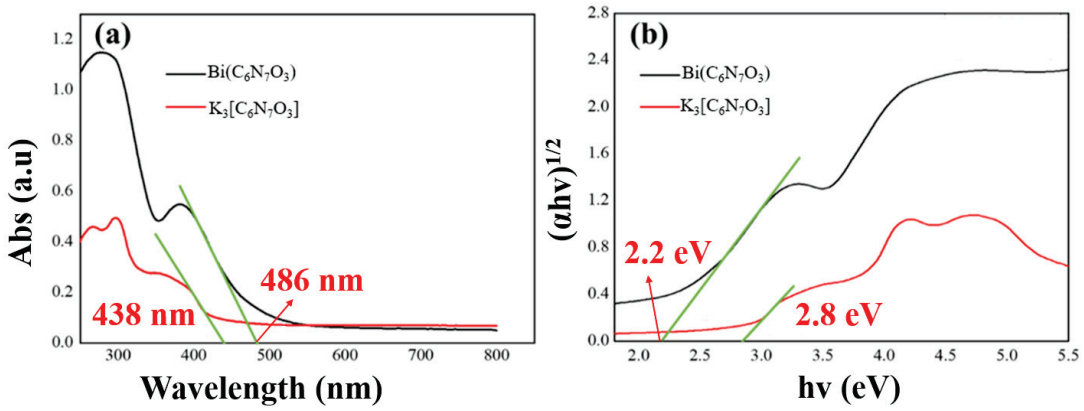


Figure 6. (**a**) UV-vis absorption spectrum of $K_3[C_6N_7O_3]$ and $Bi(C_6N_7O_3)$; (**b**) Tauc plots derived from UV-Vis spectra.

Photocurrent measurement upon light illumination is a robust indicator of the efficiency of photogenerated carrier separation and transport, which are key factors in photocatalytic performance. Figure 7a showed the photocurrent responses of g-C_3N_4, $K_3[C_6N_7O_3]$, and $Bi(C_6N_7O_3)$ under visible light irradiation in ethanol, considering the water solubility of the latter two compounds. Upon turning on the light source, both $K_3[C_6N_7O_3]$ and $Bi(C_6N_7O_3)$ exhibited significant photocurrent, with $Bi(C_6N_7O_3)$ exhibiting the highest response. This suggests that $Bi(C_6N_7O_3)$ might have a more efficient separation and migration of photoexcited carriers compared to g-C_3N_4 and $K_3[C_6N_7O_3]$. Furthermore, EIS was utilized to evaluate the electron transfer characteristics of the prepared samples, as depicted in Figure 7b. $Bi(C_6N_7O_3)$ had the smallest arc diameter among these samples, indicating the lowest electron transfer resistance. These results show that $Bi(C_6N_7O_3)$ has a narrow band gap, a high charge separation capability, and a low electron transfer resistance, which collectively improve its photocatalytic performance.

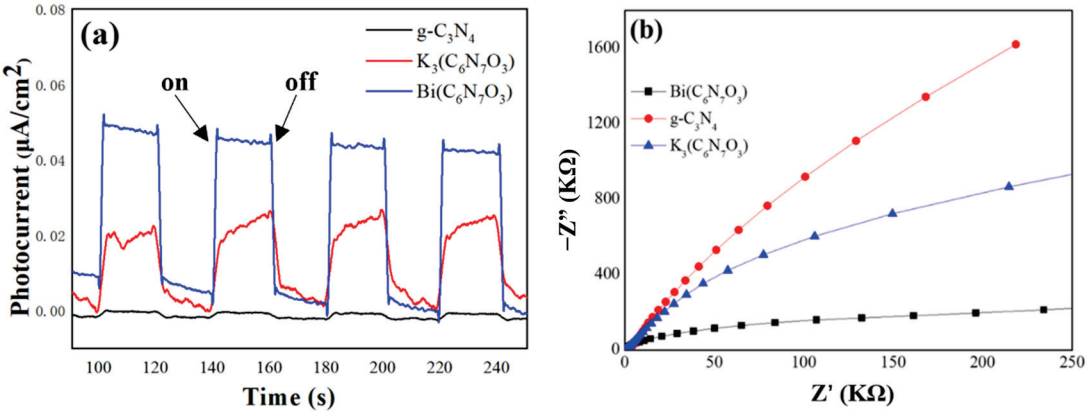


Figure 7. (**a**) Transient photocurrent response under visible light irradiation and (**b**) Electrochemical impedance spectroscopy (EIS) Nyquist plots of g-C_3N_4, $K_3[C_6N_7O_3]$, and $Bi(C_6N_7O_3)$.

As shown in Figure 8, radical trapping experiments were conducted to identify the active substances involved in the photocatalytic reactions. Ethylenediamine tetraacetic acid (EDTA-2Na), p-benzoquinone (BQ, 0.5 mM), and tert-butanol (TBA, 2 mM) were employed as the scavengers of photogenerated holes (h^+), superoxide radicals ($\cdot O_2^-$), and hydroxyl radicals (·OH), respectively. The low concentration of BQ used (0.5 mM) is well-established in the literature to specifically quench $\cdot O_2^-$ without significant side reactions under standard photocatalytic conditions [36,37]. Similarly, TBA is a highly specific scavenger for ·OH, whose steric hindrance makes reactions with $\cdot O_2^-$ or h^+ unlikely [37]. The addition

of BQ and EDTA-2Na resulted in a significant decrease in photocatalytic activity, indicating that both $\cdot O_2^-$ and h^+ were primary reactive species in the photocatalytic process. In contrast, the introduction of TBA did not affect the degradation efficiency, suggesting that ·OH had an insignificant effect in the photocatalytic process [38].

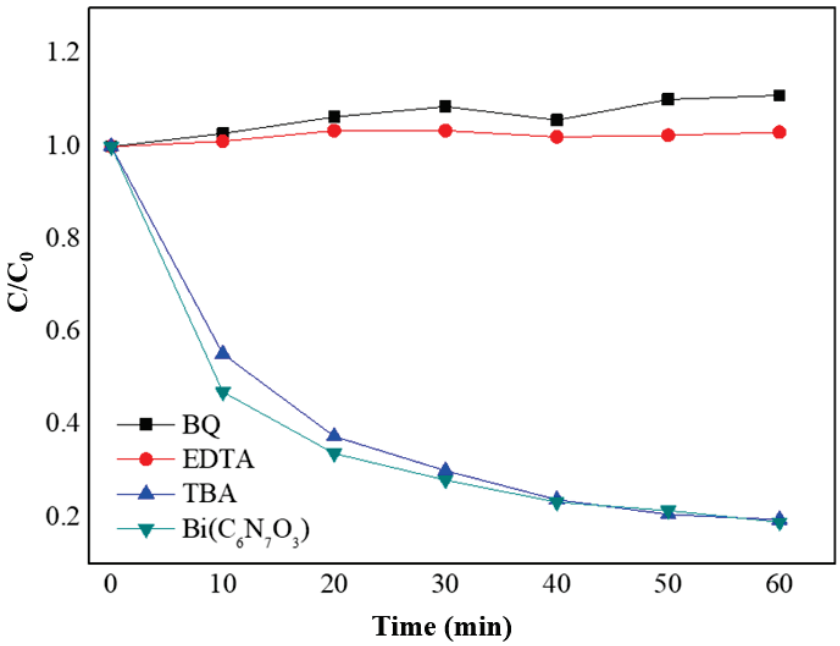


Figure 8. Effects of different radical scavengers (TBA for ·OH, EDTA-2Na for h^+, BQ for $\cdot O_2^-$) on the photocatalytic degradation of TC-HCl over $Bi(C_6N_7O_3)$.

The photocatalytic performance of the $Bi(C_6N_7O_3)$ nanospheres was compared with a recently reported Fe-TiO_2/biochar composite, similarly identifying $\cdot O_2^-$ as the predominant reactive species [39]. The k_{app} of our $Bi(C_6N_7O_3)$ catalyst for TC-HCl degradation was calculated to be 1.99 h^{-1} (from 0.03323 min^{-1}), which is higher than the k_{app} of 0.202 h^{-1} on Fe-TiO_2/biochar composite.

The Mott–Schottky plot for $Bi(C_6N_7O_3)$ displayed a positive slope, as illustrated in Figure 9a, which indicates that the sample is an n-type semiconductor. With respect to the normal hydrogen electrode, the conduction band (CB) energy level of an n-type semiconductor is measured to be −0.62 V. Typically, the conduction band energy level of an n-type semiconductor is approximately 0.1 eV less negative than the conduction band energy level of the flat-band potential [40]. Consequently, the conduction band level of $Bi(C_6N_7O_3)$ is estimated to be −0.72 V with respect to the normal hydrogen electrode (NHE), and the position of the valence band(VB) is obtained according to Equation (2) [41]:

$$E_{vB} = E_{cB} + Eg \quad (2)$$

Based on the above results, a plausible mechanism for the photocatalytic degradation is proposed. As illustrated in Figure 9b, upon illumination with visible light, the electrons (e^-) in $Bi(C_6N_7O_3)$ are excited to a conduction band, leaving behind holes (h^+) in the valence band. This process results in the formation of electron-hole pairs, where the holes possess sufficient positive potential to produce ·OH radicals. However, the radical scavenger test confirms that ·OH radicals have an insignificant role in the photocatalytic process. Rather, it is the holes at the surface of $Bi(C_6N_7O_3)$ that are primarily engaged in the photocatalytic activity. In conclusion, the active species, including superoxide radicals, photogenerated electron-positive hole pairs, are crucially involved in the photodegradation of TC-HCl.

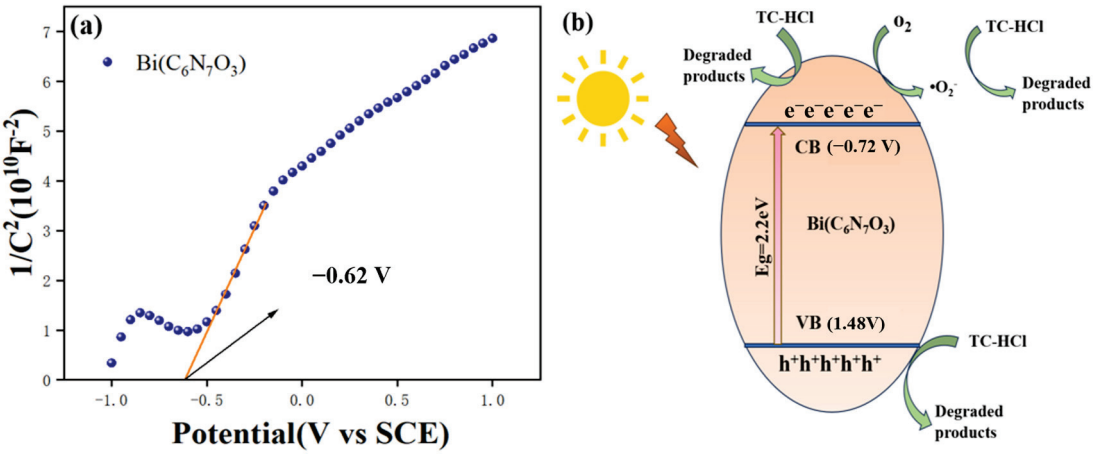


Figure 9. (**a**) Mott–Schottky curve of $Bi(C_6N_7O_3)$ and (**b**) schematic illustration of the proposed mechanism for photocatalytic degradation of TC-HCl over $Bi(C_6N_7O_3)$ nanospheres under visible light irradiation.

4. Conclusions

Bi ($C_6N_7O_3$) nanospheres are successfully prepared by replacing K^+ of as-synthesized $K_3[C_6N_7O_3]$ with Bi^{3+} ions, which are applied as a prominent homogeneous photocatalyst for dealing with the emerging pollutant in water for the first time. The as-prepared compound can combine with three surroundings $(C_6N_7O_3)^{3-}$ ions because Bi^{3+} has three positive charges. Therefore, metal ions and organic ligands can be connected by self-assembly to form a category of crystalline materials with a periodic network structure. Experiments with photocatalysis have shown that Bi ($C_6N_7O_3$) demonstrates a greatly improved photocatalytic activity, which is 79.1- and 1.8-fold greater than that of g-C_3N_4 and $K_3[C_6N_7O_3]$, respectively. The enhancement may be attributed to the increased optimized visible-light response and charge separation. This work offers a strategy to build high-performance photocatalysts by simple ion substitution and broadens the application of homogeneous photocatalysis in environmental control and other fields.

Author Contributions: Conceptualization, Z.C. and X.W. (Xiaojing Wang); methodology, R.J., Y.C. and J.C.; validation, Y.C., J.W., X.W. (Xiaozhuo Wang) and C.J.; formal analysis, H.X. and J.W.; investigation, J.W., X.W. (Xiaozhuo Wang), J.C., L.L. and C.J.; resources, R.J., H.X., L.L., C.J. and Z.C.; data curation, M.T. and M.H.; writing—original draft preparation, R.J., M.T., M.H. and Z.C.; writing—review and editing, R.J. and Z.C.; supervision, L.L. and Z.C.; project administration, Z.C. and X.W. (Xiaojing Wang); funding acquisition, Z.C. All authors have read and agreed to the published version of the manuscript.

Funding: This work is financially supported by the National Key Research and Development Program of China (2023YFF0612601), the Key Research and Development Program of Zhejiang Province (2023C02038), the Key Research and Development Program of Ningbo (2022Z178), and the Zhejiang Provincial Natural Science Foundation of China (LQ23B010003).

Data Availability Statement: The original contributions presented in this study are included in the article. Further inquiries can be directed to the corresponding authors.

Conflicts of Interest: The authors declare no conflict of interest.

References

1. Thakur, S.; Mutreja, V.; Tomar, A.; Nainwal, S.; Kaur, K.; Kaur, R.; Li, Q.; Ataya, F.S. Phytochemical-Assisted Fabrication of ZrO_2/ZnO Nanocomposites: A Sustainable Approach for Efficient Photodegradation of Tetracycline Hydrochloride. *J. Mol. Struct.* **2025**, *1330*, 141350. [CrossRef]

2. Zhou, D.; Chen, Z.; Yang, Q.; Dong, X.; Zhang, J.; Qin, L. In-Situ Construction of All-Solid-State Z-Scheme g-C_3N_4/TiO_2 Nanotube Arrays Photocatalyst with Enhanced Visible-Light-Induced Properties. *Sol. Energy Mater. Sol. Cells* **2016**, *157*, 399–405. [CrossRef]
3. Senthil, R.A.; Theerthagiri, J.; Selvi, A.; Madhavan, J. Synthesis and Characterization of Low-Cost g-C_3N_4/TiO_2 Composite with Enhanced Photocatalytic Performance under Visible-Light Irradiation. *Opt. Mater.* **2017**, *64*, 533–539. [CrossRef]
4. Mohini, R.; Lakshminarasimhan, N. Coupled Semiconductor Nanocomposite g-C_3N_4/TiO_2 with Enhanced Visible Light Photocatalytic Activity. *Mater. Res. Bull.* **2016**, *76*, 370–375. [CrossRef]
5. Sun, M.; Shen, S.; Wu, Z.; Tang, Z.; Shen, J.; Yang, J. Rice Spike-like g-C_3N_4/TiO_2 Heterojunctions with Tight-Binding Interface by Using Sodium Titanate Ultralong Nanotube as Precursor and Template. *Ceram. Int.* **2018**, *44*, 8125–8132. [CrossRef]
6. Liu, R.; Bie, Y.; Qiao, Y.; Liu, T.; Song, Y. Design of g-C_3N_4/TiO_2 Nanotubes Heterojunction for Enhanced Organic Pollutants Degradation in Waste Water. *Mater. Lett.* **2019**, *251*, 126–130. [CrossRef]
7. Liu, C.; Tan, L.; Zhang, L.; Tian, W.; Ma, L. A Review of the Distribution of Antibiotics in Water in Different Regions of China and Current Antibiotic Degradation Pathways. *Front. Environ. Sci.* **2021**, *9*, 692298. [CrossRef]
8. Chen, F.; Zhang, Y.; Huang, H. Layered Photocatalytic Nanomaterials for Environmental Applications. *Chin. Chem. Lett.* **2023**, *34*, 107523. [CrossRef]
9. Qian, X.; Chen, Z.; Yang, X.; Zhao, W.; Liu, C.; Sun, T.; Zhou, D.; Yang, Q.; Wei, G.; Fan, M. Perovskite Cesium Lead Bromide Quantum Dots: A New Efficient Photocatalyst for Degrading Antibiotic Residues in Organic System. *J. Clean. Prod.* **2020**, *249*, 119335. [CrossRef]
10. Ma, Z.; He, Y.; Li, X.; Zhou, C.; Deng, L. Ultrasonic-Assisted Efficient Degradation of Tetracycline over ZnO/BiOBr Heterojunctions: Synergistic Effect and Role of Oxidative Species. *Mater. Res. Bull.* **2022**, *146*, 111591. [CrossRef]
11. Guo, S.; Luo, H.; Li, Y.; Chen, J.; Mou, B.; Shi, X.; Sun, G. Structure-Controlled Three-Dimensional BiOI/MoS_2 Microspheres for Boosting Visible-Light Photocatalytic Degradation of Tetracycline. *J. Alloys Compd.* **2021**, *852*, 157026. [CrossRef]
12. Kandi, D.; Behera, A.; Sahoo, S.; Parida, K. CdS QDs Modified BiOI/Bi_2MoO_6 Nanocomposite for Degradation of Quinolone and Tetracycline Types of Antibiotics towards Environmental Remediation. *Sep. Purif. Technol.* **2020**, *253*, 117523. [CrossRef]
13. Jiang, W.; Li, Z.; Liu, C.; Wang, D.; Yan, G.; Liu, B.; Che, G. Enhanced Visible-Light-Induced Photocatalytic Degradation of Tetracycline Using BiOI/MIL-125(Ti) Composite Photocatalyst. *J. Alloys Compd.* **2021**, *854*, 157166. [CrossRef]
14. Li, X.; Masters, A.; Maschmeyer, T. Polymeric Carbon Nitride for Solar Hydrogen Production. *Chem. Commun.* **2017**, *53*, 7438–7446. [CrossRef]
15. Wang, D.; Huang, Y.; Yu, X.; Huang, X.; Zhong, Y.; Huang, X.; Liu, Z.; Feng, Q. Template-Free Synthesis of High Specific Surface Area Gauze-like Porous Graphitic Carbon Nitride for Efficient Photocatalytic Degradation of Tetracycline Hydrochloride. *J. Mater. Sci.* **2020**, *56*, 4641–4653. [CrossRef]
16. Fang, L.J.; Li, Y.H.; Liu, P.F.; Wang, D.P.; Zeng, H.D.; Wang, X.L.; Yang, H.G. Facile Fabrication of Large-Aspect-Ratio g-C_3N_4 Nanosheets for Enhanced Photocatalytic Hydrogen Evolution. *ACS Sustain. Chem. Eng.* **2017**, *5*, 2039–2043. [CrossRef]
17. Huang, C.; Wen, J.; Shen, Y.; He, F.; Mi, L.; Gan, Z.; Ma, J.; Liu, S.; Ma, H.; Zhang, Y. Dissolution and Homogeneous Photocatalysis of Polymeric Carbon Nitride. *Chem. Sci.* **2018**, *9*, 7912–7915. [CrossRef] [PubMed]
18. Horvath-Bordon, E.; Kroke, E.; Svoboda, I.; Fuess, H.; Riedel, R.; Neeraj, S.; Cheetham, A.K. Alkalicyamelurates, $M_3[C_6N_7O_3].xH_2O$, M = Li, Na, K, Rb, Cs: UV-Luminescent and Thermally Very Stable Ionic Tri-s-Triazine Derivatives. *Dalton Trans.* **2004**, *22*, 3900–3908. [CrossRef]
19. Wang, Z.; Pei, G.X.; Qi, H.; Zhang, S.; Liu, C.; Li, Z.; Han, K. Solar Hydrogen Generation over Carbon Nitride Photocatalyst Promoted by Water-Soluble Carbon Dots. *ChemPhotoChem* **2022**, *6*, e202200176. [CrossRef]
20. Wang, W.; Chen, Z.; Yang, X.; Audebert, P.; Sahoo, S.; Chen, J.; Liu, Y.; Pamir Alpay, S.; Xie, L.; Wei, G. Potassium Cyamelurate $K_3[C_6N_7O_3]$ Rod: A New Visible-Light Photocatalyst for Homogeneous/Heterogeneous Degradation of Antibiotics. *Appl. Catal. A Gen.* **2022**, *641*, 118669. [CrossRef]
21. Tian, Y.; Li, Q.; Zhang, M.; Nie, Y.; Tian, X.; Yang, C.; Li, Y. pH-Dependent Oxidation Mechanisms over FeCu Doped g-C_3N_4 for Ofloxacin Degradation via the Efficient Peroxymonosulfate Activation. *J. Clean. Prod.* **2021**, *315*, 128207. [CrossRef]
22. Bao, J.; Jiang, X.; Huang, L.; Quan, W.; Zhang, C.; Wang, Y.; Wang, H.; Zeng, Y.; Zhang, W.; Ma, Y.; et al. Molybdenum disulfide loading on a Z-scheme graphitic carbon nitride and lanthanum nickelate heterojunction for enhanced photocatalysis: Interfacial charge transfer and mechanistic insights. *J. Colloid Interface Sci.* **2022**, *611*, 684–694. [CrossRef]
23. Preeyanghaa, M.; Erakulan, E.S.; Thapa, R.; Ashokkumar, M.; Neppolian, B. Scrutinizing the Role of Tunable Carbon Vacancies in g-C_3N_4 Nanosheets for Efficient Sonophotocatalytic Degradation of Tetracycline in Diverse Water Matrices: Experimental Study and Theoretical Calculation. *Chem. Eng. J.* **2023**, *452*, 139437. [CrossRef]
24. Wang, D.; Li, S.; Feng, Q. Supramolecular Self-Assembled Carbon Nitride for the Degradation of Tetracycline Hydrochloride. *J. Mater. Sci. Mater. Electron.* **2018**, *29*, 9380–9386. [CrossRef]
25. Yu, H.; Shi, R.; Zhao, Y.; Bian, T.; Zhao, Y.; Zhou, C.; Waterhouse, G.I.N.; Wu, L.-Z.; Tung, C.-H.; Zhang, T. Alkali-Assisted Synthesis of Nitrogen Deficient Graphitic Carbon Nitride with Tunable Band Structures for Efficient Visible-Light-Driven Hydrogen Evolution. *Adv. Mater.* **2017**, *29*, 1605148. [CrossRef] [PubMed]

26. Jin, R.; You, J.; Zhang, Q.; Liu, D.; Hu, S.; Gui, J. Preparation of Fe-Doped Graphitic Carbon Nitride with Enhanced Visible-Light Photocatalytic Activity. *Editor. Off. Acta Phys.-Chim. Sin.* **2014**, *30*, 1706–1712. [CrossRef]
27. Zhang, S.; Zou, Y.; Chen, Z.; Li, B.; Gu, P.; Wen, T. Visible-Light-Driven Activation of Persulfate by RGO/g-C_3N_4 Composites for Degradation of BPA in Wastewater. *J. Inorg. Mater.* **2020**, *35*, 329–336. [CrossRef]
28. Zhou, Y.; Jiang, D.; Wang, Z.; Yi, L.; Sun, J.; Liu, D.; Yu, X.; Chen, Y. Bandgap Engineering of Carbon Nitride by Formic Acid Assisted Thermal Treatment for Photocatalytic Degradation of Tetracycline Hydrochloride. *Chem. Eng. J.* **2024**, *485*, 149830. [CrossRef]
29. Jourshabani, M.; Shariatinia, Z.; Badiei, A. Controllable Synthesis of Mesoporous Sulfur-Doped Carbon Nitride Materials for Enhanced Visible Light Photocatalytic Degradation. *Langmuir* **2017**, *33*, 7062–7078. [CrossRef]
30. Zhang, A.; Guo, Y.; Xie, H.; Zhang, Y.; Fu, Y.; Ye, C.; Du, Y.; Zhu, M. Green and Controllable Synthesis of Kelp-like Carbon Nitride Nanosheets via an Ultrasound-Mediated Self-Assembly Strategy. *J. Colloid Interface Sci.* **2022**, *628*, 397–408. [CrossRef]
31. Fan, X.; Zhang, Y.; Liang, H.; Zhang, M.; Sun, X.; Bai, J. Augmented Singlet Oxygen ($^1O_2$) Production via $ZnO_2/Bi_2O_2CO_3$ Heterojunction for Photodegradation of Tetracycline Hydrochloride through in-Situ Self-Fenton-like Mechanisms. *Rare Met.* **2025**. [CrossRef]
32. Ramteke, P.; Bhoyar, T.; Umare, S.S. Sulfamic Acid Coupled Polymeric Carbon Nitride: An Efficient Photocatalyst for Degradation of Tetracycline Hydrochloride and Supercapacitor Application. *J. Nanoparticle Res.* **2025**, *27*, 159. [CrossRef]
33. Nguyen, V.H.; Lee, T.; Nguyen, T.D. Synergistic Charge Separation via S-Scheme and Schottky Junctions in Ni-Decorated Melem Hydrate/g-C_3N_5 for Enhanced Photocatalytic Tetracycline Hydrochloride Degradation. *J. Mater. Sci.* **2025**, *60*, 19675–19694. [CrossRef]
34. Li, F.; Cheng, Y.; Li, P.; Yu, G. Study on the Performance of BiOCl Photocatalyst for Degradation of Tetracycline Hydrochloride. *Separations* **2025**, *12*, 242. [CrossRef]
35. Yang, X.; Li, Y.; Wang, J.; Li, M.; Zhang, H.; Yang, J.; Wei, L. Synthesis and Application of Transition Metal Ions Co-Doped CdS Photocatalyst for Tetracycline Hydrochloride Degradation. *Res. Chem. Intermed.* **2025**, *51*, 5315–5388. [CrossRef]
36. Cao, H.; Shi, X.; Wang, Y. Construction of a Z-Scheme $CoFe_2O_4/Bi_4O_7$ Heterojunction for Enhanced Photocatalytic Degradation of Tetracycline Hydrochloride. *Mater. Lett.* **2025**, *398*, 138974. [CrossRef]
37. Feng, F.; Zhang, X.; Xu, X.; Huang, Q.; Yin, H.; Li, R.; Wu, G.; Xing, W. Construction of 2D/3D Biochar Modified g-C_3N_4 for Efficient Removal of Tetracycline Hydrochloride via Photocatalytic PMS Activation. *Opt. Mater.* **2025**, *167*, 117246. [CrossRef]
38. Zhao, W.; Liu, X.; Yang, X.; Liu, C.; Qian, X.; Sun, T.; Chang, W.; Zhang, J.; Chen, Z. Synthesis of Novel 1T/2H-MoS_2 from MoO_3 Nanowires with Enhanced Photocatalytic Performance. *Nanomaterials* **2020**, *10*, 1124. [CrossRef]
39. Rosa, D.; Remmani, R.; Bavasso, I.; Bracciale, M.P.; Di Palma, L. Biochar Supported Fe–TiO_2 Composite for Wastewater Treatment: Solid-State Synthesis and Mechanistic Insights. *Chem. Eng. Sci.* **2025**, *317*, 122076. [CrossRef]
40. Wang, D.; Yin, F.-X.; Cheng, B.; Xia, Y.; Yu, J.-G.; Ho, W.-K. Enhanced Photocatalytic Activity and Mechanism of CeO_2 Hollow Spheres for Tetracycline Degradation. *Rare Met.* **2021**, *40*, 2369–2380. [CrossRef]
41. Liang, H.; Wang, A.; Cheng, R.; Chen, F.; Kannan, P.; Molochas, C.; Tsiakaras, P. Bi, K Co-Doped Graphitic Phase Carbon Nitride for Efficient Photocatalytic H_2O_2 Production. *Chem. Eng. J.* **2024**, *489*, 151145. [CrossRef]

Disclaimer/Publisher's Note: The statements, opinions and data contained in all publications are solely those of the individual author(s) and contributor(s) and not of MDPI and/or the editor(s). MDPI and/or the editor(s) disclaim responsibility for any injury to people or property resulting from any ideas, methods, instructions or products referred to in the content.

processes

MDPI

Article

Effect of Storage Conditions on the Composition and Bioactivity of Freeze-Dried Lemongrass Oil Nanoemulsions Stabilized by Salt-Sensitive Cellulose Nanocrystals and Tween 80

Kaleb D. Fisher [1] and Lingling Liu [2,*]

[1] Roy J. Carver Department of Biochemistry, Biophysics and Molecular Biology, Iowa State University, Ames, IA 50010, USA; kalebf@iastate.edu
[2] School of Environmental, Civil, Agricultural and Mechanical Engineering, University of Georgia, Athens, GA 30602, USA
* Correspondence: linglliu@uga.edu; Tel.: +1-706-542-4018

Abstract: Oil-in-water emulsions are widely used to enhance the solubility, stability, and bioactivity of essential oils in aqueous systems. Advancing the functionality and sustainability of these emulsions using renewable, eco-friendly ingredients remains an important research focus. This study developed and evaluated a lemongrass essential oil nanoemulsion stabilized by Tween 80, NaCl, and soybean stover-derived cellulose nanocrystals. After freeze-drying, the nanoemulsion was redispersed in water and analyzed for particle size, zeta potential, polydispersity index, and essential oil recovery. Freeze-drying led to significant bioactivity losses, with antifungal and antioxidant activities reduced by 77% and 31%, respectively. Antioxidant activity declined rapidly within the first two weeks of storage at room temperature but was not significantly impacted by light exposure. Storage conditions also altered the sample composition, with one new compound detected in samples stored without light exposure and eleven new peaks observed in light-exposed samples. This study provides insights into the effects of freeze-drying and storage on lemongrass essential oil-loaded nanoemulsion stabilized by Tween 80, NaCl, and cellulose nanocrystals. The findings highlight the challenges of preserving bioactivity and composition in lyophilized essential oil-loaded emulsions and suggest avenues for optimizing drying processes and formulations to improve storage stability and efficacy.

Keywords: nanoemulsion; cellulose nanocrystals; essential oil; lyophilization; antioxidant activity

1. Introduction

Identifying renewable, eco-friendly products is a part of a growing body of research set on improving the quality and environmental impact of food storage and agricultural production and processes. Of these, many natural products are plant extracts known as essential oils, which are plant products comprised of many compounds, including terpenoid and non-terpenoid hydrocarbons, aromatic volatiles, fatty acids, and more [1]. Essential oils have been studied extensively and have been shown to exhibit antimicrobial and antifungal properties [2,3]. Further, research has shown that specific compounds within essential oils are responsible for antimicrobial activity [4]. These oils with components shown to exhibit antimicrobial and antifungal behavior can be derived from lemongrass and other plant sources [2,3,5–8].

Although shown to be effective, essential oils are restricted by certain factors such as low solubility in water, low bioactivity, and high volatility, reducing storage stability [9].

Further, storage conditions like temperature, light exposure, and time have a significant effect on the composition and properties of pure oils and emulsions [10–13]. As a potential solution to these limits, oil-in-water (O/W) nanoemulsions have been explored. Nanoemulsions are defined as mixtures of at least two liquids that result in droplets on the order of 100 nm and generally contain water, oil, and an emulsifier [14]. Nanoemulsions have been shown to be effective in improving the antioxidant activity, antifungal activity, and storage stability of essential oils [15–17].

In nanoemulsion research, green emulsion stabilizers such as cellulose nanocrystals (CNCs) have been investigated for their potential to stabilize emulsions [18]. CNCs are rod-shaped nanoparticles derived from renewable sources [19], making them an appealing option for researchers developing innovative nanoemulsion systems. While nanoemulsions are known to enhance various properties of oil-in-water mixtures, improving the stability and functionality of nanoemulsions remains an active area of study. One proposed method to enhance the stability of nanoemulsions is the removal of water through drying processes such as freeze-drying or lyophilization [20]. Additionally, researchers have explored various drying techniques to identify the most effective method for water removal that preserves or enhances the emulsions' original properties [21–24].

In our previous publications, we showed that the addition of NaCl and CNC to an emulsion containing 10% Tween 80 and 5% lemongrass oil improved the thermodynamic stability of the emulsions [25,26]. In this paper, we build upon the previous work and explore a new method for further improving the storage stability of the nanoemulsion. We hypothesize that freeze-drying an essential oil-loaded nanoemulsion stabilized by salt-sensitive cellulose nanocrystals and Tween 80 will preserve the stability and bioactivity of the essential oil by delaying degradation. To test the hypothesis, we examined the effect that freeze-drying has on the antioxidant activity, antifungal activity, composition, and concentration of volatiles in nanoencapsulated lemongrass essential oil. Additionally, we explored the effect of room temperature storage and light exposure on the nanoemulsion after freeze-drying to test how these conditions change the composition and concentration of volatile components present in the nanoemulsions. As far as the authors are aware, this paper presents the first research available discussing the effects of freeze-drying on a nanoemulsion containing essential oil stabilized by cellulose nanocrystals.

2. Materials and Methods

2.1. Materials

Lemongrass essential oil (Cymbopogon Schoenanthus Oil, reagent grade, 100%) was acquired from Spectrum Chemical MFG Corp. (New Brunswick, NJ, USA). Sodium chloride (NaCl) was purchased from VWR chemicals (Radnor, PA, USA). Tween 80 (T80) was obtained from Research Products International (Mt Prospect, IL, USA). Organic solvents, methanol and acetonitrile were purchased from Fisher Chemical (Pittsburgh, PA, USA). Citral (cis and trans mixture) and 2,2-Diphenyl-2-picrylhydrazyl Free Radical were purchased from Tokyo Chemical Industry Co., Ltd. (Chuo-Ku, Tokyo, Japan). Geraniol 99% was obtained from Thermo Scientific (Waltham, MA, USA). Geranyl acetate was purchased from Sigma-Aldrich, Inc. (St. Louis, MO, USA). *Aspergillus flavus* Link 200026 NRRL 3357 strain was purchased from ATTC (Manassas, VA, USA). Potato dextrose agar (PDA) was bought from Becton, Dickinson and Company (Franklin Lakes, NJ, USA). Cellulose nanocrystals derived from soybean stover (SBS-CNC) were made according to our previous publication [25]. Namely, SBS was obtained on the farm, ground to below 1/8th of an inch, and washed. Samples then underwent an alkaline and bleaching process to remove hemicellulose and lignin, respectively. The final step included sulfuric acid hydrolysis and sonication to obtain soybean cellulose nanocrystals. Additionally, in our previous

publication [26], SBS-CNC was characterized, and the zeta potential, particle size, and polydispersity index were measured to be –50 ± 1 mV, 197 ± 6 nm, and 0.65, respectively. The crystallinity index of dried SBS-CNC was found to be 82.29% as determined by X-ray diffraction methods. Further, using transmission electron microscopy, images of the nanocrystals were taken to determine the length and width of the nanocrystals, which were measured to be 117 ± 40 and 7.3 ± 2 nm, respectively.

2.2. Nanoemulsion Preparation and Freeze-Drying

To prepare a fresh nanoemulsion, calculations were completed to ensure a final lemongrass essential oil (LGEO) concentration of 5 wt%, soybean stover-derived cellulose nanocrystals (SBS-CNC) concentration of 1 wt%, Tween 80 (T80) concentration of 10 wt%, and NaCl concentration of 40 mM. Deionized water was added to achieve a final nanoemulsion mass of 10 g. Preparation began with mixing LGEO and T80 in a glass vial, followed by preparing the aqueous phase containing SBS-CNC, water, and NaCl, which was then gradually pipetted into the LGEO-T80 mixture with continuous stirring. After complete addition, the mixture was set on a stir plate at ~1500 rpm for 5 min. Samples were then sonicated, on ice, at 60% amplitude for 5 min (pulse: 5 s on/2 s off) using a 500 W ultrasonicator (Fisher Scientific, Hampton, NH, USA). After sonication, samples were immediately used for testing.

The freeze-drying process included first creating nanoemulsion samples containing deionized water, essential oil, NaCl, SBS-CNC, and Tween 80. Samples were then freeze-dried at a pressure close to 0 bar and a temperature around −84 °C for 48 h using the Labconco FreeZone freeze-drier (Kansas City, MO, USA).

2.3. Physicochemical Characterization of Redispersed Nanoemulsion

Following methods from our previous publications [25,26], we determined the zeta potential and particle size of freshly redispersed nanoemulsion samples. First, the freeze-dried nanoemulsion was dissolved in water and further diluted 100× using water. Approximately 1 mL of sample was then aliquoted into a folded capillary zeta cell. Particle size and zeta potential were measured immediately after dilution using the Zetasizer Nano ZS (Malvern Instruments Ltd., Worcestershire, UK). Further, the essential oil recovery percentage of redispersed nanoemulsion was determined. First, the peak of LGEO was found by measuring the oil at a range of 200–800 nm on a UV–Vis spectrophotometer (Azzota Scientific, Claymont, DE, USA). To measure the essential oil recovery, a standard curve of LGEO was created using a UV–vis spectrophotometer at 243 nm, the wavelength at which the LGEO peaked. The standard curve was made using pure LGEO and 95% ethanol as a diluent at different concentrations, including 2, 5, 7, and 10 μg/mL. To quantify the essential oil recovery after freeze-drying, the redispersed nanoemulsion was diluted to a detectable value on the spectrophotometer, and the absorbance at 243 nm was recorded. Lastly, the standard curve and measured absorbances of samples were used to calculate the concentration.

2.4. Effect of Light Exposure and Room Temperature Storage on Essential Oil Composition

To test the effect of light on freeze-dried nanoemulsions, samples were prepared in triplicate, freeze-dried, and the resulting powder was equally distributed between two glass petri dishes. One glass petri dish was designated for light exposure, and the other for no light exposure. For light exposure, a rectangular box was created using PVC plastic with a polycarbonate door on one side. At the top, two 27-watt, 6500 K, compact fluorescent light bulbs were attached to span most of the length of the box (Mandala Crafts, Inc., Cedar Park, TX, USA). For light exposure, samples were placed in a glass petri dish and gently flattened into a homogenous layer. Samples were placed 42 cm away from

the surface of the light bulbs, side by side. Inside the light box, at a distance of 42 cm, there was a flux of 2950 ± 50 lux measured at the three sample locations determined by a 0–200,000 measurement range lux meter (Dr.meter, Newark, CA, USA). The door of the box was left open during experiments, and it was determined that at 42 cm, no change in the temperature of the samples would occur due to the light bulbs. Although the door remained open during experimentation, this side of the box was facing a wall, and ambient light was measured to be 0 lux in the box.

For samples receiving no light, they were similarly placed in a glass petri dish and gently flattened into a homogenous layer. These samples were placed in a drawer near the samples receiving light, and their location also received 0 lux. After 7 days, samples were rotated every 3.5 days to achieve uniform light exposure. Around 0.1 g of samples were collected from each petri dish for measurements on days 0, 7, 14, 21, and 30. A schematic detailing the design and key characteristics of the light box used for the experiments was created and included below (Figure 1).

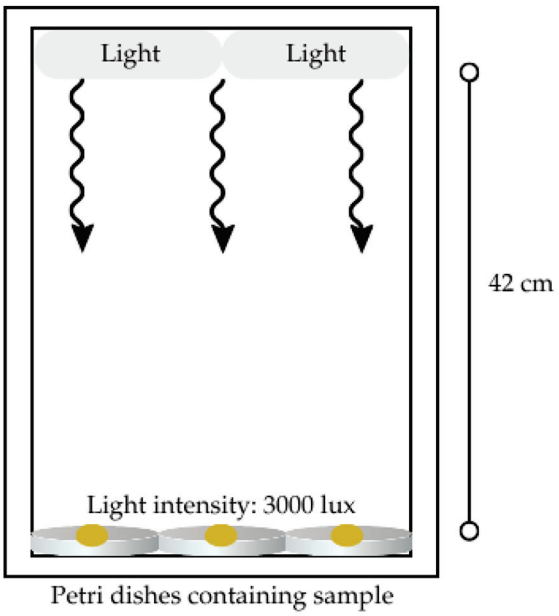


Figure 1. Diagram of the experimental setup used to expose samples to light intensity.

2.5. Antioxidant Activity of Redispersed Nanoemulsion

2,2-diphenyl-1-picrylhydrazyl (DPPH) solution in methanol was prepared fresh and diluted using methanol to a concentration of 0.0631 mM, following Jiménez-Escrig et al. [27]. Following Baliyan et al. [28], a ratio of 3 mL of DPPH to 100 µL of sample was used for the assays. To test freeze-dried samples, a small amount of powder was added to a 20 mL scintillating vial. Then, DI water was added to achieve a sample with 5% EO concentration as determined by earlier UV–vis measurements. This sample was mixed with an appropriate amount of 0.0631 mM DPPH solution to achieve the previously stated ratio. The sample labeled as pure EO refers to the essential oil diluted in methanol to achieve a final concentration of 5% EO. For samples tested on days 0 and 30, the same vials containing freeze-dried product were used. Additionally, equivalent amounts of powder and water were used to redisperse the sample on days 0 and 30 to measure the degradation of EO in samples over time. For samples that were not redispersed, 100 µL of the liquid sample was pipetted directly into 3 mL of DPPH solution.

After the combination with DPPH, the samples were mixed well by swirling. After swirling, the test tubes were stored at room temperature, away from light, for 30 min. Following incubation, samples were removed from the cabinet and mixed by swirling

again. Samples containing nanoemulsions (fresh and redispersed) were filtered using a 40 μm cell strainer. Then, 1 mL was removed from the solution and tested by UV–vis at 516 nm, the wavelength at which the spectrum of pure DPPH solution peaked. Lastly, to quantify the antioxidant properties of the sample, the following equation was used.

$$Percent\ Inhibition\ (\%) = \frac{(CA_{516} - SA_{516})}{CA_{516}} \times 100\% \quad (1)$$

where CA_{516} is the absorbance of the control at 516 nm and SA_{516} is the absorbance of the samples being tested at 516 nm [29].

2.6. Fungal Cultures

Aspergillus flavus (A. flavus) cultures were grown on potato dextrose agar (PDA) containing 0.1% (w/v) Tween 80. Specifically, 14-day-old cultures were used to inoculate fresh plates and create a new generation for future use. This procedure was conducted every 14 days to maintain fungal cultures. Additionally, 14-day-old fungal cultures were used to create the spore suspension used in antifungal experiments. Specifically, sterile water was applied to 14-day-old plates, and the spores were scraped from the surface using a sterile glass microscope slide. The suspension was then diluted to 10^5 conidia/mL, counted using a hemocytometer.

2.7. Antifungal Activity of Redispersed Nanoemulsion

Potato dextrose agar containing 0.1% (w/v) T80 was created and sterilized by autoclaving. The media was then maintained at 55 °C in a water bath until use. For freeze-dried samples, nanoemulsion powder was dissolved in DI water and measured using a UV–vis spectrometer to determine concentration. The redispersed nanoemulsion was then added to the media until the desired concentration in the media was achieved. For samples with fresh nanoemulsion, the nanoemulsion was further diluted to a desired concentration. After the addition of the nanoemulsion, the media was dispersed between four petri dishes and then allowed to dry inside a biosafety cabinet until cool. Once the media cooled to room temperature, 10 μL of *A. flavus* at a concentration of 10^5 conidia/mL was pipetted onto the center of the plates and spread using a sterile plastic inoculation loop. A circular shape was used to determine the inoculation area and was constant among all samples. Plates were then incubated at 25 °C for 14 days. The growth diameter was measured vertically and horizontally every two days over a two-week period. These values, along with the control plates, were used to calculate the mycelial growth inhibition percentage (MGI%). Mycelial growth inhibition was found using the following equation;

$$MGI\ (\%) = \frac{(CD_{avg} - SD)}{CD_{avg}} \times 100\% \quad (2)$$

In the equation above, CD_{avg} is the average growth diameter of control samples, and SD is the respective sample growth diameter.

2.8. GC/Q-TOF Characterization and Quantification of Redispersed Nanoemulsion

Gas chromatography with quadrupole time-of-flight mass spectrometry (GC/Q-TOF) (Agilent 7250 GC/Q-TOF, Agilent Technologies Inc., Santa Clara, CA, USA) was used to determine chemical composition and concentration of essential oil in various samples. For compound determination, Agilent's Masshunter Qualitative Analysis B.08.00 software and associated NIST molecular library were utilized.

For the determination of chemical compounds in LGEO, LGEO was diluted to 10,000 ppm and injected into the column (DB-5MS 30 m, 0.25 mm, 0.25 μm). GC/Q-

TOF experiments utilized a hold time and temperature ramp similar to previously reported methods [30,31]. In our experiments, samples had a hold time of 3 min and a temperature ramp of 15 °C/min starting at 45 °C and ending at 320 °C, occurring over a 21.33 min run time. Because fresh and redispersed nanoemulsions containing LGEO were not suitable for GC analysis, the samples underwent an oil extraction process. The extraction process follows de Godoi et al. (2017) [32] with modifications. Specifically, 100 µL of nanoemulsion sample was heated at 50 °C for 15 min in a water bath. Then, the sample was combined with 1 mL of acetonitrile and centrifuged at 10,000 rpm for 10 min. Lastly, the supernatant was filtered using a syringe and a 0.7 µm membrane. Finally, to measure samples, 1 µL of the filtered supernatant was injected into the GC column.

For quantification, four standards were selected following analysis of pure EO injected into the GC column, including cis- and trans-citral, geraniol, and geranyl acetate. These standards were diluted on each day of GC measurements to varying concentrations and tested. The peak area was plotted against concentration and used to determine the unknown concentration of compounds in various samples.

2.9. Statistical Analysis

For statistical analyses, the program JMP Student Edition 18 was utilized. One-way ANOVA tests with Tukey post hoc tests were employed. Additionally, a significance threshold of $p < 0.05$ was used.

3. Results and Discussion

3.1. Physico-Chemical Characterization of Redispersed Nanoemulsion

As shown in Table 1, the zeta potential of the freeze-dried nanoemulsion after redispersion in water was found to be -30.6 ± 6.3 mV. In our previous publication [26], the zeta potential of the same sample before freeze-drying (fresh nanoemulsion) had a zeta potential of -39.2 ± 3.0 mV. The range for good physical stability is -30 to -60 mV, where any absolute value larger than 60 is considered to have excellent stability [29]. Within error, the redispersed sample fell within the range describing good physical stability on the day of redispersion.

Table 1. Physico-chemical characterization of freeze-dried nanoemulsion redispersed in water.

Parameter	Result
Zeta Potential (mV)	-30.6 ± 6.3
Particle Size (nm)	158.4 ± 34.9
Polydispersity Index	0.6 ± 0.2
Essential Oil Recovery Percentage (%)	68.7 ± 12.5

The particle size of redispersed nanoemulsion samples was 158.4 ± 34.9 nm (Table 1). In our previous publication, Liu et al. [26], the particle size of fresh nanoemulsion was also determined and found to be smaller with a mean particle size of 137 ± 11 nm. In another paper, researchers noted a much larger increase in particle size of nanoemulsions after spray-drying [21]. With the increase in particle size, resolubilizing the freeze-dried nanoemulsion becomes more challenging. Further, aggregation and agglomeration that may occur during freeze-drying could lead to a reduction in the zeta potential of samples. The decreased zeta potential combined with the increased particle size suggests that the redispersed lyophilized nanoemulsion reduces its stability. Furthermore, the polydispersity index (PDI) of samples was found to be 0.6 ± 0.2, as shown in Table 1, which is in a similar range to those values of the fresh nanoemulsion, which were found to be 0.4 ± 0.1 in our previous publication [26]. Lastly, the essential oil recovery was determined to learn how

freeze-drying affects the concentration of essential oil in the samples. To measure essential oil concentration in samples, a standard curve of LGEO was developed (Figure 2).

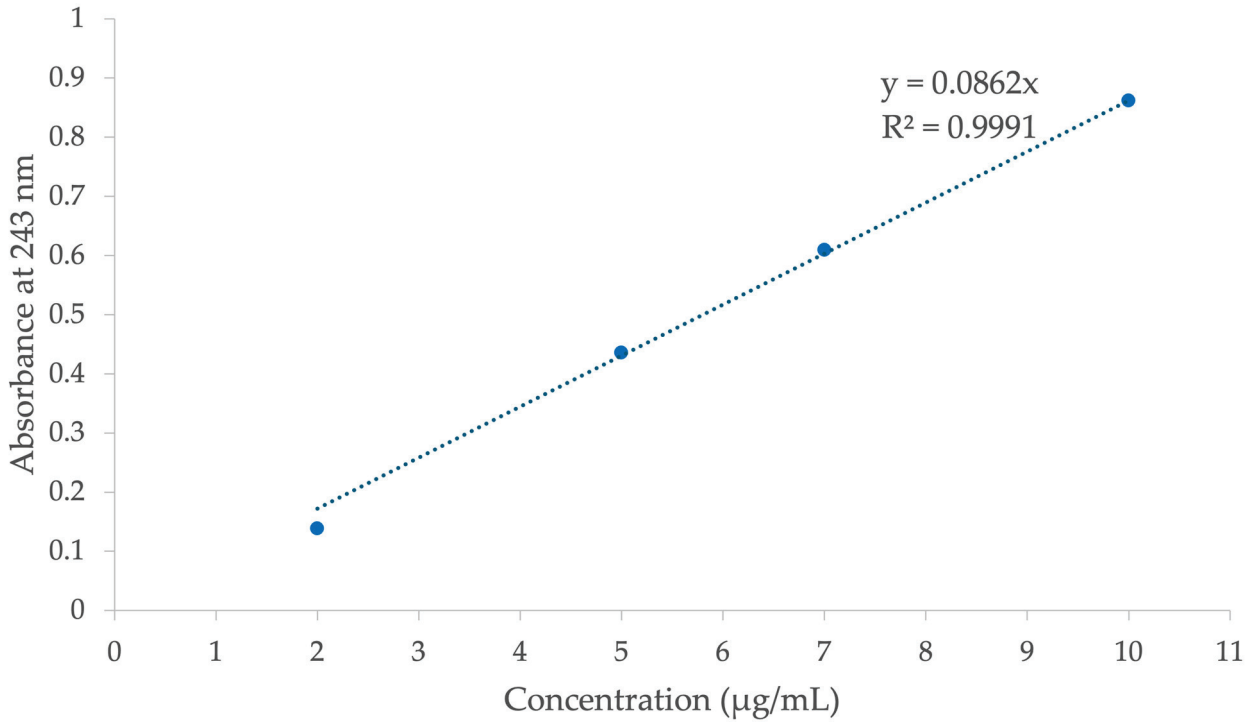


Figure 2. Standard curve of LGEO diluted in 95% ethanol.

Using the standard curve, fresh and redispersed nanoemulsions were diluted and measured using a spectrophotometer. The recovery percentage was found by comparing the concentration found for redispersed samples to that found in fresh nanoemulsion samples. The essential oil recovery percentage was measured to be 68.7 ± 12.5%. This result indicates that essential oil concentration is decreased following freeze-drying. Similarly, in another study, the encapsulation efficiency of nanoemulsions containing krill oil after freeze-drying ranged from 51.9 to 58.2% [21]. The result is indicative of an initial loss of oil after freeze-drying in different nanoemulsion systems and agrees with the results presented here.

3.2. Effect of Freeze-Drying on the Antifungal Activity of Nanoemulsion Containing LGEO Against Aspergillus Flavus

To determine the effect of freeze-drying on the antifungal activity of the nanoemulsion, mycelium growth inhibition experiments were conducted. Fresh nanoemulsion with 0.1% EO in media was able to completely inhibit mycelium growth over a 14-day period. In contrast, redispersed freeze-dried nanoemulsion at 0.10% EO in media showed an initial 77% loss in antifungal activity after only two days. At day 10, no more antifungal activity was observed (Figure 3). Additionally, images confirming the antifungal activity results are displayed in Supplementary Figure S1.

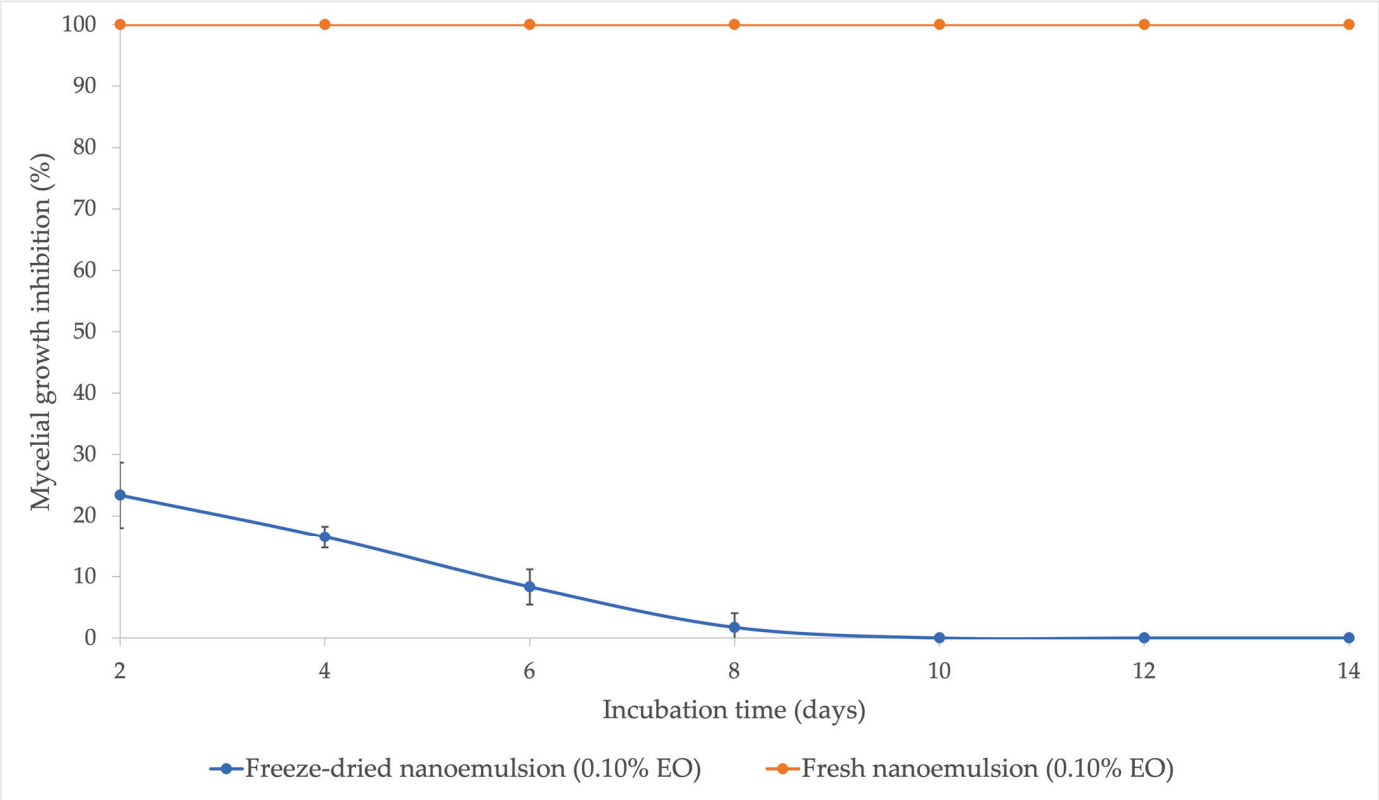


Figure 3. Antifungal activity of fresh nanoemulsion and freeze-dried nanoemulsion at 0.10%. Data points represent averages (n = 4) and error bars represent standard deviations. Data for "Fresh nanoemulsion 0.10% EO" were reported in our earlier publication (Liu et al. [26]) and are presented here again for comparison.

Many essential oils, including lemongrass, basil, Zatar, and others, have been tested against various organisms [6,14,15]. In these studies, essential oils were shown to inhibit the growth of specific fungal species. In particular, Martinazzo et al. [6] showed that *Aspergillus flavus* growth was inhibited by lemongrass oil. Additionally, lemongrass essential oil in nanoemulsion has shown complete growth inhibition and aflatoxin production in *A. flavus* [16]. Further, nanoemulsions containing Ocotea indecora essential oil were shown to inhibit the growth of multiple Aspergillus species, including *A. flavus* [33]. These results are in line with the fresh nanoemulsion result reported here (Figure 3).

In freeze-dried nanoemulsion, dramatic loss of antifungal activity is a likely consequence of vaporization of volatile components. Specifically, the loss of essential oil would be associated with a loss of volatile compounds such as citral, which makes up the majority of LGEO samples, as well as many other sources in the literature [5,34,35]. Additionally, individual components of LGEO, namely citral and geraniol, have been shown to exhibit antifungal activity when used alone [36,37]. With this, the significant loss of LGEO and its volatile components could explain the decrease in antifungal activity of nanoemulsions following freeze-drying.

Freeze-drying a nanoemulsion system containing cellulose nanocrystals can also result in changes to the morphology and physico-chemical characteristics of the CNC [22]. Some studies have shown that freeze-drying CNC results in dense agglomerates with particle sizes greater than 100 nm and flaky morphology [23]. Additionally, another source reported that after freeze-drying, CNCs were composed of large nonuniform flakes with highly decreased porosity as compared to other drying methods [24]. Changes in the shape and size of CNCs could affect the ability of the nanoemulsion to encapsulate the oil. Emulsion stabilizers and surfactants present in the nanoemulsion could reduce EO degradation

or losses. For instance, Aw et al. [38] reported that CNCs can encapsulate essential oils by serving as both physical and chemical barriers, which the authors suggested was responsible for reducing oil degradation in emulsions. The results from the literature, along with the data presented in Figure 3, suggest that the barrier provided by CNCs, which initially stabilized the nanoemulsions, was lost or damaged during freeze-drying. This loss of the barrier appears to facilitate the vaporization of antifungal volatile components from the samples.

3.3. Antioxidant Activity of LGEO, Nanoemulsion, and Redispersed Nanoemulsion over 30-Day Period

3.3.1. Antioxidant Activity of Pure Essential Oil, Fresh Nanoemulsion, and Freshly Redispersed Freeze-Dried Nanoemulsion

To test the antioxidant activity or free radical scavenging behavior of LGEO, nanoemulsion, and freeze-dried nanoemulsion, the DPPH assay was utilized. Essential oils, specifically LGEO, contain phenolic compounds known to have antioxidant activity [39,40]. On the day samples were created, 5% pure EO exhibited about 53% antioxidant activity, which was 9% lower than the 62% activity measured from fresh nanoemulsion samples made and tested on the same day (Figure 4). Both pure LGEO and fresh nanoemulsion had much higher activity than freshly redispersed nanoemulsion, which had about 33% antioxidant activity.

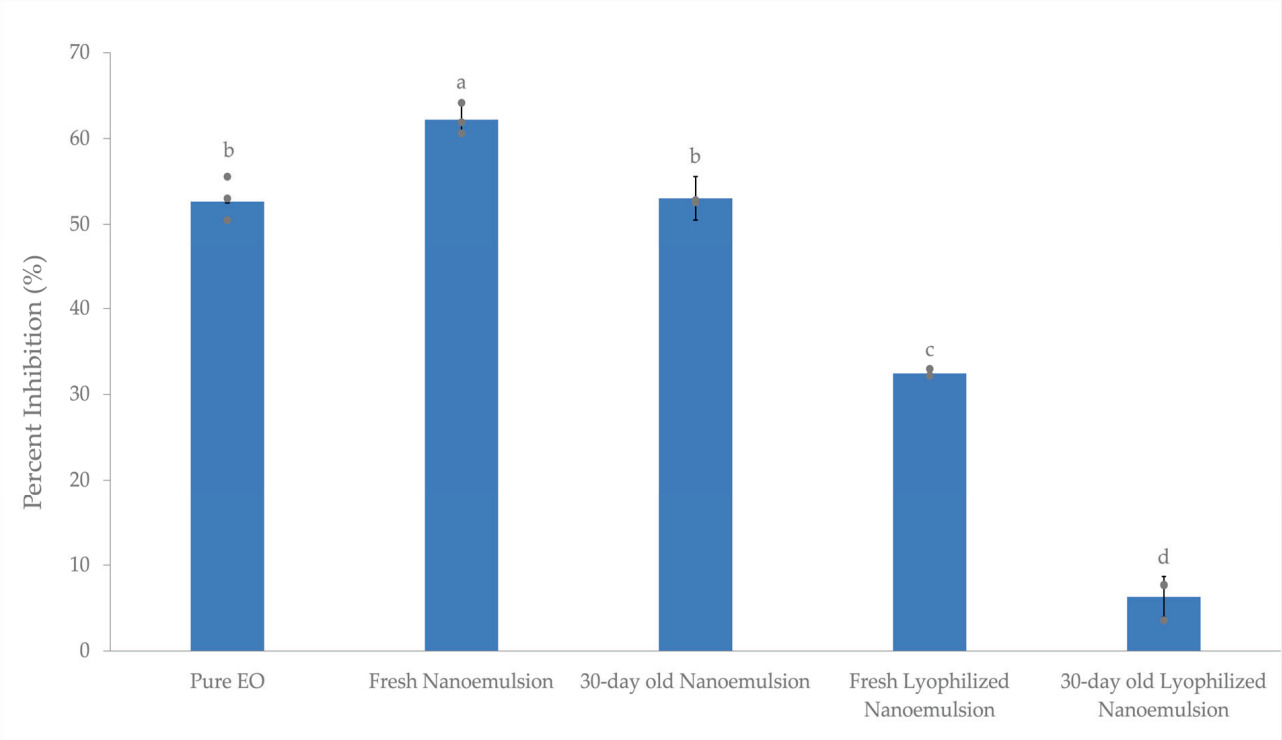


Figure 4. Antioxidant assay of pure EO, fresh nanoemulsion, and freeze-dried (i.e., lyophilized) nanoemulsion on an initial date and 30 days later. Samples without shared letter(s) are significantly different. Note: Grey circles represent individual replicates, and error bars represent standard deviation.

Results from Figure 4 suggest that the addition of nanoemulsion components increases the antioxidant activity of the sample. In other studies, nanoemulsion containing lemongrass oil, T80, ethanol, and water showed a similar result [17]. Specifically, nanoemulsion samples had around 9% higher antioxidant activity than pure EO [17]. An increase in radical scavenging activity may be attributable to a reduced loss of EO after the inclusion of Tween 80. In another study, researchers found that incorporating T80 into films at 2 and 4%

caused a slight increase in the radical scavenging activity of samples [15]. These authors speculated that the increase in radical scavenging activity could be due to a reduced loss of EO upon T80 inclusion. Our result, in combination with data in the literature, may indicate that T80 aids in the increase in antioxidant activity by itself or by increasing the retention of EO. In contrast, another source reported that Tween 80 at 0.10% (v/v) was unable to scavenge free radicals in DPPH [41], the concentration of which is substantially lower than that used in our study (10 wt%).

Another ingredient, SBS-CNC, could also play a role in the increase in antioxidant activity seen between pure EO and fresh nanoemulsion. The inclusion of cellulose nanocrystals may be aiding in increasing the radical scavenging activity of the nanoemulsions. In Yu et al. [42], researchers concluded that the addition of cellulose nanocrystals (CNC) was responsible for the increased free radical scavenging activity in the 2,2′-azino-bis (3-ethylbenzothiazoline-6-sulfonic acid (ABTS) and DPPH assays tested on packaging films. Additionally, it was found that freeze-drying decreased the antioxidant activity of the nanoemulsion sample. As described earlier in Section 3.2, this might be caused by the changes in the stabilizing matrix, leading to oil evaporation and loss of antioxidant activity.

3.3.2. Antioxidant Activity of Pure Essential Oil, Fresh Nanoemulsion, and Freeze-Dried Nanoemulsion After 30 Days of Room Temperature Storage

Another variable tested in these experiments was the effect of room temperature storage for 30 days on the antioxidant activity of samples. After 30 days of room temperature storage, pure EO dissolved in methanol showed no significant difference in the antioxidant activity as compared to freshly diluted EO. As the pure EO sample was stored for 30 days diluted in methanol, the result is not comparable to other samples after storage that were not stored in methanol; thus, the result is not shown. Fresh nanoemulsion after 30 days of storage displayed a 9% decrease in antioxidant activity as compared to the fresh product (Figure 3). This result contrasts with the findings in another study, where it is reported that after 6 months, nanoemulsion containing EO, T80, ethanol, and water lost only 8% of antioxidant activity while the pure EO sample lost around 16% [17]. In this study, the largest loss in the antioxidant activity was measured in redispersed lyophilized nanoemulsion samples. Specifically, a 27% decrease in the antioxidant activity was observed after freeze-drying, and only 6% of antioxidant activity was left for a 30-day-old lyophilized nanoemulsion sample (Figure 4).

Overall, the antioxidant activity of the nanoemulsion samples declined after 30 days of room temperature storage, with the most significant decrease observed in the redispersed nanoemulsion sample. In contrast, pure LGEO diluted in methanol did not exhibit any significant changes (result not shown). These differences could be attributed to the varying compositions of the samples. The fresh nanoemulsion contained water, T80, soybean-CNC, NaCl, and LGEO, whereas the pure LGEO sample consisted solely of essential oil in methanol. One possible explanation for the stability of the pure LGEO sample is the difference in vapor pressure between methanol and the primary essential oil components. Methanol, with a vapor pressure of 96 mmHg at 20 °C and 127 mmHg at 25 °C (as reported by the Methanol Institute [43]), evaporates more readily than the essential oil components, such as geranyl acetate and citral, which have much lower vapor pressures (0.07 mmHg at 20 °C for geranyl acetate and approximately 0.09 mmHg at 25 °C for citral, according to Sigma Aldrich). As methanol evaporates, the sample may become enriched with LGEO, which could compensate for loss in antioxidant activity over time.

3.4. GC/QTOF Analysis of the Chemical Composition and Concentration of Volatile Components in Lemongrass Essential Oil and Its Nanoemulsion

3.4.1. GC/Q-TOF Analysis of Lemongrass Essential Oil

Analysis of pure lemongrass essential oil yielded multiple peaks of volatile compounds (Figure 5). Major components of LGEO were found to be cis and trans-citral, geranyl acetate, geraniol, caryophyllene, γ-Murrolene, and 10,13-octadecadiynoic acid, methyl ester.

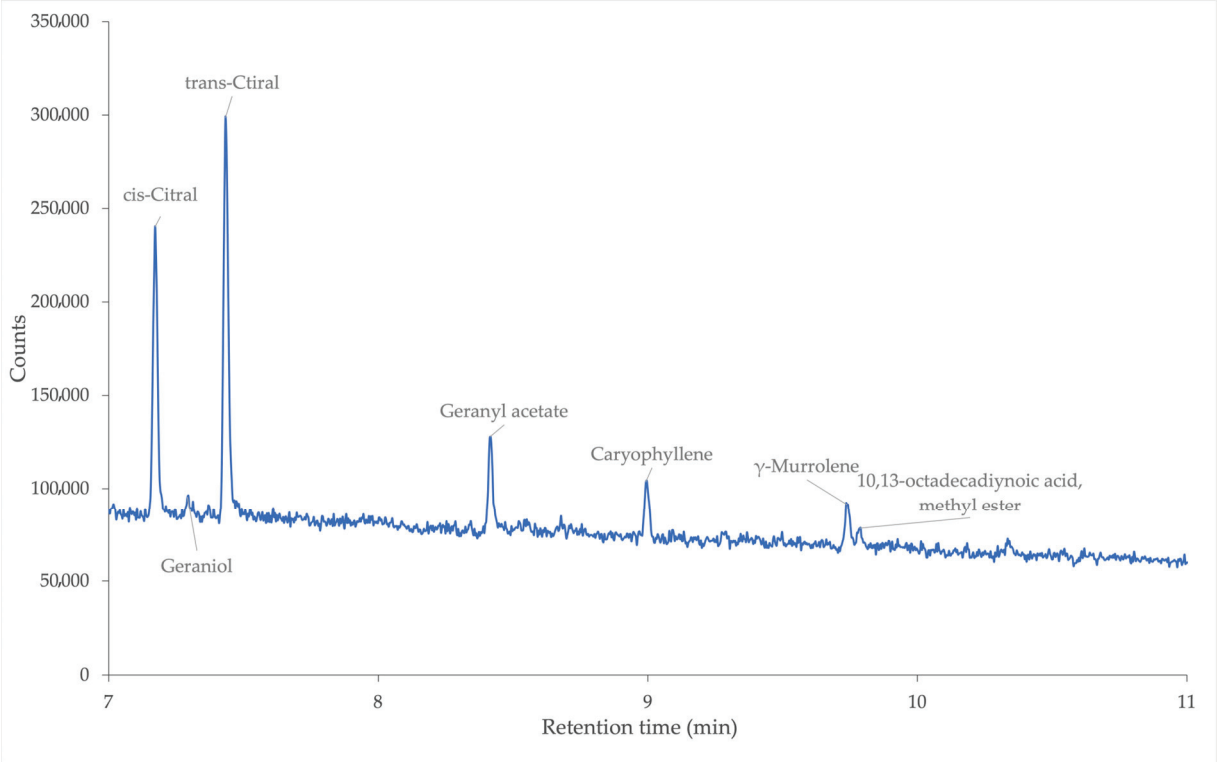


Figure 5. GC/Q-TOF chromatogram of pure essential oil at 10,000 ppm. No peaks were observed before the retention time of 7 min or after 11 min.

The largest components within the lemongrass oil were cis and trans-citral with relative percentages of 30.00 and 43.20% respectively (Table 2). In Ali et al. [44], researchers also concluded that cis and trans-citral were the most concentrated components in their lemongrass (Cymbopogon Citratus) oil sample, with relative concentrations of 30.72 and 34.80% respectively. The third most concentrated compound in our results was caryophyllene at 11.65% while in Ali et al. [44], β-myrcene was the third highest component with a relative percentage of 11.28%.

Table 2. Compound names, retention time, and relative percentage of compounds in pure lemongrass essential oil.

Compound	Retention Time (min)	Relative Percentage (%)
cis-Citral	7.172	30.00
Geraniol	7.295	2.14
trans-Citral	7.433	43.20
Geranyl acetate	8.417	11.65
Caryophyllene	8.996	6.13
γ-Muurolene	9.736	4.98
10,13-octadecadiynoic acid, methyl ester	9.789	1.90

The two primary compounds, cis- and trans-citral, appear as the most concentrated components in various studies on LGEO [5,34,35]. Other compounds such as geraniol, geranyl acetate, and caryophyllene also appear in these studies at different relative percentages. In other studies [34,35], myrcene is one of the more concentrated molecules in the lemongrass (Cymbopogon Citratus) oil, while in our results, it is not present. Another study, Mukarram et al. [5], also reported no myrcene peaks in their results. Furthermore, Mukarram et al. [5] conducted experiments using Cymbopogon flexuosus and noted that the lemongrass genus (Cymbopogon) comprises approximately 180 species. The two studies that reported the presence of myrcene utilized a species known as Cymbopogon Citratus, whereas our study focused on Cymbopogon Schoenanthus. Additionally, a study by Praveen et al. [45] identified γ-Muurolene in a lemongrass sample. The final compound detected in our analysis, 10,13-octadecadiynoic acid methyl ester, to the best of the authors' knowledge, has not been previously reported in studies on lemongrass essential oil. However, this molecule has been identified in other plant extracts, such as those from Mentha spicata [45]. While this compound has not been documented in lemongrass essential oil studies, its detection in other plant extracts suggests its potential presence in botanical samples. The variation in chemical compounds among oil samples may be attributed to the use of different Cymbopogon species. Nevertheless, it is evident that cis- and trans-citral remain the most concentrated components in lemongrass essential oil, as confirmed by the data in Table 2.

3.4.2. GC/Q-TOF Analysis of Fresh Nanoemulsion Containing Lemongrass Essential Oil

In the fresh nanoemulsion sample, the characteristic peaks of cis and trans-citral, geraniol, geranyl acetate, caryophyllene, γ-Murrolene, and 10,13-octadecadiynoic acid methyl ester peaks were still observed (Figure 6).

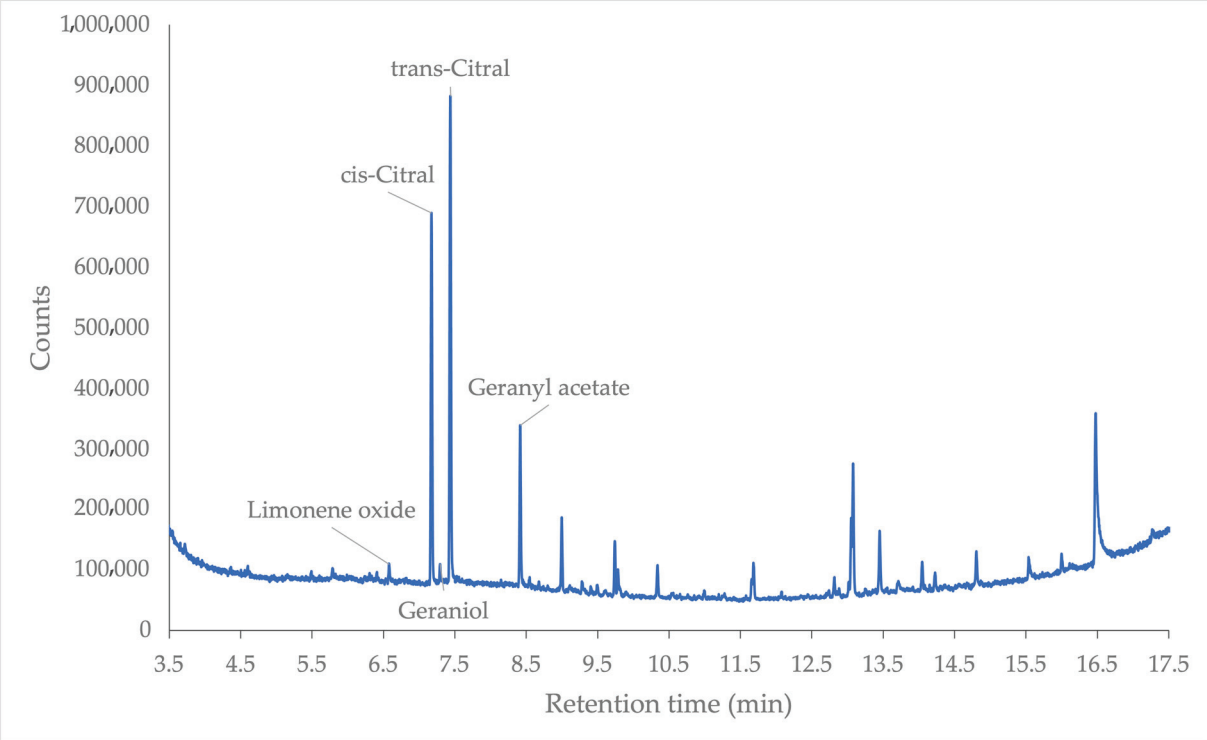


Figure 6. GC/Q-TOF chromatogram of fresh nanoemulsion extraction.

Cis- and trans-citral were again identified as the compounds with the highest relative percentages, at 18.80% and 25.64%, respectively. However, unlike the pure EO sample,

the third most abundant compound was identified at a retention time of 16.5 min as 9-Desoxo-9-x-acetoxy-3,8,12-tri-O-acetylingol. Additionally, new peaks emerged in the nanoemulsion as compared to pure EO, after the addition of T80, SBS-CNC, NaCl, and water. The most prominent new peaks appeared at retention times of approximately 13 min (two peaks) and 16.5 min (the strongest new peak) (Figure 6). At around 13 min, the two most probable compounds identified were 5,8,11-Heptadecatriynoic acid methyl ester and 1,8,15,22-Tricosatetrayne (Table 3). While these molecules have not been previously reported in lemongrass EO studies, their presence has been documented in other methanolic plant extracts [46,47]. Similarly, the compound detected at 16.5 min has not been identified in lemongrass oil studies but has been reported in the M. spicata species [45].

Table 3. Names of compounds, retention time, and relative percentage in the fresh nanoemulsion extract. Compound names were determined based on the most probable compound suggested from a single chromatogram replicate of the fresh nanoemulsion extract. Compounds labeled as numbers correspond to compounds with long chemical names.

Compound	Retention Time (min)	Relative Percentage (%)
Limonene oxide	6.578	0.783
cis-Citral	7.174	18.799
Geraniol	7.295	0.680
trans-Citral	7.439	25.644
Geranyl acetate	8.416	7.702
Caryophyllene	8.998	3.170
γ-Muurolene	9.742	2.454
Cadina-1(10),4-diene	9.785	1.562
Caryophyllene oxide	10.341	1.631
(1)	11.683	1.832
(2)	12.818	0.884
Methyl 5,8,11-heptadecatrienoate	13.052	3.181
1,8,15,22-Tricosatetrayne	13.079	6.815
(3)	13.45	3.460
(4)	13.712	0.883
α-N-Normethadol	14.046	1.485
(5)	14.806	1.812
(6)	15.536	1.534
W-18	16.476	16.474

Note: Samples labeled with numbers 1–6 correspond to compounds with names that would not fit into the table. Compounds names are as follows: (1)—4-O-Methyl-12b,13,20-triacetoxy-2,9-dihydroxy-3a-carboxy-2,3-seco-tigla-1(10),6-diene-3,9-lactone; (2)—Benzene, 1,3,5-tris(3-methyl-3-butenyl)-; (3)—5,8,11-Heptadecatriynoic acid, methyl ester; (4)—3-Pyridinecarboxylic acid, 1,6-dihydro-4-hydroxy-2-methyl-6-oxo-1-phenyl-ethyl ester; (5)—not identified, (6)—(4-Isopropylidenebicyclo[3.2.0]hept-2-en-6-ylidene)acetic acid, methyl ester.

The peak at 16.5 min showed a relative percentage of 16.47%, followed by geranyl acetate at around 7.70% and multiple other molecules with relative percentages close to 3.00% (Table 3). Outside of citral, geraniol, and geranyl acetate, all peaks mentioned were not confirmed by use of a standard; rather, the peaks were identified using the Agilent Masshunter software and NIST library. Generally, the highest probability molecule was selected, and similar results in the literature were searched for. Outside of the molecules discussed already, there were others detected that are reported in Table 3. To our knowledge, every molecule in the table after caryophyllene oxide has not been reported in lemongrass essential oil studies in the literature. Many of them have been reported in other plant extract studies, while others have not been mentioned or noticed at all. Additionally, because standards were not purchased and tested for these molecules, we cannot confirm their existence in our tested samples. To aid in the confirmation of some of these molecules

in our sample as either natural or degradation products, we researched the literature. To summarize the literature search for the source of these molecules, we created a table displaying this information in the Supplementary Materials Table S1.

3.5. Effect of Light Exposure and Room Temperature Storage on Freeze-Dried Nanoemulsion Containing LGEO

3.5.1. Effect of Light Exposure and Room Temperature Storage on the Antioxidant Activity of Freeze-Dried Nanoemulsion

After examining the effect of room temperature storage on pure EO and fresh nanoemulsion, we investigated the impact of light exposure on freeze-dried nanoemulsion. For the control, freeze-dried nanoemulsion samples stored at −80 °C until the day of the experiment were used (labeled day 0), both with and without light exposure. These samples were then stored under their respective conditions for 30 days. The highest antioxidant activity in redispersed nanoemulsion samples after freeze-drying was observed in the sample that had neither been stored at room temperature nor exposed to light, with a value of 32.37% (Figure 7).

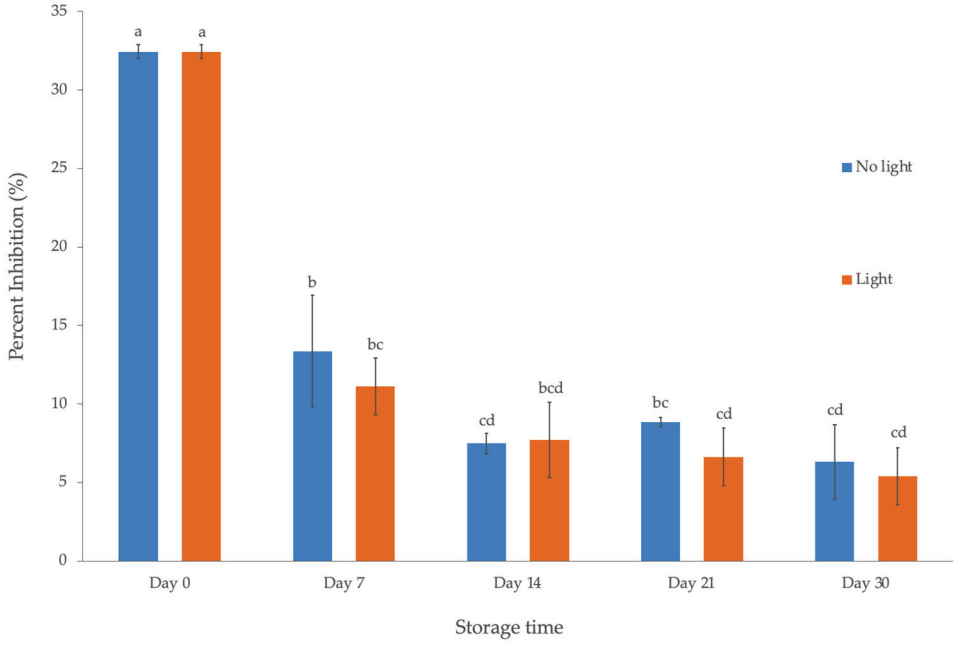


Figure 7. Effect of room temperature, storage time and light exposure on the antioxidant activity of lyophilized nanoemulsions. Samples without shared letter(s) are significantly different.

In comparison, fresh nanoemulsion retained nearly 63% antioxidant activity, while the redispersed lyophilized nanoemulsion showed only 32.37%, indicating that the antioxidant activity was nearly halved after freeze-drying. For antioxidant activity experiments, the redispersed nanoemulsion was dissolved in water and diluted to a measurable value on the UV–vis spectrometer. Calculations were performed to ensure that the initial concentration of EO in the redispersed samples was 5%, similar to that of the fresh nanoemulsion samples. Despite maintaining the same initial EO concentration, the significant decrease in antioxidant activity suggests that this loss is primarily due to the loss of the antioxidant compound in the lyophilized nanoemulsion.

Additionally, a significant decrease in the antioxidant activity was seen for all samples after 1 week of storage (Figure 7). This result aligns with a study in which citral essential oil (the main component of LGEO) was characterized in a nanoemulsion system [48]. In that study, the particle size was unstable and increased significantly every day during the

first 7 days of storage and then began to reach thermodynamic equilibrium, resulting in a more stable particle size thereafter.

After 7 days of storage, the sample without light exposure had, on average, 2.5% more antioxidant activity than the sample exposed to light (Figure 7). On day 14, samples with and without light exposure had average activity that differed by around 0.5%. Finally, samples with and without light exposure had the lowest antioxidant activity after 30 days of storage (Figure 7). On day 30, samples without light exposure had an average activity of 6.31% while the sample with light exposure had an average activity of 5.39%. Overall, the experiments revealed a trend that the antioxidant activity of samples decreases during room temperature storage with or without light exposure. Statistical analysis of results revealed that light exposure did not significantly affect the antioxidant activity, but rather, time was the significant factor. After one week of storage, the most dramatic loss of activity was measured, and small variations were measured after that. Similar findings have been reported in the literature, showing a significant decrease in antioxidant activity over time [49]. In that study, exposure to light led to a significant reduction in the antioxidant capacity of nanoemulsions containing plant extracts over a 30-day period. In the same study, significant decreases in activity were observed for samples stored at room temperature without light exposure, indicating that some antioxidant capacity was lost during storage. This decline could be attributed to a decrease in antioxidant-contributing compounds, such as citral, over time. In a similar study, researchers found that citral content decreased consistently over a 30-day period in four different nanoemulsions containing octadecane, SDS, and Brij [50]. The findings here, along with those in the literature, suggest that components responsible for antioxidant activity are being lost during storage, a point that will be further explored in the next section.

3.5.2. Effect of Light Exposure and Room Temperature Storage Time on the Composition of Lemongrass Essential Oil-Loaded Nanoemulsion

To examine the effect of encapsulated essential oil breakdown at room temperature, with and without light exposure, GC/Q-TOF compound detection and quantification methods were employed. Among the samples tested after freeze-drying and stored at room temperature without light exposure, several familiar peaks were observed (Figure 8).

Peaks corresponding to cis and trans-citral were present in all samples without light exposure, although at very low concentrations in some samples (Figure 8). While not detected in every sample, geraniol and geranyl acetate were present in samples up to day 14 (Figure 8). Recognizable peaks appeared at retention times around 13, 13.5, and 16.5 min and were detected in all samples. For these peaks, a significant decrease in peak area was observed after one week of storage, and generally, the peak areas continued to decline until day 21. On day 30, many of the peaks showed an increase in peak area; although this did not correlate with an average concentration increase (discussed in a later section), and was still significantly lower than the peaks observed on day 0.

A new peak, which had not been seen in previous samples, was discovered in freeze-dried samples. This peak appeared at around a 3.7 min retention time and was present in all replicates tested, although at significantly lower peak area values compared to day-0 samples. Among the replicates, two compounds were frequently suggested with high probabilities for this peak: styrene and benzeneethanamine, N-[(4-hydroxy)hydrocinnamoyl]-. Both compounds have been detected in plant products or essential oils; further verification with standards would be needed to confirm the compound being detected. Additionally, between 8.5 and 12.5 min, around eight peaks were detected on day 0. Each of these peaks, except for those at 10.3 and 11.7 min, was undetectable after one week.

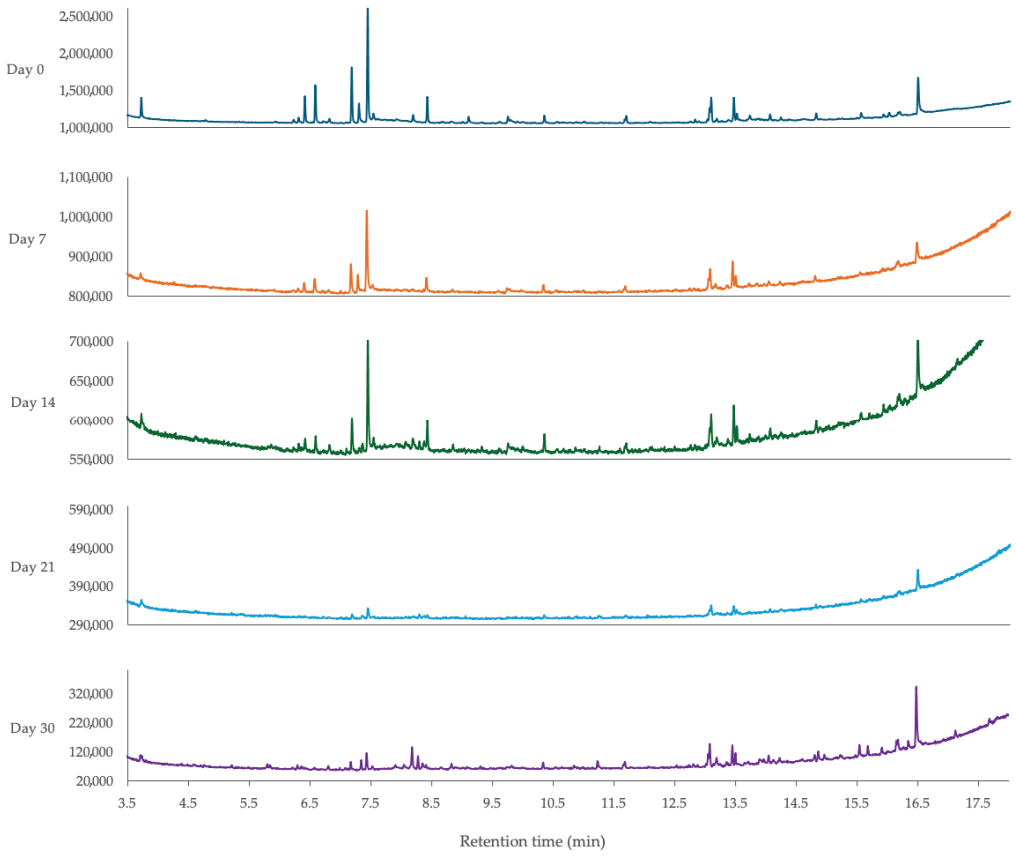


Figure 8. GC/Q-TOF results of nanoemulsion stored at room temperature without light exposure over a 30-day period.

One peak that appeared only after storage was found at 11.2 min. This peak was only present after 30 days of storage in the samples without light exposure. It was also found in increasing concentrations starting on day 14 in samples exposed to light (Figure 9).

After light exposure, the loss of distinct peaks occurred more rapidly. The peaks that were not completely extinguished by day 7 are located at retention times of 7.17, 7.43, 13.05, 13.08, and 16.48 min. The peaks at 7.17 and 7.43 min correspond to cis and trans-citral, respectively. Although both citral compounds were present after 7 days of exposure, they were no longer detected in samples beyond that point. In contrast, the peaks at 13.05, 13.08, and 16.48 min were detected throughout the entire 30-day period, with an increase in concentration observed from day 21 to day 30.

In addition to the peak at 11.2 min, the samples exposed to light revealed the appearance of several new molecules. The first of these was located at around 5.8 min. This peak was faintly noticeable on days 14 and 21 but became most prominent after 30 days of light exposure. Other peaks following a similar trend, with the most prominent peak appearing on day 30, were located at 7.35, 8.15, 8.28, 11.24, 13.18, 14.85, 15.67, and 16.35 min (Figure 9).

A final note regarding samples in either exposure condition is the dramatic loss of volatiles after only 7 days of storage. As speculated earlier, the stabilizing effect of the essential oil, which was initially present in the nanoemulsions, was no longer observed, likely leading to significantly reduced peak sizes over time. Figures 8 and 9, in combination with the earlier antifungal and antioxidant data, suggest that the morphology and physicochemical characteristics that once stabilized the oil have become less effective. Variations in the most probable compound suggested by the software were noticed between replicates, making the determination of new peaks more difficult with our data set. For interested

readers, a table describing the variation in names and their presence in the literature has been developed (Supplementary Materials Table S2).

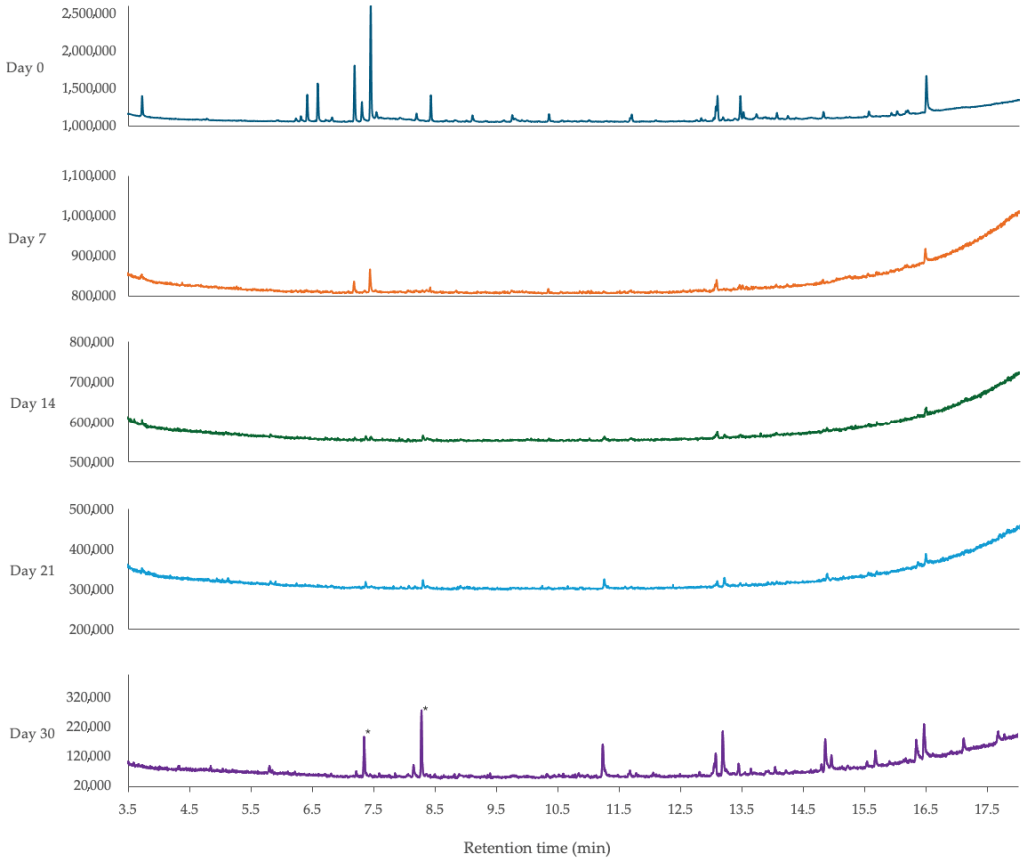


Figure 9. GC/Q-TOF results of nanoemulsion stored at room temperature with exposure to light over a 30-day time period. Note: * corresponds to peaks that appear to match peaks from the day 0 sample but have different retention times and represent different molecules.

3.5.3. Effect of Light Exposure and Room Temperature Storage on the Concentration of Four Volatile Components in Lemongrass Essential Oil-Loaded Nanoemulsion

Alongside compositional changes of the LGEO-loaded nanoemulsion, concentration changes for four volatile components were also quantified (Table 4).

Table 4. Average concentrations of four primary peaks of lyophilized nanoemulsion samples as determined by GC/Q-TOF.

Day	Condition	Cis-Citral Concentration (ppm)	Trans-Citral Concentration (ppm)	Geraniol Concentration (ppm)	Geranyl Acetate Concentration (ppm)
0	Day 0	1427.16	3804.20	898.81	107.41
7	No light	582.21	1674.69	557.66	111.76
14	No light	207.38	679.18	128.31	60.45
21	No light	82.98	169.50	0	0
30	No light	35.52	75.10	0	0
7	Light	51.35	62.43	0	17.96
14	Light	9.36	4.60	0	0
21	Light	0	0	0	0
30	Light	0	0	0	0

For compounds except geranyl acetate, the highest concentrations of volatile components were observed on day 0, before any storage or light exposure. Geranyl acetate maintained its concentration through one week of storage but then declined, becoming undetectable by day 21. The other three peaks showed consistent decreases in concentration over the storage period. Specifically, both citral peaks decreased steadily, reaching their lowest concentrations on day 30. For geraniol, the peak disappeared by day 21 and remained undetectable on day 30 (Table 4).

The reduction in volatile compounds may explain the diminished stability of the nanoemulsions after freeze-drying, potentially facilitating greater vaporization of LGEO at room temperature. Similar trends were reported by Irmak et al. [51], who observed significant losses of phenolic content and antioxidant activity in rosemary oil stored at room temperature compared to 4 °C over four weeks. To determine if a similar rate of volatile loss occurs in fresh nanoemulsions, further experiments with fresh samples stored over a 30-day period are warranted.

Light-exposed samples produced markedly different results compared to those shielded from light. By day 21, both citral peaks were undetectable in light-exposed samples, while they remained measurable in the light-shielded samples (Table 4). Additionally, in light-exposed samples, geraniol was not detected at any point, and geranyl acetate was only observed after one week of exposure. These findings suggest that light exposure accelerates the degradation of LGEO volatiles. While volatile concentrations also decreased significantly in light-shielded samples, the process was notably slower under these conditions.

Although the data in Table 4 indicate that neither exposure condition preserved sample stability, the results align with trends observed in related studies. In all conditions, the concentrations of the four volatile components declined consistently, reaching either minimal values or zero after 30 days. Notably, even light-shielded samples stored solely at room temperature exhibited substantial volatile losses, suggesting an imperfect storage method. These findings are consistent with other studies involving freeze-dried nanoemulsions, which often report diminished activity and lower volatile concentrations compared to fresh counterparts.

This indicates that freeze-drying compromises EO stability within nanoemulsions. Previous research has compared various drying methods, such as spray drying, freeze-drying, and spray freeze-drying, in CNC-based formulations across different applications [22–24]. These studies suggest that alternative or combined drying methods could better preserve morphological and chemical features, thereby maintaining volatile component stability and bioactivity. Future investigations may need to explore these methods to optimize antifungal and antioxidant activity alongside the retention of volatile components.

4. Conclusions

In this study, we developed and characterized a nanoemulsion that was freeze-dried and subsequently redispersed in water. The freeze-drying process significantly impacted the physical and chemical properties of the nanoemulsion, reducing the zeta potential from 39.2 mV to 30.6 mV and increasing particle size from 137 nm to 158 nm. Additionally, approximately 30% of the essential oil concentration was lost during freeze-drying. Redispersed lyophilized nanoemulsions also exhibited a substantial decline in bioactivity, with antifungal activity decreasing by 77% and antioxidant activity by 31%. Storage conditions further influenced stability, with light exposure accelerating the degradation of key volatile compounds—cis- and trans-citral, geraniol, and geranyl acetate—detected via GC/Q-TOF. Antioxidant activity declined sharply after one week of storage under both light-exposed and light-shielded conditions, potentially due to thermodynamic stresses,

before stabilizing at approximately 50% of the day 7 activity. Discrepancies between volatile degradation and antioxidant activity may stem from contributions by formulation components such as Tween 80, NaCl, and SBS-CNC. Light exposure also caused significant chemical changes, with 11 new compounds forming during storage compared to one in light-shielded samples. These findings suggest that light exposure accelerates chemical changes in the nanoemulsion, potentially further reducing its bioactivity and stability. Findings from this study highlight challenges in maintaining stability and bioactivity of essential oil-loaded nanoemulsions after freeze-drying, likely due to disruptions in stabilizing factors of the original O/W nanoemulsion. Despite these challenges, the fresh nanoemulsion demonstrated promising LGEO bioactivity, providing a foundation for further optimization. Refining freeze-drying protocols and formulation conditions could enhance stability and unlock new applications for renewable, bioactive nanoemulsions.

Supplementary Materials: The following supporting information can be downloaded at: https://www.mdpi.com/article/10.3390/pr13092752/s1, Figure S1. Images of antifungal activity experiments (corresponding to results in Figure 3). Images are representative of replicates.; Table S1. Literature search of components of fresh nanoemulsion extract detected by GC/Q-TOF. Columns highlight the name of the compound detected, whether the compound was detected in LGEO in other studies, whether the compound was detected in EO in general, the source of the molecule in the literature, and the citation of the publications citing the specific molecule.; Table S2. Compound compilation of molecules detected at similar retention times in freeze-dried nanoemulsion extract samples. Table contains a literature search of compounds detected in the freeze-dried nanoemulsion extract samples. Columns highlight the name of the compound detected, whether the compound was detected in LGEO in other studies, whether the compound was detected in EO in general, the source of the molecule in the literature, and the citation of the publications citing the specific molecule. References [5,34,35,44–46] are cited in the main text and Supplementary Materials. References [52–94] are cited in the Supplementary Materials.

Author Contributions: Conceptualization, L.L.; methodology, L.L. and K.D.F.; validation, L.L. and K.D.F.; formal analysis, L.L. and K.D.F.; investigation, L.L. and K.D.F.; resources, L.L.; data curation, L.L. and K.D.F.; writing—original draft preparation, K.D.F.; writing—review and editing, L.L. and K.D.F.; visualization, L.L. and K.D.F.; supervision, L.L.; project administration, L.L.; funding acquisition, L.L. All authors have read and agreed to the published version of the manuscript.

Funding: This research was supported by the Iowa Soybean Association.

Data Availability Statement: The original contributions presented in the study are included in the article; further inquiries can be directed to the corresponding author.

Acknowledgments: The authors would like to thank Lorien Radmer and Adina Howe from the Genomics and Environmental Research in Microbial Systems lab at Iowa State University for their generosity and assistance with freeze-drying samples.

Conflicts of Interest: The authors declare no conflicts of interest.

Abbreviations

The following abbreviations are used in this manuscript:

SBS-CNC	Soybean stover-derived cellulose nanocrystals
O/W	Oil-in-water
LGEO	Lemongrass essential oil
EO	Essential oil

References

1. Hüsnü Can Baser, K.; Demirci, F. Chemistry of essential oils. In *Flavours and Fragrances: Chemistry, Bioprocessing and Sustainability*; Springer: Berlin/Heidelberg, Germany, 2007; pp. 43–86.
2. Abers, M.; Schroeder, S.; Goelz, L.; Sulser, A.; St. Rose, T.; Puchalski, K.; Langland, J. Antimicrobial activity of the volatile substances from essential oils. *BMC Complement. Med. Ther.* **2021**, *21*, 124. [CrossRef]
3. Hu, F.; Tu, X.; Thakur, K.; Hu, F.; Li, X.; Zhang, Y.; Zhang, J.; Wei, Z. Comparison of antifungal activity of essential oils from different plants against three fungi. *Food Chem. Toxicol.* **2019**, *134*, 110821. [CrossRef]
4. Andoğan, B.C.; Baydar, H.; Kaya, S.; Demirci, M.; Özbaşar, D.; Mumcu, E. Antimicrobial activity and chemical composition of some essential oils. *Arch. Pharmacal Res.* **2002**, *25*, 860–864. [CrossRef]
5. Mukarram, M.; Choudhary, S.; Khan, M.A.; Poltronieri, P.; Khan, M.M.A.; Ali, J.; Kurjak, D.; Shahid, M. Lemongrass Essential Oil Components with Antimicrobial and Anticancer Activities. *Antioxidants* **2022**, *11*, 20. [CrossRef]
6. Martinazzo, A.P.; Oliveira, F.S.; Teodoro, C.E.S. Antifungal activity of *Cymbopogon citratus* essential oil against *Aspergillus flavus*. *Cienca E Nat.* **2022**, *41*, e20. [CrossRef]
7. Oxenham, S.K.; Svoboda, K.P.; Walters, D.R. Antifungal activity of the essential oil of basil (*Ocimum basilicum*). *J. Phytopathol.* **2005**, *153*, 174–180. [CrossRef]
8. Daouk, R.K.; Dagher, S.M.; Sattout, E.J. Antifungal activity of the essential oil of *Origanum syriacum* L. *J. Food Prot.* **1995**, *58*, 1147–1149. [CrossRef]
9. Barradas, T.N.; Gyselle de Holanda e Silva, K. Nanoemulsions of essential oils to improve solubility, stability and permeability: A review. *Environ. Chem. Lett.* **2021**, *19*, 1153–1171. [CrossRef]
10. Weisheimer, V.; Miron, D.; Silva, C.B.; Guterres, S.S.; Schapoval, E.E.S. Microparticles containing lemongrass volatile oil: Preparation, characterization and thermal stability. *Die Pharm. Int. J. Pharm. Sci.* **2010**, *65*, 885–890.
11. Rowshan, V.; Bahmanzadegan, A.; Saharkhiz, M.J. Influence of storage conditions on the essential oil composition of Thymus daenensis Celak. *Ind. Crops Prod.* **2013**, *49*, 97–101. [CrossRef]
12. Mehdizadeh, L.; Ghasemi Pirbalouti, A.; Moghaddam, M. Storage stability of essential oil of cumin (*Cuminum cyminum L.*) as a function of temperature. *Int. J. Food Prop.* **2017**, *20* (Suppl. S2), 1742–1750. [CrossRef]
13. Turek, C.; Stintzing, F.C. Impact of different storage conditions on the quality of selected essential oils. *Food Res. Int.* **2012**, *46*, 341–353. [CrossRef]
14. Gupta, A.; Eral, H.B.; Hatton, T.A.; Doyle, P.S. Nanoemulsions: Formation, properties and applications. *Soft Matter* **2016**, *12*, 2826–2841. [CrossRef]
15. Chu, Y.; Xu, T.; Gao, C.; Liu, X.; Zhang, N.I.; Feng, X.; Liu, X.; Shen, X.; Tang, X. Evaluations of physicochemical and biological properties of pullulan-based films incorporated with cinnamon essential oil and Tween 80. *Int. J. Biol. Macromol.* **2019**, *122*, 388–394. [CrossRef]
16. Chaudhari, A.K.; Singh, V.K.; Das, S.; Dubey, N.K. Fabrication, characterization, and bioactivity assessment of chitosan nanoemulsion containing allspice essential oil to mitigate *Aspergillus flavus* contamination and aflatoxin B1 production in maize. *Food Chem.* **2022**, *372*, 131221. [CrossRef]
17. Harleen, K.; Pranav, P.; Ramneek, K.; Shriya, A.; Manisha, S. Synthesis and characterization of Citrus limonum essential oil based nanoemulsion and its enhanced antioxidant activity with stability for transdermal application. *J. Biomater. Nanobiotechnology* **2020**, *11*, 215–236. [CrossRef]
18. Gong, X.; Wang, Y.; Chen, L. Enhanced emulsifying properties of wood-based cellulose nanocrystals as Pickering emulsion stabilizer. *Carbohydr. Polym.* **2017**, *169*, 295–303. [CrossRef]
19. Habibi, Y.; Lucia, L.A.; Rojas, O.J. Cellulose nanocrystals: Chemistry, self-assembly, and applications. *Chem. Rev.* **2010**, *110*, 3479–3500. [CrossRef]
20. do Vale Morais, A.R.; do Nascimento Alencar, É.; Júnior, F.H.X.; De Oliveira, C.M.; Marcelino, H.R.; Barratt, G.; Fessi, H.; Do Egito, E.S.T.; Elaissari, A. Freeze-drying of emulsified systems: A review. *Int. J. Pharm.* **2016**, *503*, 102–114. [CrossRef] [PubMed]
21. El-Messery, T.M.; Altuntas, U.; Altin, G.; Özçelik, B. The effect of spray-drying and freeze-drying on encapsulation efficiency, in vitro bioaccessibility and oxidative stability of krill oil nanoemulsion system. *Food Hydrocoll.* **2020**, *106*, 105890. [CrossRef]
22. Alarcón-Moyano, J.; Acuña, D.; Matiacevich, S.; Caballero, L.; Melo, F.; Quero, F.; Díaz-Calderón, P. Physico-chemical and structural characterization of cellulose nanocrystals obtained by two drying methods: Freeze-drying and spray-drying. *Food Hydrocoll.* **2023**, *140*, 108571. [CrossRef]
23. Khoshkava, V.; Kamal, M.R. Effect of drying conditions on cellulose nanocrystal (CNC) agglomerate porosity and dispersibility in polymer nanocomposites. *Powder Technol.* **2024**, *261*, 288–298. [CrossRef]
24. Abdallah, W.; Kamal, M.R. Influence of process variables on physical characteristics of spray freeze dried cellulose nanocrystals. *Cellulose* **2018**, *25*, 5711–5730. [CrossRef]
25. Liu, L.; Abiol, K.A.; Friest, M.A.; Fisher, K.D. Synergistic stabilization of nanoemulsion using nonionic surfactants and salt-sensitive cellulose nanocrystals. *Polymers* **2023**, *15*, 4682. [CrossRef]

26. Liu, L.; Fisher, K.D.; Bussey, W.D. Comparison of emulsion stabilizers: Application for the enhancement of the bioactivity of lemongrass essential oil. *Polymers* **2024**, *16*, 415. [CrossRef]
27. Jiménez-Escrig, A.; Jiménez-Jiménez, I.; Sánchez-Moreno, C.; Saura-Calixto, F. Evaluation of free radical scavenging of dietary carotenoids by the stable radical 2, 2-diphenyl-1-picrylhydrazyl. *J. Sci. Food Agric.* **2000**, *80*, 1686–1690. [CrossRef]
28. Baliyan, S.; Mukherjee, R.; Priyadarshini, A.; Vibhuti, A.; Gupta, A.; Pandey, R.P.; Chang, C.M. Determination of antioxidants by DPPH radical scavenging activity and quantitative phytochemical analysis of Ficus religiosa. *Molecules* **2022**, *27*, 1326. [CrossRef] [PubMed]
29. Kovacevic, A.; Savic, S.; Vuleta, G.; Mueller, R.H.; Keck, C.M. Polyhydroxy surfactants for the formulation of lipid nanoparticles (SLN and NLC): Effects on size, physical stability and particle matrix structure. *Int. J. Pharm.* **2011**, *406*, 163–172. [CrossRef]
30. Farouil, L.; Dias, R.P.; Popotte-Julisson, G.; Bibian, G.; Adou, A.I.; de la Mata, A.P.; Muriel, S.; James, J.H.; Cebrián-Torrejón, G. The Metabolomic Profile of the Essential Oil from *Zanthoxylum caribaeum* (syn. chiloperone) Growing in Guadeloupe FWI using GC× GC-TOFMS. *Metabolites* **2022**, *12*, 1293. [CrossRef]
31. Bashlouei, S.G.; Karimi, E.; Zareian, M.; Oskoueian, E.; Shakeri, M. Heracleum persicum essential oil nanoemulsion: A nanocarrier system for the delivery of promising anticancer and antioxidant bioactive agents. *Antioxidants* **2022**, *11*, 831. [CrossRef] [PubMed]
32. de Godoi, S.N.; Quatrin, P.M.; Sagrillo, M.R.; Nascimento, K.; Wagner, R.; Klein, B.; Ourique, A.F. Evaluation of stability and in vitro security of nanoemulsions containing Eucalyptus globulus oil. *BioMed Res. Int.* **2017**, *1*, 2723418. [CrossRef]
33. Pinto, L.D.A.; Machado, F.P.; Esteves, R.; Farias, V.M.; Köptcke, F.B.N.; Ricci-Junior, E.; Rocha, L.; Keller, L.A.M. Characterization and inhibitory effects of essential oil and nanoemulsion from Ocotea indecora (Shott) Mez in Aspergillus species. *Molecules* **2023**, *28*, 3437. [CrossRef]
34. Soliman, W.S.; Salaheldin, S.; Amer, H.M. Chemical Composition Evaluation of Egyptian Lemongrass, *Cymbopogon citratus*, Essential Oil. *Int. J. Sci. Eng. Res.* **2017**, *8*, 630–634.
35. Hanaa, A.M.; Sallam, Y.I.; El-Leithy, A.S.; Aly, S.E. Lemongrass (*Cymbopogon citratus*) essential oil as affected by drying methods. *Ann. Agric. Sci.* **2012**, *57*, 113–116. [CrossRef]
36. Silva, C.D.B.D.; Guterres, S.S.; Weisheimer, V.; Schapoval, E.E. Antifungal activity of the lemongrass oil and citral against *Candida* spp. *Braz. J. Infect. Dis.* **2008**, *12*, 63–66.
37. Tang, X.; Shao, Y.L.; Tang, Y.J.; Zhou, W.W. Antifungal activity of essential oil compounds (*geraniol* and *citral*) and inhibitory mechanisms on grain pathogens (*Aspergillus flavus* and *Aspergillus ochraceus*). *Molecules* **2018**, *23*, 2108. [CrossRef] [PubMed]
38. Aw, Y.Z.; Lim, H.P.; Low, L.E.; Singh, C.K.S.; Chan, E.S.; Tey, B.T. Cellulose nanocrystal (CNC)-stabilized Pickering emulsion for improved curcumin storage stability. *Lwt* **2022**, *159*, 113249. [CrossRef]
39. Anggraeni, N.I.; Hidayat, I.W.; Rachman, S.D.; Ersanda. Bioactivity of essential oil from lemongrass (*Cymbopogon citratus Stapf*) as antioxidant agent. *AIP Conf. Proc.* **2018**, *1927*, 030007. [CrossRef]
40. Mirghani, M.E.S.; Liyana, Y.; Parveen, J. Bioactivity analysis of lemongrass (*Cymbopogan citratus*) essential oil. *Int. Food Res. J.* **2012**, *19*, 569–575.
41. Pérez-Rosés, R.; Risco, E.; Vila, R.; Peñalver, P.; Cañigueral, S. Antioxidant activity of Tween-20 and Tween-80 evaluated through different in-vitro tests. *J. Pharm. Pharmacol.* **2015**, *67*, 666–672. [CrossRef]
42. Yu, Z.; Sun, L.; Wang, W.; Zeng, W.; Mustapha, A.; Lin, M. Soy protein-based films incorporated with cellulose nanocrystals and pine needle extract for active packaging. *Ind. Crops Prod.* **2018**, *112*, 412–419. [CrossRef]
43. Physical Properties of Pure Methanol. Available online: https://www.methanol.org/wp-content/uploads/2016/06/Physical-Properties-of-Pure-Methanol.pdf (accessed on 27 August 2025).
44. Ali, M.M.; Yusuf, M.A.; Abdalaziz, M.N. GC-MS Analysis and Antimicrobial Screening of Essential Oil from Lemongrass (*Cymbopogon citratus*). *Int. J. Pharm. Chem.* **2017**, *3*, 72–76. [CrossRef]
45. Praveen, T.; Krishnamoorthy, A.S.; Nakkeeran, S.; Sivakumar, U.; Amirtham, D. Antifungal volatiles from medicinal herbs suppress *Fusarium oxysporum* f. sp. lycopersici. *J. Entomol. Zool. Stud.* **2021**, *9*, 1083–1093.
46. Altameme, H.J.M. GC-MS and FTIR analysis Phytocomponents on different parts of *Capparis spinosa* L. (Capparidaceae) in Iraq. *J. Chem. Pharm. Sci.* **2016**, *4*, 3269–3282.
47. Pal, A.; Ray, R.; Acharya, K.; Paul, S. Assessment of the anti-leukemic and antioxidant potential of the methanol extract of a wild, edible, and novel mushroom, *Astraeus hygrometricus*, and unraveling its metabolomic profile. *J. Adv. Biotechnol. Exp. Ther.* **2021**, *4*, 388–404. [CrossRef]
48. Lu, W.C.; Huang, D.W.; Wang, C.C.; Yeh, C.H.; Tsai, J.C.; Huang, Y.T.; Li, P.H. Preparation, characterization, and antimicrobial activity of nanoemulsions incorporating citral essential oil. *J. Food Drug Anal.* **2018**, *26*, 82–89. [CrossRef]
49. Bazana, M.T.; da Silva, S.S.; Codevilla, C.F.; de Deus, C.; Lucas, B.N.; Ugalde, G.A.; Mazutti, M.A.; Flores, E.M.M.; Barin, J.S.; da Silva, C.D.B.; et al. Development of nanoemulsions containing Physalis peruviana calyx extract: A study on stability and antioxidant capacity. *Food Res. Int.* **2019**, *125*, 108645. [CrossRef] [PubMed]
50. Mei, L.; Choi, S.J.; Alamed, J.; Henson, L.; Popplewell, M.; McClements, D.J.; Decker, E.A. Citral stability in oil-in-water emulsions with solid or liquid octadecane. *J. Agric. Food Chem.* **2010**, *58*, 533–536. [CrossRef]

51. Irmak, S.; Solakyildirim, K.; Hesenov, A.; Erbatur, O. Study on the stability of supercritical fluid extracted rosemary (*Rosmarinus offcinalis* L.) essential oil. *J. Anal. Chem.* **2010**, *65*, 899–906. [CrossRef]
52. Aguirre-Becerra, H.; Pineda-Nieto, S.A.; García-Trejo, J.F.; Guevara-González, R.G.; Feregrino-Pérez, A.A.; Álvarez-Mayorga, B.L.; Pastrana, D.M.R. Jacaranda flower (*Jacaranda mimosifolia*) as an alternative for antioxidant and antimicrobial use. *Heliyon* **2002**, *6*, e05802. [CrossRef]
53. Ahmed, R.; Abdel-Rahman, A. Effect of Papaya Wastes on Quality Characteristics of Meat Burger. *New Val. J. Agric. Sci.* **2022**, *2*, 483–511. [CrossRef]
54. Ahuchaogu, A.A.; Igara, C.E. Antibacterial, GC-MS and FTIR Chemical Profiling of Methanol Leaf Extract of Cymbopogon citratus Linn. *ARC J. Pharm. Sci.* **2011**, *7*, 1–9.
55. Almalki, G.; Rabah, S.; Al-Faifi, Z.; Alharbi, A.; Sharma, M. Phytochemistry Screening, Antioxidant and Antimicrobial Activities of *Euphorbia inarticulata* Schweinf Plant Extract. *Pharmacophore* **2022**, *13*, 91–99. [CrossRef]
56. Antwi-Agyakwa, A.K.; Yusuf, A.A.; Pirk, C.W.; Mohamed, S.A.; Ekesi, S.; Torto, B. Exploring non-host plant-based management strategy with lemongrass, garlic and guava volatiles for the African citrus triozid. *J. Appl. Entomol.* **2021**, *145*, 757–766. [CrossRef]
57. Ayalew, A.A. Chromatographic and spectroscopic determination of solvent-extracted Lantana camara leaf oil. *J. Int. Med. Res.* **2020**, *48*, 300060520962344. [CrossRef]
58. Begum, N.; Akhtar, K.; Ahanger, M.A.; Iqbal, M.; Wang, P.; Mustafa, N.S.; Zhang, L. Arbuscular mycorrhizal fungi improve growth, essential oil, secondary metabolism, and yield of tobacco (*Nicotiana tabacum* L.) under drought stress conditions. *Environ. Sci. Pollut. Res.* **2021**, *28*, 45276–45295. [CrossRef]
59. Bennett, V.; Godwin, J. Proximate, Selected Metals and Metabolites Profile of Citrullus lanatus (*Watermelon*) Leaves. *Int. J. Adv. Res. Chem. Sci.* **2023**, *10*, 14–21. [CrossRef]
60. Chairgulprasert, V.; Prasertsongskun, S.; Junpra-ob, S.; Sangjun, M. Chemical constituents of the essential oil, antioxidant and antibacterial activities from *Elettariopsis curtisii* Baker. *Songklanakarin J. Sci. Technol.* **2008**, *30*, 591–596.
61. Chanthai, S.; Prachakoll, S.; Ruangviriyachai, C.; Luthria, D.L. Influence of extraction methodologies on the analysis of five major volatile aromatic compounds of citronella grass (*Cymbopogon nardus*) and lemongrass (*Cymbopogon citratus*) grown in Thailand. *J. AOAC Int.* **2012**, *95*, 763–772. [CrossRef]
62. Chen, X.; Chen, H.; Xiao, J.; Liu, J.; Tang, N.; Zhou, A. Variations of volatile flavour compounds in finger citron (*Citrus medica* L. var. sarcodactylis) pickling process revealed by E-nose, HS-SPME-GC-MS and HS-GC-IMS. *Food Res. Int.* **2020**, *138*, 109717. [CrossRef] [PubMed]
63. Chung, H.Y.; Fung, P.K.; Kim, J.S. Aroma impact components in commercial plain sufu. *J. Agric. Food Chem.* **2005**, *53*, 1684–1691. [CrossRef] [PubMed]
64. Devi, M.A.; Singh, T.B. Composition of Essential Oil of Indigenous and Exotic Species of Lemongrass Growing in Manipur. *Ann. Multidiscip. Res. Innov. Technol.* **2023**, *2*, 58–64.
65. Elsharkawy, E.R.; Abdallah, E.M.; Shiboob, M.H.; Alghanem, S. Phytochemical, antioxidant and antibacterial potential of Ducrosia anethifolia in northern border region of Saudi Arabia. *J. Pharm. Res. Int.* **2019**, *31*, 1–8. [CrossRef]
66. Ghosh, S.; Derle, A.; Ahire, M.; More, P.; Jagtap, S.; Phadatare, S.D.; Patil, A.B.; Jabgunde, A.M.; Sharma, G.K.; Shinde, V.S.; et al. Phytochemical Analysis and Free Radical Scavenging Activity of Medicinal Plants *Gnidia glauca* and *Dioscorea bulbifera*. *PLoS ONE* **2012**, *8*, e82529. [CrossRef]
67. Harlina, P.W.; Ma, M.; Shahzad, R.; Gouda, M.M.; Qiu, N. Effect of clove extract on lipid oxidation, antioxidant activity, volatile compounds and fatty acid composition of salted duck eggs. *J. Food Sci. Technol.* **2018**, *55*, 4719–4734. [CrossRef]
68. Jaafar, F.M.; Osman, C.P.; Ismail, N.H.; Awang, K. Analysis of essential oils of leaves, stems, flowers and rhizomes of Etlingera elatior (Jack) RM Smith. *Malays. J. Anal. Sci.* **2007**, *11*, 269–273.
69. Javaid, A.; Qudsia, H.; Khan, I.H.; Anwar, A.; Ferdosi, M.F. Antifungal activity of Senna occidentalis root extract against *Macrophomina phaseolina* and its GC-MS analysis. *Pak. J. Weed Sci. Res.* **2022**, *28*, 115–122. [CrossRef]
70. Jisim, K.G.D.D.S.; Terbang, M. Analysis of essential oils of *Etlingera sphaerocephala* var. grandiflora by two-dimensional gas chromatography with time-of-flight mass spectrometry. *Malays. J. Anal. Sci.* **2010**, *14*, 32–40.
71. Kamel, D.G.; Mansour, A.I.; El-Diin, M.A.N.; Hammam, A.R.; Mehta, D.; Abdel-Rahman, A.M. Using rosemary essential oil as a potential natural preservative during stirred-like yogurt making. *Foods* **2022**, *11*, 1993. [CrossRef] [PubMed]
72. Kothiyal, G.; Singh, K.; Kishor, K.; Kamal, R.; Kunar, N. GC-MS Analysis For Determination of Bioactive Compounds of Phellinus Pectinatus: A Species of Wild Mushroom from Uttarakhand Himalaya, India. *J. Chem. Health Risks* **2024**, *14*, 2005–2013.
73. Mahavirsing Dinore, J.; Shivaji Patil, H.; Farooqui, S.; Pradhan, V.; Farooqui, M. GC/MS and LC/MS phytochemical analysis of *Vigna unguiculata* L. Walp pod. *Chem. Biodivers.* **2023**, *20*, e202200048. [CrossRef]
74. Mostafa, A.A.; Al-Rahmah, A.N.; Abdel-Megeed, A. Evaluation of some plant extracts for their antifungal and antiaflatoxigenic activities. *J. Med. Plants Res.* **2011**, *5*, 231–4238.
75. Mathkoor, M.M.; Alkhfaji, E.N.; Oda, N.A. Using GC-MS Technology to Identify the Compounds Resulting from Mixing of Alcoholic Extracts of Some Medicinal Plants. *J. Med. Chem. Sci.* **2022**, *6*, 486–499.

76. Mestour, S.; Meniai, A.H.; Melloul, S.; Louaer, M. Sustainability by extraction of bioactive compounds from onion seeds. *Comptes Rendus Chimie* **2024**, *27* (Suppl. S3), 55–67. [CrossRef]
77. Moni, J.N.R.; Adnan, M.; Tareq, A.M.; Kabir, M.I.; Reza, A.A.; Nasrin, M.S.; Capasso, R. Therapeutic potentials of syzygium fruticosum fruit (seed) reflected into an array of pharmacological assays and prospective receptors-mediated pathways. *Life* **2021**, *11*, 155. [CrossRef]
78. Mwithiga, G.; Maina, S.; Muturi, P.; Gitari, J. Lemongrass (*Cymbopogon flexuosus*) agronomic traits, oil yield and oil quality under different agro-ecological zones. *J. Agric. Food Res.* **2022**, *10*, 100422. [CrossRef]
79. Mwithiga, G.; Maina, S.; Muturi, P.; Gitari, J. Lemongrass (*Cymbopogon flexuosus*) growth rate, essential oil yield and composition as influenced by different soil conditioners under two watering regimes. *Heliyon* **2024**, *10*, e25540. [CrossRef] [PubMed]
80. Ojewumi, M.E.; Adedokun, S.O.; Omodara, O.J.; Oyeniyi, E.A.; Taiwo, O.S.; Ojewumi, E.O. Phytochemical and antimicrobial activities of the leaf oil extract of Mentha spicata and its efficacy in repelling mosquito. *Int. J. Pharm. Res. Allied Sci.* **2017**, *6*, 17–27.
81. Olayemi, R.F.; Jawonisi, I.O.; Samuel, J.A. Characterization and physico-chemical analysis of essential oil of *Cymbopogon citratus* leaves. *Bayero J. Pure Appl. Sci.* **2018**, *11*, 74–81. [CrossRef]
82. Oso, B.J.; Boligon, A.A.; Oladiji, A.T. Metabolomic profiling of ethanolic extracts of the fruit of *Xylopia aethiopica* (Dunal) a. rich using gas chromatography and high-performance liquid chromatography techniques. *J. Pharmacogn. Phytochem.* **2018**, *7*, 2083–2090.
83. Prakash, N.K.U.; Sripriya, N.S.; Raj, D.D.; Deepa, S.; Bhuvaneswari, S. Antioxidant potency and GC-MS composition of *Origanum majorana* Linn. *Pak. J. Pharm. Sci.* **2019**, *32*, 2117–2122. [PubMed]
84. Selim, S.A.; Aziz, M.H.A.; Mashait, M.S.; Warrad, M.F. Antibacterial activities, chemical constitutes and acute toxicity of Egyptian *Origanum majorana* L., *Peganum harmala* L. and *Salvia officinalis* L. essential oils. *Afr. J. Pharm. Pharmacol.* **2013**, *7*, 725–735.
85. Shruthi, C.N.; Kotresha, D. Chemical Profiling and in vitro Cytotoxic Properties of *Themeda triandra* Forssk. Against Human Bone Osteosarcoma Cell Line (MG-63). *Asian J. Biol. Life Sci.* **2024**, *13*, 83. [CrossRef]
86. Singh, P.K.; Krishnan, N.; Raman, P. Quantification of hormones and profiling of metabolites from vegetative to reproductive growth phase shift in *Lagenaria siceraria* (Molina) Standl. *Sci. Hortic.* **2024**, *323*, 112464. [CrossRef]
87. Steele, D.H.; Thornburg, M.J.; Stanley, J.S.; Miller, R.R.; Brooke, R.; Cushman, J.R.; Cruzan, G. Determination of styrene in selected foods. *J. Agric. Food Chem.* **1994**, *42*, 1661–1665. [CrossRef]
88. Strelyaeva, A.V.; Kharitonova, A.G.; Vaskova, L.B.; Luferov, A.N.; Bokov, D.O.; Bondar, A.A.; Bobkova, N.V.; Jeremic, N.; Lazareva, Y.B.; Antsyshkina, A.M.; et al. Research on External Signs and Chemical Composition of Medicinal Plant Raw Material-Leaves of Ficus Elastica. *Pharmacogn. J.* **2022**, *14*, 958–972. [CrossRef]
89. Tavanappanavar, A.N.; Mulla, S.I.; Seth, C.S.; Bagewadi, Z.K.; Rahamathulla, M.; Ahmed, M.M.; Farhana, S.A. Phytochemical analysis, GC–MS profile and determination of antibacterial, antifungal, anti-inflammatory, antioxidant activities of peel and seeds extracts (chloroform and ethyl acetate) of *Tamarindus indica* L. *Saudi J. Biol. Sci.* **2024**, *31*, 103878. [CrossRef]
90. Ulqodry, T.Z.; Nugroho, R.Y.; Khotimah, N.N.; Putri, W.A.E.; Aryawati, R.; Mohamed, C.A.R. Insecticidal Activity and Phytochemical Profiles of *Avicennia marina* and *Excoecaria agallocha* Leaves Extracts. *Indones. J. Mar. Sci.* **2023**, *28*, 148–160.
91. Villa-Ruano, N.; Pacheco-Hernández, Y.; Zárate-Reyes, J.A.; Cruz-Durán, R.; Lozoya-Gloria, E. Volatile composition and biological activities of the leaf essential oil from *Zanthoxylum limoncello* grown in Oaxaca, México. *Chem. Biodivers.* **2019**, *16*, e1800498. [CrossRef]
92. Vintisen, R.; Krishnan, K.T.; Veloo, K.V.; Rajandas, H.; Parimannan, S.; Ravichandran, M. Gas chromatography-mass spectrometry (GC-MS) analysis of phytocompounds isolated from *Hydnophytum formicarum* Jack tuber extracts. *J. Trop. Resour. Sustain. Sci.* **2024**, *12*, 36–46. [CrossRef]
93. Yan, L.; Xie, Y.; Wang, Y.; Zhu, J.; Li, M.; Liu, X.; Zhao, D. Variation in contents of active components and antibacterial activity in different parts of Thunb. *Asian Biomed.* **2020**, *14*, 19–26. [CrossRef]
94. Zheljazkov, V.D.; Cantrell, C.L.; Astatkie, T.; Cannon, J.B. Lemongrass productivity, oil content, and composition as a function of nitrogen, sulfur, and harvest time. *Agron. J.* **2011**, *103*, 805–812. [CrossRef]

Disclaimer/Publisher's Note: The statements, opinions and data contained in all publications are solely those of the individual author(s) and contributor(s) and not of MDPI and/or the editor(s). MDPI and/or the editor(s) disclaim responsibility for any injury to people or property resulting from any ideas, methods, instructions or products referred to in the content.

processes

MDPI

Article

Mechanochemical Loading of Doxorubicin on the Surface of Magnesium and Zinc-Based Layered Double Hydroxides

Minerva Guadalupe Ventura Muñoz, Jesús Alfredo Lara Cerón, Manuel de Jesús Gallegos Saucedo and Gregorio Guadalupe Carbajal Arizaga *

Department of Chemistry, Universidad de Guadalajara, Marcelino García Barragán 1421, Guadalajara C.P. 44430, Jalisco, Mexico; minerva.ventura@alumnos.udg.mx (M.G.V.M.); jesusalfredo.lara@academicos.udg.mx (J.A.L.C.); jesus.gallegos@academicos.udg.mx (M.d.J.G.S.)
* Correspondence: gregorio.carbajal@academicos.udg.mx

Abstract: In the search for technologies and materials to improve the safety and efficacy of active ingredients used in treating diseases, layered double hydroxides (LDHs) have been proposed as drug carriers since they can enhance the effects of active ingredients and even reduce toxicity. Doxorubicin (DOX) is one of the most widely used and studied antitumor drugs due to its broad spectrum; however, due to its low plasma bioavailability and slow systemic clearance, only a small fraction of the drug reaches and acts on the tumor, so LDHs have been proposed as vehicles to solve these disadvantages. The most used method to load the drug is incubating LDH particles in DOX solutions. In this work, two additional methods, co-precipitation, and mechanochemical reaction, were explored to evaluate the structural stability of the vehicle and the amount of DOX retained by LDHs structured by magnesium/aluminum and zinc/aluminum cations, which are the two most common compositions to design materials for biomedical applications. The zinc/aluminum LDH structure degraded in the loading process, whereas the magnesium/aluminum LDH particles were stable against the three loading processes. The mechanochemical procedure, a green and sustainable technology, loaded the highest content of DOX.

Keywords: hydroxide; doxorubicin; vehicles; loading process

1. Introduction

One strategy to improve therapies and treatments against diseases is the development of vehicles or forms of administration of known drugs. Liposomes are one of the most efficient routes for the transport of poorly soluble drugs. However, micelles can become destabilized when in contact with different chemical environments during the trajectory within the body. A proposal that has been explored by several research groups is the use of layered double hydroxide (LDH) nanoparticles as transport vehicles [1,2].

These particles can tune the release rate of drugs [3] and even control the release in the stomach or intestine environments, depending on their chemical composition [4]. Layered double hydroxides are inorganic structures whose composition is represented by the general formula $M(II)_{1-x}M(III)_x(OH)_2]^{x+}A^{n-}{}_{x/n}$, where M(II) and M(III) are metal cations organized in a two-dimensional structure upon coordination with -OH ions. The resulting layer retains a charged residue (x+) that is stabilized by interlayer anions, $A^{n-}{}_{x/n}$ [5]. A particle of LDH results from an alternate stacking of cationic layers and anions.

The popularity of LDHs lies in the wide range of compositions enabled by the large number of metal cations that can be combined, the different values of X, and the interlaminar anions that can be selected. Additionally, the exchangeability of the A^{n-} anion is

exploited on many occasions for substitution by the drug to be transported. This exchange approach is preferable for compounds that form stable anions, such as carboxylates, resulting in LDH particles retaining the drug within the crystal lattice. However, LDHs can also transport drugs on external surfaces, i.e., without intercalation, with the same advantages as that of a drug transported by a nanovehicle. The external adsorption phenomena occur in molecules like doxorubicin (DOX) [6]. In addition to the flexibility of its chemical composition, there is also the diversity of structures, shapes, and sizes, enabling several applications [5]. One example of its use is as a lubricant. It can act as a matrix to hold organic gasses and allow their carbonization. They are also environmentally friendly by reducing the amount of inorganic waste from synthesis processes, as occurred with the formation of NiAl-CO_3 LDH particles, which has significantly improved the tribological performance of in situ carbon layers that can be used as lubricants under extreme loads and high shear stresses without the need for inspection and reworking of coatings [7].

LDHs are also used as delivery systems for cosmetic active ingredients due to their potential to stabilize them and improve rheological properties, specifically in emulsions.

Cinnamic acid and its derivative, p-methoxy cinnamic acid, have been inserted into the interlayer space of an LDH. LHDs show a great capacity for attenuating UV rays while being transparent in the region of visible light. It has also been reported that the oxidation of castor oil added to cosmetic and nutritional formulations caused by the air decreases when cinnamic acids are intercalated in the LDHs [8,9].

A novel application is the use of LDHs as an alternative to the white pigments currently used in the food, cosmetic, and pharmaceutical industries. To this end, LDHs were prepared with magnesium and aluminum, and surface-modified with casein and carboxymethylcellulose (CMC), and compared with currently used whiteners such as food-grade titanium dioxide (E171), rice starch, and silicon dioxide (E551). The experiment showed that the aqueous suspension of LDH is heat and pH-stable and outperforms current alternatives such as rice starch and silicon dioxide (E551) [10].

Likewise, strategies for recovery from spinal cord injury have been explored using magnesium and aluminum LDH, evaluating the functions of neuronal regeneration and immune regulation in mice. The experiment achieved significant performance in accelerating neural stem cell (NSC) migration, neural differentiation, L-Ca^{2+} channel activation, and the generation of inducible action potentials [11].

The bottom-up synthesis of LDHs from soluble salts of M(II) and M(III) cations, and the addition of the drug to this solution, producing particles when alkalinized with sodium hydroxide, is another common procedure for drug loading in LDHs. This procedure retains the drug inside the particles during crystal formation. This method, known as co-precipitation, is efficient for molecules with carboxylate groups, such as ibuprofen [12]. However, in some cases, the co-precipitation is not successful for the intercalation of some molecules, especially those that do not produce stable anions, like polyphenols. In this case, the retention occurs by adsorption onto the external surfaces, and the formed particles retain the activity of the organic compounds [13]. Therefore, it can be concluded that there is no absolute method of synthesis and that for each molecule to be loaded into or onto an LDH particle, different methods must be explored to select the most appropriate one.

In the case of DOX, the synthesis method to produce the loading is achieved by dispersing LDH nanoparticles in a DOX solution, which is a wet impregnation [6]. This work aims to compare the traditional wet synthesis methods and include the mechanochemical process, which to date has been widely explored for LDH synthesis, but not for forming intercalation products [14]. This method has the advantage of avoiding the use of solvents during the synthesis and reducing energy consumption.

In this article, we explore the traditional "exchange" process to incorporate DOX in LDH particles and compare it with the co-precipitation and mechanochemical procedures. The assays were conducted with the magnesium and zinc-based compositions of LDHs, which are proposed for biomedical studies owing to their null or low toxicity [15,16].

2. Materials and Methods

All reagents were of analytical grade and no additional purifications were performed.

2.1. Magnesium (MgAl-NO_3) and Zinc (ZnAl-CO_3) Layered Double Hydroxides

A 100 mL solution was prepared with magnesium nitrate and aluminum nitrate in a Mg:Al molar ratio of 2.5:1. The suspension was stirred and 12% NH_4OH was added until pH 9.5 was reached. The suspension was stirred for 24 h. Then, the product was recovered by centrifugation, washed with deionized water, and dried for 72 h at 55 °C. The solid obtained was ground in an agate mortar and identified as MgAl-NO_3. The reaction with zinc nitrate was prepared with a solution of zinc nitrate and aluminum nitrate in the ratio of 2.5:1 following the above procedure. The product was identified as ZnAl-NO_3.

2.2. Loading Attempt by Anion Exchange

In a beaker containing 25 mL of deionized water, 0.030 g of doxorubicin (DOX) was added. The solution was stirred until DOX dissolution was achieved. Subsequently, 0.104 g of MgAl-NO_3 (or ZnAl-NO_3) was added, and the mixture was stirred until homogenized. A drop of 1 M NaOH was added to adjust the pH to 7. The suspension was stirred for 24 h. Then, the solid was recovered by centrifugation and dried in an oven for 24 h at 50 °C. The resulting purple powder was pulverized in an agate mortar until a fine powder was obtained. The samples were labeled as MgAl-DOX/Exch and ZnAl-DOX/Exch.

2.3. Loading Attempt by Co-Precipitation

20 mL of solution containing the metal cations Mg(II) and Al(III) were prepared by dissolving the mass of salts indicated in Section 2.1. To this solution, 0.010 g of DOX was added and stirred until homogenized. Then, 6% NH_4OH was added to pH 8.5 to induce the formation and precipitation of LDHs with doxorubicin.

The zinc-based sample was prepared by switching to a solution of Zn(II) and Al(III) cations. Both experiments were left in agitation for one day. They were then centrifuged to separate the solid. The products were washed with deionized water and dried for 24 h at 55 °C. They were then pulverized in agate mortar until a fine powder was obtained and labeled as MgAl-DOX/Exch and ZnAl-DOX/Exch.

2.4. Loading Attempt by Mechanochemical Reaction

A mixture was prepared with 0.100 g of MgAl-NO_3 (or ZnAl-NO_3) with 0.030 g of DOX. The mixture was placed in an agate mortar and ground for 20 min. A few drops of ethanol were added to form a paste to facilitate homogenization. Subsequently, the paste was transferred to a centrifuge tube, mixed with 25 mL of deionized water, and stirred to promote the release of DOX from the LDHs and ensure that the recovered powder contained exclusively DOX, chemically attached to the particles. The sample was then centrifuged at 5000 rpm for 5 min, and the washing process was repeated three times. The sample was transferred to a drying oven for 24 h at 55 °C and pulverized in agate mortar until a fine powder was obtained. The sample was labeled as MgAl-DOX/Mec (or ZnAl-DOX/Mec).

2.5. Solid-State Characterization

All powder samples were placed directly in a glass sample holder. The analysis was performed on a PANalytical diffractometer model Empyream (PANalytical, Malvern, UK); such equipment used a copper anode producing radiation with a wavelength of 0.154 nm. Reading was conducted in the 5 to 70 degrees (2θ) range with a step of 0.02 degrees and 25 s of exposure. The infrared data were collected, averaging 16 scans with a resolution of 4 cm^{-1} in the ATR mode with a Thermo Scientific apparatus model iS50 ATR (FTIR, Waltham, MA, USA).

Energy-dispersive X-ray spectroscopy (EDS) data were acquired with an OXFORD detector (Oxford model X-MaxN, High Wycombe, UK) assembled to a JEOL JSM-6610LV scanning electron microscope (SEM, Musashimurayama-shi, Tokyo, Japan) located at the Instituto Transdisciplinar de Investigación y Servicios—ITRANS, at the University of Guadalajara. The powder samples were adhered to a carbon tape. EDS data were obtained using SEM images acquired using a beam with 15 kV and 1 k magnification. The element content was measured in five zones for each sample and averaged manually. The computer program reports mass percentages, which are manually converted to moles per 100 g by dividing each percentage by the atomic weight.

3. Results and Discussion

3.1. Magnesium-Based LDH Loaded with DOX

The diffraction profile observed in the LDH MgAl-NO_3 sample mainly resembles the profile of a hydrotalcite structure [17] (Figure 1).

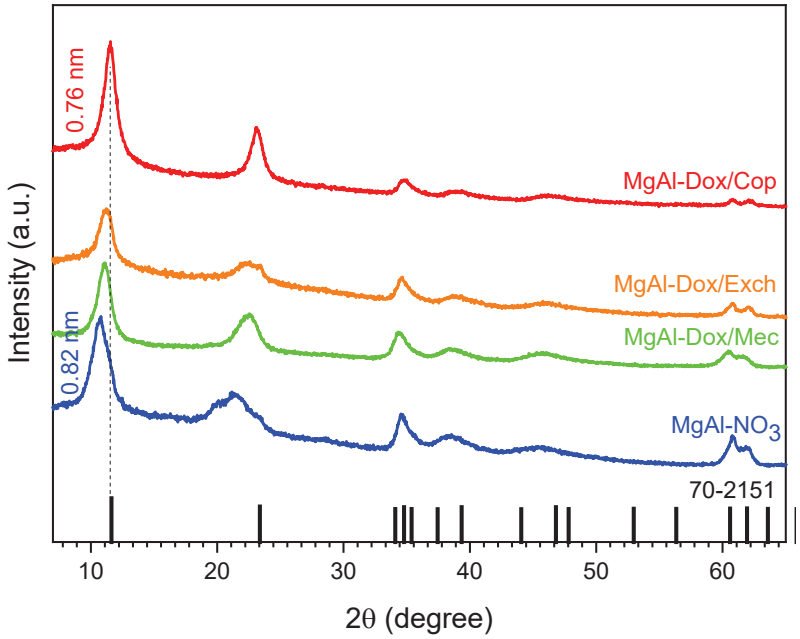


Figure 1. X-ray diffraction profiles of the MgAl-NO_3 pristine matrix and the doxorubicin (DOX) products processed by mechanochemical, exchange, and co-precipitation techniques.

However, in the diffractogram, a very broad peak is formed between 17 and 23 degrees (2 theta), which is not present in the card. In both structures, the most intense reflection appears in the same position, but the second reflection is shifted. Figure 2 shows the experimental diffractogram and the simulated profiles of hydrotalcite-type structures obtained with the MAUD (Version 2.9997) program based on two structures belonging to the space group P −6 2 m (space group 189) [18] and R −3 m (space group 166) [17]. This overlapping demonstrates the observed broadening of the MgAl-NO_3 profile.

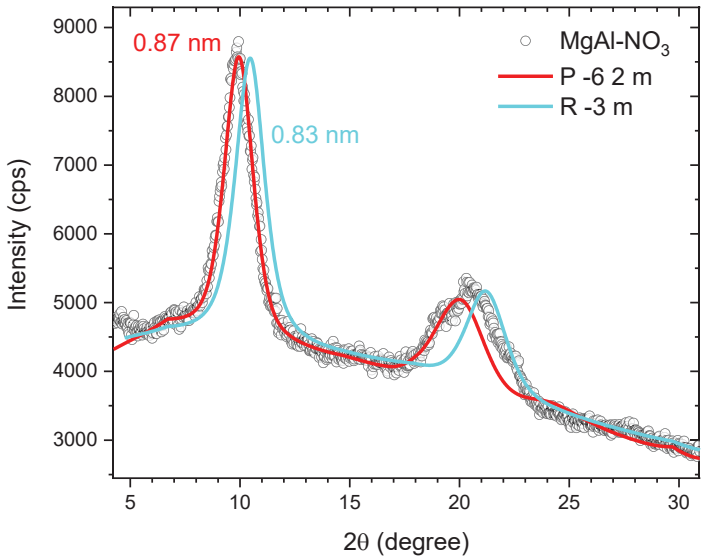


Figure 2. XRD profile of the basal reflections in the MgAl-NO_3 sample and the theoretical profiles of LDHs with two different crystal groups.

The most intense reflection in both profiles corresponds to crystal planes formed by the distance between two contiguous layers, called basal distance, and depends on the size of the anion intercalated between the layers [19]. The position of the peak transformed to a distance in the LDH Mg/Al-NO_3 sample, when calculated with the Bragg equation, corresponds to 0.87 and 0.83 nm for the P −6 2 m and R −3 m phase, respectively, which are consistent with the presence of interlayer nitrate [20,21].

When the DOX loading processes are carried out, the XRD profiles are maintained (Figure 1), especially the reflections above 30 degrees (2 theta). However, the basal reflection is slightly shifted to 0.76 nm. This lower value is associated with carbonate intercalated between the layers; this fact occurs by reaction with CO_2 from the atmosphere [22], and the aqueous medium favors it since it does not occur in the mechanochemical reaction.

IR spectroscopy analysis was performed to detect the presence of DOX in the samples (Figure 3). Firstly, MgAl-NO_3 presented a high intensity and width band around 3400 cm^{-1} related to the H-O stretching found in water and OH groups of the layers [23]. At 1360 cm^{-1}, bands related to the symmetric stretching of nitrate ions are observed [24]. Finally, below 680 cm^{-1}, bands of metal–oxygen or O-M-O stretching appear [23].

The control DOX spectrum is composed of several signals, but the bands that allow its identification in the other compounds stand out, such as the O-H and N-H and C-H signals between 3600 and 2900 cm^{-1}, C=O stretching at 1740 cm^{-1}, N-H stretching at 1650 cm^{-1}, and the high-intensity signal at 1050 cm^{-1} coming from C-O-C [25], which are shadowed in Figure 3. When evaluating the presence of this profile in the samples, the one prepared by the mechanochemical method presents the most pronounced signals at 2950, 1720, and 1050 cm^{-1}, indicating that it is the one that retained the highest amount of DOX. It is followed in intensity by the MgAl-DOX/Exch sample, with signals at 1720 cm^{-1} and slightly at 1020 cm^{-1}. It can be said that MgAl-DOX/Mec retains the greatest amount of DOX, while the MgAl-DOX/Cop sample has the least contribution to the DOX signal.

As inferred from the diffraction data, the interlayer space of the LDH particles treated with DOX is populated by carbonate anions, as represented in Figure 4. Then, the loading of the DOX molecules occurred over the external surface instead of the typical exchange reactions where the drug substitutes carbonate. The loading over the surface particles occurred regardless of the presence of two polytypes of LDH structures in the pristine sample.

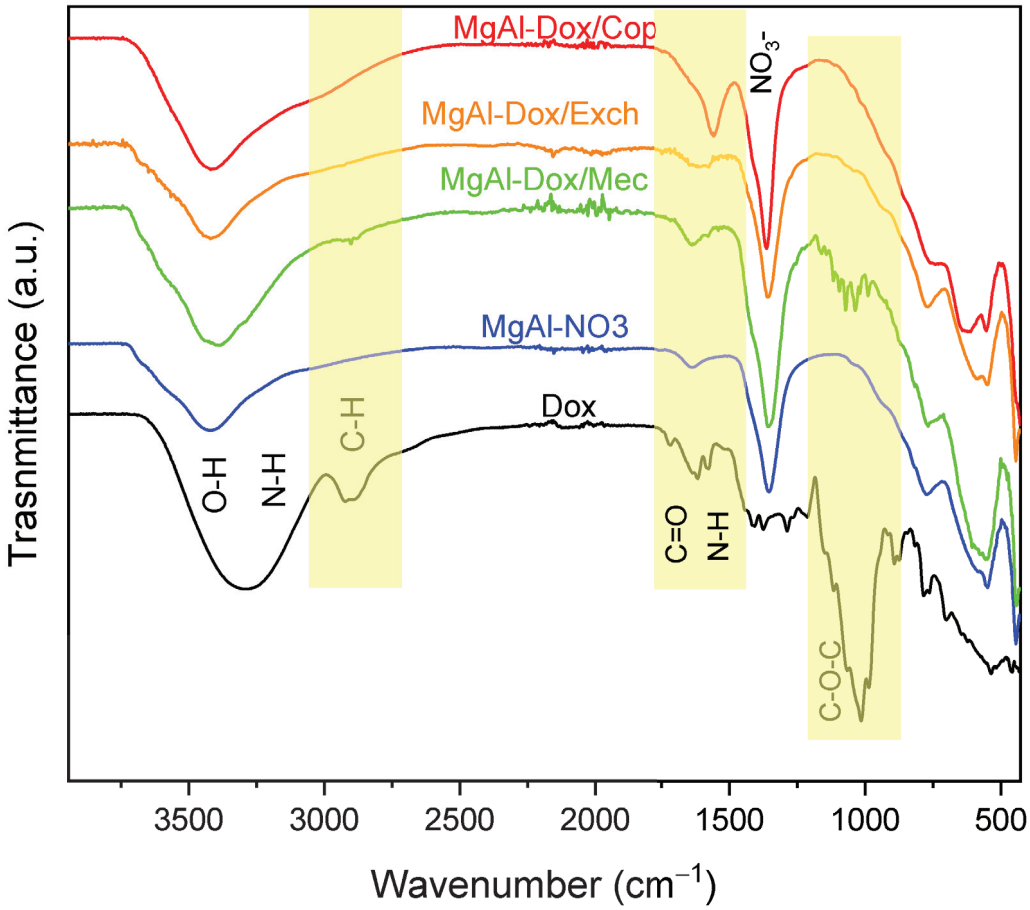


Figure 3. Infrared spectra of the Mg-NO_3 pristine matrix and the doxorubicin (DOX) products processed by mechanochemical, exchange, and co-precipitation techniques.

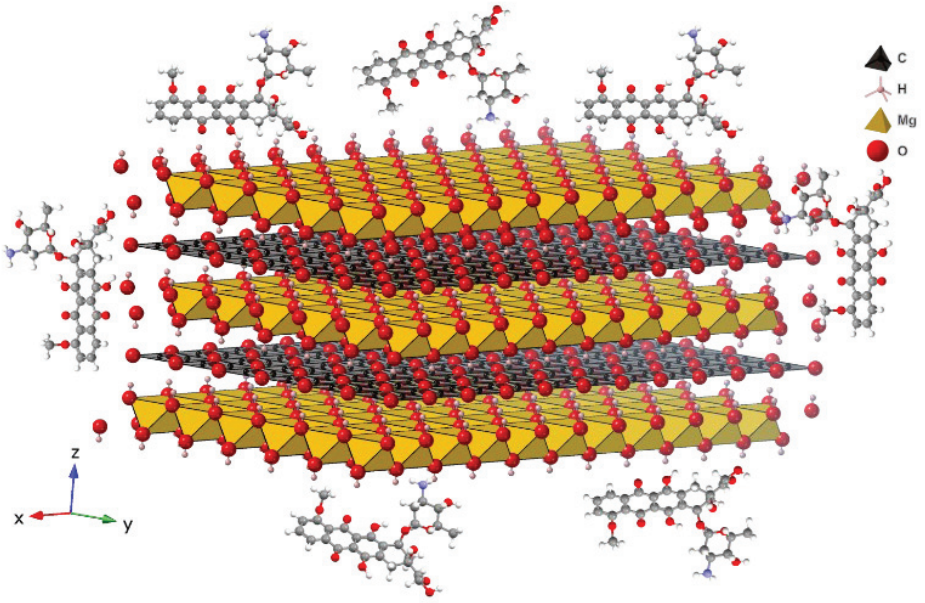


Figure 4. Representation of an LDH particle with the composition MgAl-NO_3 and DOX obtained by the mechanochemical procedure. Generated using CrystalMaker 11®. CrystalMaker Software Ltd., Oxford, UK (www.crystalmaker.com).

The data from element quantification using the EDS technique was treated to obtain the carbon content, which is an indicator of retained DOX (Figure 5a). The highest content in MgAl-DOX/Mec was 1.8 mol per 100 g of sample, which agrees with the infrared result

and confirms that the mechanochemical method is the most efficient procedure to load DOX in a LDH with hydrotalcite composition. The content of the other element taking as reference the aluminum (Figure 5b) also demonstrates the highest content of carbon in MgAl-DOX/Mec; additionally, this plot shows the molar ratio of Mg with respect to aluminum is close to 2.5:1 (dotted line in Figure 5b) indicating the chemical stability of the LDH structure.

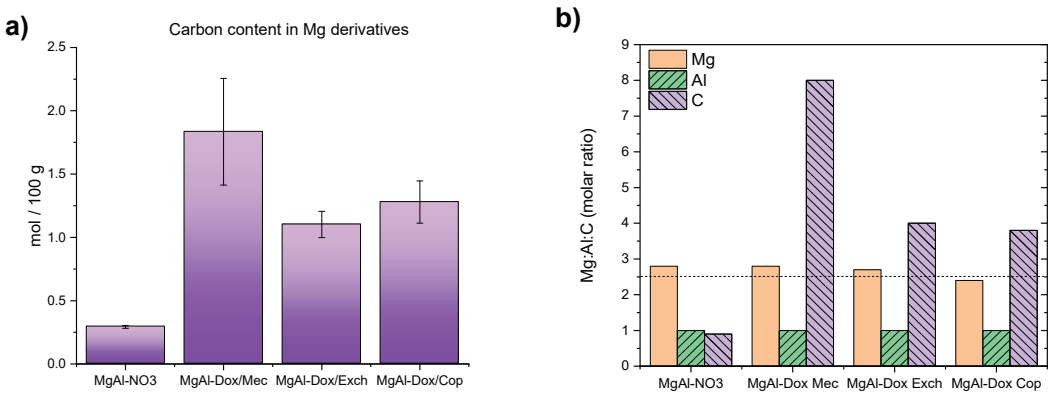


Figure 5. (**a**) Carbon content in the magnesium LDH loaded with DOX by the mechanochemical, co-precipitation and exchange procedures and (**b**) the magnesium:aluminum:carbon molar ratio in the same samples.

3.2. Zinc-Based LDH Loaded with DOX

The zinc-based matrix was analyzed by XRD (Figure 6); the profile of the ZnAl-NO_3 sample matches the profile of the 38-0486 card corresponding to an LDH of composition, $Zn_6Al_2(OH)_{16}CO_3{\cdot}4H_2O$ [26], and corresponds to a structure with R −3 m symmetry, similar to one of those found in the magnesium sample.

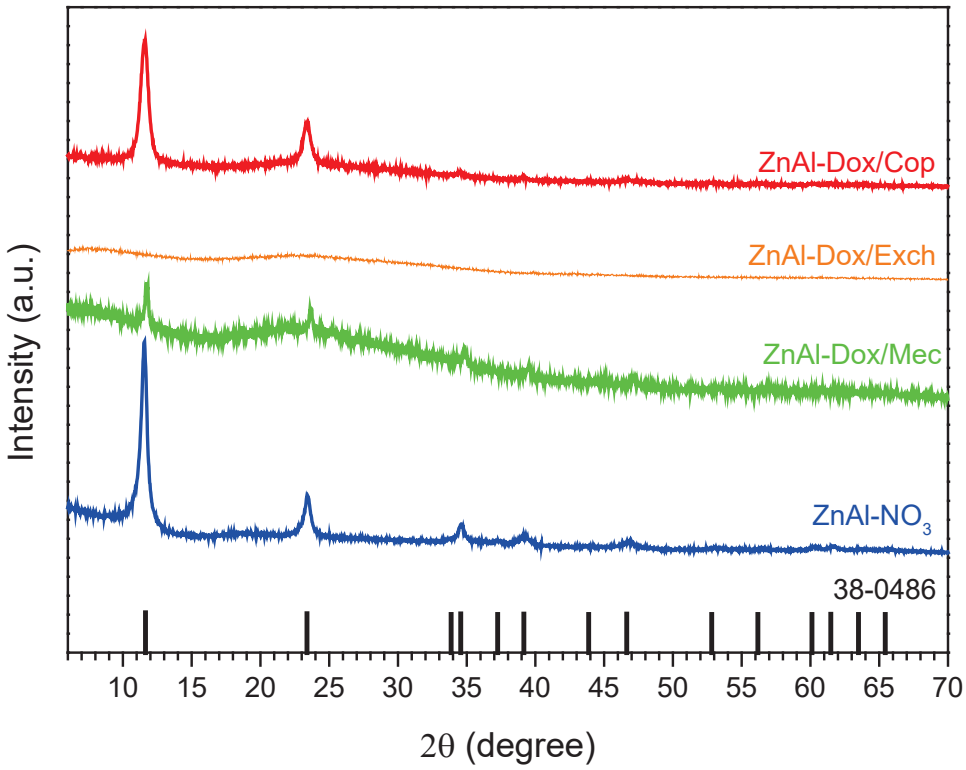


Figure 6. X-ray diffraction profiles of the ZnAl-CO_3 pristine matrix and the doxorubicin (DOX) products processed by mechanochemical, exchange, and co-precipitation techniques.

When evaluating the basal reflection, the distance between two contiguous layers is 0.76 nm, which suggests the presence of interlayer carbonate [22,27], so it can be said that a zinc-based LDH is more susceptible to carbonate contamination than a magnesium-based LDH.

Except for the ZnAl-DOX/Cop sample, where no diffraction signals were obtained indicating destruction of the crystalline arrangement, the products obtained from the mechanochemical and exchange methods present the initial LDH diffraction profile, indicating that these two methods do not destroy the LDH matrix.

Infrared spectroscopy shows that the spectrum of ZnAl-NO_3 is the same as that of the MgAl-NO_3 sample, thereby confirming the composition of an LDH (Figure 7). Even when the band at 1360 cm^{-1} is assigned to nitrate ions [23], carbonate vibrations also appear in the same wavenumber [22,27]; the presence of carbonate is corroborated by the high content of carbon (0.72 mol C/100 g) in ZnAl-NO_3 (Figure 8a) compared with MgAl-NO_3 (0.23 mol C/100 g). These data agree with the low basal space identified by XRD.

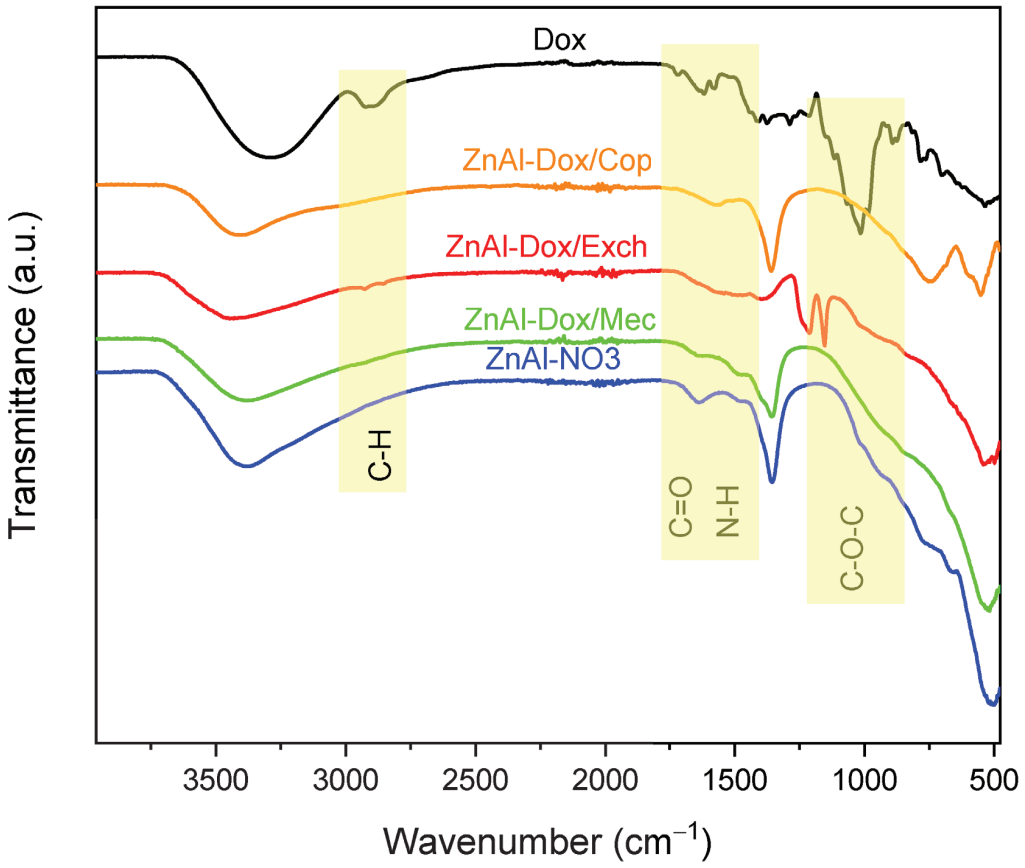


Figure 7. Infrared spectra of the ZnAl-NO_3 pristine matrix and the doxorubicin (DOX) products processed by mechanochemical, exchange, and co-precipitation techniques.

The presence of DOX in the loading products is suggested by the weak C=O and N-H signals in ZnAl-DOX/Mec and ZnAl-DOX/Exch; however, the ZnAl-DOX/Exch sample is not a layered material as inferred from XRD data. Then, ZnAl-DOX/Mec was the only sample loaded with Dox, probably causing the increase of carbon to 0.95 mol C/100 g (Figure 8a). However, the Zn:Al molar ratio in this sample is 0.5:1 instead of the expected 2.5:1, indicating a high content of aluminum (Figure 8b), then the carbon comes from a probable amorphous aluminum carbonate phase. Therefore, the zinc-containing LDH particles are less stable as vehicles for DOX compared to the magnesium LDH.

Among the novelties of our work was the addition of the mechanochemical method to the traditional synthesis methods used for LDHs. In the experimental design, three synthesis processes and two LDH compositions accepted in biological applications were tested. The expected result was not obtained in one of the compositions, ZnAl, once it was degraded, while the MgAl composition was stable.

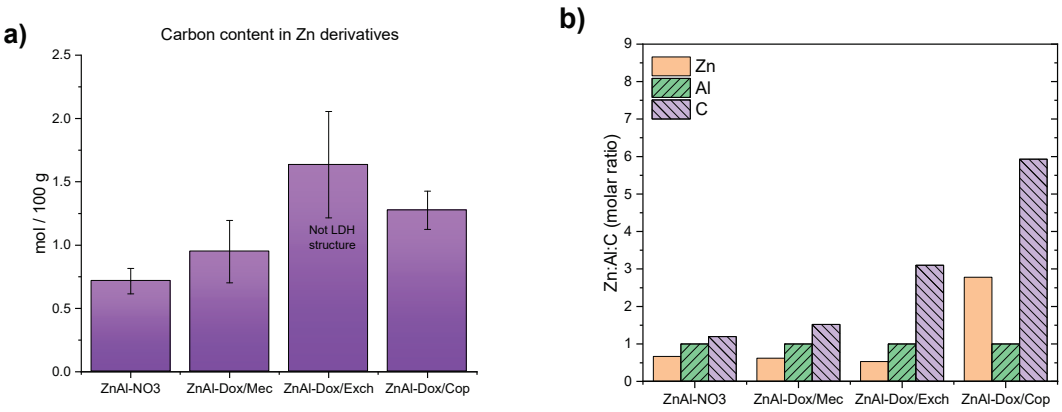


Figure 8. (**a**) Carbon content in the zinc materials loaded with DOX by the mechanochemical, co-precipitation, and exchange procedures and (**b**) the magnesium:aluminum:carbon molar ratio.

The novel result was in the product obtained by the mechanochemical process, which showed a higher DOX loading, allowing scaling-up since it is the least expensive, and does not require large amounts of sample, time, or sophisticated equipment. In these results, we demonstrate that certain compositions and synthesis methods are the most suitable in terms of cost, reaction, and operating time, as they are more efficient in loading complex or bulky drugs such as DOX in a more straightforwardly and economically, without causing any structural modification of the drug or LDHs. In addition, the environmental impact is reduced by not generating the waste of conventional synthesis processes, thus addressing some of the principles of green chemistry [28].

Solvents play an important role in conventional synthesis, and their toxicity is often the main challenge to overcome. Mechanochemical synthesis is more efficient because the reaction can be carried out by milling with or without a small amount of solvent [29,30].

Now, the further challenge is to evaluate the release profile of the most promising samples, and especially to choose a model of application. For example, it has recently been demonstrated that inorganic particles based on metal oxides have the potential for use as drug-eluting stents, especially, magnesium, and zinc oxides are used in the medical field, because they are bioabsorbable, inexpensive, and stable, and applied as alternatives in orthopedic implants in which they serve as delivery systems for anti-inflammatory drugs, antibiotics, growth factors, and antiresorptives. Little attention has been paid to metallic drug-releasing systems compared to polymeric systems. These systems are intelligent and sensitive and are increasingly popular in personalized medicine and pharmacotherapy as they can respond to key variables such as pH changes caused by inflammatory processes, thus allowing the system to release its bioactive load, reaching the desired site for the therapeutic effect [31–33].

One major problem is the rapid corrosion of magnesium-based biomaterials, which represents a significant obstacle to their application but can be reduced by adding elements such as aluminum and zinc [34]. The most effective way to improve the corrosion resistance of these biomaterials without impairing their mechanical strength is surface modification. For example, most metal-based drug delivery systems involve embedding drugs in polymeric or ceramic coatings applied to metal implants. There are also other methods for incorporating the drug itself into the metal surface through covalent bonds,

self-assembled layers, and silver nanoparticles [31]. Here, the LDHs loaded with drugs by the mechanochemical method could find an application.

4. Conclusions

The typical anions exchange reaction to load DOX on LDH particles was compared with the co-precipitation and mechanochemical processes. The MgAl LDH composition is stable and tolerates the three loading processes. The mechanochemical method retained the largest content of DOX. The ZnAl LDH was unstable against the exchange reaction since the structure was destroyed and the amount retained was low. The mechanochemical method was then the best procedure for the zinc-based composition. Therefore, the grinding process arises as a suitable green method to produce LDH vehicles for DOX, retaining the structural integrity of the LDH structure and reducing the use of reagents.

Author Contributions: Conceptualization, G.G.C.A.; data curation, M.d.J.G.S. and G.G.C.A.; formal analysis, M.G.V.M.; investigation, M.G.V.M., J.A.L.C., M.d.J.G.S. and G.G.C.A.; methodology, J.A.L.C.; writing—original draft, M.d.J.G.S.; writing—review and editing, G.G.C.A. All authors have read and agreed to the published version of the manuscript.

Funding: M.G.V.M. received fellowship (2021-000018-02NACF-08398, CVU number 891242) from "Secretaría de Ciencia, Humanidades, Tecnología e Innovación (SECIHTI)", Mexico, formerly "Consejo Nacional de Humanidades, Ciencia y Tecnología (CONAHCYT)". Funds were obtained from the Project "Ciencia de Frontera CF-2023-I-885" sponsored by the "Consejo Nacional de Humanidades, Ciencias y Tecnologías, CONAHCYT", Mexico.

Data Availability Statement: Data are available on request.

Conflicts of Interest: The authors declare no conflicts of interest.

References

1. Li, Y.; Liu, D.; Ai, H.; Chang, Q.; Liu, D.; Xia, Y.; Liu, S.; Peng, N.; Xi, Z.; Yang, X. Biological evaluation of layered double hydroxides as efficient drug vehicles. *Nanotechnology* **2010**, *21*, 105101. [CrossRef]
2. Choi, G.; Piao, H.; Aalothman, Z.; Vinu, A.; Yun, C.O.; Choy, J.H. Anionic clay as the drug delivery vehicle: Tumor targeting function of layered double hydroxide- methotrexate nanohybrid in C33A orthotopic cervical cancer model. *Int. J. Nanomed.* **2016**, *11*, 337–348. [CrossRef]
3. Senapati, S.; Thakur, R.; Verma, S.P.; Duggal, S.; Mishra, D.P.; Das, P.; Shripathi, T.; Kumar, M.; Rana, D.; Maiti, P. Layered double hydroxides as effective carrier for anticancer drugs and tailoring of release rate through interlayer anions. *J. Control. Release* **2016**, *224*, 186–198. [CrossRef]
4. Li, B.; He, J.; Evans, D.G.; Duan, X. Enteric-coated layered double hydroxides as a controlled release drug delivery system. *Int. J. Pharm.* **2004**, *287*, 89–95. [CrossRef]
5. Kovalenko, V.; Kotok, V.; Murashevych, B. Layered double hydroxides as the unique product of target ionic construction for energy, chemical, foods, cosmetics, medicine and ecology applications. *Chem. Rec.* **2023**, *24*, e202300260. [CrossRef]
6. Anirudhan, T.S.; Sekhar, V.C. Fabrication of functionalized layered double hydroxide/chitosan nanocomposite with dual responsive drug release for the targeted therapy of breast cancer. *Eur. Polym. J.* **2020**, *139*, 109993. [CrossRef]
7. Huynh, K.K.; Tieu, A.K.; Lu, C.; Smillie, L.; Nguyen, C.; Pham, S.T. In-situ engineering catalytically active surfaces for tribocatalysis with layered double hydroxide nanoparticles. *Carbon* **2024**, *228*, 119324. [CrossRef]
8. Pillai, S.K.; Kleyi, P.; de Beer, M.; Mudaly, P. Layered double hydroxides: An advanced encapsulation and delivery system for cosmetic ingredients—An overview. *Appl. Clay Sci.* **2020**, *199*, 105868. [CrossRef]
9. Talwan, P.; Gautam, D.; Kumar, R.; Sharma, S.; Dhiman, S.; Gill, R.; Thakur, A.; Sharma, D.; Sharma, S.; Kumar, A. A review of the chemical composition, modification, and biomedical application of *Ricinus communis*. *Indian J. Nat. Prod. Resour.* **2024**, *15*, 21–42. [CrossRef]
10. Ngew, E.; Phue, W.H.; Liu, Z.; George, S. Composite of layered double hydroxide with casein and carboxymethylcellulose as a white pigment for food application. *Foods* **2022**, *11*, 1120. [CrossRef]
11. Zhu, R.; Zhu, X.; Zhu, Y.; Wang, Z.; He, X.; Wu, Z.; Xue, L.; Fan, W.; Huang, R.; Xu, Z.; et al. Immunomodulatory layered double hydroxide nanoparticles enable neurogenesis by targeting transforming growth factor-β receptor 2. *ACS Nano* **2021**, *15*, 2812–2830. [CrossRef] [PubMed]

12. Gaskell, E.E.; Ha, T.; Hamilton, A.R. Ibuprofen intercalation and release from different layered double hydroxides. *Ther. Deliv.* **2018**, *9*, 653–666. [CrossRef] [PubMed]
13. Pagano, C.; Perioli, L.; Blasi, F.; Bastianini, M.; Chiesi, C.; Cossignani, L. Optimisation of phenol extraction from wine using layered double hydroxides and technological evaluation of the bioactive-rich powder. *Int. J. Food Sci. Technol.* **2017**, *52*, 2582–2588. [CrossRef]
14. Belskaya, O.B.; Likholobov, V.A. Mechanochemical synthesis of layered double hydroxides as a promising method for the preparation of adsorbents and catalysts. *Kinet. Catal.* **2022**, *63*, 615–641. [CrossRef]
15. Nomicisio, C.; Taviot-Guého, C.; Ruggeri, M.; Forano, C.; Vigani, B.; Viseras, C.; Rossi, S.; Sandri, G. Layered double hydroxides for biomedical purposes: Sustainable and green synthesis. *Appl. Clay Sci.* **2024**, *258*, 107480. [CrossRef]
16. Li, L.; Soyhan, I.; Warszawik, E.; van Rijn, P. Layered double hydroxides: Recent progress and promising perspectives toward biomedical applications. *Adv. Sci.* **2024**, *11*, e2306035. [CrossRef]
17. Bellotto, M.; Rebours, B.; Clause, O.; Lynch, J.; Bazin, D.; Elkaïm, E. A reexamination of hydrotalcite crystal chemistry. *J. Phys. Chem.* **1996**, *100*, 8527–8534. [CrossRef]
18. Arakcheeva, A.V.; Pushcharovskii, D.Y.; Rastsvetaeva, R.K.; Atencio, D.; Lubman, G.U. Crystal structure and comparative crystal chemistry of $Al_2Mg_4(OH)_{12}(CO_3)\cdot 3H_2O$, a new mineral from the hydrotalcite-manasseite group. *Crystallogr. Rep.* **1996**, *41*, 1024–1034. (In Russian)
19. Soulé, S.; Durand, P.; El-Kirat-Chatel, S.; Quilès, F.; Carteret, C. Structural features and dynamic behaviour of the interlayer space of layered double hydroxide coatings. *Mater. Today Chem.* **2024**, *35*, 101897. [CrossRef]
20. Zhang, J.; Xia, Q.; Hong, X.; Chen, J.; Liu, D. Synthesis of layered double hydroxides with nitrate and its adsorption properties of phosphate. *Water Sci. Technol.* **2021**, *83*, 100–110. [CrossRef]
21. Wu, Q.; Olafsen, A.; Vistad, Ø.B.; Roots, J.; Norby, P. Delamination and restacking of a layered double hydroxide with nitrate as counter anion. *J. Mater. Chem.* **2005**, *15*, 4695. [CrossRef]
22. Ram Reddy, M.K.; Xu, Z.P.; Lu, G.Q.; Diniz da Costa, J.C. Layered double hydroxides for CO_2 capture: Structure evolution and regeneration. *Ind. Eng. Chem. Res.* **2006**, *45*, 7504–7509. [CrossRef]
23. Jiang, L.; Liu, J.; Zhang, C.; Duan, T.; Li, Y.; Zou, L.; Qian, G. Synthesis of layered double hydroxides with fermentation liquid of organic waste to extract short-chain fatty acids as a biodenitrification carbon source. *ACS Sustain. Chem. Eng.* **2017**, *5*, 9095–9101. [CrossRef]
24. Khitous, M.; Salem, Z.; Halliche, D. Removal of phosphate from industrial wastewater using uncalcined MgAl-NO_3 layered double hydroxide: Batch study and modeling. *Desalination Water Treat.* **2016**, *57*, 15920–15931. [CrossRef]
25. Bansal, R.; Singh, R.; Kaur, K. Quantitative analysis of doxorubicin hydrochloride and arterolane maleate by mid IR spectroscopy using transmission and reflectance modes. *BMC Chem.* **2021**, *15*, 27. [CrossRef]
26. Kabekkodu, S.N.; Dosen, A.; Blanton, T.N. PDF-5+: A comprehensive Powder Diffraction File^{TM} for materials characterization. *Powder Diffr.* **2024**, *39*, 47–59. [CrossRef]
27. Wang, J.; Zhou, J.; Li, Z.; Liu, Q.; Yang, P.; Jing, X.; Zhang, M. Design of magnetic and fluorescent Mg–Al layered double hydroxides by introducing Fe_3O_4 nanoparticles and Eu^{3+} ions for intercalation of glycine. *Mater. Res. Bull.* **2010**, *45*, 640–645. [CrossRef]
28. de Marco, B.A.; Rechelo, B.S.; Tótoli, E.G.; Kogawa, A.C.; Salgado, H.R.N. Evolution of green chemistry and its multidimensional impacts: A review. *Saudi Pharm. J.* **2019**, *27*, 1–8. [CrossRef]
29. Dubadi, R.; Huang, S.D.; Jaroniec, M. Mechanochemical synthesis of nanoparticles for potential antimicrobial applications. *Materials* **2023**, *16*, 1460. [CrossRef]
30. Penczner, S.H.; Kumar, P.; Patel, M.; Bouchard, L.-S.; Iacopino, D.; Patel, R. Innovations in mechanochemical synthesis: Luminescent materials and their applications. *Mater. Today Chem.* **2024**, *39*, 102177. [CrossRef]
31. Alshimaysawee, S.; Obaid, R.F.; Al-Gazally, M.E.; Ramírez-Coronel, A.A.; Bathaei, M.S. Recent advancements in metallic drug-eluting implants. *Pharmaceutics* **2023**, *15*, 223. [CrossRef] [PubMed]
32. Bordbar-Khiabani, A.; Yarmand, B.; Mozafari, M. Functional PEO layers on magnesium alloys: Innovative polymer-free drug-eluting stents. *Surf. Innov.* **2018**, *6*, 237–243. [CrossRef]
33. Al-Hawary, S.I.S.; Habash, R.T.; Abosaooda, M.; Hjazi, A.; Saleh, E.A.M.; Hassan, Z.F.; Bathaei, M.S. TiO_2/PEG as smart anticorrosion and drug-eluting platforms in inflammatory conditions. *Heliyon* **2024**, *10*, e25605. [CrossRef] [PubMed]
34. Bordbar-Khiabani, A.; Yarmand, B.; Sharifi-Asl, S.; Mozafari, M. Improved corrosion performance of biodegradable magnesium in simulated inflammatory condition via drug-loaded plasma electrolytic oxidation coatings. *Mater. Chem. Phys.* **2020**, *239*, 122003. [CrossRef]

Disclaimer/Publisher's Note: The statements, opinions and data contained in all publications are solely those of the individual author(s) and contributor(s) and not of MDPI and/or the editor(s). MDPI and/or the editor(s) disclaim responsibility for any injury to people or property resulting from any ideas, methods, instructions or products referred to in the content.

processes

MDPI

Article

Enhanced Tribological Performance of Laser-Textured TiN-Coated Ti_6Al_4V Alloy Surfaces: A Comparative Study with Untextured Surfaces

Arulkumar Muniyappan [1,*], Prem Ananth Muthuvel [1,*], Anandhavelu Sanmugam [2], Mohammad Ahmad Wadaan [3], Almohannad Baabbad [3], Nallal Muthuchamy [4,*] and Kang Hyun Park [4,*]

[1] Department of Mechanical Engineering, Sri Venkateswara College of Engineering, Pennalur, Sriperumbudur 602117, Tamil Nadu, India
[2] Department of Applied Chemistry, Sri Venkateswara College of Engineering, Pennalur, Sriperumbudur 602117, Tamil Nadu, India; sranand2204@gmail.com
[3] Department of Zoology, College of Science, King Saud University, P.O. Box 2455, Riyadh 11451, Saudi Arabia; wadaan@ksu.edu.sa (M.A.W.); almbaabbad@ksu.edu.sa (A.B.)
[4] Department of Chemistry, Pusan National University, Busan 46241, Republic of Korea
* Correspondence: arulkumar@svce.ac.in (A.M.); premananth@svce.ac.in (P.A.M.); muthuchamyn89@gmail.com (N.M.); chemistry@pusan.ac.kr (K.H.P.)

Abstract: Titanium alloy is widely used as a biomaterial due to its strength, lightweight nature, and corrosion resistance. Despite its strength and lightweight nature, its low wear resistance limits its uses in prosthetic components. Laser surface texturing (LST) was used to improve the wear resistance of titanium alloys by creating textured surfaces before applying protective coatings. A biocompatible TiN composite protective coating was applied using physical vapour deposition (PVD) with a thickness of 4 μm. Response surface methodology (RSM) was used to predict the tribological properties by varying input parameters such as material type (TI, T2, T3, and T4), load in N, and sliding velocity in m/s. A pin-on-disc tribometer was used to conduct a unidirectional sliding wear test based on the RSM design. Tribological properties were studied to determine the impact of laser texturing on the bonding strength of the coating. As a result, material type T4 exhibits an improved coefficient of friction and specific wear resistance under varying sliding velocity and load conditions compared to other material types. The study was further supported by an ANSYS simulation, which revealed stress reduction affecting the coefficient of friction and, consequently, wear. The textured surface topography, wear mechanisms, and coating compositions were examined using scanning electron microscopy.

Keywords: TiN coating; surface texturing; ANSYS simulation; wear resistance

1. Introduction

In recent decades, there has been an increase in joint replacements due to accidental injuries and injuries sustained by soldiers. As a result, biomaterials have gained significant recognition as artificial and natural materials used to replace lost or diseased biological structures, thereby restoring both form and function. These biomaterials are classified into three categories based on the body's response: biotolerant, bioactive, and bioinert materials. Bioactive materials are commonly preferred for joint replacements because of their superior bone integration and biocompatibility [1–4]. Metallic biomaterials, such as 316L stainless steel, cobalt chromium alloy, magnesium alloy, and titanium alloy, are primarily utilized in load-bearing applications. Among these, titanium alloys, particularly the Ti_6Al_4V alloy,

stand out in the aerospace and biomedical industries due to their favourable combination of high strength, low density, and corrosion resistance [5,6]. Although Ti_6Al_4V has a lower Young's modulus (55–110 GPa) compared to stainless steel (210 GPa) and cobalt–chromium alloys (240 GPa), it is still higher than that of human cortical bone (10–30 GPa), causing stress shielding and bone resorption [7]. Despite its strength and low density, Ti_6Al_4V has poor wear resistance, which limits its use in high-friction environments. Additionally, the presence of vanadium and aluminium in the alloy has been linked to the potential development of Alzheimer's disease for long-term implants [8,9]. To address these limitations, two approaches can be explored: 1. The introduction of new beta-type materials by incorporating tantalum (Ta), zirconium (Zr), and niobium (Nb) can reduce the release of toxic substances into the body and improve cell viability and growth rates compared to Ti_6Al_4V [10,11]. 2. Implementing various surface modification techniques can enhance the tribological properties of Ti_6Al_4V. These techniques aim to improve osseointegration and antibacterial properties by altering surface characteristics. Surface modification methods—such as physical, chemical, mechanical, and oxygen hardening—can improve biocompatibility, wear resistance, and corrosion resistance [12–14]. One mechanical surface modification technique, known as laser surface texturing, involves creating specific patterns on the surface that can influence friction and wear characteristics. Laser surface texturing enhances tribological performance by modifying surface topography, which impacts lubrication retention and wear debris management. Textured surfaces can act as reservoirs for lubricants, reducing friction and wear during sliding conditions [15–18]. Studies have shown that textured surfaces exhibit lower friction coefficients than their untextured counterparts, particularly under lubricated conditions [19]. Coatings such as ZrO_2, TiC, and TiXN provide enhanced wear resistance due to their higher hardness and lower elastic modulus. Additionally, titanium nitride (TiN) demonstrates favourable biocompatibility when utilized as a surface modification for titanium implants. The plasma nitriding process introduces nitrogen to titanium alloy surfaces, forming TiN or Ti_2N compounds. TiN shows good corrosion resistance and increased hardness compared to untreated base materials when applied as a coating. Recent studies have indicated that ZrN and TiN coatings on titanium enhance not only the mechanical properties but also antibacterial activity and cytotoxicity, making them suitable for biomedical applications [20–25]. Under similar testing conditions, TiN-coated Ti_6Al_4V samples generally exhibit superior tribological performance compared to uncoated surfaces, largely due to the coating's inherent hardness and lubrication capabilities [26,27]. The findings suggest that combining laser texturing with TiN coating generates synergistic effects that enhance overall performance, compared to using each approach independently. This synergy can be attributed to improving the mechanical advantages of both surface modifications [28,29]. Response surface methodology (RSM) is a set of mathematical and statistical techniques used to predict tool life, surface roughness, wear resistance, and other similar factors [30–32]. Predictive modelling tools, such as artificial neural networks (ANNs) and regression techniques, have proven to be valuable for understanding the complex interactions involved in these processes [33–35]. The Finite Element Method (FEM) serves as a foundational tool for simulating the tribological behaviour of engineering materials. ANSYS software is widely used for conducting wear analysis through FEM, which enables researchers to approach complex contact problems with improved accuracy [21,36–38]. This study investigates the enhancement of tribological performance in Ti_6Al_4V alloy surfaces through laser texturing and TiN (titanium nitride) coating. It focuses on understanding how surface topography affects friction and wear behaviour compared to untextured and uncoated surfaces. To evaluate the friction coefficient and specific wear rate, a pin-on-disc sliding wear tribometer test was conducted on laser-textured TiN-coated Ti_6Al_4V alloy surfaces, as well as on untex-

tured uncoated surfaces, textured uncoated surfaces, and untextured TiN-coated surfaces. The surface morphology and topography of the laser-textured TiN-coated, laser-textured uncoated, and untextured TiN-coated Ti_6Al_4V alloy surfaces were analysed using scanning electron microscopy (SEM), atomic force microscopy (AFM), and a surface roughness tester. Additionally, the microstructure and phase composition of the TiN coating were examined using energy-dispersive X-ray spectroscopy (EDX). To determine the impact of various input parameters—such as applied load (in N) and sliding velocity (in m/s)—on friction and wear rates, a response surface methodology (RSM) study was performed. Furthermore, a simulated study was conducted using ANSYS software to explore the effects of laser texturing and TiN coating on the Ti_6Al_4V surfaces. Integrating laser surface texturing with TiN coatings on Ti_6Al_4V alloy surfaces represents a promising approach for enhancing tribological performance.

2. Experimentation

A comparative analysis was conducted on four categories of Ti_6Al_4V alloy, each with distinct surface modifications. Table 1 presents the names of the alloy specimens and their corresponding surface modification techniques. The experimental work encompassed all four categories to examine the impact of texturing and coating on the Ti_6Al_4V alloy.

Table 1. Specimen categories.

Specimen Name	Type of Surface Modification
T1	Ti_6Al_4V Reference sample without any modifications
T2	Ti_6Al_4V Untextured TiN—Coated
T3	Ti_6Al_4V Textured Uncoated
T4	Ti_6Al_4V Textured TiN—Coated

2.1. Material Preparation

Titanium alloy Ti_6Al_4V grade 5 alloy was sourced in the form of a rod from M/s Prashanth Steel & Alloy suppliers in Mumbai. The alloy possesses the following chemical composition and mechanical properties, as shown in Tables 2 and 3. A pin-on-disc tribometer wear test was conducted according to the American Society of Testing Materials (ASTM) standard G99 guidelines, and the cylindrical pins were machined using a wire electrical discharge machining (WEDM) technique to achieve a minimum tolerance. The pins were cut into dimensions of 28 mm × 10 mm, as shown in Figure 1. These dimensions were selected to precisely fit the pin holder in the Ducom Tribometer machine. The facility was supported by the Tribological Research Cell of Sri Venkateswara College of Engineering.

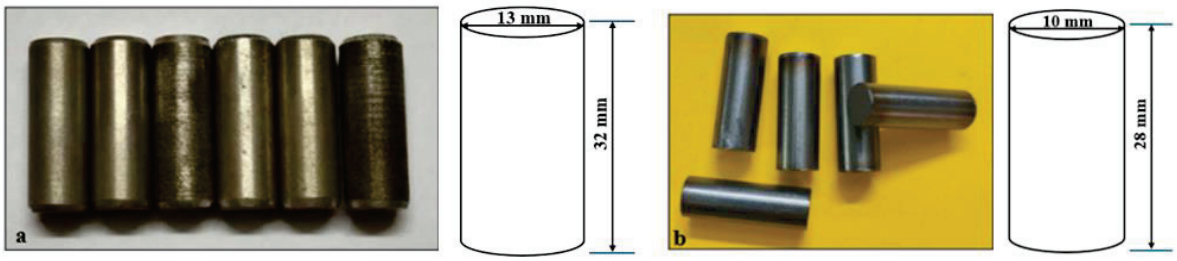


Figure 1. (**a**) Procured Ti_6Al_4V alloys, (**b**) machined specimens with dimensions of 28 mm × 10 mm.

Table 2. Chemical composition of Ti_6Al_4V alloy.

Chemical Element	Titanium	Aluminium	Vanadium	Iron	Others
Weight%	91	5.5 to 6.75	3.5 to 4.5	<0.4	<0.2

Table 3. Mechanical properties of Ti_6Al_4V alloy.

Parameters	Density Kg/m^3	Ultimate Tensile Strength MPa	Shear Modulus GPa	Modulus of Elasticity GPa	Poisson's Ratio
Value	4420	1100	44	90	0.34

2.2. Methodology

This study presents a comparative investigation of four different Ti_6Al_4V alloy specimens, as outlined in Figure 2. Specimen T1 underwent sliding wear testing using a pin-on-disc tribometer to investigate friction and wear. Specimen T2 first underwent surface modification processes, specifically TiN coating applied through physical vapour deposition (PVD), and was subsequently tested for friction and wear using the same pin-on-disc tribometer. Specimen T3 underwent a surface modification process involving laser surface texturing using a laser marking machine before being tested for friction and wear in the tribometer. Lastly, specimen T4 received two surface modification techniques: first, texturing using a laser marking machine, followed by TiN coating through PVD, and then it was tested for friction and wear using the pin-on-disc tribometer.

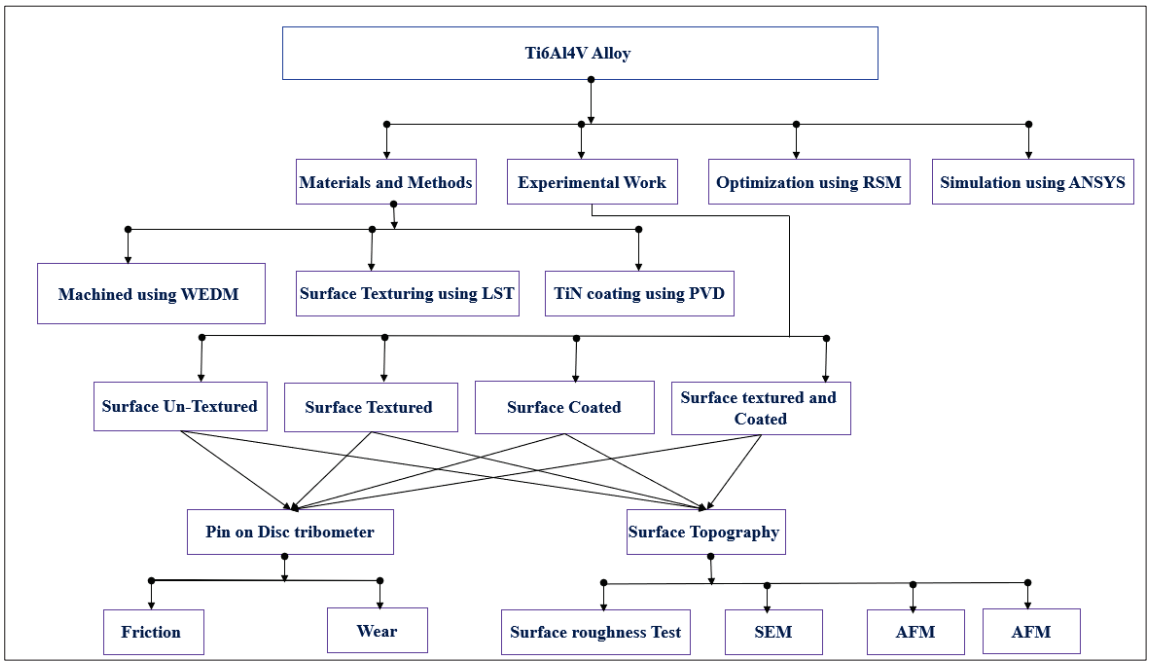


Figure 2. Methodology.

2.3. Surface Modification

Achieving optimal bonding strength to a coating is possible through surface texturing. To texture the surface of a machined alloy specimen, cylindrical pins with a 28 mm diameter × 10 mm top surface were used in a laser surface texturing machine (LST). The LST machine specifications are as follows: laser type—diode-pumped Nd: YAG laser; laser power—20 W; laser wavelength—1064 nm; marking field—200 × 200 mm; scanning speed—10,000 mm/s;

operating temperature—0 to 40 °C. The surface was textured using the LST machine on Ti_6Al_4V alloy with the specified parameters in a single pass. The step-by-step process flow for laser surface texturing is illustrated in Figure 3.

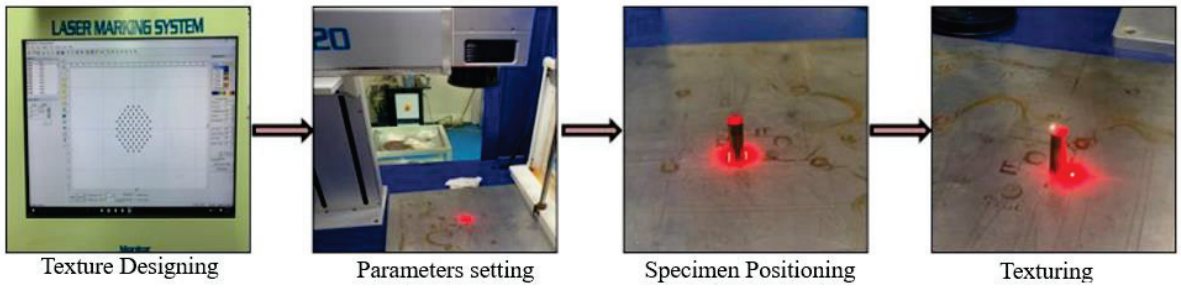


Figure 3. Process flow of laser surface texturing.

The texturing pattern was designed using AutoCAD software and uploaded in the EZCAD software of the laser surface texturing machine. Using the uploaded image, the LST machine generates a laser beam to create the textured pattern on top of the material surface, as shown in Figure 3. The textured Ti_6Al_4V alloy surface was coated with a TiN, which is a universally accepted biocompatible coating. The reason for this choice lies in the addition of aluminium, which forms aluminium oxide on the material's surface. This increases the operational temperature range of the coating. The structure results in an optimal relation of high hardness to residual compressive stress, preventing any form of erosion to the inner layers of these compounds and improving the elastic modulus [20–22]. PVD techniques were used to create the TiN coating with a thickness of 4 μm, facilitated by Oerlikon Balzers Coating India Private Limited, Chennai. PVD coating techniques were chosen for their hardness, wear and corrosion resistance, more uniform deposition, improved adhesion, and environmental friendliness. Surface modification (surface texturing and TiN coating) on the Ti_6Al_4V alloy specimens is shown in Figure 4.



Figure 4. Ti_6Al_4V—textured uncoated; Ti_6Al_4V—untextured TiN-coated; Ti_6Al_4V—textured TiN-coated.

2.4. Pin-on-Disc Tribometer

The dry sliding wear test was conducted using a Ducom TR-20 pin-on-disc tribometer, as shown in Figure 5. The tribometer's specifications are as follows: pin specimen holder diameter: 8 mm, 10 mm, and 12 mm; disc size: 165 mm × 8 mm; wear track diameter: 50 mm–130 mm; disc speed: 200–2000 rpm; normal load: 0.5–20 Kg; frictional force: 0–200 N; wear: 0–2000 μm.

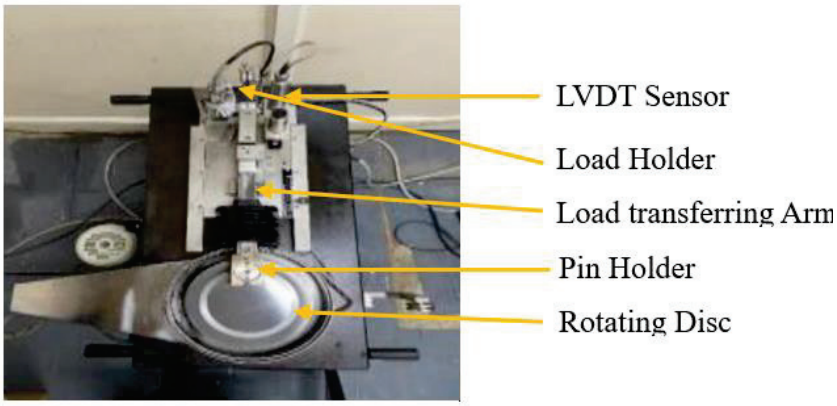


Figure 5. Pin-on-disc tribometer.

Experimental work was conducted under the conditions shown in Table 4 using a pin-on-disc tribometer to obtain tribological properties such as friction and wear rate.

Table 4. Testing parameters.

Testing Parameters	Specification
Normal load in N	60, 80, and 100
Sliding velocities in m/s	1.25, 2.1, and 3.2
Temperature	Room temperature
Testing time in min	20 min/samples
Wear track diameter in mm	50 mm to 130 mm

Bergmann et al. (2014) discussed the load distribution on the knee concerning the body weight conversion factor (minimum 1.5 times) of the person under various conditions such as walking on a flat surface, inclined surface, and step walking [39]. The load acting on the knee sliding area was calculated by considering the average knee sliding area of 850.15 mm^2 and the average body weight of a human being of 539.55 N [40,41]. To calculate the load acting on the pin surface, the pin area (78.55 mm^2) was multiplied by the average body weight of a human and divided by the knee sliding area of 850.15 mm^2. According to these data, the knee experiences a load of 60 N, 80 N, and 100 N. A 60 N load represents low-to-moderate joint loads and physical activity such as standing or walking, allowing for an evaluation of implant performance under minimal loading conditions. An 80 N load simulates moderate joint loads, typical of daily activities like climbing stairs or squatting, bridging the gap between low and high loads and providing an intermediate testing condition. A 100 N load represents high joint loads, simulating strenuous activities like running or jumping, and enables the assessment of implant performance under extreme loading conditions (Liu et al. 2021). Experimentally, the linear sliding speeds were determined to be 1.2 m/s during walking and 3.2 m/s during running using a portable motion analysis system among a group of athletes [42].

For the experiment, Ti_6Al_4V alloy specimens (T1, T2, T3, and T4) were placed on a rotating disc of EN8 material and exposed to varying loads (60 N, 80 N, and 100 N) and sliding velocities (1.25 m/s, 2.1 m/s, and 3.2 m/s) at room temperature. Data-acquisition systems were connected to record and monitor the values of frictional force and sliding distance in meters over a specific period. The recorded values obtained from the data-acquisition system were used to determine the coefficient of friction and specific wear.

3. Numerical Methods

3.1. Simulation Using ANSYS

Wear analysis using the simulation software Ansys Workbench 2018 provides valuable insights into the mechanical behaviour of titanium alloys under tribological conditions. Figure 6 shows the step-by-step procedure for performing an ANSYS simulation for the pin-on-disc tribometer wear test. The results can be used to optimise the material operating conditions to minimise wear performance.

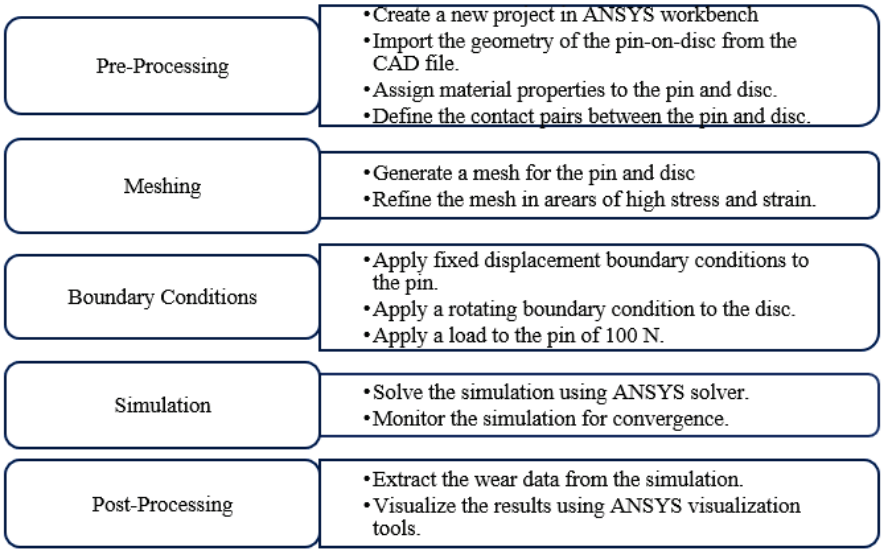


Figure 6. Steps to perform ANSYS simulation.

3.2. Design of Experiments Using RSM

The analysis of the mathematical model is used to study the responses based on different input factor combinations and to predict the output responses. RSM is a powerful statistical technique used to design experiments and predict models related to surface modification [11–13]. In the present study, RSM was used as a statistical analysis tool to predict the output response. Table 5 shows the factors considered for this statistical research, where applied load and sliding velocity are numeric, and specimen type is a categorical factor. The response parameters considered were specific wear rate and coefficient of friction.

Table 5. Testing parameters and their levels for RSM.

Factors	Levels			
Material type	T1	T2	T3	T4
Load (N)	60	80	100	-
Sliding velocity (m/s)	1.25	2.1	3.2	-

4. Result and Discussion

4.1. Analysis of Surface Characterisation

4.1.1. Atomic Force Microscopy (AFM)

The atomic force microscopy (AFM) images provided in Figure 7a offer detailed insights into the surface topography of the coated sample. In Figure 7b, showing the surface topography of the coated sample, the image represents a 2D topographical map of the coated surface. The colour gradient indicates the height variations across the sample's surface, with darker regions corresponding to lower areas and lighter regions representing

higher areas. The surface appears relatively smooth with uniform features, typical of a high-quality coating.

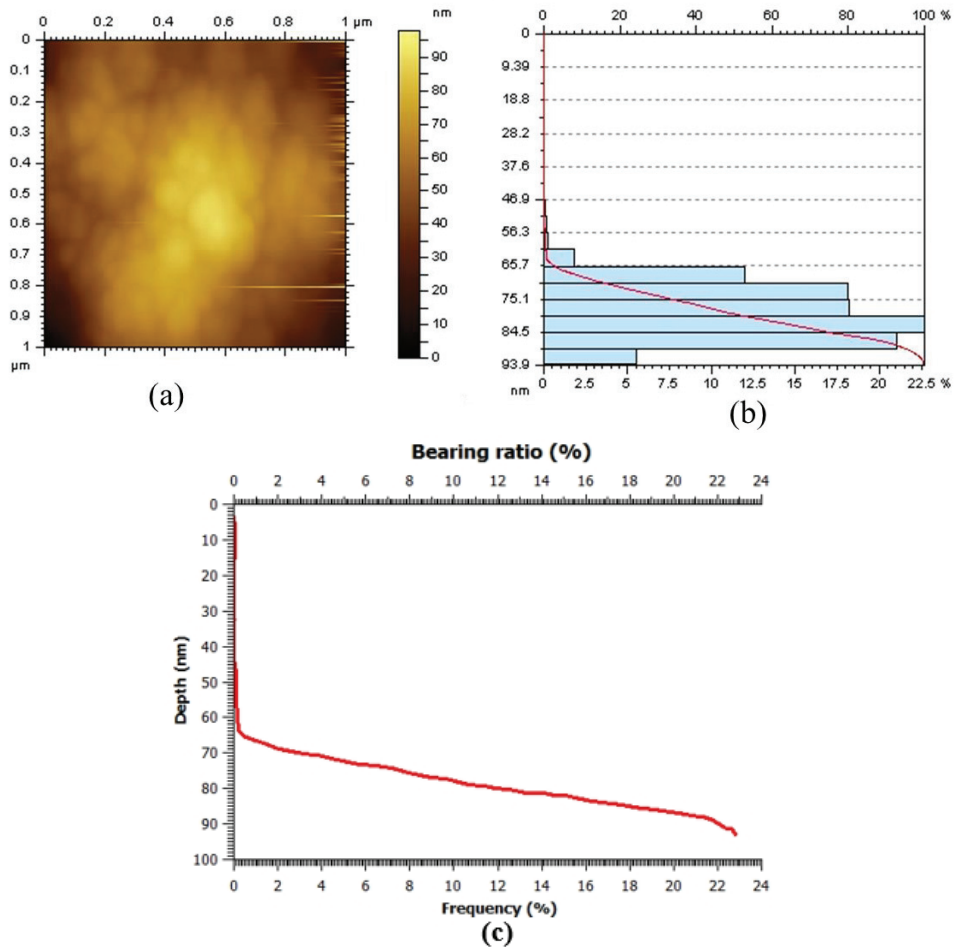


Figure 7. TiN-coated Ti_6Al_4V alloy surface: (**a**) 2D image of coated surface; (**b**) histogram image; and (**c**) Abbott–Firestone curve.

The graph in Figure 7c provides a quantitative analysis of the surface topography, indicating the distribution of surface heights across the sample. Most of the surface height is concentrated around a narrow range, indicating a relatively smooth surface with minor height variations.

The overall trend is relatively stable, reflecting the uniformity of the DLC coating. The AFM results provide valuable information regarding the surface quality and uniformity of the coating.

4.1.2. Scanning Electron Microscope

This study conducted scanning electron microscope (SEM) analyses on all experimentally tested samples. The results of the SEM analysis, both before and after the wear tests, for the samples T1, T2, T3, and T4 are presented in Figure 8a–h. The T1 samples exhibited the maximum wear rate and the highest amount of wear debris, as shown in Figure 8b. In comparison, the T2 sample, which features a TiN coating applied to the Ti_6Al_4V alloy surface, demonstrated a lower wear rate than the T1 sample, as illustrated in Figure 8d. The T3 sample, which has a textured Ti_6Al_4V alloy surface, showed more wear debris than the T2 sample but less than the T1 sample, as seen in Figure 8f. Finally, the T4 sample, which consists of a laser-textured TiN coating on the Ti_6Al_4V alloy surface, exhibited a comparatively lower wear rate and less wear debris than the T1, T2, and T3 samples.

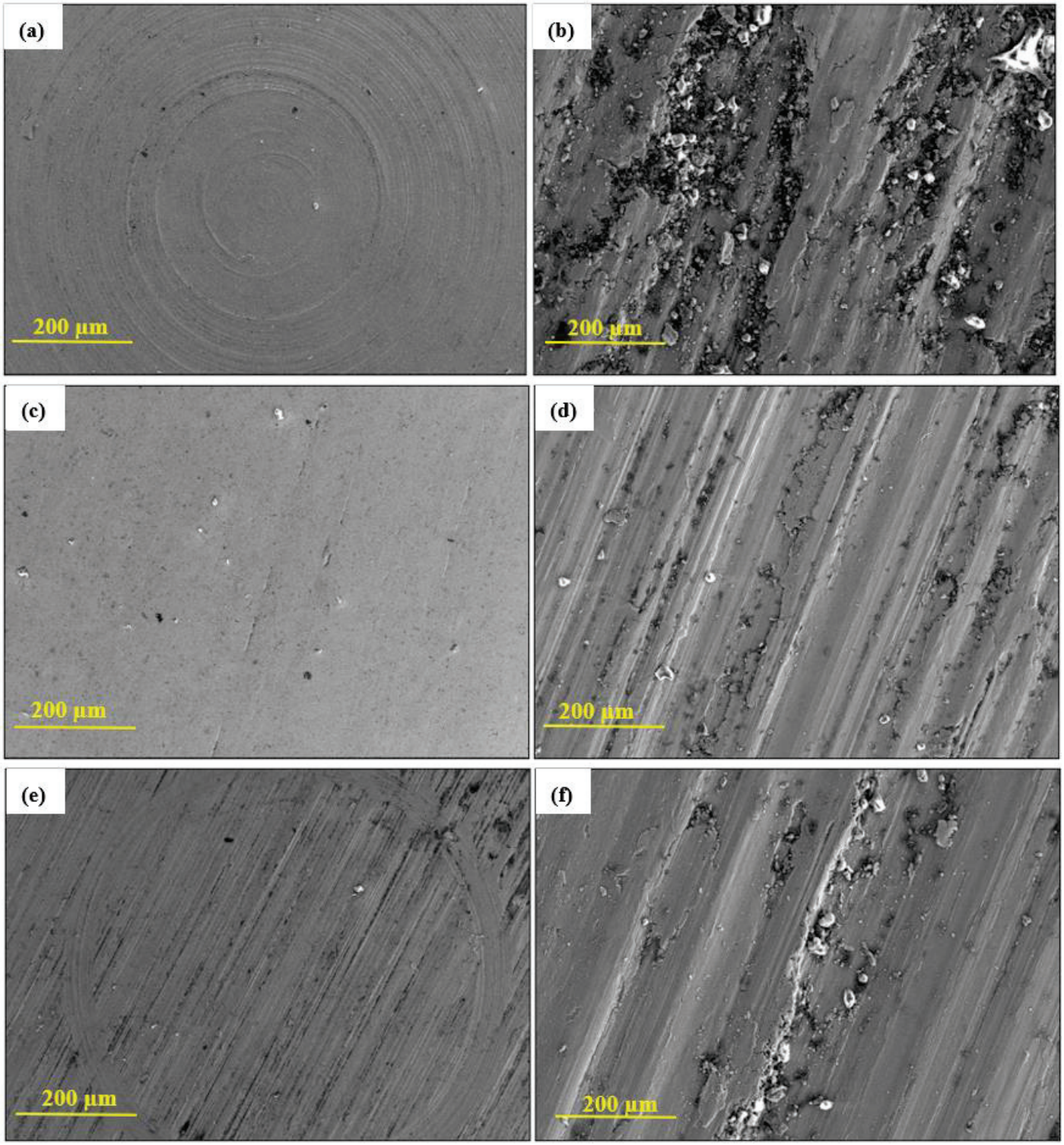


Figure 8. *Cont*.

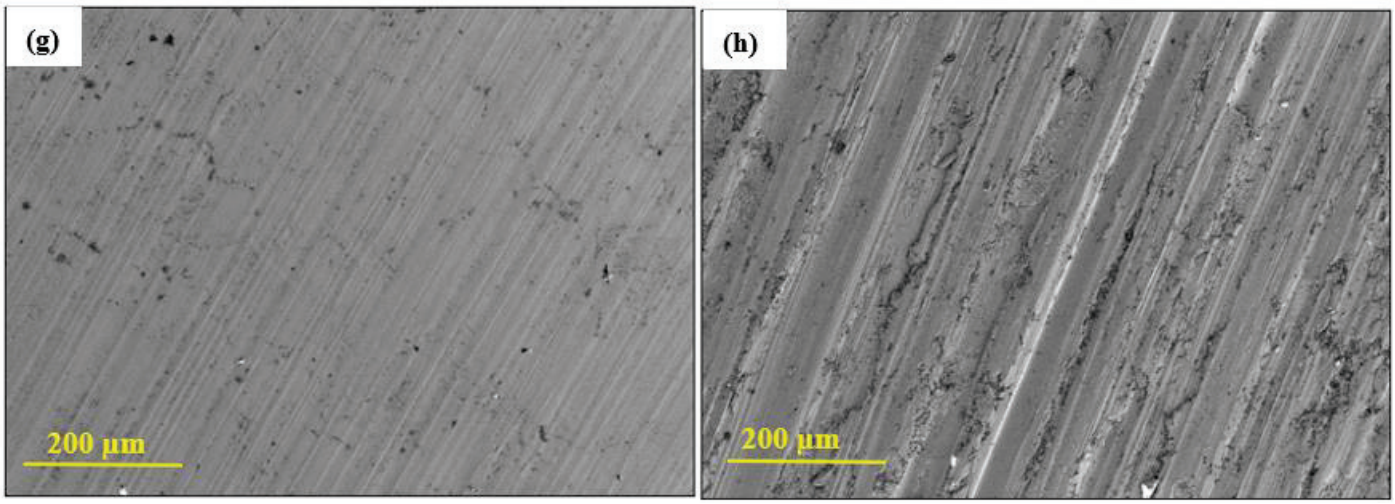
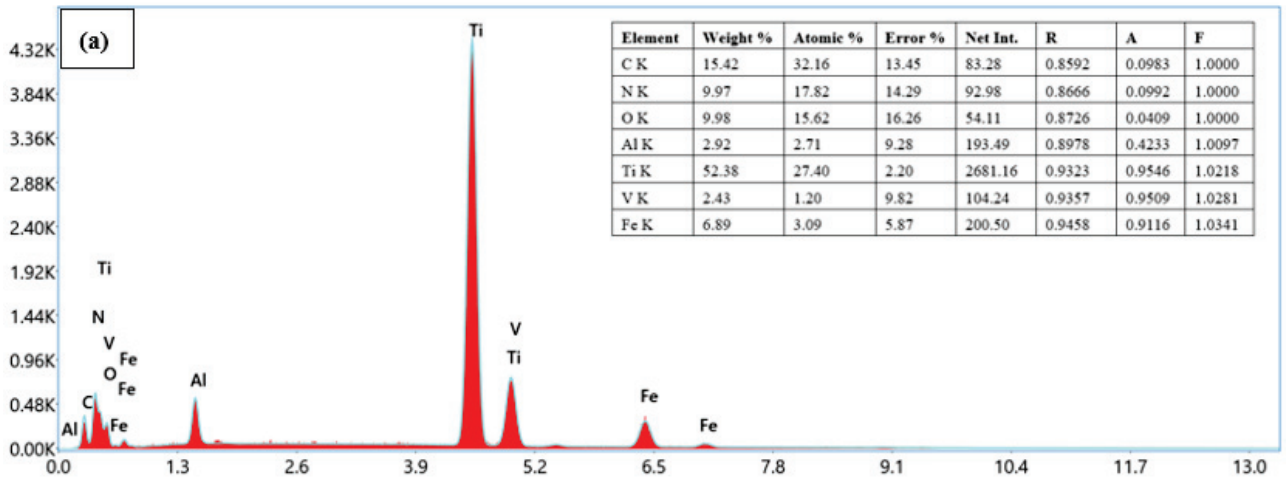


Figure 8. SEM images of Ti_6Al_4V alloy: (**a**) T1 before wear test, (**b**) T1 after wear test, (**c**) T2 before wear test, (**d**) T2 after wear test, (**e**) T3 before wear test, (**f**) T3 after wear test, (**g**) T4 before wear test, (**h**) T4 after wear test.

4.1.3. Energy-Dispersive X-Ray Spectroscopy (EDX)

This study conducted energy dispersive X-ray (EDX) analyses on all experimental specimens to determine their elemental composition. Figure 9a presents the EDX analysis results for the T1 specimen before the wear test, which shows only a trace of the base material element composition on the surface of the Ti_6Al_4V alloy. Figure 9b displays the EDX analysis results for the T2 specimen before the wear test, revealing a trace of the TiN-coated element composition on the Ti_6Al_4V alloy's surface. Finally, Figure 9c illustrates the EDX analysis results for the T4 specimen after the wear test, which shows traces of both the base material and the TiN-coated element composition on the surface of the Ti_6Al_4V alloy.



Element	Weight %	Atomic %	Error %	Net Int.	R	A	F
C K	15.42	32.16	13.45	83.28	0.8592	0.0983	1.0000
N K	9.97	17.82	14.29	92.98	0.8666	0.0992	1.0000
O K	9.98	15.62	16.26	54.11	0.8726	0.0409	1.0000
Al K	2.92	2.71	9.28	193.49	0.8978	0.4233	1.0097
Ti K	52.38	27.40	2.20	2681.16	0.9323	0.9546	1.0218
V K	2.43	1.20	9.82	104.24	0.9357	0.9509	1.0281
Fe K	6.89	3.09	5.87	200.50	0.9458	0.9116	1.0341

Figure 9. *Cont.*

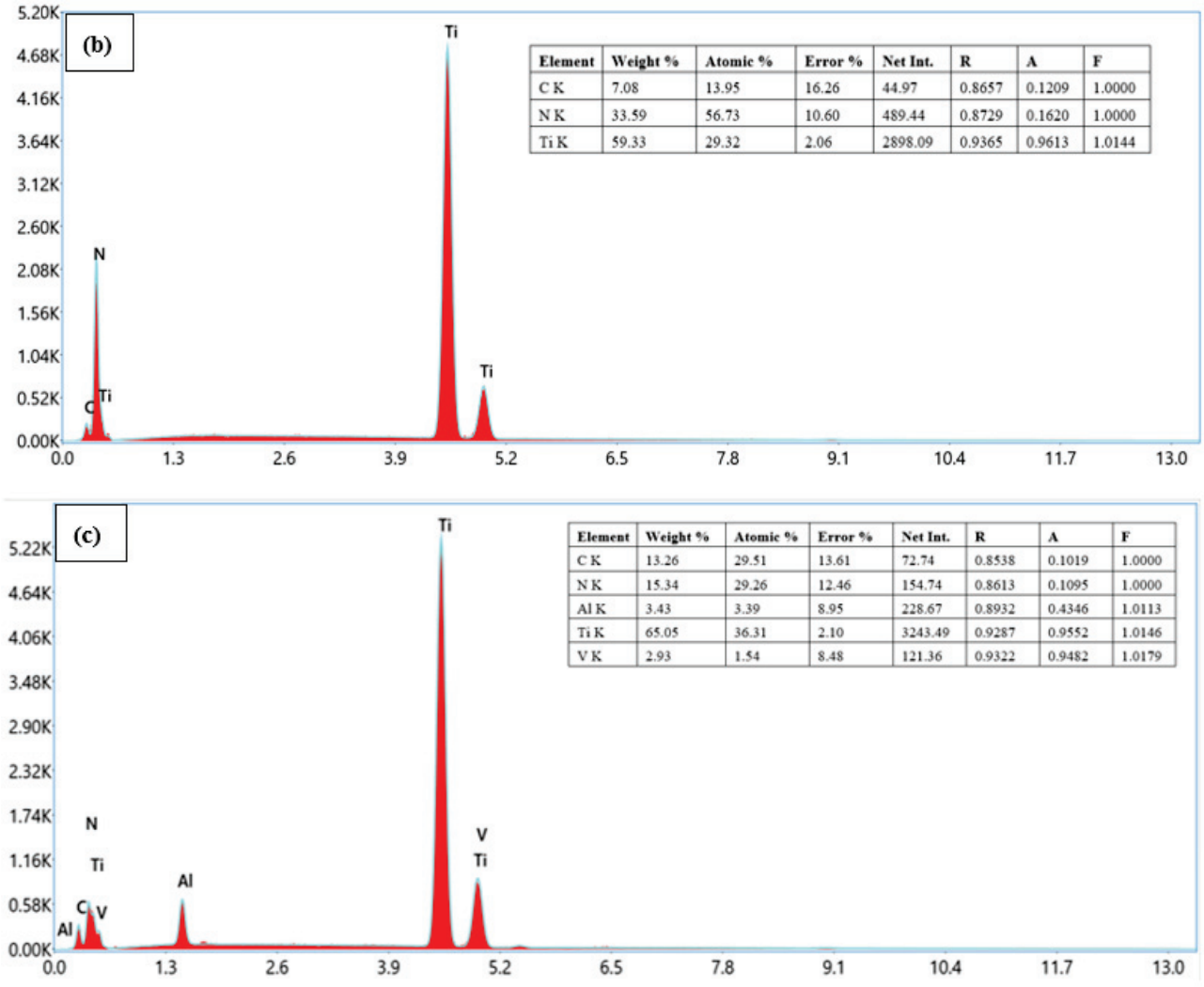


Figure 9. EDX analysis: (**a**) T1 specimen, (**b**) T2 specimen, and (**c**) T4 specimen after wear test.

4.2. Coefficient of Friction

The coefficient of friction of the experimental samples (T1, T2, T3, and T4) was compared against varying applied loads of 60 N, 80 N, and 100 N, as shown in Figure 10. As the load in the normal direction increases, the coefficient of friction (COF) also increases for both coated and uncoated conditions and textured and untextured conditions. The texturing and coating material interaction on the counter body disc significantly reduces the friction coefficient. Bahi et al.'s research [27] revealed that the COF of a TiN/TiO_2 multilayer coating on a Ti_6Al_4V alloy fluctuates and becomes less stable as the sliding distance increases. The same was observed in our study, where the average COF for the reference sample is greater than that of a modified sample such as the textured and coated with TiN sample, which exhibits a lower COF, as shown in Figure 8. Additionally, increasing sliding velocity decreases the coefficient of friction for all load-applied conditions, as shown in Figure 8b–d. This decreasing trend in the coefficient of friction may be due to thermal softening, surface smoothing, and tribo-chemical reactions. The coefficient of friction shows a significant deviation with an increase in all load conditions. When a force of 60 N is applied, the T1 specimens show a wider range of friction values, ranging from 0.41 to 0.36, as the sliding velocity increases. On the other hand, the T4 specimens exhibit a narrower range of friction values, varying from 0.29 to 0.27. When the force is increased to 100 N, the trend reverses, with the T4 specimen showing more variation in friction values

compared to the T1 specimens. This indicates that the surface-modified specimens are significantly affected by the applied load compared to the reference specimen. In general, textured specimens have higher friction values than coated specimens. Specifically, the T4 specimen—textured and coated with TiN—exhibits a low coefficient of friction. The texturing process creates micro-pockets, reducing the actual contact area between surfaces, which in turn leads to lower friction. Additionally, textures can generate hydrodynamic pressure, improving lubrication and reducing friction. Meanwhile, the coating fills in micro-valleys, reducing surface roughness and friction.

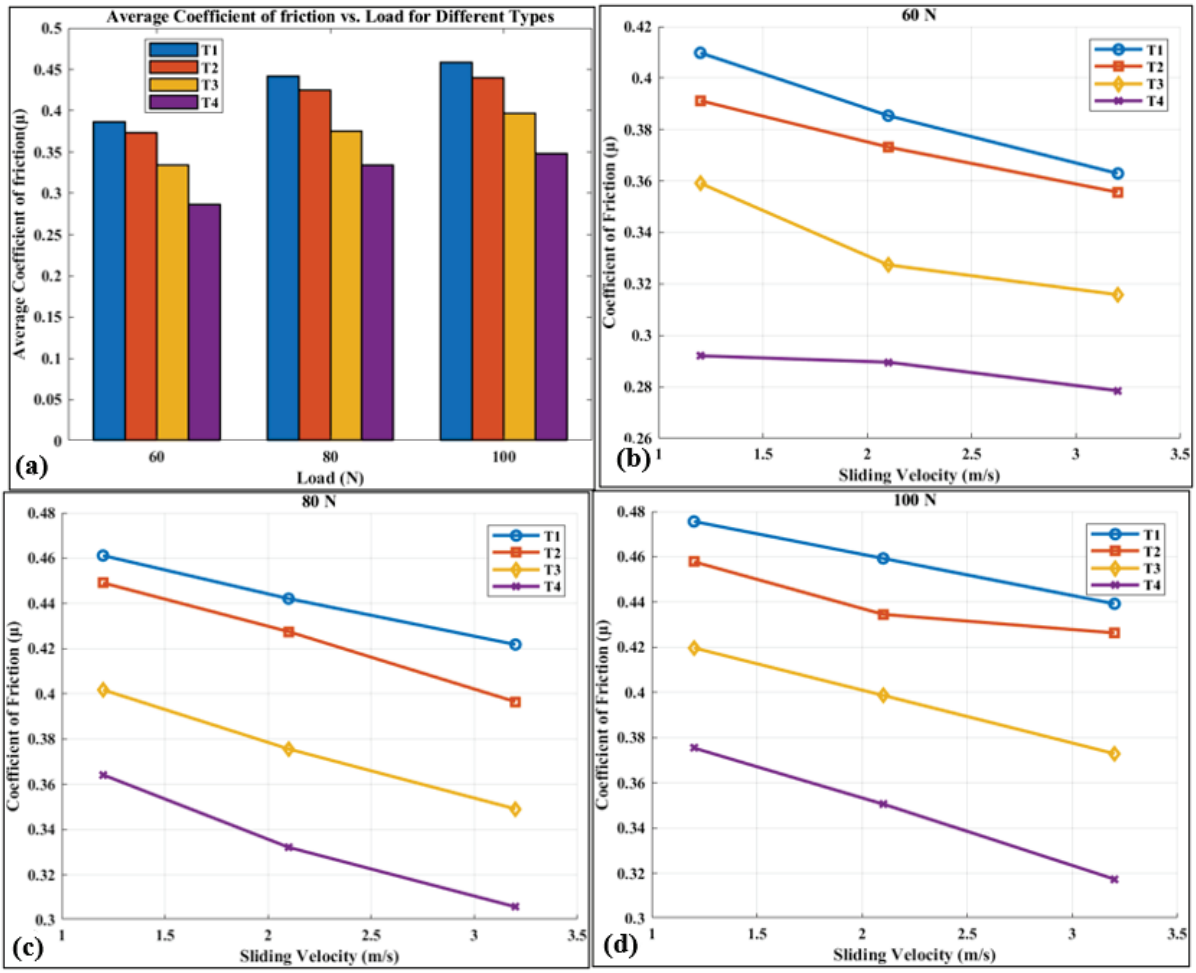


Figure 10. Friction coefficient for experimentally tested samples: (**a**) average friction coefficient versus load, (**b**) friction coefficient versus sliding velocity at 60 N, (**c**) friction coefficient versus sliding velocity at 80 N, and (**d**) friction coefficient versus sliding velocity at 100 N.

4.3. Specific Wear Rate

The specific wear rate in mm^3/N-m is determined through the initial and final mass of the sample in g, the density of the sample in Kg/mm^3, the sliding distance of the pin in m, and the normal applied load in N, as shown in Equation (5). The specific wear rate of the experimental samples (T1, T2, T3, and T4) versus the applied load is shown in Figure 11a. T4 specimens exhibit less wear rate compared to other specimens for all load conditions. An increasing sliding velocity exhibits a slightly decreasing specific wear rate at varying load conditions, as shown in Figure 11b–d. The decreasing specific wear rate with increasing sliding distance is due to the higher velocities generating heat, which can lead to the thermal softening of materials and promote the formation of a protective oxide layer reducing metal-to-metal contact. Overall, the textured specimens exhibit less specific

wear than the coated specimens due to the texture reducing the number of contact points and subsequently reducing wear.

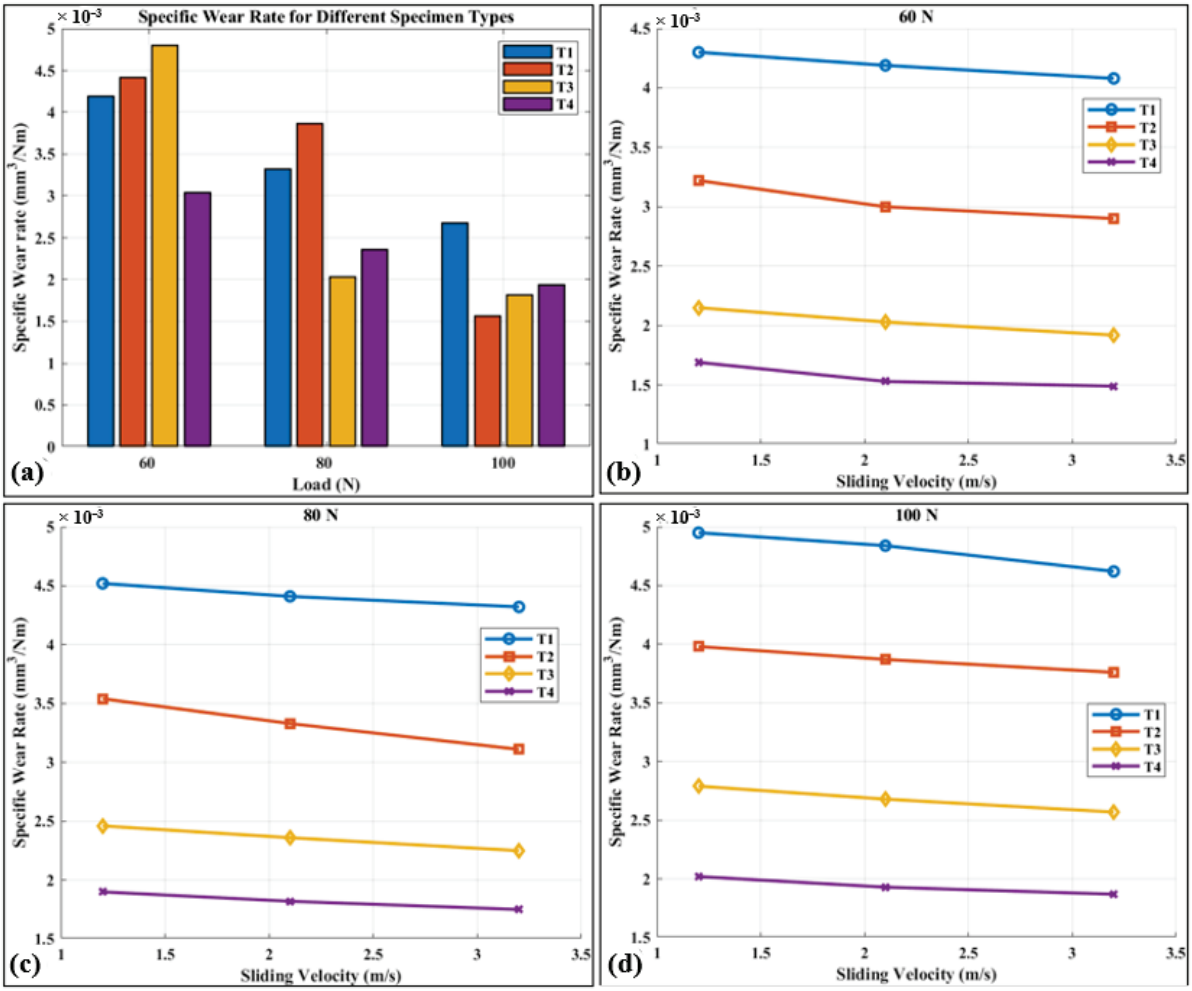


Figure 11. Specific wear rate for experimentally tested samples: (**a**) specific wear rate versus applied load, (**b**) specific wear rate versus sliding velocity at 60 N, (**c**) specific wear rate versus sliding velocity at 80 N, and (**d**) specific wear rate versus sliding velocity at 100 N.

4.4. Surface Roughness Measurement

The surface roughness measurement test was conducted for all specimens (T1, T2, T3, and T4) before the experimental test. The purpose of the test was to determine the surface roughness after the surface had been modified with texturing and coating. Figure 12 presents the surface roughness measurements before the tribological test, which include the parameters for average roughness (Ra), mean roughness (Rz), and root mean square (Rq). Ra measures the average deviation of the surface from the mean line, Rz measures the average distance between the highest peak and the lowest valley, and Rq measures the square root of the average of the squared deviations. The data in Figure 12 show that the mean roughness profile Ra ranges from 0.30 μm to a maximum roughness of 0.56 μm. The Ti_6Al_4V sample treated with laser surface texturing and TiN coating has higher values for roughness parameters Ra, Rz, and Rq compared to the reference sample of Ti_6Al_4V. On the other hand, the roughness parameters of the Ti_6Al_4V sample treated with TiN-coating indicate no significant changes compared to the reference sample. Additionally, the figure indicates that the surfaces treated with laser texturing have higher roughness parameters

than the TiN-coated surfaces, indicating that the laser-textured surface possesses more influential parameters than the TiN-coated surface, as shown in Figure 13.

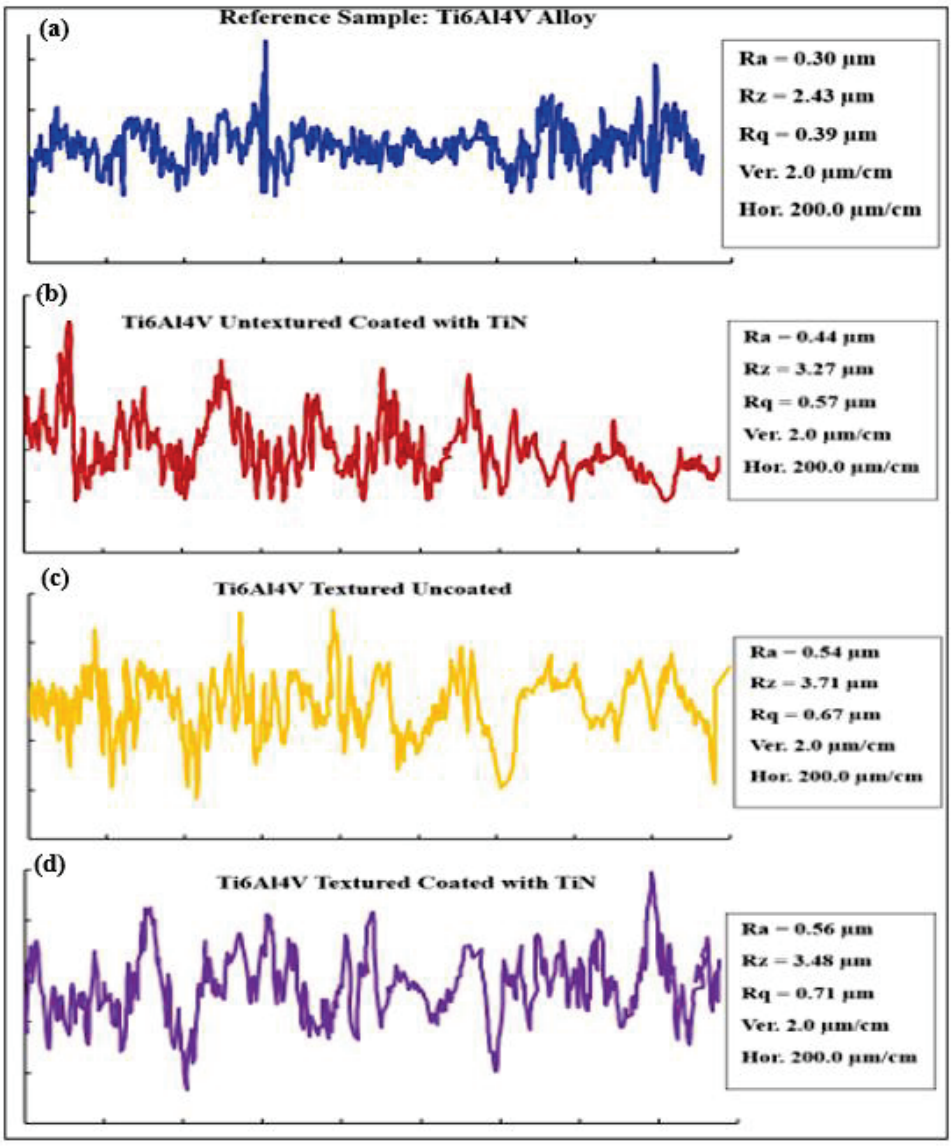


Figure 12. Surface topography Ti_6Al_4V alloy samples: (**a**) T1 specimen, (**b**) T2 specimen, (**c**) T3 specimen, and (**d**) T4 specimen.

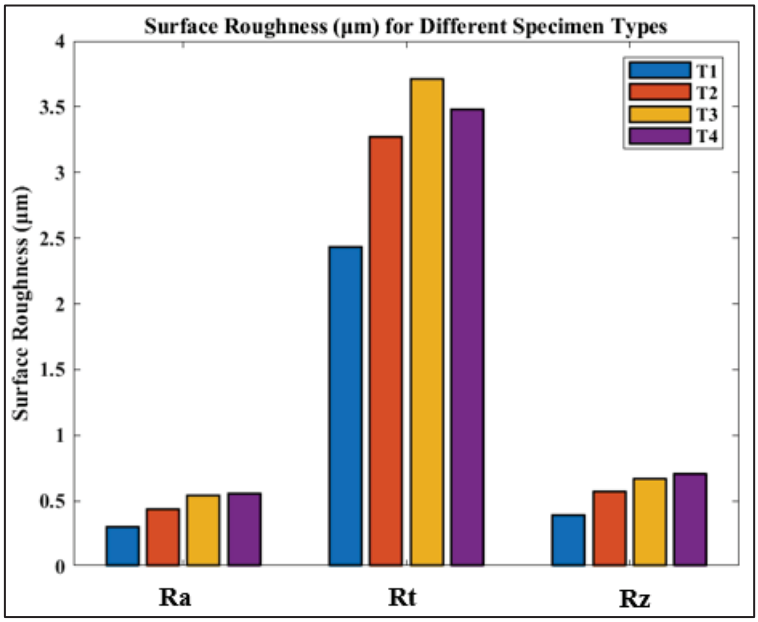


Figure 13. Surface roughness values of T1, T2, T3, and T4.

4.5. Wear Analysis Using Simulation Software

A wear analysis study has been carried out using Ansys simulation software shown in Figure 14. The colour coding of the images shows the stress distribution for different samples in N/mm^2. The study compares a reference sample with surfaces that underwent treatment with TiN coating (see Figure 12a), laser texturing (see Figure 12b), and a combination of laser texturing and TiN coating (see Figure 12c). The analysis indicates a significant impact of TiN coating and laser texturing on the surfaces compared to the reference sample. The Ansys simulation study results showed that both the TiN-coated and laser-textured surfaces display a higher wear rate compared to the reference sample.

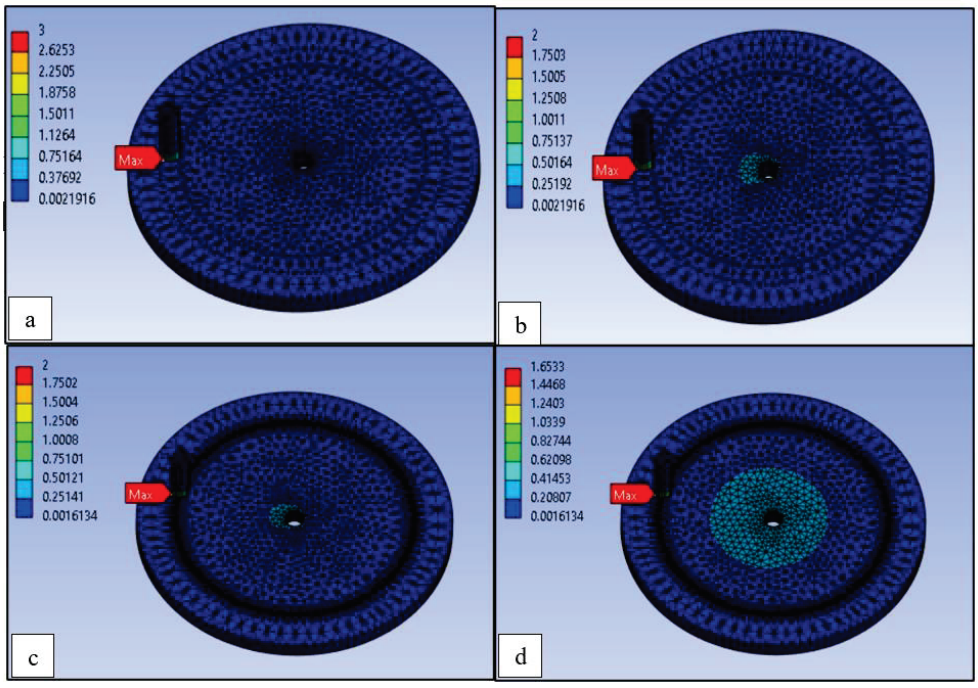


Figure 14. Wear analysis result of Ansys simulation: (**a**) reference sample, (**b**) untextured coated TiN, (**c**) textured uncoated TiN, (**d**) textured coated TiN.

4.6. Analysis of Response Surface Methodology

The study examined load, sliding velocity, and specimen type as variables. The wear test results are detailed in Table 6. Experimental plans were devised to establish a quadratic model for a particular wear rate and friction coefficient. The Design Expert program was employed to input these results for further investigation.

Table 6. Experimental results for friction and wear.

Run	Input Factors			Response	
	Type	Load (N)	Sliding Velocity (m/s)	Coefficient of Friction	Specific Wear Rate (mm^3/Nm)
1	T4	60	1.25	0.2921	0.00169
2	T2	80	3.2	0.3965	0.00311
3	T3	80	2.1	0.3756	0.00236
4	T3	100	1.25	0.4197	0.00279
5	T4	100	1.25	0.3754	0.00202
6	T4	60	1.25	0.2921	0.00169
7	T4	60	3.2	0.2785	0.00149
8	T3	60	1.25	0.3591	0.00215
9	T4	60	3.2	0.2785	0.00149
10	T1	80	1.25	0.4612	0.00452
11	T2	60	3.2	0.3556	0.00290
12	T3	60	3.2	0.3158	0.00192
13	T2	60	2.1	0.3732	0.00300
14	T1	60	3.2	0.3629	0.00408
15	T1	60	1.25	0.4098	0.00430
16	T1	80	3.2	0.4218	0.00432
17	T3	80	3.2	0.3491	0.00225
18	T2	80	1.25	0.4491	0.00354
19	T2	100	2.1	0.4345	0.00387
20	T4	100	1.25	0.3754	0.00202
21	T1	100	1.25	0.4756	0.00495
22	T2	100	3.2	0.4263	0.00376
23	T3	100	1.25	0.4197	0.00279
24	T1	100	3.2	0.4392	0.00462
25	T3	60	1.25	0.3591	0.00215

4.6.1. RSM Analysis on Coefficient of Friction

Based on statistical calculation and analysis of variance (ANOVA), a suitable model was chosen to conduct rigorous tests to validate the model's effectiveness. A low *p*-value helped identify important factors in the model. This value also indicated how well the model explained the data's variability. Detailed ANOVA analyses were performed for both the coefficient of friction (COF) and specific wear rate using the chosen cubic and quadratic mixture models. The results are presented in Tables 7 and 8. Table 7 (COF) clearly shows that load, sliding speed, and their interaction significantly affect the COF. The extremely low *p*-values (<0.0001) indicate a high confidence level (over 95%) in these findings. Moreover, the coefficient of determination (R^2) for the COF model is an impressive 0.9975. This signifies an excellent fit between the model's predictions and the actual measurements. Figure 15a visually confirms this by plotting the actual vs. predicted COF values. The normal probability plot (Figure 15b) for COF reveals a near-perfect linear distribution of residuals, with no outliers, further supporting the model's robustness. Similarly, the scattered pattern of residuals in Figure 15c suggests their independence. Figure 15d provides additional insights. It allows researchers to identify if any specific experimental runs significantly influence the overall analysis. This is helpful when certain data points deviate significantly from the norm. Finally, Figure 15e reveals the relationship between the studied factors and COF. It shows that COF decreases with increasing sliding speed but increases with increasing applied load.

Equations (1)–(4) represent the resulting quadratic model for COF.

$$\begin{aligned} T1 = 0.170601 \quad & +0.007147 \times \text{LOAD} - 0.068158 \times \text{SLIDING VELOCITY} \\ & +0.000052 \times \text{LOAD} \times \text{SLIDING VELOCITY} - 0.000034 \times \text{LOAD}^2 \\ & +0.009671 \times \text{SLIDING VELOCITY}^2 \end{aligned} \quad (1)$$

$$\begin{aligned} T2 = 0.175735 \quad & +0.006999 \times \text{LOAD} - 0.070894 \times \text{SLIDING VELOCITY} \\ & +0.000052 \times \text{LOAD} \times \text{SLIDING VELOCITY} - 0.000034 \times \text{LOAY}^2 \\ & +0.009671 \times \text{SLIDING VELOCITY}^2 \end{aligned} \quad (2)$$

$$\begin{aligned} T3 = 0.142742 \quad & +0.006871 \times \text{LOAD} - 0.071866 \times \text{SLIDING VELOCITY} \\ & +0.000052 \times \text{LOAD} \times \text{SLIDING VELOCITY} - 0.000034 \times \text{LOAD}^2 \\ & +0.009671 \times \text{SLIDING VELOCITY}^2 \end{aligned} \quad (3)$$

$$\begin{aligned} T4 = 0.012715 \quad & +0.007504 \times \text{LOAD} - 0.053121 \times \text{SLIDING VELOCITY} \\ & +0.000052 \times \text{LOAD} \times \text{SLIDING VELOCITY} - 0.000034 \times \text{LOAD}^2 \\ & +0.009671 \times \text{SLIDING VELOCITY}^2 \end{aligned} \quad (4)$$

Table 7. ANOVA for coefficient of friction.

Source	Sum of Squares	Degree of Freedom	Mean Square	F-Value	*p*-Value	
Model	0.078	14	0.0056	281.53	<0.0001	significant
A-LOAD	0.0205	1	0.0205	1035.69	<0.0001	
B-SLIDING VELOCITY	0.0064	1	0.0064	324.74	<0.0001	
C-MATERIAL	0.0322	3	0.0107	542.52	<0.0001	
AB	6.89×10^{-06}	1	6.89×10^{-06}	0.348	0.5683	
AC	0.0003	3	0.0001	5.85	0.0142	
BC	0.0007	3	0.0002	12.3	0.0011	
A^2	0.0006	1	0.0006	31.33	0.0002	
B^2	0.0002	1	0.0002	8.05	0.0176	
Residual	0.0002	10	0			
Lack of Fit	0.0002	5	0			
Pure Error	0	5	0			
Cor Total	0.0782	24				

Table 8. ANOVA for specific wear rate.

Source	Sum of Squares	Degree of Freedom	Mean Square	F-Value	*p*-Value	
Model	0	12	2.37×10^{-06}	682.66	<0.0001	significant
A-LOAD	1.53×10^{-06}	1	1.53×10^{-06}	440.07	<0.0001	
B-SLIDING VELOCITY	2.63×10^{-07}	1	2.63×10^{-07}	75.64	<0.0001	
C-MATERIAL	0	3	7.41×10^{-06}	2131.47	<0.0001	
AB	1.60×10^{-09}	1	1.60×10^{-09}	0.459	0.5109	
AC	1.18×10^{-07}	3	3.93×10^{-08}	11.3	0.0008	
BC	2.41×10^{-09}	3	8.03×10^{-10}	0.2308	0.8731	
Residual	4.17×10^{-08}	12	3.48×10^{-09}			
Lack of Fit	4.17×10^{-08}	7	5.96×10^{-09}			
Pure Error	0	5	0			
Cor Total	0	24				

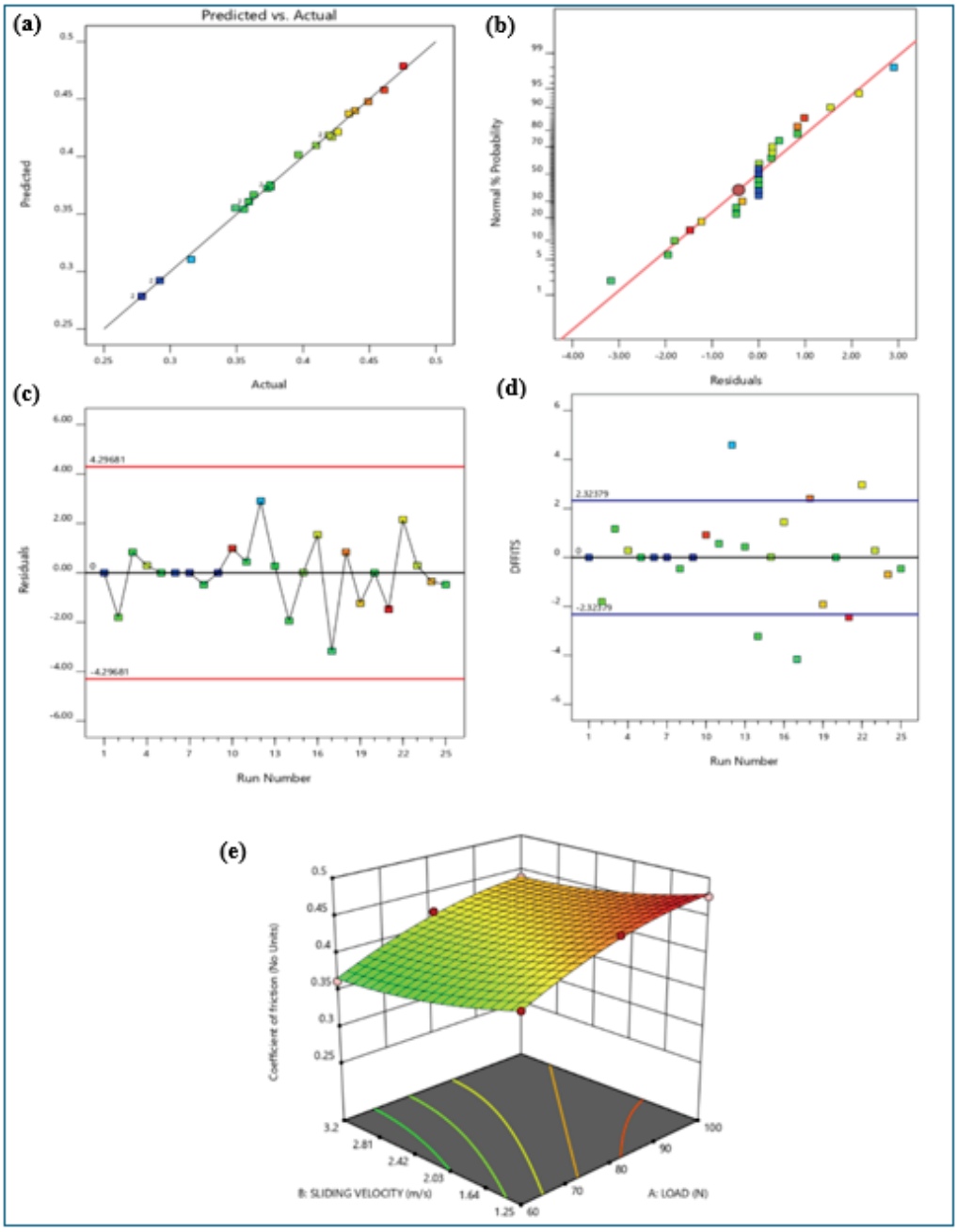


Figure 15. RSM for coefficients of friction: (**a**) actual versus predicted, (**b**) residuals versus normal probability, (**c**) run number versus residuals, (**d**) run number versus DFFITS, and (**e**) 3D surface plot.

4.6.2. RSM Analysis on Specific Wear Rate

Table 8′s statistical analysis shows that load, sliding speed, and their interaction significantly affect the specific wear rate. The extremely low *p*-values (less than 0.0001) indicate a high confidence level (over 95%) in these findings. The coefficient of determination (R^2) for the specific wear rate model is an impressive 0.9985, confirming its accuracy in predicting actual results. Figure 16a visually confirms this by plotting the actual vs. predicted wear rate values. The normal probability plot (Figure 16b) for the specific wear rate reveals a near-perfect linear distribution of residuals, with no outliers, further supporting the model's robustness. Similarly, the scattered pattern of residuals in Figure 16c suggests their independence. Figure 16d provides additional insights. It allows researchers to identify if any specific experimental runs significantly influence the overall analysis. This is helpful when certain data points deviate significantly from the norm. Finally, Figure 16e reveals the

relationship between the studied factors and the specific wear rate. It shows how changes in sliding speed and applied load affect the wear rate. Equations (5)–(8) represent the resulting quadratic model for specific wear rates.

$$\begin{aligned} T1 = 0.003421 \quad & +0.000017 \times \text{LOAD} - 0.000065 \times \text{SLIDING VELOCITY} \\ & -7.64683 \times 10^{-07} \text{LOAD} \times \text{SLIDING VELOCITY} \end{aligned} \tag{5}$$

$$\begin{aligned} T2 = 0.001850 \quad & +0.000024 \times \text{LOAD} - 0.000091 \times \text{SLIDING VELOCITY} \\ & -7.64683 \times 10^{-07} \text{LOAD} \times \text{SLIDING VELOCITY} \end{aligned} \tag{6}$$

$$\begin{aligned} T3 = 0.001238 \quad & +0.000017 \times \text{LOAD} - 0.000058 \times \text{SLIDING VELOCITY} \\ & -7.64683 \times 10^{-07} \text{LOAD} \times \text{SLIDING VELOCITY} \end{aligned} \tag{7}$$

$$\begin{aligned} T4 = 0.001270 \quad & +9.13085\text{E} - 06 \times \text{LOAD} - 0.000057 \times \text{SLIDING VELOCITY} \\ & -7.64683 \times 10^{-07} \text{LOAD} \times \text{SLIDING VELOCITY} \end{aligned} \tag{8}$$

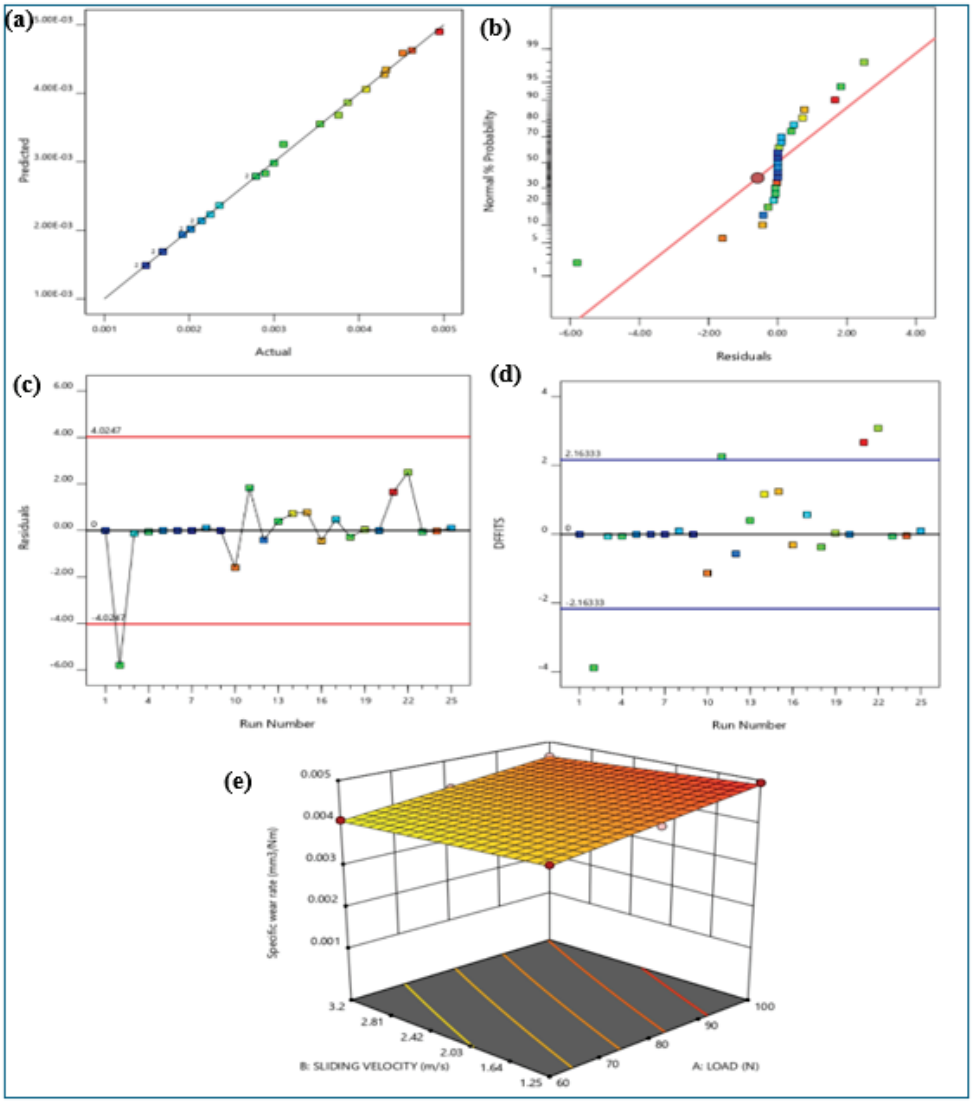


Figure 16. RSM for specific wear rate: (**a**) actual versus predicted, (**b**) residuals versus normal probability, (**c**) run number versus residuals, (**d**) run number versus DFFITS, and (**e**) 3D surface plot.

5. Confirmation Test

The mathematical model represented by equations 1 to 8 was used to predict the coefficient of friction and specific wear rate. These predicted values are presented in Table 9. Model adequacy tests confirm a good fit between the experimental and predicted values. The coefficient of determination (R^2) and adjusted R^2 for the coefficient of friction are 0.9975 and 0.9939, respectively. Similarly, the R^2 and adjusted R^2 for specific wear rates are 0.9985 and 0.9971. The close agreement between R^2 and adjusted R^2 suggests that the model data accurately reflect the experimental results. Furthermore, both models boast R^2 and adjusted R^2 values exceeding 95%, indicating their suitability for predicting solutions. Table 9 utilizes Cook's distance, a regression statistic, to identify potentially influential outliers within the independent variables. This helps detect experimental points that may negatively impact the model and pinpoint regions with good correlations. For both the coefficient of friction and specific wear rate, Cook's distance values range from 0 to 1. Interestingly, experiments 12, 17, and 22 stand out for the coefficient of friction, while experiments 22, 21, and 11 have elevated Cook's distances for the specific wear rate. These points fall outside the typical 0–1 range, suggesting they might be influential outliers requiring further investigation.

Table 9. Confirmation table.

Run Order	Coefficient of Friction				Specific Wear Rate			
	Actual Value	Predicted Value	Residual	Cook's Distance	Actual Value	Predicted Value	Residual	Cook's Distance
1	0.2921	0.2921	0	0	0.0017	0.0017	0	0
2	0.3965	0.401624	−0.00512	0.177933	0.0031	0.0033	−0.0001	0.312
3	0.3756	0.373402	0.002198	0.093645	0.0024	0.0024	-6.88×10^{-06}	0
4	0.4197	0.418701	0.000999	0.005854	0.0028	0.0028	-2.79×10^{-06}	0
5	0.3754	0.3754	0	0	0.002	0.002	0	0
6	0.2921	0.2921	0	0	0.0017	0.0017	0	0
7	0.2785	0.2785	0	0	0.0015	0.0015	0	0
8	0.3591	0.360719	−0.00162	0.015125	0.0021	0.0021	4.73×10^{-06}	0.001
9	0.2785	0.2785	0	0	0.0015	0.0015	0	0
10	0.4612	0.45801	0.00319	0.056751	0.0045	0.0046	−0.0001	0.087
11	0.3556	0.354339	0.001261	0.022976	0.0029	0.0028	0.0001	0.327
12	0.3158	0.310565	0.005235	0.805218	0.0019	0.0019	0	0.027
13	0.3732	0.372519	0.000681	0.013939	0.003	0.003	0	0.013
14	0.3629	0.366859	−0.00396	0.540404	0.0041	0.0041	0	0.108
15	0.4098	0.409781	1.88×10^{-05}	2.35×10^{-05}	0.0043	0.0043	0	0.123
16	0.4218	0.41711	0.00469	0.12267	0.0043	0.0043	0	0.008
17	0.3491	0.355293	−0.00619	0.605471	0.0023	0.0022	0	0.027
18	0.4491	0.44786	0.00124	0.39715	0.0035	0.0036	0	0.012
19	0.4345	0.437378	−0.00288	0.232491	0.0039	0.0039	1.52×10^{-06}	0
20	0.3754	0.3754	0	0	0.002	0.002	0	0
21	0.4756	0.478809	−0.00321	0.355039	0.0049	0.0049	0	0.479
22	0.4263	0.421479	0.004821	0.42962	0.0038	0.0037	0.0001	0.509
23	0.4197	0.418701	0.000999	0.005854	0.0028	0.0028	-2.79×10^{-06}	0
24	0.4392	0.439931	−0.00073	0.035457	0.0046	0.0046	-8.39×10^{-06}	0
25	0.3591	0.360719	−0.00162	0.015125	0.0021	0.0021	4.73×10^{-06}	0.001

6. Conclusions

This study aimed to conduct experimental and analytical investigations on the surface of Ti_6Al_4V alloys treated with laser texturing and TiN coating. The study unveiled the following novel findings regarding the treated sample surfaces:

1. Images from the scanning electron microscope (SEM) revealed changes in the surface topography of the specimens before and after the wear test. The T1 sample showed a higher wear rate and more wear debris compared to the T2, T3, and T4 samples. Additionally, the laser-textured sample T3 demonstrated a greater wear rate than the TiN-coated samples. In contrast, the combination of the laser-textured and TiN-coated sample resulted in a lower wear rate and less wear debris than the other samples.
2. The impact of laser texturing on samples T3 and T4 led to significant irregularities in the geometry of the roughness profile, resulting in elevated roughness parameter values of 0.54 and 0.67 and 0.56 and 0.71. In contrast, the TiN coating in sample T2 and the reference sample T1 exhibited minimal irregularities in the roughness profile geometry, yielding lower roughness parameter values of 0.30 and 0.39 and 0.44 and 0.57.
3. Tribological properties, such as the friction coefficient and wear rate, were evaluated using a pin-on-disc tribometer. The results showed that increasing the applied load generally led to an increase in the friction coefficient for all samples, ranging from 0.2867 to 0.4580. Among the samples tested, the laser-textured and TiN-coated samples (T4) exhibited lower friction coefficients, measuring 0.2867, 0.3340, and 0.3478 for applied loads of 60 N, 80 N, and 100 N, respectively. Similar to the friction coefficient, the specific wear rate exhibits comparable trends with increasing load, ranging from 0.001570 to 0.004803. The laser-textured TiN-coated samples (T4) demonstrated a lower specific wear rate, measuring 0.001570, 0.001822, and 0.001938 for applied loads of 60 N, 80 N, and 100 N, respectively
4. The Ansys simulation study revealed significant changes in wear rates for the TiN-coated and laser-textured surface-treated samples compared to the reference sample. For the T1 sample, a uniform stress distribution with high-stress concentrations around the edges was observed. In the T2 sample, slight variations in stress distribution resulted from the TiN coating, which introduced residual stress between the substrate and the coating. The T3 sample exhibited altered stress distribution due to the effects of texturing. In the T4 sample, the stress distribution was likely influenced by both the texturing pattern and the residual stresses introduced by the TiN coating. Overall, the stress distribution depends on the interaction between these two factors.
5. Design of Experiments was used to determine the most significant factors affecting the tribological behaviour of TiN-coated titanium alloy. Their analysis found that applied load, sliding speed, material type, the interaction between load and speed, and the combined effects of load and speed have the greatest influence on friction and wear rate. The coefficient of determination (R^2) for the coefficient of friction is 0.9975, while the adjusted R^2 is 0.9939. Similarly, the R^2 for specific wear rates is 0.9985, and the adjusted R^2 is 0.9971. The predicted values indicate a 95% confidence level for both the coefficient of friction and the specific wear rate.
6. According to observations made through EDX analysis, the bonding strength of the coating with the substrate improves with surface texturing. Additionally, the friction coefficient decreases due to the PVD coating, enhancing the wear resistance of the titanium alloy surface under dry sliding contact conditions.

Author Contributions: Writing—original draft preparation, A.M.; Conceptualization, A.M.; writing—review and editing, M.A.W., A.B., N.M. and K.H.P.; Data curation, A.S.; Resources, A.M. and K.H.P.; Formal analysis, A.M., A.S. and N.M.; Investigation, P.A.M. and N.M.; resources, K.H.P.; visualization, N.M.; Validation, P.A.M.; supervision, K.H.P.; funding acquisition, K.H.P. All authors have read and agreed to the published version of the manuscript.

Funding: This research was supported by the development of response technology for response to changes in the carbon-neutral marine environment of the Korea Institute of Marine Science & Technology Promotion (KIMST), funded by the Korea Coast Guard (KIMST-G22002398261). The author expresses their sincere appreciation to the Researchers Supporting Project Number (RSP2025R466) King Saud University, Riyadh, Saudi Arabia.

Data Availability Statement: The original contributions presented in this study are included in the article. Further inquiries can be directed to the corresponding author(s).

Acknowledgments: The authors express their sincere appreciation to the Researchers Supporting Project Number (RSP2025R466) King Saud University, Riyadh, Saudi Arabia. The authors express their gratitude to the Korea Institute of Marine Science & Technology Promotion (KIMST), funded by the Korea Coast Guard (KIMST-G22002398261). The authors express their appreciation to tribology research cell of Sri Venkateswara College of Engineering.

Conflicts of Interest: The authors confirm that there is no conflict of interest in the findings of this study.

References

1. Xiao, J.; Zhang, Y.; Hu, B.; Liu, X.; Liang, Z.; Zhao, Z. Tribological Properties of Ti_6Al_4V Alloy Composite Texture Fabricated by Ultrasonic Strengthening Grinding and Laser Processing. *Materials* **2023**, *16*, 355. [CrossRef]
2. Bertolini, R.; Ghiotti, A.; Bruschi, S. Wear Behavior of Ti_6Al_4V Surfaces Functionalized through Ultrasonic Vibration Turning. *J. Mater. Eng. Perform.* **2021**, *30*, 7597–7608. [CrossRef]
3. Wang, X.; Xu, S.; Zhou, S.; Xu, W.; Leary, M.; Choong, P.; Qian, M.; Brandt, M.; Xie, Y.M. Topological design and additive manufacturing of porous metals for bone scaffolds and orthopaedic implants: A review. *Biomaterials* **2016**, *83*, 127–141. [CrossRef] [PubMed]
4. Abd-Elaziem, W.; Darwish, M.A.; Hamada, A.; Daoush, W.M. Titanium-Based alloys and composites for orthopedic implants Applications: A comprehensive review. *Mater. Des.* **2024**, *241*, 112850. [CrossRef]
5. Kaur, M.; Singh, K. Review on titanium and titanium based alloys as biomaterials for orthopaedic applications. *Mater. Sci. Eng. C* **2019**, *102*, 844–862. [CrossRef] [PubMed]
6. Geetha, M.; Singh, A.K.; Asokamani, R.; Gogia, A.K. Ti based biomaterials, the ultimate choice for orthopaedic implants—A review. *Prog. Mater. Sci.* **2009**, *54*, 397–425. [CrossRef]
7. Marin, E.; Lanzutti, A. Biomedical Applications of Titanium Alloys: A Comprehensive Review. *Materials* **2024**, *17*, 114. [CrossRef]
8. Okazaki, Y.; Gotoh, E. Comparison of metal release from various metallic biomaterials In Vitro. *Biomaterials* **2005**, *26*, 11–21. [CrossRef]
9. Raganya, M.L.; Moshokoa, N.M.; Obadele, B.; A Olubambi, P.; Machaka, R. The microstructural and mechanical characterization of the β-type Ti-11.1Mo-10.8Nb alloy for biomedical applications. In *IOP Conference Series: Materials Science and Engineering*; IOP Publishing: Bristol, UK, 2019; Volume 655, p. 012025. [CrossRef]
10. Kopova, I.; Stráský, J.; Harcuba, P.; Landa, M.; Janeček, M.; Bačákova, L. Newly developed Ti–Nb–Zr–Ta–Si–Fe biomedical beta titanium alloys with increased strength and enhanced biocompatibility. *Mater. Sci. Eng. C* **2016**, *60*, 230–238. [CrossRef] [PubMed]
11. Okazaki, Y. A New Ti–15Zr–4Nb–4Ta alloy for medical applications. *Curr. Opin. Solid State Mater. Sci.* **2001**, *5*, 45–53. [CrossRef]
12. Nikolova, M.P.; Nikolova, V.; Ivanova, V.L.; Valkov, S.; Petrov, P.; Apostolova, M.D. Mechanical properties and in vitro biocompatibility evaluation of TiN/TiO_2 coated Ti_6Al_4V alloy. *Mater. Today Proc.* **2020**, *33*, 1781–1786. [CrossRef]
13. Jakovljević, S.; Alar, V.; Ivanković, A. Electrochemical behaviour of PACVD TiN-coated CoCrMo medical alloy. *Metals* **2017**, *7*, 231. [CrossRef]
14. Kao, W.H.; Su, Y.L.; Hsieh, Y.T. Effects of Duplex Nitriding and TiN Coating Treatment on Wear Resistance, Corrosion Resistance and Biocompatibility of Ti_6Al_4V Alloy. *J. Mater. Eng. Perform.* **2017**, *26*, 3686–3697. [CrossRef]
15. Lin, N.; Li, D.; Zou, J.; Xie, R.; Wang, Z.; Tang, B. Surface texture-based surface treatments on Ti_6Al_4V titanium alloys for tribological and biological applications: A mini review. *Materials* **2018**, *11*, 487. [CrossRef]
16. Etsion, I. State of the art in laser surface texturing. *J. Tribol.* **2005**, *127*, 248–253. [CrossRef]
17. Shivakoti, I.; Kibria, G.; Cep, R.; Pradhan, B.B.; Sharma, A. Laser surface texturing for biomedical applications: A review. *Coatings* **2021**, *11*, 124. [CrossRef]

18. Conradi, M.; Kocijan, A.; Klobčar, D.; Podgornik, B. Tribological response of laser-textured Ti_6Al_4V alloy under dry conditions and lubricated with Hank's solution. *Tribol. Int.* **2021**, *160*, 107049. [CrossRef]
19. Arulkumar, M.; Rangan, R.P.; Ananth, M.P.; Srividhyasakthi, V.; Aaditya, R. Experimental verification on the influence of surface texturing on biomaterials and study of its tribological characteristics. *Mater. Today Proc.* **2023**, in press. [CrossRef]
20. Fang, Y.; Wang, Q.; Yang, Z.; Yang, W.; Wang, L.; Ma, J.; Fu, Y. An efficient approach to endow TiNbTaZr implant with osteogenic differentiation and antibacterial activity in vitro. *Mater. Des.* **2022**, *221*, 110987. [CrossRef]
21. Vijay, R.; Kumar, V.N.A.; Sadiq, A.; Pillai, R.R. Numerical Analysis of Wear Characteristics of Zirconia Coated Aluminum 6061 Alloy. In *IOP Conference Series: Materials Science and Engineering*; IOP Publishing: Bristol, UK, 2021; Volume 1059, p. 012020. [CrossRef]
22. Bahi, R.; Nouveau, C.; Beliardouh, N.; Ramoul, C.; Meddah, S.; Ghelloudj, O. Surface performances of Ti-6Al-4V substrates coated PVD multilayered films in biological environments. *Surf. Coat. Technol.* **2020**, *385*, 125412. [CrossRef]
23. Strel'Nitskij, V.; Vasylyev, V.; Makarov, V.; Lazarenko, H. Diamond-like carbon coatings pin-on-disk wear testing. *Phys. Chem. Solid State* **2023**, *24*, 520–529. [CrossRef]
24. Priyadarshini, B.; Rama, M.; Chetan; Vijayalakshmi, U. Bioactive coating as a surface modification technique for biocompatible metallic implants: A review. *J. Asian Ceram. Soc.* **2019**, *7*, 397–406. [CrossRef]
25. Narayan, J.; Fan, W.; Narayan, R.; Tiwari, P.; Stadelmaier, H. Diamond, diamond-like and titanium nitride biocompatible coatings for human body parts. *Mater. Sci. Eng. B* **1994**, *25*, 5–10. [CrossRef]
26. Kumar, D.; Deepak, K.B.; Muzakkir, S.M.; Wani, M.F.; Lijesh, K.P. Enhancing tribological performance of Ti-6Al-4V by sliding process. *Tribol.-Mater. Surfaces Interfaces* **2018**, *12*, 137–143. [CrossRef]
27. Muniyappan, A.; Muthuvel, P.A. Taguchi Optimisation of Friction and Wear Properties of Ti_6Al_4V Alloy Coated with TiAlN for Orthopaedic Applications. *Trans. Famena* **2024**, *48*, 17–32. [CrossRef]
28. Joshi, B.; Tripathi, K.; Gyawali, G.; Lee, S.W. The effect of laser surface texturing on the tribological performance of different Sialon ceramic phases. *Prog. Nat. Sci.* **2016**, *26*, 415–421. [CrossRef]
29. Danışman, Ş.; Odabaş, D.; Teber, M. The Effect of TiN, TiAlN, TiCN Thin Films Obtained by Reactive Magnetron Sputtering Method on the Wear Behavior of Ti_6Al_4V Alloy: A Comparative Study. *Coatings* **2022**, *12*, 1238. [CrossRef]
30. Chauhan, S.R.; Dass, K. Dry sliding wear behaviour of titanium (Grade 5) alloy by using response surface methodology. *Adv. Tribol.* **2013**, *2013*, 1–9. [CrossRef]
31. Sreesha, R.B.; Chandraker, S.; Kumar, D. Optimization of tribological parameters to enhance wear and friction properties of Ti_6Al_4V alloy using Taguchi method. *Proc. Inst. Mech. Eng. Part J J. Eng. Tribol.* **2022**, *236*, 1761–1781. [CrossRef]
32. Outeiro, J.; Cheng, W.; Chinesta, F.; Ammar, A. Modelling and Optimization of Machining of Ti-6Al-4V Titanium Alloy Using Machine Learning and Design of Experiments Methods. *J. Manuf. Mater. Process.* **2022**, *6*, 58. [CrossRef]
33. Mushtaq, Z.; Hanief, M.; Manroo, S.A. Prediction of Friction and Wear During Ball-On-Flat Sliding Using Multiple Regression and ANN: Modeling and Experimental Validation. *J. Tribol.* **2021**, *28*, 117–128.
34. Kumar, A.; Chhibber, R. Investigation of the Wetting Behavior of Formulated SMAW Electrode Coating Fluxes With Regression and ANN Model. *Met. Mater. Trans. B* **2023**, *54*, 287–302. [CrossRef]
35. Muniyappan, A.; Muthuvel, P.A. Predictive Modelling of Wear and Friction in Surface Textured TiAlN Coated Ti_6Al_4V Alloy Using Artificial Neural Networks. In *High-Performance Sustainable Materials and Structures*; Lazar, P., Palani, I.A., Kumar, M., Eds.; Springer Nature: Cham, Switzerland, 2024; pp. 131–142.
36. Gupta, A.; Mohan, I.; Jude, R.R.; Suryawanshi, A.; Behera, N. Investigation of stress and tribological properties of dental composite materials using FEM. *Proc. Inst. Mech. Eng. Part J J. Eng. Tribol.* **2022**, *237*, 1070–1084. [CrossRef]
37. Manjunatha, T.; Basavaraj, Y.; Ramana, V.V.; Babu, K.A. Experimental and finite element analysis of wear rate of Al7075 reinforced with B4C. *Mater. Today Proc.* **2022**, *54*, 543–547. [CrossRef]
38. Kumar, P.; Kumar, B. Numerical simulation of linear reciprocating wear mechanism of hybrid aluminum metal matrix composite using finite element method. *Model. Simul. Mater. Sci. Eng.* **2023**, *31*, 085013. [CrossRef]
39. Bergmann, G.; Bender, A.; Graichen, F.; Dymke, J.; Rohlmann, A.; Trepczynski, A.; Heller, M.O.; Kutzner, I. Standardized Loads Acting in Knee Implants. *PLoS ONE* **2014**, *9*, e86035. [CrossRef]
40. Portier, K.; Tolson, J.K.; Roberts, S.M. Body weight distributions for risk assessment. *Risk Anal.* **2007**, *27*, 11–26. [CrossRef]
41. Helmert, U.; Strube, H. Die Entwicklung der Adipositas in Deutschland imZeitraum von 1985 bis 2002. *Gesundheitswesen* **2004**, *66*, 409–415. [CrossRef]
42. Liu, R.; Qian, D.; Chen, Y.; Zou, J.; Zheng, S.; Bai, B.; Lin, Z.; Zhang, Y.; Chen, Y. Investigation of normal knees kinematics in walking and running at different speeds using a portable motion analysis system. *Sports Biomech.* **2021**, *23*, 417–430. [CrossRef]

Disclaimer/Publisher's Note: The statements, opinions and data contained in all publications are solely those of the individual author(s) and contributor(s) and not of MDPI and/or the editor(s). MDPI and/or the editor(s) disclaim responsibility for any injury to people or property resulting from any ideas, methods, instructions or products referred to in the content.

processes

MDPI

Review

Applications of Nanomaterial Coatings in Solid-Phase Microextraction (SPME)

Taiwo Musa Adeniji, Naila Haroon and Keith J. Stine *

Department of Chemistry and Biochemistry, University of Missouri-Saint Louis, Saint Louis, MO 63121, USA; tmaqmy@umsl.edu (T.M.A.); nhyym@umsl.edu (N.H.)
* Correspondence: kstine@umsl.edu

Abstract: This review explores the advances in developing adsorbent materials for solid-phase microextraction (SPME), focusing on nanoparticles, nanocomposites, and nanoporous structures. Nanoparticles, including those of metals (e.g., gold, silver), metal oxides (e.g., TiO_2, ZnO), and carbon-based materials (e.g., carbon nanotubes, graphene), offer enhanced surface area, improved extraction efficiency, and increased selectivity compared to traditional coatings. Nanocomposites, such as those combining metal oxides with polymers or carbon-based materials, exhibit synergistic properties, further improving extraction performance. Nanoporous materials, including metal–organic frameworks (MOFs) and ordered mesoporous carbons, provide high surface area and tunable pore structures, enabling selective adsorption of analytes. These advanced materials have been successfully applied to various analytes, including volatile organic compounds (VOCs), polycyclic aromatic hydrocarbons (PAHs), pesticides, and heavy metals, demonstrating improved sensitivity, selectivity, and reproducibility compared to conventional SPME fibers. The incorporation of nanomaterials has significantly expanded the scope and applicability of SPME, enabling the analysis of trace-level analytes in complex matrices. This review highlights the significant potential of nanomaterials in revolutionizing SPME technology, offering new possibilities for sensitive and selective analysis in environmental monitoring, food safety, and other critical applications.

Keywords: nanomaterials; solid-phase microextraction (SPME); porous materials; nanoporous carbons; gas chromatography coupled SPME; SPME fiber coatings; selective adsorption; environmental monitoring; trace analysis

1. Introduction

Microextraction is a sampling technique characterized by the use of a significantly smaller volume of extractant (liquid or solid) relative to the sample volume. Consequently, only a portion of the analyte is extracted, resulting in a non-exhaustive process. SPME is a specific microextraction method that relies on analyte partitioning between a sample matrix and a stationary phase immobilized on a fiber. This equilibrium-based process is governed by Nernst's partition coefficient, with higher values indicating greater analyte extraction efficiency. The selection of the fiber coating is crucial, as it determines the selectivity and capacity for different analytes [1,2].

Invented in the late 1980s, SPME revolutionized sample preparation by offering a solvent-free, single-step approach. SPME eliminates the need for bulky extraction processes, allowing for rapid analysis both in the lab and at the sampling site. This innovative technique utilizes a tiny fiber coated with a specific material to directly extract and concentrate

analytes from the sample. This translates to faster processing times, reduced waste disposal costs, and potentially improved detection limits [3–5].

SPME is a solventless sample preparation method that relies on achieving equilibrium between the sample and a coated fiber, and involves these steps:

1. Extraction: A fused silica fiber with a specific coating (polymer or sorbent) is exposed to the sample matrix. Target analytes partition from the sample into the coating based on their affinities for each. This selectively concentrates the analytes on the fiber. Extraction can be achieved through direct immersion (DI) or headspace (HS) sampling [6].
2. Desorption: The fiber, loaded with concentrated analytes, is then transferred to an instrument like a gas chromatograph (GC) or high-performance liquid chromatograph (HPLC). Inside the instrument's injector, the analytes are desorbed from the coating and introduced into the analytical system for separation and quantification [7]. Desorption is primarily accomplished by exposing fibers to high temperatures in the GC injector, although solvent immersion can also be used [6].

With two opposing effects, the extraction temperature in SPME has a complicated role. On the one hand, analytes' diffusion coefficient increases with increasing temperature, encouraging their migration towards the extraction phase. In contrast, high temperatures decrease the analytes' distribution constant, which lessens their retention on the fiber because adsorption is an exothermic process. Pawliszyn developed a unique mechanism that cools the fiber and heats the sample at the same time in order to address this difficulty. This dual-action configuration optimizes both the diffusion and adsorption processes, increasing the mass transfer of analytes from the sample to the fiber coating and increasing extraction efficiency [8].

The type of coating applied to the SPME fiber is critical to its extraction and desorption effectiveness because it influences the distribution coefficient of analytes between the stationary and bulk phases. It serves to distinguish analytes from other substances. Various coatings have been created to improve the extraction of a wide spectrum of analytes. For SPME procedures to be effective under different conditions, a robust sorbent must be properly selected. Surface active groups, molecule size, and polarity all affect the selectivity of coating materials [9,10].

In the traditional in-fiber mode of SPME, a sorptive phase immobilized on an inert support is used to extract analytes directly from the sample or its headspace. Polymeric coatings' exceptional chemical and thermal durability makes them popular sorptive phases. For a wide variety of target analytes, their polarity can be adjusted by mixing various materials, resulting in the best extraction performance. Metal–organic frameworks (MOFs), carbon fiber, graphene, polypropionates, polydimethylsiloxane (PDMS), polyacrylate (PA), Carbowax, polydimethylsiloxane–divinylbenzene (PDMS–DVB), and carboxen–polydimethylsiloxane (CAR-PDMS) are examples of common coatings. Despite their widespread use, polymer coatings have significant drawbacks, including low heat resistance, swelling when organic solvents are present, and limited extraction efficiency. To tackle these problems, scientists have looked into nanomaterials, which have benefits like a large surface area, mechanical strength, and special chemical and physical characteristics. Materials including nanofibers, nanoparticles, and nanotubes have greatly improved SPME fiber extraction efficiency and capacity. They successfully surpass the restrictions placed by the small diameter of conventional fibers thanks to their large surface area and large number of active adsorption sites. The continuous creation of new coatings, such as molecularly imprinted polymers, polymeric ionic liquids, and other nanomaterials, is still a key area of SPME research. By strengthening the technique's selectivity, sensitivity, and

adaptability, these developments hope to make it possible to use it in more challenging analytical situations [10–15].

Nanotechnology enables the design of materials with exceptional properties [16]. Nanomaterials with remarkable chemical and physical attributes are gaining significant attention in the field of separation science. Nanomaterials are now being used in extraction procedures because they have tiny pores and high surface areas that make them more efficient at extracting substances. These materials are also used as SPME coatings because they can withstand high temperatures. Future reviews on SPME coatings and nanomaterials in analytical sample preparation should focus on the use of nanomaterials for SPME coatings [17,18].

In order to obtain the necessary results, an analytical procedure usually consists of several steps, such as sample preparation (including sampling), chromatographic methods (LC or GC), capillary electrophoresis, detection, and data processing. SPME has become a useful technique for sample preparation because of its ease of use, effectiveness, and capacity to combine extraction and preconcentration in a single step. The enhancement of SPME and other sample preparation methods is greatly aided by nanoparticles. Their physical characteristics and chemical characteristics, like sorption capacities, are frequently advantageous. In order to simplify procedures and make it possible to analyze very small sample volumes, nanoparticles—or chemically modified variants—are utilized for sample cleanup and analyte preconcentration. This development is especially helpful for performing studies with small sample amounts or for investigating novel sample matrices where the sample amount is minimal [19].

The objective of this review is to evaluate the performance of various nanomaterials used in SPME fibers, with a particular emphasis on sensitivity, selectivity, durability, and suitability for detecting specific analytes. The assessment seeks to determine which materials and production techniques have exhibited the best overall performance across a variety of applications.

In this review, we focus on the different applications of nanomaterials as coatings on SPME fibers. We also review the different types of nanomaterials that could be used as coatings, for example, metal oxide nanoparticles, carbon nanoparticles, metal nanoparticles, and others. We conclude the review by looking at the performances of the different types of nanomaterials as SPME coatings.

2. The SPME Device

2.1. The SPME Design

The SPME device resembles a syringe with a small, cylindrical fused silica fiber attached to stainless steel tubing for added durability, as seen in Figure 1. The fiber is traditionally coated with a thin layer of various polymeric stationary phases, enabling it to effectively adsorb analytes from different sample matrices. The coated fiber is inserted into a needle, which is part of the syringe-like structure [20–22]. The SPME device can be replaced and reused. The fiber is easier to put into samples or headspace for analyte extraction because of its compact form and cylindrical structure. Furthermore, without requiring adjustments to the equipment, it may be easily positioned in the interface of a high-performance liquid chromatograph (HPLC) or the desorption chamber of a gas chromatograph (GC). For reliable results during adsorption and desorption, precise control over plunger movement and timing is crucial. Analyte loss can be caused by improper handling, especially during field sampling. Analyte escape can be minimized by cooling the needle opening or sealing it with a septum [23].

2.2. Working Operation of the SPME

In SPME, as seen in Figure 2 (working principle), the fiber is initially retracted into the syringe needle and inserted into a sealed vial with a septum cap. The choice of fused silica fiber depends on the analyte being studied. Prior to analysis, the fiber must be cleaned with solvent to remove any contaminants that could affect the chromatogram. SPME extraction is commonly performed in two ways: (1) headspace SPME (HS-SPME), where the fiber is exposed to the vapor phase above the sample, and (2) direct-immersion SPME (DI-SPME), where the fiber is immersed in liquid. Analytes are typically desorbed from the fiber via thermal desorption in a gas chromatograph, eliminating the need for organic solvents. For liquid chromatography (LC), desorption can be performed using polar organic solvents like methanol or acetonitrile, which allows for increased sensitivity. Depending on how strongly the analytes are adsorbed, desorption can be dynamic (with a moving mobile phase) or static (with the fiber immersed in solvent for a set time).

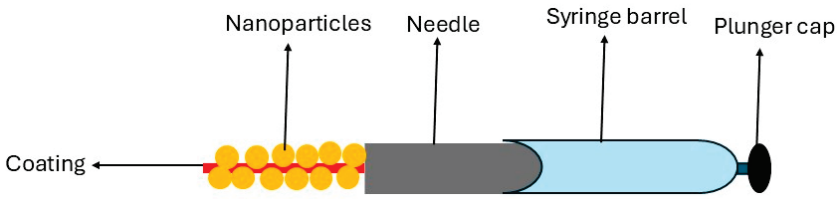


Figure 1. The SPME device.

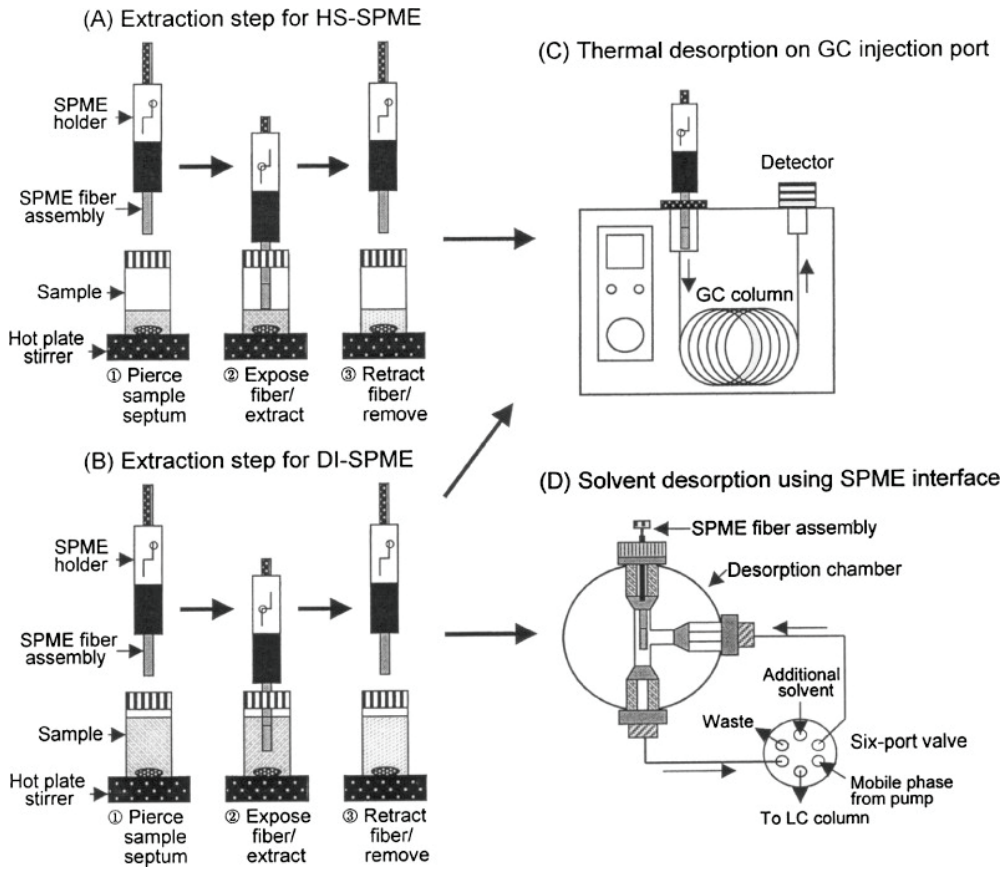


Figure 2. (**A**,**B**) Working principle of SPME using different extraction techniques. (**C**,**D**) Desorption of analytes from SPME fiber injected into the GC injection port. Reprinted with permission from [24]. Copyright 2004, Wiley.

3. Range of Compounds to Which SPME Has Been Applied

SPME has been applied to the analysis of different compounds including volatile organic compounds (VOCs), food components, environmental analytes, flavors, and so on. In this section, we will look at the range of compounds to which SPME analysis has been applied.

3.1. Volatile Organic Compounds (VOCs)

The non-invasive nature of volatile organic compound (VOC) analysis and its comparatively inexpensive sample and analysis costs make it a viable method for identifying putative cancer biomarkers and other applications. Since its introduction by Pawliszyn in 1989, SPME has gained popularity as a method for extracting volatile organic compounds (VOCs) from both in vitro and in vivo samples. Because of its ease of use, lack of solvents, automation potential, and compatibility with both liquid and gas chromatography, SPME is widely used in many different industries [25].

Lim et al.'s study identified twelve compounds that distinguish rice from Korea and China by analyzing white rice from the two nations using DVB/CAR/PDMS-SPME with GC-MS. More research is needed on 10 new hydrocarbon determinants, while hexanal and 1-hexanol levels were related to storage and environmental conditions. They came to the conclusion that additional food products could benefit from this technique, which can differentiate white rice based on its origin [26].

A study by Poli et al. evaluated the potential of aldehydes, which are biomarkers of oxidative stress, as non-small-cell lung cancer (NSCLC) diagnostic tools. Linear aldehydes (C3–C9) in exhaled breath were quantified by the researchers using a solid-phase microextraction (SPME) technology with GC/MS analysis. With detection and quantification limits of 1×10^{-12} M and 3×10^{-12} M, respectively, the approach showed excellent linearity over a range of 3.3–333.3 $\times 10^{-12}$ M. Precision (as a percentage RSD) was between 7.2 and 15.1%, while accuracy was above 93%. At +4 °C, aldehyde stability in a Bio-VOC® tube lasted 10–17 h, but with certain fiber storage, it lasted for more than 10 days. In a clinical study, breath samples from 40 NSCLC patients and 38 asymptomatic non-smokers revealed significantly higher aldehyde levels in the NSCLC group, with age and smoking having no effect. A 90% discrimination power based on aldehyde patterns was verified by multivariate analysis, indicating that these chemicals may improve the sensitivity and specificity of VOC-based diagnostics for non-small-cell lung cancer. The study emphasizes aldehydes' potential as trustworthy biomarkers for the early diagnosis of lung cancer [27].

To identify and measure volatile organic chemicals (VOCs) in human breath as possible lung cancer biomarkers, Rudnicka et al. conducted a study. Using gas chromatography–time-of-flight mass spectrometry (GC–TOF/MS) for analysis and SPME for preconcentration, the method produced quick and sensitive detection at parts-per-billion (ppb) levels. Linearity between 0.83 and 234.05 ppb, detection limits between 0.31 and 0.75 ppb, and precision with relative standard deviations (RSDs) below 10% were all displayed by the accuracy-optimized approach. Using sophisticated statistical techniques, the study found important volatile organic compounds (VOCs) linked to lung cancer, indicating that this non-invasive technique is a promising early screening tool [28].

In order to collect volatile organic compounds (VOCs) from biological materials such as blood, breath, buccal swabs, and urine, Kusano et al. devised and refined a headspace SPME approach employing forensic and clinical kits. Using this method, different samples from the same person might be directly compared. VOCs could be detected with great sensitivity using their optimized SPME-GC/MS approach; urine had the highest detection limits while breath samples had the lowest [29].

3.2. Food

Evaluating nutritional value, guaranteeing freshness, processed products' quality control, and detecting dangerous pollutants and food additives all depend heavily on food analysis [30]. Analysis is difficult since dietary components constitute a complex matrix. Since analytes are frequently present in trace levels, an optimal approach should combine isolation, preconcentration, and precise quantification [23]. With its expanding applications, SPME is becoming more and more significant in food sample pretreatment. Solid-phase extraction (SPE), Continuous-Steam Distillation Extraction (SDE), headspace (HS), Nitrogen Purge and Trap (NPT), and Supercritical Fluid Extraction (SFE) are some of the conventional extraction techniques over which SPME provides a number of clear advantages [31].

Barboni et al. identified 44 chemicals in a study that used HS-SPME/GC and/or GC/MS to analyze 67 juices from mandarin, clementine, and hybrids. According to their findings, mandarin juice had higher levels of γ-terpinene (21.1%) and lower levels of limonene (66.3%) than clementine juice, which was highest in limonene (90.0%) and lowest in γ-terpinene (1.2%). The limonene/γ-terpinene ratios of hybrid juices varied, but their profiles were similar. According to their findings, 7% of hybrids displayed abnormal profiles because of para-cymene or terpinen-4-ol, 48% resembled clementine, and 45% were more like mandarin [32].

Using cutting-edge methods (HS-SPME and GC-O (gas chromatography–olfactometry)), Mounchili et al. investigated the effects of giving fresh silage to nursing cows prior to milking. They discovered that using butane-2-one and dimethyl sulfide levels as markers may result in milk having an unpleasant flavor. While Mounchili et al. encouraged more research using absolute VOC concentrations, they also stated that these data might support a diagnostic tool as an alternative to sensory testing. They determined that rather than specific molecules, off-flavors are caused by changes in concentrations of common aromatic compounds (AACs), and they recommended more research to measure these AACs and look into the effects of bacteria on milk volatiles [33].

3.3. Environmental Analysis

There is a great deal of research showing detrimental impacts of environmental organic pollutants on both humans and animals, making human exposure to them a serious concern. Understanding the bioaccumulation and toxicity of these contaminants in environmental toxicology and clinical studies requires the monitoring of these pollutants and endogenous metabolites in organisms [34].

SPME is a well-established, green process for extracting and preconcentrating analytes across a wide range of matrices. Since its inception in the early 1990s, SPME has swiftly progressed in terms of coating materials, geometries, and uses. SPME was originally developed for environmental investigations, but it has now become a major method for analyzing volatile and semi-volatile organic compounds (VOCs and SVOCs). SPME's versatility, particularly in its headspace version (HS-SPME), has made it widely used for pollutants with diverse physicochemical features, including medicines, insecticides, and metal–organic compounds. This adaptability addresses issues in traditional sample preparation, indicating a significant impact on future analytical procedures [35,36].

In their work on the procedure for the control of butyl and phenyl tin pollution in the environment by GC-FPD, Aguerre et al. found that $NaBEt_4$ ethylation–SPME extraction–GC-FPD (gas chromatography–flame photometric detection), supplemented with acidic extraction for solid matrices, is a promising method for identifying organotin chemicals in water and complicated environmental samples. They discovered that mechanical stirring greatly enhanced analytical performance during adsorption, with detection

limits that are 10–700 times lower than classical liquid–liquid extraction and 2–20 times lower than SPME with magnetic stirring. Their optimized SPME approach produces results comparable to isooctane extraction and detects organotins at concentrations lower than 1 ng/L as Sn in aqueous samples. While co-extracted organic matter in complex matrices can influence triphenyl tin (TPhT) responses, recent research on adsorption–desorption behavior suggests that this approach is a useful tool for routine organotin detection in water [37].

Table 1 contains information about the different types of compounds that have been detected by SPME, the types of nanoparticles used in SPME fiber coating, and their analytical applications.

Table 1. Classes of compounds analyzed using solid-phase microextraction based on nanomaterial coatings.

Type of Compound	Examples	SPME Coating Materials	Applications	Reference
Volatile Organic Compounds (VOCs)	Benzene, Toluene, Ethylbenzene, Xylenes (BTEX)	Carbon-ZrO_2 Nanocomposites, PDMS, MOFs	Environmental monitoring, water analysis	[38]
Polycyclic Aromatic Hydrocarbons (PAHs)	Naphthalene, Anthracene, Pyrene	Mesoporous Carbon, Carbon Nanotubes (CNTs)	Food safety, environmental analysis	[39]
Pesticides	Organochlorines, Organophosphates	3D graphene–Iron Oxide Nanocomposite (3D-G-Fe_3O_4)	Food and water analysis	[40]
Nicotine and Metabolites	Nicotine, Cotinine, Nornicotine	Nitrogen-rich Porous Polymers	Neuroscience research, pharmacokinetics	[41]

4. Advances in the Adsorbent Type Used in the Extraction Phase of the SPME Fiber

The most common SPME setup consists of a fused silica rod with a thin polymeric coating, but this configuration has several limitations, including low operating temperatures, instability in organic solvents, limited mechanical durability, and difficulty extracting polar compounds from aqueous solutions. These difficulties have prompted ongoing advances in SPME geometries, setups, and extraction phases, with recent efforts focusing on trace analysis and challenging applications. SPME research focuses on the development of new sorbents and fiber coatings to improve selectivity, sorptive capacity, and thermal, chemical, and mechanical stability. This work intends to improve device lifetime and sensitivity by refining the enrichment process and expanding SPME's applicability, particularly in complicated matrices for a variety of analytical applications [42–44]. Figure 3 is a description of the advances in materials chemistry to fabricate different materials for use in SPME [45]. In this section, we further discuss the different types of sorbent materials that can be used to increase extraction efficiency in SPME operations, including nanoparticles, silicon-containing nanostructures, nanocomposites, and others.

4.1. SPME Based on Nanoparticles

Nanoparticles are generally defined as being in the range of about 1–100 nanometers in diameter. Compared to bulk materials, their physical and chemical properties are different because they contain fewer atoms, with a larger percentage at or close to the surface. Definitions of nanoparticle size can differ, but when a property differs sufficiently (by a few percent) from the bulk material, a practical upper limit is attained [46].

Researchers frequently use nanoparticles to clean and recover target analytes from intricate sample matrices. Their large surface area and strong affinity for particular analytes make them excellent sorbents that greatly improve the sensitivity and selectivity of analytical procedures. Furthermore, nanoparticles are prized for their remarkable adsorption characteristics, high preconcentration factors, reusability, and simplicity of surface modifications. These characteristics help improve the sample preparation procedure [47].

Nanoparticles (NPs) are effective as adsorbents in various separation and preconcentration procedures, such as SPE, SPME, and μ-solid-phase extraction (μSPE), making them crucial for environmental pollutant analysis. They are also used in chromatographic procedures such as GC and HPLC in which NP-coated columns act as stationary phases. NPs are preferred for extraction methods due to their large surface area and porosity, which improves extraction efficiency and greater extraction rates. Their superior mechanical, chemical, and thermal stabilities make them ideal for SPME coatings. Ongoing research focuses on producing cost-effective extractive materials that improve selectivity and capacity while reducing sample and solvent usage. Furthermore, these materials are sought out for adequate stability to allow reproducibility and reuse [48–50]. Recent reviews have focused on several types of nanoparticles and their applications in microextraction; we will also be focusing on the different types of nanoparticles used in SPME subsequently.

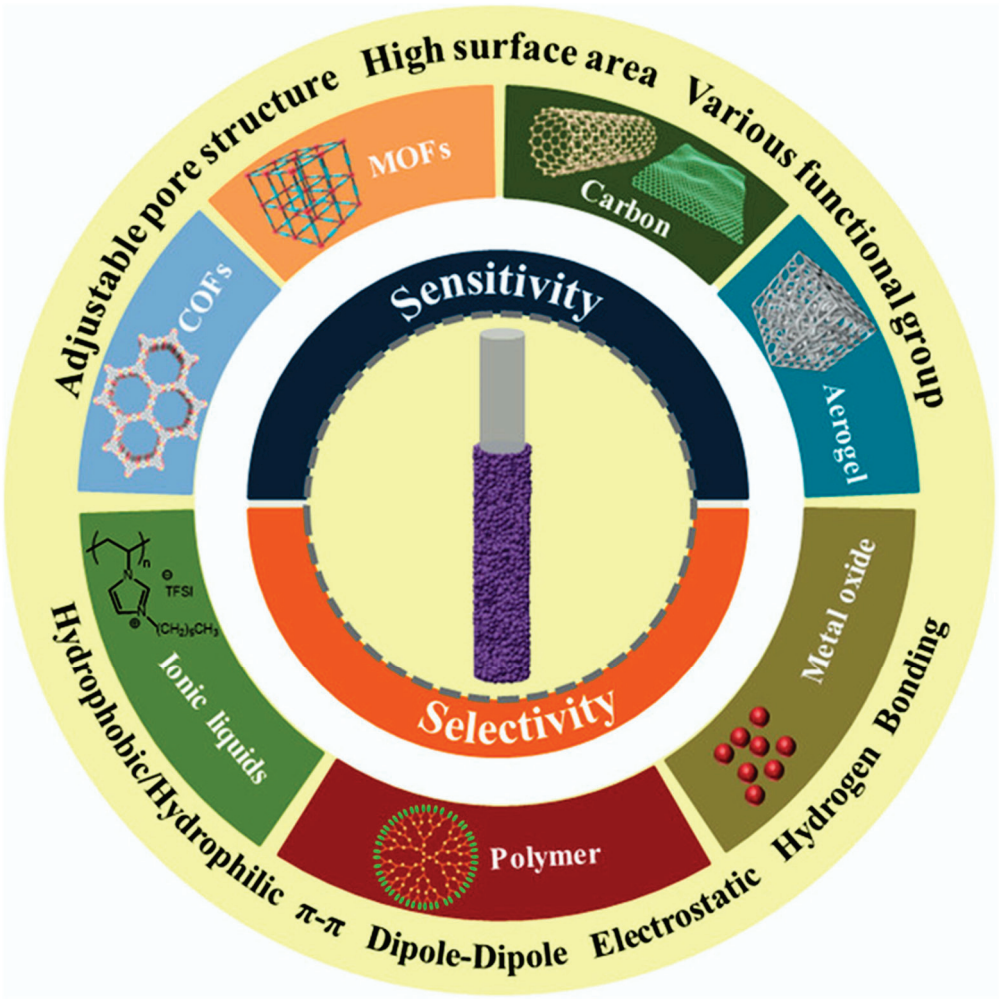


Figure 3. Advances in materials chemistry for the fabrication of different materials for use in SPME fibers. Printed with permission from [45]. Copyright 2022, John Wiley and Sons.

4.1.1. Metal Nanoparticles in SPME

Metallic nanoparticles, particularly those containing metals such as silver and gold, have unique visual, physical, chemical, and biological properties that make them useful in a variety of applications. Their high affinity for both inorganic and organic mercury species enables them to be used efficiently in mercury extraction methods. These nanoparticles can also help separate heavy metals, organic chemicals (including pyrene, olefins, and methylene blue), and gaseous species (like NO and SO_2) [51]. Metal nanoparticles (MNPs)

are crucial for the effective and selective extraction of analytes from various matrices. The application of metal nanoparticles in SPME has focused significantly on gold nanoparticles, due to the special properties they possess as an adsorbent material.

Gold Nanoparticles as Sorbent Material in SPME

Gold nanoparticles (AuNPs) are particularly notable due to their strong affinity for binding organic compounds with thiol groups and their effectiveness with other functional groups. AuNPs can spontaneously adsorb biomolecules containing thiol (SH) or amino (NH_2) groups, resulting in the formation of self-assembled monolayers. Despite their extensive surface area for interactions with analytes and column surfaces, research on AuNPs within separation science is limited. Their high surface-to-volume ratio, long-term stability, ease of synthesis, and favorable chemical modification properties make AuNPs promising candidates for diverse applications [48,52].

In a work by Wen et al., gold nanoparticles (AuNPs) were in situ coated on ordered mesoporous carbon (OMC) to generate an SPME covering with better extraction capacity and aniline selectivity. The researchers discovered that this composite significantly improved extraction efficiency, with enrichment factors for anilines ranging from 1143 to 3420, while such factors for alcohols and phenols ranged from 45 to 845 and 86 to 545, respectively, indicating notable aniline selectivity due to strong interactions between gold and amino groups. The approach quantified four anilines using gas chromatography and flame ionization detection, with limits of detection ranging from 0.072 to 0.18 μg/L and good precision (1.9% to 3.8% RSD). The technique was successfully applied to river and drinking water samples, with recoveries ranging from 83.9% to 107.7% for river samples and 94.0% to 113.1% for drinking water. The authors concluded that the AuNP/OMC composite fiber outperformed individual AuNPs, OMC, and commercial coatings in terms of extraction efficiency, emphasizing its potential for preconcentrating trace anilines in environmental samples and its strong affinity for thiol-containing compounds due to gold interactions [53].

In another study, Yang et al. developed a poly(3,4-ethylenedioxythiophene)@Au nanoparticle (PEDOT@AuNP) coating for SPME using a self-assembled monomer on AuNPs that was electropolymerized on stainless steel. They described the coating as having a cauliflower-like microstructure with exceptional heat stability (up to 330 °C) and durability, able to withstand over 160 extractions without losing performance. Because of its hydrophobic interactions with PEDOT and affinity for AuNPs, the coating has a high extraction capacity for polycyclic aromatic hydrocarbons (PAHs). The researchers used gas chromatography (GC) to obtain low detection limits (2.5–25 ng/L) and high repeatability, with recovery rates ranging from 89.9% to 112% in a variety of environmental water samples. Yang et al. found that the PEDOT@AuNP coating is an effective, long-lasting solution for PAH analysis in environmental settings [54].

An SPME coating based on gold nanoparticles was designed by Guitierrez et al. to detect organochlorine pesticides in ambient water samples. They explained that a layer-by-layer assembly method was used to apply the nanoparticles to SPME fibers, producing consistent coatings that were roughly 3 μm thick. Gallic acid or H_2O_2 was used as a reducing agent in the synthesis of the nanoparticles. Despite the thinner coating, the researchers observed that these fibers had detection limits as low as 0.13 μg/L and partition coefficients twice as high as those of commercial polyacrylate fibers. They also noted that after more than 100 extractions, the fibers showed good durability and repeatability, with relative standard deviation values ranging from 8.67% to 21.3% [55].

In conclusion, gold nanoparticles (AuNPs) are extremely versatile substances with proven physical and chemical characteristics that are available using established synthesis

techniques. Because of their readily adjustable surface chemistry, they are very appealing for incorporation into a range of applications. AuNPs are now a popular option in academic research and an essential part of many industrial and point-of-care medical devices because of their qualities. They are perfect candidates for improving fiber coatings in the context of SPME because of their high stability and adjustable surface characteristics, which will improve analyte adsorption and increase the technique's application in a variety of analytical problems [52].

Silver Nanoparticles as Sorbent Material in SPME

It is well known that silver ions can chemically combine with double-bonded molecules to produce strong interactions. In this interaction, electrons from the compound's π orbital are donated to the silver ion's empty s orbital, forming σ-bonds, and electrons from the silver ion's d orbital are formed from the compound's π* antibonding orbital. These chemical bonds are reversible, breakable at high temperatures, and stronger than van der Waals forces [56]. Silver chemistry has been studied in the creation of assisted transport membranes and stationary phases in chromatography (such as argentation chromatography), which are used to separate olefin/paraffin combinations [57,58].

Despite being more affordable than gold nanoparticles (AuNPs), there has been less research on the application of silver nanoparticles (AgNPs) as SPME coatings. Graphene oxide and polymers are combined as hybrid composites for the majority of AgNP applications, while the other components mostly drive extraction [59]. For SPME, other silver-based structures have also been investigated. These consist of electrodeposited silver dendrites, silver nanoplates or dendrites on copper wire supports, silver wires functionalized by sol–gel processes or conditioned by etching, and silver mirror coatings on stainless steel. To improve performance, these structures frequently need extra changes such as the use of polymer sheets [60–65].

Silver nanoparticles (AgNPs) made with glucose or gallic acid as reducing agents were used to develop a unique SPME coating, according to Gutiérrez-Serpa et al. They stated that a layer-by-layer technique was used to deposit the AgNPs onto stainless steel wires that had already been coated with a silver mirror, allowing for exact control over coating thickness. In close agreement with theoretical estimations, they observed that the coatings measured 3.2 μm thick for fibers prepared with gallic acid and 3.5 μm thick for fibers prepared with glucose. These fibers were used for the direct-immersion SPME-GC-FID analysis of sixteen polycyclic aromatic hydrocarbons (PAHs) in water, according to the scientists. They stressed that the AgNP fibers, especially those made with gallic acid, achieved remarkable analytical performance, including detection limits as low as 0.6 ng·mL^{-1}, RSDs below 26%, and durability for roughly 150 extraction/desorption cycles, despite the thinner coatings when compared to standard PDMS fibers. After testing the technique on environmental water samples that had been tampered with, they came to the conclusion that it worked well [59].

When compared to common macroscale materials like alumina, silver nanoparticles (Ag NPs) have garnered interest as sorbents in SPME because of their improved intrinsic features, such as greater chemical activity and ultrafine grain size. These nanoparticles can be chemically modified with particular reagents to create highly selective coatings for SPME fibers, which will enable the more effective and specific preconcentration and extraction of metal ions [52].

4.1.2. Metal Oxide Nanoparticles in SPME

Metal oxide nanoparticles (MONPs) are important in physics, chemistry, and materials research because of their various structural shapes and electrical characteristics, ranging

from being insulators to being conductors. MONPs such as iron oxide, aluminum oxide, titanium oxide, and others are gaining popularity as efficient and cost-effective sorbents. Their nanoscale size results in a vast surface area and strong reactivity, making them excellent for removing heavy metals and dyes from aquatic environments. Furthermore, their functional properties—which are influenced by factors including crystal structure, composition, and morphology—support a variety of pollution control applications, especially as ecologically friendly adsorbents in wastewater treatment [66–72]. Metal oxides are becoming more and more popular in chemical sensors and extraction materials, particularly for SPME, because of their excellent stability, adsorption capacity, and affordability. Environmental applications can benefit from the high surface-to-volume ratio and superior thermal stability of metal oxides such as cobalt oxide, titanium dioxide, lead oxide, zirconium oxide, and zinc oxide. Their special qualities, which change depending on their structure and content, make them very efficient sorbents.

TiO_2, Fe_3O_4, MnO_2, ZnO, and CuO are examples of metal oxide nanoparticles (MONPs) that are frequently employed in wastewater treatment to eliminate heavy metals and dyes. Their expanding relevance in pollution management and green chemistry solutions is highlighted by their usefulness for environmental remediation due to their photocatalysis, adsorption, and antibacterial action properties [45,66,73,74]. Subsequently, we will review some of these MONPs in detail.

Titanium Oxide Nanoparticles as Sorbents for SPME

The natural form of titanium, titanium dioxide (TiO_2), comes in three main crystal forms: brookite (which has a rhombohedral structure), metastable anatase (both of which have tetragonal structures), and stable rutile. The electrical structure, crystal form, size, shape, and any doping present influence the distinctive physicochemical characteristics of TiO_2 crystals [75]. It has been reported that TiO_2 nanotubes (TDNTs) possess notable qualities such as inertness, chemical and thermal stability, non-toxicity, low cost, durability, and corrosion resistance, making them highly suitable for various applications. These include environmental purification, photocatalysis, self-cleaning coatings, hydrogen generation and storage, gas sensing, biomedical uses, and electrode materials for solar cells. The structure of TDNTs is typically hydrogen titanate, with TiO_2 sheets rolled and separated by H+ ions, giving them a multi-walled, scroll-like appearance with large internal and external surfaces. These features make TDNTs ideal for use as sorbents. TiO_2, in various forms like nanowires, nanoparticles, and nanotubes, is a versatile and cost-effective material with significant potential in photocatalysis, electronics, and electrochemical systems, especially in analytical chemistry due to its high surface area and adsorption capabilities [14,76].

Anodized TiO_2 nanotube fibers were used by Shu et al. for in-headspace SPME in conjunction with gas chromatography–mass spectrometry (GC–MS) to identify volatile organic chemicals like xylenes (BTEX), benzene, toluene, and ethylbenzene. The research examined how the anodizing duration and annealing temperature affected the formation of TiO_2 nanotubes while maximizing the conditions for adsorption (time, ionic strength, and temperature) and desorption (time and temperature) for BTEX measurement. The technique showed linearity between 0.5 and 15,000 μg/L (R2 > 0.9954) and obtained detection limits for individual BTEX chemicals between 0.1 and 2.0 μg/L. The strategy demonstrated the potential of TiO_2 nanotube fibers as an efficient method for BTEX analysis by producing recoveries ranging from 92% to 97% when applied to actual samples [77].

Li et al. anodized titanium wire in ethylene glycol using NH_4F to create TiO_2-nanosheet-coated fibers for SPME. After extracting polycyclic aromatic hydrocarbons, phthalates, and UV filters using TiO_2 nanosheets that were roughly 1 μm long, 300 nm wide, and 80 nm thick, HPLC-UV detection was performed. With detection limits of

0.026–0.089 μg/L and calibration ranges of 0.1–400 μg/L, the fibers demonstrated excellent extraction efficiency and selectivity. With recoveries ranging from 88.8% to 107%, the technique reliably identified UV filters in environmental water samples and showed strong repetition (4.50–8.76%) and reproducibility (7.75–9.64%). The fibers were repeatable, robust, and stable [78].

Iron Oxide Nanoparticles as Sorbents for SPME

The emergence of nanotechnology has revolutionized science by making it possible to create materials at the nanoscale (1–100 nm), which have special qualities because of their small size and high surface area-to-volume ratio. Iron oxide nanoparticles (IONPs) stand out among them due to their remarkable superparamagnetism, especially when they are between 2 and 20 nm in size. In the absence of an external magnetic field, this behavior, which is characterized by random variations in magnetization direction influenced by temperature and time (sometimes referred to as the Néel relaxation time), precludes net bulk magnetization. They are more magnetically susceptible than paramagnets, nevertheless, when exposed to a magnetic field. When designing and synthesizing IONPs for use, their magnetic behavior is crucial, especially in separation technologies where significant magnetization is necessary. Because of their easy surface modification, low cost of synthesis, and nanoscale property manipulation capabilities, iron oxide nanoparticles are widely used in various domains. They are also appropriate for biological applications due to their low toxicity, chemical inertness, and biocompatibility. Also, they are useful tools for environmental cleanup because of their enormous surface area, adaptability, and compatibility with adsorption technologies [79–82].

Iron oxide nanoparticles can take several forms, such as wüstite (FeO), ferrihydrite, goethite, magnetite (Fe_3O_4), maghemite (γ-Fe_2O_3), and hematite (α-Fe_2O_3), depending on their stoichiometry and oxidation state. Magnetite (Fe_3O_4) and maghemite (γ-Fe_2O_3) have been extensively investigated for their distinct crystalline phases. Superparamagnetic iron oxide nanoparticles (SPIONs), particularly Fe_3O_4, are widely used in a variety of applications due to their ability to exhibit superparamagnetic properties when smaller than 20 nm [83]. Iron oxide nanoparticles and magnetite (FeO_4) are common magnetic materials used in water treatment because they provide a low-maintenance substitute for conventional adsorbents. FeO_4 nanoparticles are excellent nano-adsorbents for purifying wastewater, especially when functionalized, which improves their catalytic and adsorption capabilities. These nanoparticles are well known for their excellent adsorption capacity, stability, and reusability and can be readily recovered using an external magnetic field [84–87].

Ghiasvand et al. developed a new SPME fiber by embedding FeO_4/SiO_2 core–shell silica nanoparticles in polypyrrole (PPy) on stainless steel wire. Using direct-immersion (DI-) and headspace (HS)-SPME, this fiber was utilized to extract hexanal and heptanal from urine samples. GC-FID quantification was then performed. SEM and FT-IR were used to characterize the fiber, and important extraction parameters were refined. With detection limits of 0.1 and 0.5 ng/mL for hexanal and heptanal using HS-SPME-GC-FID and 0.1 and 1.0 ng/mL for DI-SPME-GC-FID, the calibration curves demonstrated good linearity (R2 > 0.99). The DI-SPME and HS-SPME replication studies had relative standard deviations of 6.5–6.6% and 5.1–5.3%, respectively. Urine samples without derivatization were successfully treated with both techniques; however, HS-SPME-GC-FID demonstrated better analytical performance and a longer fiber lifetime [88].

For the purpose of magnetic solid-phase extraction (MSPE) of organophosphorus pesticides (OPPs) from juice samples, Sereshti et al. fabricated a magnetic 3D graphene-iron oxide nanocomposite (3D-G-Fe_3O_4). This was followed by gas chromatography–nitrogen

phosphorus detection (GC-NPD). Characterization of the 3D-G-FeO_4 was performed with SEM, FT-IR, and VSM. After optimizing key extraction parameters, low detection limits (1.2–5.1 ng/L) and excellent linearity (R2 = 0.9973–0.9999) were obtained. The technique demonstrated good repeatability, with fruit juice OPP recovery rates ranging from 86.6% to 107.5%. GC-MS validation confirmed the findings, showing that the nanocomposite's 3D structure and magnetic characteristics gave it an exceptional extraction capability [40].

Manganese Oxide Nanoparticles as Sorbents for SPME

Manganese oxide, or MnO, is a common mineral that can be found in a variety of natural settings, including soil, silt, and aquifers. It frequently occurs as discrete particles, gels, or mixtures with other minerals like iron. MnO's special qualities allow it to potentially affect how pollutants behave in the environment through adsorption, photodegradation, and catalytic oxidation [89–91]. Manganese dioxide nanoparticles (MnO_2 NPs) have a vast surface area, strong oxidizing and adsorptive properties, and durability even in acidic environments. MnO_2 NPs are well known for their ability to effectively remove organic contaminants and heavy metals from water. They can be effectively separated using an external magnetic field because they are frequently boosted by magnetic compounds. These nanoparticles' chemical and physical interactions with polymers make them popular for removing dyes, and their supermagnetic characteristics make the separation process easier at ambient temperature. Through adsorption, ion exchange, and coprecipitation, MnO_2 also efficiently eliminates heavy metal ions [92,93].

Eskandarpour and Sereshti's study involved the electrospinning of manganese oxide (MnO) nanoparticles into a nanofibrous polycaprolactam (polyamide 6, PA6) coating. This coating was used as a novel fiber coating for the HS-SPME of specific phthalate esters (PEs) in water samples before GC-μECD analysis. Thermogravimetric analysis (TGA), Fourier transform infrared (FT-IR) spectroscopy, and SEM were used to characterize the coating. Important factors that affect the effectiveness of HS-SPME were optimized, such as extraction temperature, ionic strength, and extraction/desorption periods. The technique demonstrated a linear dynamic range of 0.500–500 ng/mL, limits of detection ranging from 0.0400 to 0.193 ng/mL, and relative standard deviations between 1.86% and 10.9% under these circumstances. The technique obtained relative recoveries of 90.3% to 107% when used on actual water samples, such as soda, river water, bottled water, and mineral water, proving its efficacy in identifying phthalate esters in a range of aqueous matrices [94].

Eskandarpour and Sereshti once more investigated the extraction and identification of carcinogenic nitrophenols (NPs), whereby contamination of soil and water poses serious health dangers. Using electrospinning, they created polyurethane–manganese oxide (PU-MnO) composite nanofibers and showed how effective they were in extracting mono-nitrophenols. Gas chromatography–microelectron capture detection (GC-μECD) in conjunction with a green HS-SPME technique used these nanofibers as adsorbents. The researchers obtained a linear dynamic range of 0.100–500 ng/mL, relative standard deviations (RSDs) of 2.53–11.2% (n = 3), and limits of detection of 0.0201 and 0.138 ng/mL after optimizing critical extraction parameters. Relative recoveries for river and wastewater samples using this approach ranged from 90.3% to 105%. The efficiency of the environmentally friendly analytical technique and PU-MnO nanofibers for identifying mono-nitrophenols in actual water samples was validated by the investigation [95].

Zinc Oxide Nanoparticles as Sorbents for SPME

The distinct electrical and optical characteristics of one-dimensional (1D) ZnO nanostructures, which result from their size and dimensionality, make them highly desirable.

They are useful for basic research and as useful parts of nanodevices because of these characteristics. Their employment as interconnectors is also made possible by their 1D shape. Applications of 1D ZnO nanostructures demonstrate their versatility and promise in cutting-edge technologies, including field-emission devices, gas sensors, UV photodetectors, solar cells, light-emitting diodes, and nanolasers [96,97]. More importantly, ZnO nanoparticles (NPs) are less expensive and easier to create than other nanomaterials. They can also be deposited on a wide range of substrates with precise and perfectly aligned orientations [98]. Also, all of these properties make them a good candidate in SPME fiber applications.

Duarte et al. studied the utilization of zinc oxide (ZnO)-coated glass fibers for assessing trihalomethanes (THMs) by HS-SPME-GC. Energy-dispersive X-ray spectroscopy and scanning electron microscopy were used to characterize the homogenous and porous ZnO layer that was applied on LiO–ZrO_2–BaO–SiO_2 glass fibers. To improve the analytical response, the study added 15% (*m*/*v*) salt and optimized the incubation (15 min), extraction (15 min), and desorption (10 min) periods. With dynamic ranges of 20–500 μg/L for trichloromethane, 15–250 μg/L for dichlorobromomethane and dibromochloromethane, and 10–100 μg/L for tribromomethane, the method showed excellent linearity for THMs in water. The reliability of the approach was confirmed by the fact that all compounds had correlation coefficients more than 0.9900 [99].

Additionally, Zhang et al. used a sol–gel technique to create a graphene-supported ZnO SPME fiber. ZnO was nucleated by graphite oxide (GO), and the resulting ZnO/graphene composite was integrated into a long-lasting sol–gel network. Adsorption sites were improved by the addition of graphene, which raised the BET surface area from 1.2 m^2/g to 169.4 m^2/g. With an enrichment ratio of 1087 for 1-octanethiol and less than 200 for non-sulfur compounds, the ZnO/graphene fiber demonstrated exceptional sensitivity and selectivity for sulfur compounds. It performed better than PDMS/DVB fibers and commercial PDMS. The fiber efficiently examined sulfur volatiles in Chinese chives and garlic sprouts when combined with GC-MS, achieving recoveries of 73.2–91.6%, RSDs of 3.6–9.1%, and detection limits of 0.1–0.7 μg/L [100].

While many metal oxide nanoparticles (MONPs) are suitable for SPME applications, this review concentrates on three of the most notable. Many other MONPs have significant features for this purpose, but we focused on a few to emphasize their distinctive contributions.

4.1.3. Carbon Nanoparticles in SPME

There are several different allotropic forms of carbon; the spherical C60 fullerene was the first to be discovered in 1985. Since then, other allotropes have been created or found, frequently by accident. Because of their exceptional electrical, mechanical, thermal, and adsorptive qualities, carbon nanotubes are the most often utilized of these for analytical reasons. Advanced materials such as fullerenes, carbon nanotubes, nanocones, and nanodiamonds have been used in the field of solid-phase extraction to provide analytical procedures that offer notable advantages over traditional approaches [19,101,102].

Carbon nanomaterials are popular nano-adsorbents in wastewater management due to their abundance, strong adsorption capabilities, cost-effectiveness, and high chemical and thermal stability. Activated carbon (AC), known for its high porosity and large surface area, has been a widely used adsorbent, though its cost drives the need for more economical options. As a result, alternatives such as graphene, carbon nanotubes (CNTs), carbon nitride (g-C_3N_4), and carbon dots have been explored for adsorption applications. The excellent regeneration potential of these nanomaterials further supports their use in contaminant removal from wastewater. Carbon-based nanomaterials like fullerenes and graphene, recognized by Nobel Prizes in 1996 and 2010, offer unique properties for a range of applications.

Additionally, diverse carbon nanomaterials, including carbon nanoparticles, graphitic carbon nitride, ordered mesoporous carbon, and microporous carbon nanospheres, as shown in Figure 4 below, have been adapted as SPME fiber coatings [11,103,104].

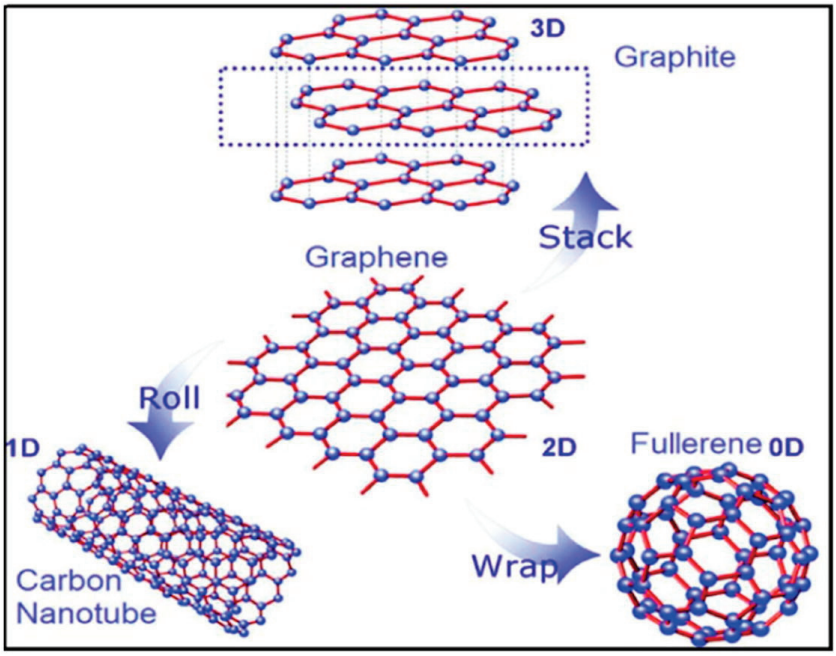


Figure 4. The basic building blocks of carbon nanomaterials. Printed with permission from [104]. Copyright 2020, Elsevier.

The structural conformation and hybridization state of carbon-based nanomaterials are intimately related to their electrical, chemical, and physical characteristics. The ground-state arrangement of the six electrons in carbon is $1s^2$, $2s^2$, and $2p^2$. Carbon can hybridize into sp, sp^2, or sp^3 configurations depending on its bonding with nearby atoms because of the promotion of an electron from the s orbital to an empty p orbital made possible by the tiny energy gap between the 2s and 2p shells. The higher energy of the promoted electron is offset by the energy obtained via covalent connections with nearby atoms. After taking into account the out-of-plane bonding from π bonds created by unhybridized p orbitals, this compensation is almost identical for both sp^2 and sp^3 hybridization [105,106]. The unique characteristics of these materials, including their high surface areas, large aspect ratios, and exceptional mechanical strength, along with excellent electrical and thermal conductivities, have led to a wide array of applications [107]. Carbon nanoparticles have been widely used as sorbent materials in SPME.

Carbon Nanotubes (CNTs) as Sorbent Materials in SPME

Considered tiny tubes made from rolled graphite sheets, carbon nanotubes (CNTs) come in two structural varieties: single-walled (SWCNTs) and multi-walled (MWCNTs). SWCNTs may range in length from hundreds of nanometers to several microns, with diameters usually between 1 and 10 nm. However, because MWCNTs are made up of numerous concentric cylinders held together by van der Waals forces, they have larger diameters, ranging from 5 nm to several hundred nanometers [108,109]. Sumio Iijima reported synthesizing a new carbon structure with needle-like tubes (carbon nanotubes) in 1991. These tubes were created using an arc-discharge evaporation procedure, which is similar to the synthesis of fullerenes [110].

Carbon nanotubes' extraordinary qualities open the door to new developments in engineering and research. In wastewater treatment and environmental monitoring, these

materials offer a variety of uses for identifying and eliminating pollutants. CNTs are interesting options for SPME coatings because of their large adsorption area and high porosity. Their practical usefulness is further enhanced by their greater thermal and physical stability as compared to traditional SPME coatings [108]. As stated above, CNTs have two structural forms, namely single-walled (SWCNTs) and multi-walled (MWCNTs).

Single-walled carbon nanotubes (SWNTs) are nanoscale tubes formed from a single rolled graphite layer, with diameters in the nanometer range and lengths reaching several micrometers, making them a prime example of one-dimensional materials. Because of the lack of mass and charge, photons are a great tool for studying and characterizing their unique structure [111,112].

Multi-walled carbon nanotubes (MWCNTs) are cylindrical nanostructures composed of sp^2 carbon. They have aspect ratios ranging from 10 to 10 million with diameters ranging from 3 to 30 nm and lengths up to several centimeters. MWCNTs are more rigid than single-walled nanotubes because of their multi-layered structure. They are also different from carbon nanofibers in that they have a hollow center, smaller exterior diameters, and a different wall structure [113].

Riboni et al. described a novel method for assessing aroma compounds in water that employs a recently developed SPME coating based on multi-walled carbon nanotubes (MWCNTs). They emphasized the use of helical MWCNTs as an excellent adsorbent because of their high extraction efficiency. The study used a desirability functions method to optimize extraction time and temperature, which improved the process's performance. The validation results show that this approach is very dependable for detecting analytes at ultra-trace levels, with detection limits ranging from 0.2 to 13 ng/L, good precision (relative standard deviations < 20%), and high recovery rates (80 $\pm$ 12% to 111 $\pm$ 11%) [114].

Rastkari et al. investigated the viability of using single-walled carbon nanotubes (SWCNTs) as an SPME adsorbent to detect monobutyltin, dibutyltin, and tributyltin in seawater. They stated that they adjusted key elements determining extraction efficiency, such as extraction and desorption time, temperature, and salinity. The approach showed linear calibration curves ($r > 0.992$) for concentrations ranging from 12 to 2000 ng/L, with detection limits < 5 ng/L, matching International Conference on Harmonization (ICH) criteria. They observed that, in comparison to commercial carboxen/polydimethylsiloxane fibers, the SWCNT fiber had greater heat stability (over 350 °C) and endurance, with a lifespan of more than 150 uses. They also stated that the procedure was successfully applied to Persian Gulf harbor seawater samples, where butyl tins were discovered, confirming SWCNTs' potential as a reliable SPME adsorbent for environmental analysis of butyltins in seawater [115].

Wang et al. developed a novel SPME method for analyzing polybrominated diphenyl ethers (PBDEs) in environmental samples that uses multi-walled carbon nanotubes (MWCNTs) as the fiber coating for gas chromatography with electron capture detection (GC-ECD). They found that the MWCNT coating had much larger enhancement factors (616–1756) than poly (5% dibenzene-95% dimethylsiloxane) (139–384) and activated carbon coatings (193–423). A 30 min extraction of a 10 mL sample yielded detection limits of 3.6–8.6 ng/L, with high linearity ($r^2 > 0.995$). They found great precision in peak area and retention duration at the 500 ng/L level, with relative standard deviations (RSDs) of 6.9–8.8% and 0.6–0.9%, respectively. The method was successfully applied to real samples such as local river water, wastewater, and milk. Their research revealed PBDE recoveries ranging from 90% to 119% for boosted samples. No PBDEs were found in river water or skimmed milk samples; however, they found PBDE levels of 134–215 ng/L in wastewater, 13–484 ng/L in whole fat milk, and 21 ng/L of BDE-47 in a semi-skimmed milk sample [116].

A study by Yazdi et al. examined the identification of ultra-trace amounts of polycyclic aromatic hydrocarbons (PAHs) in complex coffee and tea samples using hollow-fiber solid-phase microextraction (HF-SPME) in conjunction with high-performance liquid chromatography and UV detection (HPLC-UV). They clarified that for such matrices, HF-SPME is a better option than direct-immersion SPME (DI-SPME), since DI-SPME offers little sample cleanup in intricate, "dirty" samples. According to Yazdi et al., the high porosity of the hollow fiber in HF-SPME enhances analyte selectivity and cleanup by preferentially adsorbing analytes from complicated mixtures. As the fiber sorbent, they created a new multi-walled carbon nanotube/zirconium oxide (MWCNT/ZrO_2) nanocomposite, which they attribute to hydrophobic interactions and π–π stacking for its high PAH adsorption. The technique produced low detection limits (0.033–0.16 μg L^{-1}) and a wide linear range (0.1–200 μg L^{-1}) with high precision (RSD < 6.6%). The authors concluded that the MWCNT/ZrO_2 HF-SPME approach is very effective for PAH analysis in complex matrices after reporting relative recoveries of 92.0–106.0% for PAHs spiked in water, coffee, and tea samples [117].

This section covered a variety of nanostructured materials, such as carbon-based nanoparticles, metal oxide nanoparticles, and metal nanoparticles, that can be employed as fiber materials in SPME. Because of their high surface area, structural adaptability, and superior adsorption capabilities, carbon-based nanomaterials—in particular, carbon nanotubes—have demonstrated superior performance among these. These materials are very promising for upcoming SPME applications since they offer improved extraction sensitivity and efficiency.

5. SPME Based on Nanocomposite Materials

Nanocomposites (NCs) are nanoscale materials made by combining organic and inorganic components, allowing them to incorporate each constituent's distinct features while also generating new functions to fulfill modern material demands. NCs, defined as having at least one component smaller than 100 nm, are solid structures with nanometer-scale spacing between phases. These materials can be made up of an organic matrix and an inorganic nanofiller, or vice versa, or from the hybridization of various organic and inorganic phases at different doping levels. NCs can contain nanoparticles (such as metal or silica), fibrous nanomaterials (such as nanofibers and nanotubes), and layered substances (such as graphite or layered silicates). NCs frequently outperform their individual components in terms of mechanical, electrical, optical, and catalytic qualities. NCs' multifunctional capabilities stem from more than just the sum of their components, with the high surface area-to-volume ratio playing an important role in their distinct structure–property relationships [118–121].

According to Bashtani et al., a nanocomposite composed of graphene oxide (GO), poly(methyl methacrylate) (PMMA), and FeO_4 nanoparticles was created specifically for the magnetic solid-phase extraction (MSPE) of aromatic amines. After coating magnetite nanoparticles with GO and PMMA, they created the composite (PMMA@GO-Fe_3O_4) and used SEM, TEM, XRD, VSM, and FTIR techniques to characterize it. Their results showed that the composite had preconcentration factors ranging from 139 to 173, successfully extracting amines including aniline and N,N-dimethylaniline. Along with precision with relative standard deviations ranging from 5.9% to 8.6%, they reported detection limits of 2–6 pg/mL. With recoveries of 90.3% to 99.0% when the technique was successfully applied to spiked water samples, its potential for environmental applications was demonstrated [122].

Farjaminezhad et al. used the sol–gel technique to create a superparamagnetic magnetite nanoparticle (SMNP) and polyethylene glycol (PEG) nanocomposite fiber, which

chemically bonded the fiber to a silica surface that had been treated. According to their findings, 13 volatile organic compounds (VOCs) were successfully extracted from water samples using this new fiber. The fiber showed good thermal stability and a long lifespan by adjusting the mass ratio of SMNPs to PEG. According to Farjaminezhad et al., the SMNP/PEG fiber demonstrated a broad linear range (0.001–450,000 ng/L), lower detection limits (0.008–0.063 ng/L), and higher extraction efficiency when compared to commercial fibers made of polyacrylate (PA) and polydimethylsiloxane (PDMS). With intraday and interday accuracy ranging from 4.13 to 10.08% and reproducibility ranging from 7.35 to 14.79%, they found that this fiber had good repeatability and reproducibility. According to the authors, the fiber's longevity and chemical stability rendered it appropriate for use in gas chromatography–mass spectrometry (GC–MS) in conjunction with headspace solid-phase microextraction (HS-SPME) in VOC measurement. Its dependability in environmental applications was further proven by tests conducted on tap water, surface water, and groundwater [123].

Bagheri et al. reported the development of a zinc-based metal–organic framework/polyethersulfone (TMU-4/PES) nanocomposite coating on stainless steel wire for the headspace solid-phase microextraction (HS-SPME) of organophosphorous pesticides (OPPs) from environmental water and soil samples. They stated that the unique characteristics of the TMU-4/PES composite, including its high surface area, porous structure, and π–electron interactions from the PES polymer, contribute to a strong affinity for OPPs. After thermal desorption, OPPs were detected using gas chromatography with a nitrogen–phosphorus detector (GC-NPD). The authors noted the coating's simplicity, stability, and reusability, with up to 100 extraction cycles possible. Using a central composite design to optimize parameters, they achieved detection limits of 5–8 ng mL^{-1} for diazinon, fenitrothion, malathion, and chlorpyrifos. Bagheri et al. highlighted the method's effectiveness, demonstrating average repeatability and fiber-to-fiber reproducibility of 6.5% and 8.7%, respectively, and noted good recovery rates (88–108%) and reproducibility (5.9–10.1%) when applied to spiked environmental samples. The efficacy of the procedure was demonstrated by Bagheri et al., who observed good recovery rates (88–108%) and reproducibility (5.9–10.1%) when applied to spiked ambient samples, with average repeatability and fiber-to-fiber reproducibility of 6.5% and 8.7%, respectively [120].

Saraji et al. developed a mesoporous carbon–ZrO_2 nanocomposite coating on stainless steel wire as a novel SPME fiber, using direct carbonization of a Zr-based MOF without additional carbon sources. Optimized for BTEX analysis in water via GC-FID, the fiber showed excellent linearity (0.2–200 μg L^{-1}), low detection limits (0.05–0.56 μg L^{-1}), and high recovery (93–107%) with relative standard deviations of 3.5–6.7%. The study demonstrated its effectiveness in environmental analysis [38].

6. SPME Based on Nanoporous Structures

Porous structures are prevalent in nature, appearing in materials such as wood, cork, trabecular bone, and plant parenchyma. The invention of synthetic porous materials was a great leap in human civilization. Early examples included polymeric porous materials, termed "polymeric foams", with pore diameters exceeding 200 μm [124].

Nanoporous materials allow for selective adsorption depending on molecular configurations since their pores are similar in size to those of tiny molecules. For applications like fixed-bed devices that need good adsorption selectivity and capacity, zeolites—which are mostly made of silicon and oxygen—are perfect since they are plentiful, stable, and reasonably priced. Zeolitic imidazolate frameworks (ZIFs), covalent organic frameworks (COFs), and metal–organic frameworks (MOFs) are new types of nanoporous materials that provide substantial void volumes, great stability, and tunable, uniform cavities. In

general, porous materials have interconnected voids that might or might not show three-dimensional translational repetition. As an illustration, consider porous silica frameworks (PSFs), porous organic frameworks (POFs), and layered double hydroxides (LDHs). Applications in adsorption, separation, and catalysis are driven by their wide gas–solid interfaces, as demonstrated by solid foams, a simple porous system [125–127]. From conventional applications such as desiccants to more sophisticated ones, nanoporous materials have enormous potential in materials science. They function as size- and shape-selective reaction chambers for purification, which includes symmetric or asymmetric synthesis, heterogeneous catalysis, adsorption, and optical resolution of enantiomers. Modern technologies like chemical sensors, electrodes, data storage, imaging materials, and lasers are also using them more and more [128].

Overcoming difficulties in creating distinct phases at the nanoscale is necessary to fabricate nanoporous polymeric materials. Numerous methods have been devised, such as foaming, phase separation, molecular imprinting, microemulsion templating, and selective block removal in nanostructured copolymers. These techniques, which are frequently seen with scanning electron microscopy (SEM) and transmission electron microscopy (TEM), allow polymers to develop nanoscale porous architectures [124,129].

In general, pores fall into one of three shapes: slit, inkbottle, or cylindrical. They can be arranged to create 2D, 3D, crystalline, semi-crystalline, or amorphous structures. Analytes can be adsorbed by porous frameworks according to host–guest interactions (MOFs, POFs), anion exchange (LDHs), hydrophilicity (aluminosilicates), size (zeolites), or hydrophobicity (pure silica sieves) [125].

By functionalizing hexagonally ordered nanoporous silica (SBA-15) with 3-amino propyl triethoxysilane (APTES), Gholavind et al. reported creating a highly porous fiber covering a specialized solid-phase microextraction (SPME) apparatus for use in conjunction with gas chromatography–mass spectrometry (GC–MS) for the detection of trace levels of polycyclic aromatic hydrocarbons (PAHs) in water samples. Temperature, duration, ionic strength, and sonication were among the extraction parameters that were optimized, the researchers noted, one factor at a time. According to their findings, detection limits under ideal circumstances varied from 4.2 to 26.1 pg/mL, with relative standard deviations ranging from 3.3% to 7.7%. They also pointed out that the SPME fiber maintained a consistent extraction efficiency throughout 50 extractions, proving its robustness and appropriateness for environmental study [130].

Zhang et al. reported the effective synthesis of high-surface-area nanoporous carbon (NPC) using the metal–organic framework ZIF-90 as both a template and precursor, with furfuryl alcohol serving as a secondary carbon source. The resulting ZIF-90-NPC was applied to a stainless steel wire to form an SPME fiber. When combined with gas chromatography–microelectron capture detection (GC-μECD), the approach demonstrated large enhancement factors (984–2869), low detection limits (0.1–0.5 ng g^{-1}), and good linearity (0.3–50 ng g^{-1}) for detecting pyrethroid pesticides in fruits and vegetables. The RSDs for six replicate extractions ranged from 4.3% to 8.0%. The recoveries of spiked pesticides (5 ng g^{-1} and 20 ng g^{-1}) were between 86.0 and 104.0% and between 86.0 and 103.5%, with RSDs of 4.8–12.9% and 5.0–10.8%, respectively. The fiber performed consistently during 100 extraction cycles, with no notable loss of efficiency. The approach was successfully used to identify pyrethroids in fruit and vegetable samples [131].

According to Rahimi et al., CMK-3 nanoporous carbon was prepared and characterized as a highly porous fiber coating for solid-phase microextraction (SPME) that possesses an ordered carbon structure. According to their explanation, the material was immobilized onto copper, stainless steel, and platinum wires to produce new SPME fibers, with the copper–CMK-3 fiber exhibiting the best performance. The fiber was tuned for the

gas chromatography–mass spectrometry (GC–MS) extraction of phenolic chemicals, the researchers observed. According to them, the following ideal conditions were achieved by applying a simplex optimization method: 13 mL sample volume, 56 °C extraction temperature, 7 min extraction time, 5.5 min ultrasonic duration, pH 5, and 8.9% salt concentration. In comparison to a commercial product, Rahimi et al. demonstrated the fiber's selectivity for polar phenolic chemicals and observed higher extraction efficiency. They added that linear calibration curves with correlation coefficients above 0.99 and detection limits between 0.002 and 0.068 μg/mL were provided by the fiber. For at least 40 applications, the fiber's extraction effectiveness remained constant, and it was effectively used to examine phenolic chemicals in natural water samples [132].

7. Recent Advances in the Type of Fiber Material Used in SPME

In the food, environmental, and medicinal industries, solid-phase microextraction (SPME) is frequently used to preconcentrate and remove trace amounts of harmful and beneficial substances from natural goods. High efficiency, minimal resource use, ease of use, and speed are some of its main advantages. A key factor in improving extraction efficiency and selectivity is the sorbent material selection. Graphene (G), graphene oxide (GO), functionalized carbon nanotubes (CNTs), metal–organic frameworks (MOFs), covalent organic frameworks (COFs), molecularly imprinted polymers (MIPs), and other inorganic nanomaterials are all popular materials because of their large surface areas, tunable structures, high porosity, and chemical stability. Furthermore, because of their effectiveness and selectivity, environmentally friendly sorbents such as carbon black, aerogels, and zeolites have become more popular [133]. In this review, we did not look into MOFs as sorbent materials because the application of MOFs to SPME is another subject matter on its own, which we might look at separately in the future. Also, while MOFs have broad applicability, many suffer from water instability, degrading upon contact, which poses challenges for preparing water-based biological samples. Additionally, issues like recycling, waste management, and scalable production require further improvement [134].

In designing SPME fiber coatings, two key principles must be considered: the coating material should strongly and specifically interact with analytes to achieve effective enrichment, and it must be easily and securely immobilized on a supporting substrate. The evolution of SPME fiber coatings, as illustrated in Figure 5, highlights three key components: the coating material (blue dot), support material (green dot), and coating method (red dot). While the timelines show progress in certain areas, such as the shift from silica to metal fibers for better mechanical and chemical stability, other aspects have seen less development. The transition to metallic supports has improved the durability and lifespan of fibers due to their toughness and rigidity, replacing the more brittle silica fibers [45].

Han et al. demonstrated the progress of SPME fibers by creating a new substance specifically designed for the analysis of benzene series in oilfield wastewater. Through the use of an ionic liquid-assisted wet spinning process, metal–organic framework development, and pyrolysis, they modified graphene fibers with ordered mesoporous carbon nanotube arrays (CNTAs) to generate a unique fiber structure. Due to the crumpled graphene fiber stem and CNTAs acting as "hairs", the resulting "hair-brush-like" microfiber design greatly improves extraction efficiency. Verified by gas chromatography–mass spectrometry, this novel architecture provides a large surface area, a large number of binding sites, and remarkable enrichment capabilities for toluene, m-xylene, p-xylene, benzene, and ethylbenzene. In terms of extraction efficiency, the fibers outperformed commercial fibers thanks to their wide linear detection ranges (0.2–600 μg L^{-1}), low detection limits (0.005–0.03 mg L^{-1}), and exceptional repeatability (3.2–5.5% for one fiber, 2.1–6.7% for fiber-to-fiber) [39].

To measure nicotine and six metabolites in different parts of the rat brain, Zhang et al. developed a new hydrophilic–lipophilic SPME probe employing benzene diimine triazine benzodioxane–methylbenzodioxane (BDTB-MBD), a nitrogen-rich porous polymer coating. According to their findings, the coating material had balanced hydrophilic and hydrophobic qualities, a large surface area of 1001.7 m^2/g, an ideal pore diameter of 5.28 nm, and outstanding stability. Ultra-high-performance liquid chromatography–triple quadrupole mass spectrometry (UHPLC-MS/MS) in conjunction with the SPME method produced high recovery rates (77.1% to 99.6%), low detection limits (0.002 to 0.020 μg L^{-1}), and wide linearity (0.01 to 100 μg L^{-1}). The investigation established the adsorption mechanism by revealing strong non-covalent interactions between BDTB-MBD and analytes. It effectively monitored the pharmacokinetics of nicotine in rat brain tissues, demonstrating its quick absorption, widespread distribution, and conversion to cotinine, nornicotine, and other metabolites. The researchers underlined that this strategy has uses in drug monitoring and neuroscience and provides a more effective and sensitive substitute for conventional techniques like solid-phase extraction [41].

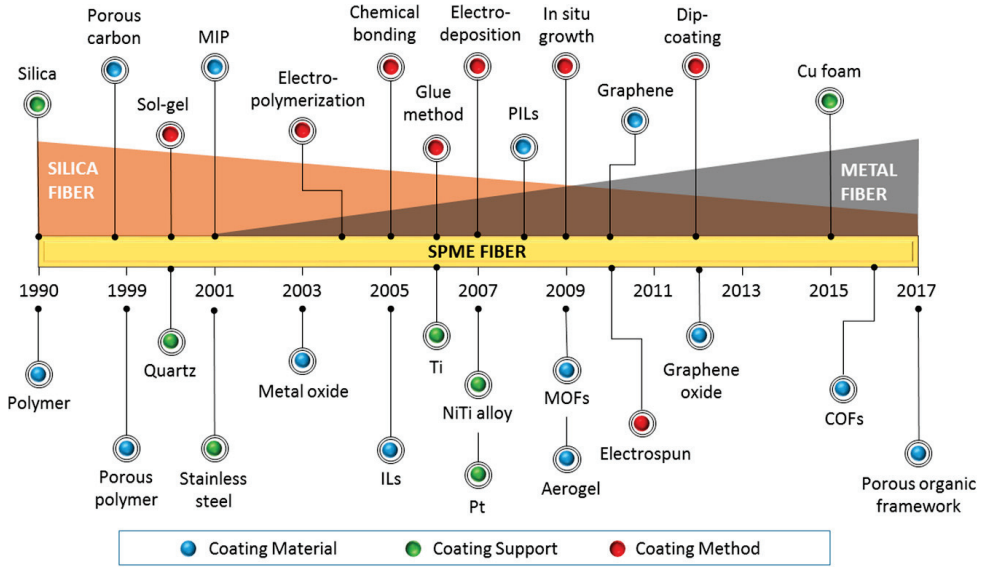


Figure 5. The timeline shows the main advancements in SPME fiber coatings, highlighting improvements in three areas: coating materials (blue dots), supporting materials (green dots), and coating methods (red dots). Printed with permission from [45]. Copyright 2022, John Wiley and sons.

For sensitive analyte detection, in-tube solid-phase microextraction (IT-SPME), which has become a popular and eco-friendly sample preparation method, is frequently used in conjunction with mass spectrometry or chromatography. This technique minimizes the usage of organic solvents, increases accuracy, and cuts down on analytical time. To improve enrichment efficiency, a variety of sorbent materials and extraction tools have been developed, including fiber-filled tubes, monolithic columns, sorbent-coated tubes, and particle-packed tubes. Although sample preparation is still difficult despite improvements in analytical equipment, solid-phase extraction has essentially supplanted conventional solvent-based techniques because of its ease of use and lower solvent use. To further reduce sample volume, minimize solvent use, and facilitate automation, microextraction techniques such as magnetic bead extraction, stir bar sorptive extraction, micro solid-phase extraction, and dispersive micro solid-phase extraction have been developed. All things considered, IT-SPME is a "green" technology that combines eco-friendly practices, online automation, and miniaturization [135,136].

8. Evaluation of Nanomaterial Performance in SPME

Table 2 summarizes the performance characteristics of a range of nanomaterials employed for use on SPME fibers.

Table 2. Evaluation of different types of nanomaterials and substrates employed in SPME fibers for the microextraction of different types of compounds and their detection efficiencies in detection devices.

Nanomaterial	Analyte	SMPE Substrate	Techniques	Number of Extraction Cycles	LOD	Linear Range	References
-	Butyltins and phenyltins	Polydimethylsiloxane (PDMS) fiber	GC-FPD	-	0.006–0.031 ng Sn l^{-1} for butyltins and 0.2–0.6 ng Sn l^{-1} for phenyltins	-	[37]
AuNPs/OMC	Aniline	Stainless steel wire	GC-FID		0.072–0.18 μg L^{-1}	0.1–1000 μg L^{-1}	[53]
PEDOT/AuNPs	Polycyclic aromatic hydrocarbons (PAHs)	Stainless steel wire	GC	160	2.5–25 ng L^{-1}	0.01–100 g L^{-1}	[54]
Helical MWCNTs	Fragrance materials	Bare fused silica fibers	GC-MS		0.2–13 22 ng/L		[114]
SWCNTs	Butyltins	Stainless steel wire	GC-MS	150	2–5 ng L^{-1}	6–2000 ng L^{-1}	[115]
MWCNTs	Polybrominated diphenyl ethers (PBDEs)	Fused silica fiber	GC-ECD	100	3.6–8.6 ng L^{-1}	28–2800 ng L^{-1}	[116]
MWCNT/ZrO_2	PAHs	Accurel Q polypropylene hollow fibers	HPLC-UV	5	0.033–0.16 g L^{-1}	0.1–200 g L^{-1}	[117]
CNTs/silica polymer	PAHs	Needle trap device (NTD)	Needle trap extraction (NTE) and GC-MS	3	0.001–0.01 ng mL^{-1}	0.01–20 ng mL^{-1}	[120]
PMMA@GO-Fe_3O_4	Aromatic amines	Fused silica	GC	139–173	2–6 pg mL^{-1}	0.007–100 ng mL^{-1}	[122]
Fe_3O_4/polyethylene glycol	Volatile organic compounds	Optical fiber	GC-MS	200	0.008–0.063 ng/L	0.001–450 × 104 ng/L	[123]
Hexagonally ordered nanoporous silica (SBA-15)	PAHs	Stainless steel wire	GC-MS	50	4.2 and 26.1 pg mL^{-1}.	-	[130]
ZIF-90 templated NPC (ZIF-90-NPC)	Pyrethroids pesticides	Stainless steel wire	gas chromatography-microelectron capture detection (GC-μECD),	100	0.1–0.5 ng g^{-1}	0.3–50 ng g^{-1}	[131]
CMK-3 nanoporous carbon	Polar phenolic compounds	Copper metal wires	GC-MS	40	0.002 to 0.068 g mL^{-1}	-	[132]
Pyrrole, carbon nanotubes, and titanium oxide (PPy-CNT-TiO_2)	Volatile aromatic compounds (BTEX)	Stainless stee wire	GC-FID	100	0.01 to 0.04 ng mL^{-1}	0.03–500 ng mL^{-1}	[137]

9. Conclusions and Future Perspectives in SPME

An important turning point in analytical chemistry was reached with the use of nanoparticles as fiber coatings in solid-phase microextraction (SPME). The sensitivity, selectivity, and reliability of extraction methods have been significantly enhanced by these cutting-edge materials, which include silica-based composites, metal–organic frameworks (MOFs), nanoporous carbons, and covalent organic frameworks (COFs). In environmental applications, the SPME method is frequently recommended for the extraction of several analytes. Due to their efficiency, NMs are a perfect substitute for traditional materials when it comes to the SPME of several analytes in environmental samples. Environmental sample SPME has made extensive use of nanomaterials (NMs), including polymer-based NMs, nanoparticles, nanofibers, nanoflakes, nanocomposites, nanorods, nanotubes, nanohorns, nanosheets, nanocubes, and nanospheres. Among these NMs' many benefits are their large

specific surface area, strong catalytic activity, ease of synthesis, and favorable mechanical, electrical, optical, and physical characteristics [9].

As demonstrated by their capacity to endure numerous extraction cycles without suffering appreciable efficiency loss, nanomaterial-based fibers have exceptional stability, durability, and reusability. The use of novel functionalization methods has increased their range of applications even more. Water, food, and environmental samples are just a few of the matrices to which these fibers can adapt effectively. They also function well in a variety of settings, including high ionic strengths, high temperatures, and when subjected to sonication. Furthermore, their selectivity for analytes—whether controlled by hydrophobicity, size exclusion, or host–guest interactions—highlights their adaptability and customized functionality for particular uses.

For the development of SPME devices, nanomaterials—particularly those produced via the bottom-up approach—offer significant cost advantages. For effective analyte extraction, this technique reduces material waste and permits the accurate fabrication of high-performance nanostructures. Its scalability facilitates mass production, which lowers manufacturing costs while improving the functionality of the gadget. The bottom-up method increases extraction efficiency and lowers material consumption by producing nanomaterials with high surface areas and regulated porosity, increasing the accessibility of SPME devices. In order to promote greener and more sustainable analytical techniques, these cost savings are essential for growing SPME applications in domains like environmental monitoring and medical diagnostics.

In the future, analytical science could undergo yet another revolution as nanomaterials and SPME are combined. Improved functionalization techniques and a wider variety of nanomaterials may result in fibers with higher resilience and specificity. Furthermore, the accuracy and sensitivity of analytical procedures will be further improved by developments in connecting these materials with cutting-edge detection systems like gas chromatography–mass spectrometry (GC-MS) or microelectron capture detection (μECD). A bright future for this area of study lies ahead of us as nanomaterial-based SPME fibers stand to be crucial in tackling new issues in food safety, pharmaceutical analysis, environmental monitoring, and other areas.

In conclusion, SPME research and development should focus more on promoting its use in a traditional laboratory and increasing its contribution to routine sample analysis or daily detection, even though the development of novel fiber coatings—particularly those with broad-spectrum applicability, high sensitivity, or exceptional selectivity for certain compounds—remains a key area of focus. This calls for the technology to be incorporated into higher education's teaching and practice system as a standard analysis method, becoming as well known as liquid-phase extraction and SPE. It also calls for ongoing product innovation and cost reductions based on the assurance of superior performance for the technology to become a standard piece of laboratory equipment and instrument. Nanomaterial coatings produced by robust processes involving fewer steps will prove appealing from a cost perspective. Furthermore, a key factor in encouraging the use of SPME technology is its application in the establishment of relevant national and industrial standard procedures [45].

Author Contributions: Conceptualization, K.J.S., N.H. and T.M.A.; writing—original draft preparation, N.H. and T.M.A.; writing—review and editing, K.J.S. All authors have read and agreed to the published version of the manuscript.

Funding: This research received no external funding.

Data Availability Statement: No new data were created or analyzed in this study.

Conflicts of Interest: The authors declare no conflicts of interest.

References

1. Chen, J.; Pawliszyn, J.B. Solid phase microextraction coupled to high-performance liquid chromatography. *Anal. Chem.* **1995**, *67*, 2530–2533. [CrossRef]
2. Reyes-Garcés, N.; Gionfriddo, E.; Gómez-Ríos, G.A.; Alam, M.N.; Boyacı, E.; Bojko, B.; Singh, V.; Grandy, J.; Pawliszyn, J. Advances in Solid Phase Microextraction and Perspective on Future Directions. *Anal. Chem.* **2018**, *90*, 302–360. [CrossRef]
3. Risticevic, S.; Niri, V.H.; Vuckovic, D.; Pawliszyn, J. Recent developments in solid-phase microextraction. *Anal. Bioanal. Chem.* **2009**, *393*, 781–795. [CrossRef]
4. Pawliszyn, J. Solid phase microextraction. In *Headspace Analysis of Foods and Flavors: Theory and Practice*; Springer: Berlin/Heidelberg, Germany, 2001; pp. 73–87.
5. Merkle, S.; Kleeberg, K.K.; Fritsche, J. Recent Developments and Applications of Solid Phase Microextraction (SPME) in Food and Environmental Analysis—A Review. *Chromatography* **2015**, *2*, 293–381. [CrossRef]
6. Portillo-Castillo, O.J.; Castro-Ríos, R.; Chávez-Montes, A.; González-Horta, A.; Cavazos-Rocha, N.; Waksman de Torres, N.H.; Garza-Tapia, M. Developments of solid-phase microextraction fiber coatings for environmental pharmaceutical and personal care products analysis. *Rev. Anal. Chem.* **2018**, *37*, 2018. [CrossRef]
7. Dietz, C.; Sanz, J.; Cámara, C. Recent developments in solid-phase microextraction coatings and related techniques. *J. Chromatogr. A* **2006**, *1103*, 183–192. [CrossRef]
8. de Fátima Alpendurada, M. Solid-phase microextraction: A promising technique for sample preparation in environmental analysis. *J. Chromatogr. A* **2000**, *889*, 3–14. [CrossRef]
9. Murtada, K. Trends in nanomaterial-based solid-phase microextraction with a focus on environmental applications—A review. *Trends Environ. Anal. Chem.* **2020**, *25*, e00077. [CrossRef]
10. Ghaemi, F.; Amiri, A.; Yunus, R. Methods for coating solid-phase microextraction fibers with carbon nanotubes. *TrAC Trends Anal. Chem.* **2014**, *59*, 133–143. [CrossRef]
11. Sun, M.; Feng, J.; Qiu, H.; Fan, L.; Li, L.; Luo, C. A solid-phase microextraction fiber with carbon nanoparticles as sorbent material prepared by a simple flame-based preparation process. *J. Chromatogr. A* **2013**, *1300*, 173–179. [CrossRef]
12. Wang, L.; Hou, X.; Li, J.; Liu, S.; Guo, Y. Graphene oxide decorated with silver nanoparticles as a coating on a stainless-steel fiber for solid-phase microextraction. *J. Sep. Sci.* **2015**, *38*, 2439–2446. [CrossRef] [PubMed]
13. Guo, J.; Park, S.-J.; Meng, L.-Y.; Jin, X. Applications of carbon-based materials in solid phase micro-extraction: A review. *Carbon Lett.* **2017**, *24*, 10–17.
14. García-Valverde, M.T.; Lucena, R.; Cárdenas, S.; Valcárcel, M. Titanium-dioxide nanotubes as sorbents in (micro)extraction techniques. *TrAC Trends Anal. Chem.* **2014**, *62*, 37–45. [CrossRef]
15. Xu, J.; Zheng, J.; Tian, J.; Zhu, F.; Zeng, F.; Su, C.; Ouyang, G. New materials in solid-phase microextraction. *TrAC Trends Anal. Chem.* **2013**, *47*, 68–83. [CrossRef]
16. Baig, N.; Kammakakam, I.; Falath, W. Nanomaterials: A review of synthesis methods, properties, recent progress, and challenges. *Mater. Adv.* **2021**, *2*, 1821–1871. [CrossRef]
17. Mehdinia, A.; Aziz-Zanjani, M.O. Recent advances in nanomaterials utilized in fiber coatings for solid-phase microextraction. *TrAC Trends Anal. Chem.* **2013**, *42*, 205–215. [CrossRef]
18. Gholivand, M.B.; Shamsipur, M.; Shamizadeh, M.; Moradian, R.; Astinchap, B. Cobalt oxide nanoparticles as a novel high-efficiency fiber coating for solid phase microextraction of benzene, toluene, ethylbenzene and xylene from aqueous solutions. *Anal. Chim. Acta* **2014**, *822*, 30–36. [CrossRef]
19. Lucena, R.; Simonet, B.M.; Cárdenas, S.; Valcárcel, M. Potential of nanoparticles in sample preparation. *J. Chromatogr. A* **2011**, *1218*, 620–637. [CrossRef] [PubMed]
20. Aulakh, J.S.; Malik, A.K.; Kaur, V.; Schmitt-Kopplin, P. A Review on Solid Phase Micro Extraction—High Performance Liquid Chromatography (SPME-HPLC) Analysis of Pesticides. *Crit. Rev. Anal. Chem.* **2005**, *35*, 71–85. [CrossRef]
21. Spietelun, A.; Pilarczyk, M.; Kloskowski, A.; Namieśnik, J. Current trends in solid-phase microextraction (SPME) fibre coatings. *Chem. Soc. Rev.* **2010**, *39*, 4524–4537. [CrossRef]
22. Lord, H.; Pawliszyn, J. Evolution of solid-phase microextraction technology. *J. Chromatogr. A* **2000**, *885*, 153–193. [CrossRef]
23. Balasubramanian, S.; Panigrahi, S. Solid-Phase Microextraction (SPME) Techniques for Quality Characterization of Food Products: A Review. *Food Bioprocess Technol.* **2011**, *4*, 1–26. [CrossRef]
24. Vas, G.; Vekey, K. Solid-phase microextraction: A powerful sample preparation tool prior to mass spectrometric analysis. *J. Mass Spectrom.* **2004**, *39*, 233–254. [CrossRef] [PubMed]
25. Schmidt, K.; Podmore, I. Solid phase microextraction (SPME) method development in analysis of volatile organic compounds (VOCS) as potential biomarkers of cancer. *J. Mol. Biomark. Diagn.* **2015**, *6*, 1000253. [CrossRef]
26. Lim, D.K.; Mo, C.; Lee, D.-K.; Long, N.P.; Lim, J.; Kwon, S.W. Non-destructive profiling of volatile organic compounds using HS-SPME/GC–MS and its application for the geographical discrimination of white rice. *J. Food Drug Anal.* **2018**, *26*, 260–267. [CrossRef]

27. Poli, D.; Goldoni, M.; Corradi, M.; Acampa, O.; Carbognani, P.; Internullo, E.; Casalini, A.; Mutti, A. Determination of aldehydes in exhaled breath of patients with lung cancer by means of on-fiber-derivatisation SPME–GC/MS. *J. Chromatogr. B* **2010**, *878*, 2643–2651. [CrossRef]
28. Rudnicka, J.; Kowalkowski, T.; Ligor, T.; Buszewski, B. Determination of volatile organic compounds as biomarkers of lung cancer by SPME–GC–TOF/MS and chemometrics. *J. Chromatogr. B* **2011**, *879*, 3360–3366. [CrossRef]
29. Kusano, M.; Mendez, E.; Furton, K.G. Development of headspace SPME method for analysis of volatile organic compounds present in human biological specimens. *Anal. Bioanal. Chem.* **2011**, *400*, 1817–1826. [CrossRef]
30. Kataoka, H.; Lord, H.L.; Pawliszyn, J. Applications of solid-phase microextraction in food analysis. *J. Chromatogr. A* **2000**, *880*, 35–62. [CrossRef] [PubMed]
31. Xu, C.-H.; Chen, G.-S.; Xiong, Z.-H.; Fan, Y.-X.; Wang, X.-C.; Liu, Y. Applications of solid-phase microextraction in food analysis. *TrAC Trends Anal. Chem.* **2016**, *80*, 12–29. [CrossRef]
32. Barboni, T.; Luro, F.; Chiaramonti, N.; Desjobert, J.-M.; Muselli, A.; Costa, J. Volatile composition of hybrids Citrus juices by headspace solid-phase micro extraction/gas chromatography/mass spectrometry. *Food Chem.* **2009**, *116*, 382–390. [CrossRef]
33. Mounchili, A.; Wichtel, J.; Bosset, J.; Dohoo, I.R.; Imhof, M.; Altieri, D.; Mallia, S.; Stryhn, H. HS-SPME gas chromatographic characterization of volatile compounds in milk tainted with off-flavour. *Int. Dairy J.* **2005**, *15*, 1203–1215. [CrossRef]
34. Gong, X.; Lin, S.; Huang, X.; Peng, S.; Shen, M.; Ouyang, S.; Zheng, J.; Xu, J.; Ouyang, G. Applications of in vivo SPME based on mass spectrometry for environmental pollutants analysis and non-target metabolomics: A review. *Green Anal. Chem.* **2022**, *1*, 100004. [CrossRef]
35. Naccarato, A.; Tagarelli, A. Recent applications and newly developed strategies of solid-phase microextraction in contaminant analysis: Through the environment to humans. *Separations* **2019**, *6*, 54. [CrossRef]
36. Yu, M.; Roszkowska, A.; Pawliszyn, J. In vivo solid-phase microextraction and applications in environmental sciences. *ACS Environ. Au* **2021**, *2*, 30–41. [CrossRef] [PubMed]
37. Aguerre, S.; Bancon-Montigny, C.; Lespes, G.; Potin-Gautier, M. Solid phase microextraction (SPME): A new procedure for the control of butyl-and phenyltin pollution in the environment by GC-FPD. *Analyst* **2000**, *125*, 263–268. [CrossRef]
38. Saraji, M.; Mehrafza, N. Mesoporous carbon–zirconium oxide nanocomposite derived from carbonized metal organic framework: A coating for solid-phase microextraction. *J. Chromatogr. A* **2016**, *1460*, 33–39. [CrossRef]
39. Han, Z.; Li, G.; Li, M.; Zhang, Y.; Meng, Z. Ordered mesoporous hairbrush-like nanocarbon assembled microfibers for solid-phase microextraction of benzene series in oilfield sewage. *Anal. Sci.* **2024**, *40*, 1031–1041. [CrossRef] [PubMed]
40. Mahpishanian, S.; Sereshti, H. Three-dimensional graphene aerogel-supported iron oxide nanoparticles as an efficient adsorbent for magnetic solid phase extraction of organophosphorus pesticide residues in fruit juices followed by gas chromatographic determination. *J. Chromatogr. A* **2016**, *1443*, 43–53. [CrossRef]
41. Zhang, W.; Wang, Y.; Zhang, Q.; Fan, W.; Chai, G.; Guo, L.; Mao, J.; Zhu, C.; Zhang, S.; Xie, J. Nitrogen-rich porous polymer as a solid-phase microextraction coating for the ultrasensitive analysis of nicotine and its metabolites in different rat brain regions. *Chem. Eng. J.* **2024**, *503*, 158186. [CrossRef]
42. Silva, E.A.S.; Risticevic, S.; Pawliszyn, J. Recent trends in SPME concerning sorbent materials, configurations and in vivo applications. *TrAC Trends Anal. Chem.* **2013**, *43*, 24–36. [CrossRef]
43. Augusto, F.; Carasek, E.; Silva, R.G.C.; Rivellino, S.R.; Batista, A.D.; Martendal, E. New sorbents for extraction and microextraction techniques. *J. Chromatogr. A* **2010**, *1217*, 2533–2542. [CrossRef]
44. Hashemi, B.; Zohrabi, P.; Shamsipur, M. Recent developments and applications of different sorbents for SPE and SPME from biological samples. *Talanta* **2018**, *187*, 337–347. [CrossRef] [PubMed]
45. Peng, S.; Huang, X.; Huang, Y.; Huang, Y.; Zheng, J.; Zhu, F.; Xu, J.; Ouyang, G. Novel solid-phase microextraction fiber coatings: A review. *J. Sep. Sci.* **2022**, *45*, 282–304. [CrossRef]
46. Banfield, J.F.; Zhang, H. Nanoparticles in the environment. *Rev. Mineral. Geochem.* **2001**, *44*, 1–58. [CrossRef]
47. Erarpat, S.; Bodur, S.; Bakırdere, S. Nanoparticles Based Extraction Strategies for Accurate and Sensitive Determination of Different Pesticides. *Crit. Rev. Anal. Chem.* **2022**, *52*, 1370–1385. [CrossRef]
48. Jagirani, M.S.; Soylak, M. A review: Recent advances in solid phase microextraction of toxic pollutants using nanotechnology scenario. *Microchem. J.* **2020**, *159*, 105436. [CrossRef]
49. González-Fuenzalida, R.A.; Moliner-Martinez, Y.; Verdú-Andrés, J.; Molins-Legua, C.; Herráez-Hernández, R.; Jornet-Martinez, N.; Campíns-Falcó, P. Microextraction with phases containing nanoparticles. *Bioanalysis* **2015**, *7*, 2163–2170. [CrossRef]
50. Dastafkan, K.; Khajeh, M.; Ghaffari-Moghaddam, M.; Bohlooli, M. Silver nanoparticles for separation and preconcentration processes. *TrAC Trends Anal. Chem.* **2015**, *64*, 118–126. [CrossRef]
51. Hagarová, I.; Nemček, L. Application of Metallic Nanoparticles and Their Hybrids as Innovative Sorbents for Separation and Pre-concentration of Trace Elements by Dispersive Micro-Solid Phase Extraction: A Minireview. *Front. Chem.* **2021**, *9*, 672755. [CrossRef]

52. Ibrahim, W.A.W.; Sutirman, Z.A.; Qaderi, J.; Bakar, K.A.; Basir, S.H.M.; Aouissi, I.E. A review on applications of gold and silver-based sorbents in solid phase extraction and solid phase microextraction. *Malays. J. Anal. Sci.* **2020**, *24*, 464–483.
53. Wen, C.-Y.; Chen, J.; Li, M.; Xue, Y.; Aslam, S.; Subhan, F.; Zhao, R.; Yu, J.; Zeng, J.; Chen, X. Gold nanoparticles deposited on mesoporous carbon as a solid-phase sorbent with enhanced extraction capacity and selectivity for anilines. *Microchim. Acta* **2017**, *184*, 3929–3936. [CrossRef]
54. Yang, L.; Zhang, J.; Zhao, F.; Zeng, B. Electrodeposition of self-assembled poly (3, 4-ethylenedioxythiophene)@ gold nanoparticles on stainless steel wires for the headspace solid-phase microextraction and gas chromatographic determination of several polycyclic aromatic hydrocarbons. *J. Chromatogr. A* **2016**, *1471*, 80–86. [CrossRef]
55. Gutiérrez-Serpa, A.; Rocío-Bautista, P.; Pino, V.; Jiménez-Moreno, F.; Jiménez-Abizanda, A.I. Gold nanoparticles based solid-phase microextraction coatings for determining organochlorine pesticides in aqueous environmental samples. *J. Sep. Sci.* **2017**, *40*, 2009–2021. [CrossRef] [PubMed]
56. Trujillo-Rodríguez, M.J.; Anderson, J.L. Silver-based polymeric ionic liquid sorbent coatings for solid-phase microextraction: Materials for the selective extraction of unsaturated compounds. *Anal. Chim. Acta* **2019**, *1047*, 52–61. [CrossRef]
57. Ortiz, A.; Ruiz, A.; Gorri, D.; Ortiz, I. Room temperature ionic liquid with silver salt as efficient reaction media for propylene/propane separation: Absorption equilibrium. *Sep. Purif. Technol.* **2008**, *63*, 311–318. [CrossRef]
58. Won, J.; Kim, D.B.; Kang, Y.S.; Choi, D.K.; Kim, H.S.; Kim, C.K.; Kim, C.K. An ab initio study of ionic liquid silver complexes as carriers in facilitated olefin transport membranes. *J. Membr. Sci.* **2005**, *260*, 37–44. [CrossRef]
59. Gutiérrez-Serpa, A.; Napolitano-Tabares, P.I.; Pino, V.; Jiménez-Moreno, F.; Jiménez-Abizanda, A.I. Silver nanoparticles supported onto a stainless steel wire for direct-immersion solid-phase microextraction of polycyclic aromatic hydrocarbons prior to their determination by GC-FID. *Microchim. Acta* **2018**, *185*, 1–10. [CrossRef]
60. Liu, Z.; Wang, L.; Bian, W.; Zhang, M.; Zhan, J. Porous silver coating fiber for rapidly screening organotin compounds by solid phase microextraction coupled with surface enhanced Raman spectroscopy. *RSC Adv.* **2017**, *7*, 3117–3124. [CrossRef]
61. Li, J.; Ma, L.; Tang, M.; Xu, L. C12-Ag wire as solid-phase microextraction fiber for determination of benzophenone ultraviolet filters in river water. *J. Chromatogr. A* **2013**, *1298*, 1–8. [CrossRef]
62. Feng, J.; Sun, M.; Li, J.; Liu, X.; Jiang, S. A novel silver-coated solid-phase microextraction metal fiber based on electroless plating technique. *Anal. Chim. Acta* **2011**, *701*, 174–180. [CrossRef] [PubMed]
63. Yang, Y.; Guo, M.; Zhang, Y.; Song, W.; Li, Y.; Wang, X.; Du, X. Self-assembly of alkyldithiols on a novel dendritic silver nanostructure electrodeposited on a stainless steel wire as a fiber coating for solid-phase microextraction. *RSC Adv.* **2015**, *5*, 71859–71867. [CrossRef]
64. Hasanli, F.; Mohammadiazar, S.; Bahmaei, M.; Sharif, A.A.M. Coating of Sol–Gel Film on Silver Nanodendrite as a Novel Solid-Phase Microextraction Fiber for Determination of Volatile Aldehydes in Edible Oils. *Food Anal. Methods* **2018**, *11*, 2149–2157. [CrossRef]
65. Zhu, S.; Zhang, X.; Cui, J.; Shi, Y.-e.; Jiang, X.; Liu, Z.; Zhan, J. Silver nanoplate-decorated copper wire for the on-site microextraction and detection of perchlorate using a portable Raman spectrometer. *Analyst* **2015**, *140*, 2815–2822. [CrossRef] [PubMed]
66. Ghosh, N.; Das, S.; Biswas, G.; Haldar, P.K. Review on some metal oxide nanoparticles as effective adsorbent in wastewater treatment. *Water Sci. Technol.* **2022**, *85*, 3370–3395. [CrossRef]
67. Dixit, S.; Hering, J.G. Comparison of Arsenic(V) and Arsenic(III) Sorption onto Iron Oxide Minerals: Implications for Arsenic Mobility. *Environ. Sci. Technol.* **2003**, *37*, 4182–4189. [CrossRef]
68. Coston, J.A.; Fuller, C.C.; Davis, J.A. Pb2+ and Zn2+ adsorption by a natural aluminum- and iron-bearing surface coating on an aquifer sand. *Geochim. Cosmochim. Acta* **1995**, *59*, 3535–3547. [CrossRef]
69. Hua, M.; Zhang, S.; Pan, B.; Zhang, W.; Lv, L.; Zhang, Q. Heavy metal removal from water/wastewater by nanosized metal oxides: A review. *J. Hazard. Mater.* **2012**, *211–212*, 317–331. [CrossRef] [PubMed]
70. Patra, A.K.; Dutta, A.; Bhaumik, A. Self-assembled mesoporous γ-Al2O3 spherical nanoparticles and their efficiency for the removal of arsenic from water. *J. Hazard. Mater.* **2012**, *201–202*, 170–177. [CrossRef]
71. Pena, M.E.; Korfiatis, G.P.; Patel, M.; Lippincott, L.; Meng, X. Adsorption of As(V) and As(III) by nanocrystalline titanium dioxide. *Water Res.* **2005**, *39*, 2327–2337. [CrossRef]
72. Van Benschoten, J.E.; Reed, B.E.; Matsumoto, M.R.; McGarvey, P. Metal removal by soil washing for an iron oxide coated sandy soil. *Water Environ. Res.* **1994**, *66*, 168–174. [CrossRef]
73. Henglein, A. Small-particle research: Physicochemical properties of extremely small colloidal metal and semiconductor particles. *Chem. Rev.* **1989**, *89*, 1861–1873. [CrossRef]
74. El-Sayed, M.A. Some Interesting Properties of Metals Confined in Time and Nanometer Space of Different Shapes. *Acc. Chem. Res.* **2001**, *34*, 257–264. [CrossRef]
75. Ghosh, S.; Das, A. Modified titanium oxide (TiO2) nanocomposites and its array of applications: A review. *Toxicol. Environ. Chem.* **2015**, *97*, 491–514. [CrossRef]

76. Miyauchi, M.; Tokudome, H. Synthesis and applications of titanium oxide nanotube thin films. In *Inorganic and Metallic Nanotubular Materials: Recent Technologies and Applications*; Springer: Berlin/Heidelberg, Germany, 2010; pp. 45–57.
77. Shu, H.C.; Chen, Y.S.; Huang, Z.X. Titanium dioxide nanotube fiber using in headspace solid-phase microextraction with GC–MS for BTEX detection. *J. Chin. Chem. Soc.* **2023**, *70*, 2005–2015. [CrossRef]
78. Li, Y.; Zhang, M.; Yang, Y.; Wang, X.; Du, X. Electrochemical in situ fabrication of titanium dioxide-nanosheets on a titanium wire as a novel coating for selective solid-phase microextraction. *J. Chromatogr. A* **2014**, *1358*, 60–67. [CrossRef]
79. Cundy, A.B.; Hopkinson, L.; Whitby, R.L. Use of iron-based technologies in contaminated land and groundwater remediation: A review. *Sci. Total Environ.* **2008**, *400*, 42–51. [CrossRef]
80. Neyaz, N.; Siddiqui, W.A.; Nair, K.K. Application of surface functionalized iron oxide nanomaterials as a nanosorbents in extraction of toxic heavy metals from ground water: A review. *Int. J. Environ. Sci.* **2014**, *4*, 472–483.
81. Ambashta, R.D.; Sillanpää, M. Water purification using magnetic assistance: A review. *J. Hazard. Mater.* **2010**, *180*, 38–49. [CrossRef]
82. Baalousha, M. Aggregation and disaggregation of iron oxide nanoparticles: Influence of particle concentration, pH and natural organic matter. *Sci. Total Environ.* **2009**, *407*, 2093–2101. [CrossRef]
83. Doan, L. Modifying Superparamagnetic Iron Oxide Nanoparticles as Methylene Blue Adsorbents: A Review. *ChemEngineering* **2023**, *7*, 77. [CrossRef]
84. Keshta, B.E.; Gemeay, A.H.; Kumar Sinha, D.; Elsharkawy, S.; Hassan, F.; Rai, N.; Arora, C. State of the art on the magnetic iron oxide Nanoparticles: Synthesis, Functionalization, and applications in wastewater treatment. *Results Chem.* **2024**, *7*, 101388. [CrossRef]
85. Li, X.-M.; Xu, G.; Liu, Y.; He, T. Magnetic Fe3O4 nanoparticles: Synthesis and application in water treatment. *Nanosci. Nanotechnol.-Asia* **2011**, *1*, 14–24.
86. Chen, D.; Awut, T.; Liu, B.; Ma, Y.; Wang, T.; Nurulla, I. Functionalized magnetic Fe_3O_4 nanoparticles for removal of heavy metal ions from aqueous solutions. *e-Polymers* **2016**, *16*, 313–322. [CrossRef]
87. Phouthavong, V.; Yan, R.; Nijpanich, S.; Hagio, T.; Ichino, R.; Kong, L.; Li, L. Magnetic adsorbents for wastewater treatment: Advancements in their synthesis methods. *Materials* **2022**, *15*, 1053. [CrossRef] [PubMed]
88. Ghiasvand, A.; Heidari, N.; Abdolhosseini, S. Iron oxide/silica/polypyrrole nanocomposite sorbent for the comparison study of direct-immersion and headspace solid-phase microextraction of aldehyde biomarkers in human urine. *J. Pharm. Biomed. Anal.* **2018**, *159*, 37–44. [CrossRef]
89. Islam, M.A.; Ali, I.; Karim, S.M.A.; Hossain Firoz, M.S.; Chowdhury, A.-N.; Morton, D.W.; Angove, M.J. Removal of dye from polluted water using novel nano manganese oxide-based materials. *J. Water Process Eng.* **2019**, *32*, 100911. [CrossRef]
90. Chen, R.; Yu, J.; Xiao, W. Hierarchically porous MnO_2 microspheres with enhanced adsorption performance. *J. Mater. Chem. A* **2013**, *1*, 11682–11690. [CrossRef]
91. Feng, X.H.; Zhai, L.M.; Tan, W.F.; Liu, F.; He, J.Z. Adsorption and redox reactions of heavy metals on synthesized Mn oxide minerals. *Environ. Pollut.* **2007**, *147*, 366–373. [CrossRef] [PubMed]
92. Dawadi, S.; Gupta, A.; Khatri, M.; Budhathoki, B.; Lamichhane, G.; Parajuli, N. Manganese dioxide nanoparticles: Synthesis, application and challenges. *Bull. Mater. Sci.* **2020**, *43*, 277. [CrossRef]
93. Kim, E.-J.; Lee, C.-S.; Chang, Y.-Y.; Chang, Y.-S. Hierarchically Structured Manganese Oxide-Coated Magnetic Nanocomposites for the Efficient Removal of Heavy Metal Ions from Aqueous Systems. *ACS Appl. Mater. Interfaces* **2013**, *5*, 9628–9634. [CrossRef] [PubMed]
94. Eskandarpour, N.; Sereshti, H. Electrospun polycaprolactam-manganese oxide fiber for headspace-solid phase microextraction of phthalate esters in water samples. *Chemosphere* **2018**, *191*, 36–43. [CrossRef] [PubMed]
95. Eskandarpour, N.; Sereshti, H. Electrospun polyurethane fibers doped with manganese oxide nanoparticles as an effective adsorbent for determination of priority pollutant mono-nitrophenols in water samples. *J. Environ. Chem. Eng.* **2019**, *7*, 102926. [CrossRef]
96. Wang, D.; Zhang, Z.; Luo, L.; Li, T.; Zhang, L.; Chen, G. ZnO nanorod array solid phase micro-extraction fiber coating: Fabrication and extraction capability. *Nanotechnology* **2009**, *20*, 465702. [CrossRef]
97. Alizadeh, R.; Kashkoei, P.K.; Kazemipour, M. Zinc oxide-copper oxide nanoplates composite as coating for solid phase microextraction combined with high performance liquid chromatography-UV detection for trace analysis of chlorophenols in water and tomato juice samples. *Anal. Bioanal. Chem.* **2016**, *408*, 3727–3736. [CrossRef]
98. Zeng, J.; Liu, H.; Chen, J.; Huang, J.; Yu, J.; Wang, Y.; Chen, X. Octadecyltrimethoxysilane functionalized ZnO nanorods as a novel coating for solid-phase microextraction with strong hydrophobic surface. *Analyst* **2012**, *137*, 4295–4301. [CrossRef]
99. Duarte, A.P.; De Campos, E.A.; Schneider, R.; De Campos, S.D.; Cottica, S.M.; Favreto, W.A.J. ZnO-coated glass fibers for the analysis of trihalomethanes by headspace-solid phase microextraction-gas chromatography. *Talanta* **2010**, *83*, 549–552. [CrossRef]
100. Zhang, S.; Du, Z.; Li, G. Graphene-supported zinc oxide solid-phase microextraction coating with enhanced selectivity and sensitivity for the determination of sulfur volatiles in Allium species. *J. Chromatogr. A* **2012**, *1260*, 1–8. [CrossRef]

101. Kroto, H.W.; Heath, J.R.; O'Brien, S.C.; Curl, R.F.; Smalley, R.E. C60: Buckminsterfullerene. *Nature* **1985**, *318*, 162–163. [CrossRef]
102. Valcárcel, M.; Cárdenas, S.; Simonet, B.M. Role of Carbon Nanotubes in Analytical Science. *Anal. Chem.* **2007**, *79*, 4788–4797. [CrossRef]
103. Hou, X.; Wang, L.; Guo, Y. Recent Developments in Solid-phase Microextraction Coatings for Environmental and Biological Analysis. *Chem. Lett.* **2017**, *46*, 1444–1455. [CrossRef]
104. Gusain, R.; Kumar, N.; Ray, S.S. Recent advances in carbon nanomaterial-based adsorbents for water purification. *Coord. Chem. Rev.* **2020**, *405*, 213111. [CrossRef]
105. Ajayan, P.M. Nanotubes from carbon. *Chem. Rev.* **1999**, *99*, 1787–1799. [CrossRef]
106. Hu, Y.; Shenderova, O.A.; Brenner, D.W. Carbon nanostructures: Morphologies and properties. *J. Comput. Theor. Nanosci.* **2007**, *4*, 199–221. [CrossRef]
107. Liang, X.; Liu, S.; Wang, S.; Guo, Y.; Jiang, S. Carbon-based sorbents: Carbon nanotubes. *J. Chromatogr. A* **2014**, *1357*, 53–67. [CrossRef] [PubMed]
108. Pyrzynska, K. Carbon nanotubes as sorbents in the analysis of pesticides. *Chemosphere* **2011**, *83*, 1407–1413. [CrossRef]
109. Wepasnick, K.A.; Smith, B.A.; Bitter, J.L.; Howard Fairbrother, D. Chemical and structural characterization of carbon nanotube surfaces. *Anal. Bioanal. Chem.* **2010**, *396*, 1003–1014. [CrossRef]
110. Iijima, S. Helical microtubules of graphitic carbon. *Nature* **1991**, *354*, 56–58. [CrossRef]
111. Reich, S.; Thomsen, C.; Maultzsch, J. *Carbon Nanotubes: Basic Concepts and Physical Properties*; John Wiley & Sons: Hoboken, NJ, USA, 2008.
112. Jorio, A.; Dresselhaus, G.; Dresselhaus, M.S. *Carbon Nanotubes: Advanced Topics in the Synthesis, Structure, Properties and Applications*; Springer: Berlin/Heidelberg, Germany, 2008; Volume 111.
113. Kukovecz, Á.; Kozma, G.; Kónya, Z. Multi-walled carbon nanotubes. In *Springer Handbook of Nanomaterials*; Springer: Berlin/Heidelberg, Germany, 2013; pp. 147–188. [CrossRef]
114. Riboni, N.; Fornari, F.; Bianchi, F.; Careri, M. A simple and efficient solid-phase microextraction–gas chromatography–mass spectrometry method for the determination of fragrance materials at ultra-trace levels in water samples using multi-walled carbon nanotubes as innovative coating. *Talanta* **2021**, *224*, 121891. [CrossRef]
115. Rastkari, N.; Ahmadkhaniha, R.; Samadi, N.; Shafiee, A.; Yunesian, M. Single-walled carbon nanotubes as solid-phase microextraction adsorbent for the determination of low-level concentrations of butyltin compounds in seawater. *Anal. Chim. Acta* **2010**, *662*, 90–96. [CrossRef]
116. Wang, J.-X.; Jiang, D.-Q.; Gu, Z.-Y.; Yan, X.-P. Multiwalled carbon nanotubes coated fibers for solid-phase microextraction of polybrominated diphenyl ethers in water and milk samples before gas chromatography with electron-capture detection. *J. Chromatogr. A* **2006**, *1137*, 8–14. [CrossRef]
117. Yazdi, M.N.; Yamini, Y.; Asiabi, H. Multiwall carbon nanotube-zirconium oxide nanocomposite hollow fiber solid phase microextraction for determination of polyaromatic hydrocarbons in water, coffee and tea samples. *J. Chromatogr. A* **2018**, *1554*, 8–15. [CrossRef] [PubMed]
118. Ayazi, Z. Application of nanocomposite-based sorbents in microextraction techniques: A review. *Analyst* **2017**, *142*, 721–739. [CrossRef]
119. Ajayan, P.M. Bulk Metal and Ceramics Nanocomposites. In *Nanocomposite Science and Technology*; John Wiley & Sons: Hoboken, NJ, USA, 2003; pp. 1–75.
120. Bagheri, H.; Ayazi, Z.; Aghakhani, A. A novel needle trap sorbent based on carbon nanotube-sol–gel for microextraction of polycyclic aromatic hydrocarbons from aquatic media. *Anal. Chim. Acta* **2011**, *683*, 212–220. [CrossRef]
121. Oliveira, M.; Nogueira, R.; Machado, A.V. Synthesis of aluminium nanoparticles in a PP matrix during melt processing: Effect of the alkoxide organic chain. *React. Funct. Polym.* **2012**, *72*, 703–712. [CrossRef]
122. Bashtani, E.; Amiri, A.; Baghayeri, M. A nanocomposite consisting of poly (methyl methacrylate), graphene oxide and Fe_3O_4 nanoparticles as a sorbent for magnetic solid-phase extraction of aromatic amines. *Microchim. Acta* **2018**, *185*, 1–8. [CrossRef] [PubMed]
123. Farjaminezhad, M.; Tehrani, M.S.; Aberoomand Azar, P.; Bohlooli, S.; Hussain, S.W. Fe_3O_4/polyethylene glycol nanocomposite as a solid-phase microextraction fiber coating for the determination of some volatile organic compounds in water. *J. Sep. Sci.* **2017**, *40*, 717–724. [CrossRef]
124. Notario, B.; Pinto, J.; Rodriguez-Perez, M.A. Nanoporous polymeric materials: A new class of materials with enhanced properties. *Prog. Mater. Sci.* **2016**, *78*, 93–139. [CrossRef]
125. Khataei, M.M.; Yamini, Y.; Shamsayei, M. Applications of porous frameworks in solid-phase microextraction. *J. Sep. Sci.* **2021**, *44*, 1231–1263. [CrossRef]
126. Polarz, S.; Smarsly, B. Nanoporous materials. *J. Nanosci. Nanotechnol.* **2002**, *2*, 581–612. [CrossRef]
127. Dubbeldam, D.; Walton, K.S.; Vlugt, T.J.; Calero, S. Design, parameterization, and implementation of atomic force fields for adsorption in nanoporous materials. *Adv. Theory Simul.* **2019**, *2*, 1900135. [CrossRef]

128. Langley, P.; Hulliger, J. Nanoporous and mesoporous organic structures: New openings for materials research. *Chem. Soc. Rev.* **1999**, *28*, 279–291. [CrossRef]
129. Hentze, H.P.; Antonietti, M. Porous polymers and resins for biotechnological and biomedical applications. *Rev. Mol. Biotechnol.* **2002**, *90*, 27–53. [CrossRef] [PubMed]
130. Gholivand, M.B.; Abolghasemi, M.M.; Fattahpour, P. A Hexagonally Ordered Nanoporous Silica-Based Fiber Coating for SPME of Polycyclic Aromatic Hydrocarbons from Water Followed by GC–MS. *Chromatographia* **2011**, *74*, 807–815. [CrossRef]
131. Zhang, S.; Yang, Q.; Yang, X.; Wang, W.; Li, Z.; Zhang, L.; Wang, C.; Wang, Z. A zeolitic imidazolate framework based nanoporous carbon as a novel fiber coating for solid-phase microextraction of pyrethroid pesticides. *Talanta* **2017**, *166*, 46–53. [CrossRef]
132. Rahimi, A.; Hashemi, P.; Badiei, A.; Arab, P.; Ghiasvand, A.R. CMK-3 nanoporous carbon as a new fiber coating for solid-phase microextraction coupled to gas chromatography–mass spectrometry. *Anal. Chim. Acta* **2011**, *695*, 58–62. [CrossRef]
133. Jin, H.-F.; Shi, Y.; Cao, J. Recent advances and applications of novel advanced materials for solid-phase microextraction in natural products. *TrAC Trends Anal. Chem.* **2024**, *178*, 117858. [CrossRef]
134. Młynarczyk, M.; Belka, M.; Hewelt-Belka, W. Novel materials and approaches for solid-phase (micro) extraction in LC-MS-based metabolomics. *TrAC Trends Anal. Chem.* **2024**, *180*, 117941. [CrossRef]
135. Kataoka, H.; Ishizaki, A.; Saito, K.; Ehara, K. Developments and Applications of Molecularly Imprinted Polymer-Based In-Tube Solid Phase Microextraction Technique for Efficient Sample Preparation. *Molecules* **2024**, *29*, 4472. [CrossRef]
136. Juanjuan, F.; Jiang, Z.; Ding, Y.; Li, X.; Sun, M. Preparation and application of novel sorbents for in-tube solid-phase microextraction. *TrAC Trends Anal. Chem.* **2024**, *181*, 118047. [CrossRef]
137. Sarafraz-Yazdi, A.; Rounaghi, G.; Vatani, H.; Razavipanah, I.; Amiri, A. Headspace solid phase microextraction of volatile aromatic hydrocarbons using a steel wire coated with an electrochemically prepared nanocomposite consisting of polypyrrole, carbon nanotubes, and titanium oxide. *Microchim. Acta* **2015**, *182*, 217–225. [CrossRef]

Disclaimer/Publisher's Note: The statements, opinions and data contained in all publications are solely those of the individual author(s) and contributor(s) and not of MDPI and/or the editor(s). MDPI and/or the editor(s) disclaim responsibility for any injury to people or property resulting from any ideas, methods, instructions or products referred to in the content.

MDPI AG
Grosspeteranlage 5
4052 Basel
Switzerland
Tel.: +41 61 683 77 34

Processes Editorial Office
E-mail: processes@mdpi.com
www.mdpi.com/journal/processes



Disclaimer/Publisher's Note: The title and front matter of this reprint are at the discretion of the Guest Editor. The publisher is not responsible for their content or any associated concerns. The statements, opinions and data contained in all individual articles are solely those of the individual Editor and contributors and not of MDPI. MDPI disclaims responsibility for any injury to people or property resulting from any ideas, methods, instructions or products referred to in the content.





Academic Open
Access Publishing

mdpi.com

ISBN 978-3-7258-8814-6